

AN ABSTRACT OF THE DISSERTATION OF

Jesse Loren Paris for the degree of Doctor of Philosophy in Wood Science and Materials Science presented on February 21, 2014.

Title: Wood-Adhesive Bondline Analyses with Micro X-ray Computed Tomography.

Abstract approved: _____
Frederick A. Kamke

There is no doubt that adhesive penetration plays an important role in wood bondline joint performance and durability; yet, to date there is no direct experimental evidence linking penetration depth with bond performance. This is, in part, because adhesive penetration is commonly assessed with various 2D microscopy techniques that are destructive to the specimen, and are incapable of detecting the 3D penetration path followed during bond formation. Micro x-ray computed tomography (XCT) is a non-destructive imaging technique, capable of providing 3D bondline data. A significant challenge, however, has been generating sufficient x-ray attenuation contrast between cured adhesive polymers and wood cell walls for quantitative material segmentation. In this work, three separate wood-adhesive types, phenol formaldehyde, polymeric diphenylmethane diisocyanate, and a hybrid polyvinyl acetate, were uniformly tagged with iodine to overcome these challenges. Laminate bondlines, prepared with these

adhesives and three different wood species, Douglas-fir, loblolly pine, and hybrid poplar, were analyzed with synchrotron-based, micro XCT. Resulting bondline reconstructions had approximately 1.5 μm voxel dimensions, and were segmented into wood and adhesive material phases with simple gray-scale image histogram threshold operations.

Elemental analyses and fluorescence microscopy were used to confirm iodine tags remained associated with adhesive polymers in the liquid resins, and throughout the bonding process. Both iodine concentration and cured adhesive density were demonstrated to significantly impact x-ray attenuation behavior. Furthermore, XCT acquisition parameters were compared and optimized for the highest absorption contrast in these wood-bondline specimens. However, phase-contrast edge enhancement artifacts were also discussed, and the use of a quantitative phase retrieval reconstruction method was demonstrated with one wood-bondline specimen.

Volumetric penetration behavior was quantified and compared between six XCT replicates from nine different adhesive/species treatment combinations, using two different calculations. Results showed penetration variability between different treatment combinations, between individual replicates within a particular treatment, along the length of a single specimen, and from one side of the bondline to the other. Penetration behavior appears to be correlated with adhesive viscosity, but is also strongly dependent on the wood anatomy in the vicinity of the bondline. Cell wall penetration behavior was also observed around adhesive-filled lumens for some of the treatment types; though, distinguishing between the pure material signals inside the wood cell walls was below the resolution limits in this study. XCT penetration results showed good agreement with

results from fluorescence micrographs of specimens excised from the same laminates.

However, the 3D adhesive-phase sub-volumes provided novel views of the cured adhesive networks and morphology, previously indistinguishable with conventional 2D surface microscopy techniques.

Undamaged XCT specimens, 3D penetration results, and digital, segmented bondline data from this work are being used in a broader, ongoing project to develop a micro-mechanics numerical model to assess wood-bondline joint performance, while quantitatively accounting for the role of adhesive penetration.

©Copyright by Jesse Loren Paris

February 21, 2014

All Rights Reserved

Wood-Adhesive Bondline Analyses with Micro X-ray Computed Tomography

by

Jesse Loren Paris

A DISSERTATION

submitted to

Oregon State University

in partial fulfillment of
the requirements for the
degree of

Doctor of Philosophy

Presented February 21, 2014

Commencement June 2014

Doctor of Philosophy dissertation of Jesse Loren Paris presented on February 21, 2014.

APPROVED:

Major Professor, representing Wood Science and Materials Science

Head of the Department of Wood Science and Engineering

Director of the Materials Science Program

Dean of the Graduate School

I understand that my dissertation will become part of the permanent collection of Oregon State University libraries. My signature below authorizes release of my dissertation to any reader upon request.

Jesse Loren Paris, Author

ACKNOWLEDGEMENTS

I wish to express my sincere gratitude to my major advisor, Dr. Fred Kamke, for his support and guidance throughout this project. Additionally, I wish to extend thanks to Dr. John Nairn, Dr. Lech Muszyński, and Matthew Schwarzkopf for being part of the collaborative team working on the broader research project, of which this work was one component. Special thanks are also offered to Drs. Dorthe Wildenschild and Kate Lajtha for their service and support on my graduate defense committee.

My sincere appreciation is also extended to the Wood-Based Composite Center (WBC) for funding this work, and to the WBC member companies for technical advice and feedback throughout the project. Special recognition and thanks are given to the research team at Arclin in Springfield, Oregon, for technical assistance and donating materials to this work. Also, many thanks are given to the research scientists at the Advanced Photon Source, at the Argonne National Laboratory in Argonne Illinois, and the Advanced Light Source at the Lawrence Berkeley National Laboratory in Berkeley California, where the bulk of this data was collected. In particular, I wish to recognize and thank Drs. Xianghui Xiao and Dula Parkinson for assistance with data collection and interpretation.

I also wish to thank my fellow students, the faculty, and the staff in the Department of Wood Science and Engineering at Oregon State University; with special recognition for Milo Clausen, whose advice no grad student could survive without. Lastly, I wish to thank my dearest friends and family, especially my parents, Kevin and Cindy Paris, whose love and support have been unwavering throughout this journey.

CONTRIBUTION OF AUTHORS

Dr. Frederick A. Kamke assisted with data interpretation, and was involved with the design and writing of Chapters 3 – 6. Dr. Kamke was also the lead author of Appendix A. Scientists Reginald Mbachu and Sara K. Gibson assisted with data collection and interpretation for Chapter 3. Dr. Xianghui Xiao was involved in data collection, and assisted in writing Chapter 4 and Appendix A. Drs. John Nairn and Lech Muszyński, and scientist Matthew Schwarzkopf assisted in the data collection and interpretation for Chapter 5, and with writing Appendix A.

TABLE OF CONTENTS

	<u>Page</u>
Chapter 1. Introduction	1
1.1 Background and Justification	1
1.2 Technical Objectives	6
1.3 Dissertation Structure	8
Chapter 2. Literature Review	11
2.1 Wood Adhesion	11
2.1.1 Mechanisms of Adhesion	12
2.1.2 Wood Adherends	15
2.1.3 Wood-Adhesives	19
2.1.4 Joint Performance	29
2.2 Adhesive Penetration	34
2.2.1 Measurement	36
2.2.2 Impacts on Joint Performance	42
2.3 X-Ray Computed Tomography	45
2.3.1 Background and Instrumentation	45
2.3.2 X-ray Tomography of Wood and Wood-Composites	59
2.4 References – Introduction and Literature Review	75
Chapter 3. Phenol Formaldehyde Adhesives Formulated for Advanced X-ray Imaging in Wood-Composite Bondlines	98
3.1 Abstract	100
3.2 Introduction	101
3.3 Experimental	104
3.3.1 Adhesive formulation	104
3.3.2 Gel permeation and ion chromatography	104

TABLE OF CONTENTS (Continued)

	<u>Page</u>
3.3.3 Powder density, neutron activation analysis, and x-ray radiography	105
3.3.4 Composite specimen preparation	106
3.3.5 Fluorescence and scanning electron microscopy (FM and SEM, respectively) and energy dispersive spectroscopy (EDS)	106
3.3.6 Synchrotron, micro x-ray computed tomography (XCT)	108
3.4 Results and Discussion	109
3.4.1 Adhesive properties	113
3.4.2 Adhesive x-ray attenuation	115
3.4.3 Tag mobility assessment	121
3.5 Conclusions	125
3.6 Acknowledgements	126
3.7 References	126
Chapter 4. X-ray Computed Tomography of Wood-Adhesive Bondlines: attenuation and phase contrast effects.....	134
4.1 Abstract	136
4.2 Introduction	136
4.3 Experimental	141
4.3.1 Adhesive formulation and bonding.....	141
4.3.2 Adhesive cure and elemental analysis	142
4.3.3 Micro X-ray Computed Tomography	144
4.4 Results and Discussion.....	146
4.4.1 Tag efficacy and adhesive X-ray attenuation.....	147
4.4.2 Adhesive absorption contrast	153
4.4.3 Quantitative Phase Retrieval.....	164
4.5 Conclusions	168

TABLE OF CONTENTS (Continued)

	<u>Page</u>
4.6 Acknowledgements	169
4.7 References	169
Chapter 5. Wood-Adhesive Penetration: Non-Destructive, 3D Visualization and Quantification.....	178
5.1 Abstract	180
5.2 Introduction	181
5.3 Materials and Methods.....	184
5.3.1 Composite specimen preparation.....	184
5.3.2 Synchrotron, micro X-ray computed tomography (XCT)	184
5.3.3 Image processing and penetration analysis.....	185
5.4 Discussion	186
5.4.1 XCT material segmentation	187
5.4.2 Comparison of 3D adhesive penetration behavior.....	192
5.5 Conclusions	195
5.6 Acknowledgements	196
5.7 References	196
Chapter 6. Quantitative Wood-Adhesive Penetration with X-ray Computed Tomography	201
6.1 Abstract	203
6.2 Introduction	203
6.3 Materials and Methods.....	208
6.3.1 Viscosity determination	208
6.3.2 Fluorescent microscopy (FM) and image analysis	209
6.3.3 Measurement of adhesive penetration	211
6.4 Results and Discussion.....	214

TABLE OF CONTENTS (Continued)

	<u>Page</u>
6.4.1 Adhesive viscosity	214
6.4.2 3D wood-adhesive penetration	217
6.5 Conclusion.....	230
6.6 Acknowledgements	231
6.7 References	231
Chapter 7. Summary and Conclusions.....	239
7.1 Summary	239
7.2 Conclusions	241
7.3 Limitations and Future Work.....	244
Appendix A. Methodology for micro-mechanical analysis of wood-adhesive bonds using xct and numerical modeling	248
Appendix B. Replicate Weighted Penetration Results	281

LIST OF FIGURES

<u>Figure</u>	<u>Page</u>
2-1 Resol phenol formaldehyde resin formulation and representative structures (a) methylation at ortho and para sites, and condensation to quinone methide ions (b) quinone methide polymerization with phenol (I) or methylolphenols (II), (c) direct polymerization between methylol phenols and the release of formaldehyde upon heating, and (d) resin cure where reactive poly-phenol pre-polymers cross-link	23
2-2 (a) One of many potential MDI monomer units, (b) isocyanate reaction with water, representing the common pMDI cure mechanism, (c) possible isocyanate reaction with hydroxyl-rich wood polymers	25
2-3 PVAc polymerization and resulting (a) homopolymer or (b) a more flexible copolymer with ethylene-bridge.....	28
2-4 Wood-adhesive bondline, dark, grey and white regions represent pure wood phase, wood-adhesive <i>interphases</i> and pure adhesive phases, respectively; rings represent the property gradient due to resin penetration	35
2-5 Cartoon representation of traditional 2D x-ray radiography	46
2-6 Fundamental x-ray tomography imaging system; images correspond to typical tomographic wood-composite specimen from this study	51
3-1 Cross-section XCT slices of each specimen type with indicated scan energy. Sub-areas of wood and air only (top row), and region containing a horizontal bondline (bottom row) were selected from the same reconstructed image (scale bars = 100 μm). Parent images were first normalized to utilize the full 256 bit gray-scale range. Gray-scale histograms correspond to the respective sub-areas, and each histogram pair has the same area under the curve (vertical axis = pixel count).....	111
3-2 XCT sub-volume (1.71 mm^3) virtually excised from the same HP, IPF2 specimen in Figure 3-1e. (a) Solid 3D volume; (b) segmented, adhesive phase not including the wood material occupying the same internal space	113
3-3 Repeat units and molecular formulae for (a) cellobiose and (b) cured resol-PF adhesive polymers used to calculate theoretical attenuation coefficients for each material as a function of beam energy (c); plot key indicates specific molecular formulae and density values used for each attenuation prediction.....	117
3-4 (top) Mean x-ray transmission (gray-scale) intensity through air and adhesive powder with increasing wt% iodine, error bars indicate ± 1 standard deviation; (bottom) mean intensity ratio, I/I_0 , and fitted regression line; measured wt% I, apparent densities and void-volume fractions are also provided.....	119

LIST OF FIGURES (Continued)

<u>Figure</u>	<u>Page</u>
3-5 FM images (left) and EDS elemental maps (right) of the same specimen surface for composites bonded with RbPF (a & b, DF), BrPF (c & d, SYP), IPF1 (e & f, HP) and IPF2 (g - i, HP). BrPF FM image (c) acquired with 'blue' filterset and (a , e & g) acquired with UV filterset. EDS red phase represents oxygen signal and green indicates tag-element of interest: Rb (b), Br (d), I (f & h) and Na (i). Scale bars = 100 μm	123
4-1 Hybrid PVAc (a, c, e) and IpMDI (b, d, f) bondlines in wood paired by FM (a - b) and EDS (c - f) images; adhesive appears dark in FM images; EDS elemental signal for oxygen shown in red, element of interest in green (c & d – iodine, e – sodium, and f – chlorine); scale bars = 200 μm	149
4-2 (a - c) theoretical dimer repeat units for each modified adhesive system, and (d) calculated x-ray attenuation coefficients for each cured adhesive; the legend provides the specific molecular formula and density (ρ) values used in the calculation; the vertical line at 15.3 KeV indicates the XCT scan energy	152
4-3 IPF bonded wood shown as XCT gray-scale sub-volumes (a - b), segmented adhesive (c - d), and "trimmed" 8-bit gray-scale histograms (top - gray value and 1 st derivative, bottom –average 2 nd derivative); species (Left – DF, right – SYP); sub-volume bounding box dimensions in μm	155
4-4 (a) Cross-section slice from DF IPF sub-volume in Figure 4-3 showing earlywood (left) and latewood (right), after histogram normalization (top) and trimming (bottom), and (b) gray value plots corresponding to the 100 μm line segments in (a).....	157
4-5 IpMDI bonded wood shown as XCT gray-scale sub-volumes (a - b), segmented wood and adhesive (c - d), segmented adhesive (e - f), and "trimmed" 8-bit gray-scale histograms (top - gray value and 1 st derivative, bottom –average 2 nd derivative); species (Left – DF, right – HP); sub-volume bounding box dimensions in μm	160
4-6 Hybrid IPF/PVAc bonded SYP XCT gray-scale sub-volumes (a - b), segmented adhesive (c - d), and "trimmed" 8-bit gray-scale histograms (e - f; top - histogram and 1 st δ , bottom – true and 5X moving average 2 nd δ); sub-volume bounding box dimensions in μm	162
4-7 Gray-scale histograms and corresponding SYP IpMDI composite XCT slice (same specimen view) scanned at 8 or 30 mm specimen-to-scintillator distances, and reconstructed with an FBP or QPR algorithm; histograms: (a) normalized, and (b) trimmed at the specified value and converted to 8-bit data; images: (c - e) normalized, and (f – h) 8-bit; scale bars = 200 μm	166

LIST OF FIGURES (Continued)

<u>Figure</u>	<u>Page</u>
5-1 Gray-scale histogram and first derivative curves for processed ROIs with lines indicating the material segmentation threshold values (a) DF_hybrid PVAc, (b) HP_IPF and (c) SYP_IpMDI (voxel count in millions).....	189
5-2 ROI for specimen DF_hybrid PVAc (1.71 mm ³ , bounding box dimensions in μm); (a) gray-scale XCT view corresponding to the histogram in Figure 5-1a, (b) segmented composite and (c) segmented hybrid PVAc adhesive	191
5-3 ROI for specimen HP_IPF (1.71 mm ³ , bounding box dimensions in μm); (a) gray-scale XCT view corresponding to the histogram in Figure 5-1b, (b) segmented composite, (c) segmented total adhesive phase, (d) segmented pure IPF and (e) segmented IPF in wood cell walls	192
5-4 ROI for specimen SYP_IpMDI (1.71 mm ³ , bounding box dimensions in μm); (a) gray-scale XCT view corresponding to the histogram in Figure 5-1c, (b) segmented composite, (c) segmented total adhesive phase, (d) segmented pure IpMDI and (e) segmented IpMDI in wood cell walls	192
5-5 EP and WP box plots for DF_hybrid PVAc, HP_IPF and SYP_IpMDI; measured values represent the total adhesive area, including cell wall penetration; plots include the median (center line) and mean (bold diamond) for each distribution; ‘Top’ and ‘Bottom’ correspond to the respective top or bottom laminate as shown in Figures 5-2 to 5-4, while ‘Mean’ refers to the average penetration between the top and bottom laminates	193
6-1 FM adhesive segmentation of a hybrid PVAc bondline: (a) original RGB image; (b) result of ‘B’ + ‘G’ - ‘R’ color channels; (c) moving average histogram and 1 st derivative from ‘b’; (d) binary adhesive; (e) adhesive overlain on original image, pure adhesive layer (dark) and penetrated adhesive (light); scale bars = 200 μm.....	211
6-2 FM image of HP IpMDI bondline; black line = defined wood-lamina interface, and minimizes y-coordinate position error between the ten, equally-spaced, black points across the image; scale bar = 100 μm	212
6-3 Average (n = 3) steady-state viscosity flow curves for the iodine-tagged and control adhesives, bars = ± 1 standard deviation.....	215
6-4 XCT (left) and FM (right) adhesive penetration results for each wood adhesive/species treatment; (a – b) WP; (c – d) EP; and (e – f) total adhesive area; results are the average from both sides of the bondline; boxplots (a and c) each contain ≈ 9000 data points (1500 slices x 6 replicates) per treatment, center circles = treatment means; stacked data points (b, d, e, and f) = replicate means (6 for XCT, and 3 for FM).....	221

LIST OF FIGURES (Continued)

<u>Figure</u>	<u>Page</u>
6-5 SYP IpMDI FM (left) vs. XCT (right) comparison; (a – b) original images, (c) segmented adhesive, overlain on original image, (d) binary bulk adhesive + cell wall penetration, and (e – f) 8-bit gray-scale histograms indicating threshold values (vertical lines); scale bars = 100 μm	222
6-6 Adhesive XCT WP results (average of both bondline sides) by replicate for (a) SYP IpMDI, (b) SYP IPF, and (c) DF hybrid PVAc; $n \approx 1500$ slices per replicate; center circles = specimen means; replicates 1 – 3 and 4 – 6 were excised from 2 separate original laminates	225
6-7 DF hybrid PVAc replicate 4 sub-volume: (a - b) RL planes show effects of grain angle, ray cells and a fusiform ray (arrows) on penetration, (c – d) transverse planes, 23 μm apart, above and in fusiform ray, (e) TL view into fusiform ray, and (f) 3D adhesive sub-volume (μm box dimensions); scale bars = 100 μm (a – e).....	227
6-8 IpMDI bubbles in HP vessel; (a) sub-volume top slice, (b) 400 μm below top ($\sim 1/3$ length), (c) RL plane through vessel, and (d) segmented adhesive column (μm box dimensions); scale bars = 100 μm (a – c)	228
6-9 IPF cured adhesive cracks in HP vessels; (a) segmented bulk adhesive, and (b) total adhesive including cell wall penetration (μm box dimensions)	230

LIST OF TABLES

<u>Table</u>	<u>Page</u>
1-1 Acronyms and abbreviations used throughout document.....	10
3-1 XCT acquisition parameters for tagged-PF wood composites	108
3-2 Adhesive material properties. Molecular weight data includes number average (Mn), weight average (Mw) and PDI (Mw:Mn). Standard deviation in parentheses (n=3). BrPF and IPF NAA results are from a single replicate. RbPF results were adopted from another report (Modzel 2009); RbPF density was estimated.....	114
4-1 Average cured adhesive solids content, powder density, and iodine content; n = 3, standard deviation in parentheses	151
6-1 XCT mean adhesive penetration results and coefficient of variation (COV) for each wood adhesive/species treatment	219
A-1 Mechanical properties assumed for global FEA and local MPM simulations	264

LIST OF APPENDIX FIGURES

<u>Figure</u>	<u>Page</u>
A-1 (a) Universal test machine showing lap-shear specimen and DIC optical measurement system; (b) Example of a lap-shear specimen with ends bonded to graphite-epoxy tabs for attachment to test machine; 1 cameras, 2 beam splitter, 3 microscope objective, 4 specimen, 5 load cell, 6 test frame, 7 grip, 8 graphite-epoxy tab	254
A-2 Poplar and IPF lap-shear specimen; a) Transverse view of reconstructed tomogram; b) Radial slice from (a) showing microtomed surface; c) Segmented sub-volume from (a, box) showing adhesive phase; d) Segmented sub-volume from (c) showing adhesive phase; e) UV fluorescence micrograph of microtomed surface; f) Same surface as (e) with speckle pattern applied for DIC displacement measurement.....	256
A-3 Example of tomogram of poplar bonded with IPF (0.3 mm x 1 mm x 1mm). Reference planes are shown for transverse (end-grain), radial, and tangential surfaces; Reference directions, relative to anatomy of wood, indicated at right: longitudinal (L), radial (R), tangential (T)	259
A-5 Tomogram images showing radial surface to illustrate the spatial resolution and feature recognition; pixel size = 1.45 μm	266
A-6 Histogram plot of gray-scale values for a sub-volume of a tomogram. Gray-scale values have been linearly normalized from 0 to 255. Voxels, with gray-scale values indicated, have been assigned to represent voids (0 - 83), cell wall (84 - 141) and adhesive (142 - 255)	267
A-7 Progression of shear strain development during tension loading in half of a lap-shear specimen (notch at right) as calculated from DIC measurement; a) 0 N, b) 10 N, c) 20 N, d) 30 N	268
A-8 The displacements in the z direction (w) and y direction (v) on the top (z = 0) and bottom (z = 2.068) of the modeled subvolume; Gray lines are experimental results by DIC; Black lines are FEA calculations; Dotted lines are fits to FEA results that provided functions to input for MPM boundary conditions	269
A-9 (a) Experimental DIC results for displacements in z-direction (horizontal); (b) The same displacements estimated by the MPM model	270
A-10 (a) Normal strain in z-direction, and (b) shear strain measured by DIC; (c) Normal strain in z-direction, and (d) shear strain from MPM results	270
A-11 MPM simulation results for lap-shear specimen loaded in z-direction as viewed in x-y plane; a) equivalent strain, b) equivalent stress	272

LIST OF APPENDIX FIGURES (Continued)

<u>Figure</u>	<u>Page</u>
A-12 MPM simulation results showing notched end of lap-shear specimen; (a) Regions of high equivalent strain; (b) Regions of high equivalent stress. Both plots are colored by material, where dark blue is adhesive and yellow is cell wall substance.....	273
B-1 IPF WP results by replicate for (a) DF, (b) HP, and (c) SYP; center circles = specimen means.....	281
B-2 Hybrid PVAc WP results by replicate for (a) DF, (b) HP, and (c) SYP; center circles = specimen means	282
B-3 IpMDI WP results by replicate for (a) DF, (b) HP, and (c) SYP; center circles = specimen means.....	282

CHAPTER 1. INTRODUCTION

1.1 Background and Justification

Adhesively-bonded wood products have been used for centuries in both structural and non-structural applications. The process of breaking down solid wood into smaller components, and reforming them into integral laminate or composite products, through adhesive bonding, can extend the use of the wood resource, randomize natural variability, produce a variety of product sizes and geometries, and improve dimensional stability (Frihart 2005; River et al. 1991; Sellers 1994). Today, wood-based composites play a vital role, and are still growing in use, in furniture manufacturing, construction and engineering applications. However, global pressures, such as resource availability, rising energy costs, and environmental policy, continue to challenge industrial composite and wood-adhesive manufacturers to utilize more sustainable and ecofriendly materials and processes. In turn, significant research efforts have focused on the design and development of novel composite and adhesive technologies, as well as on the fundamental science and mechanisms governing wood-adhesion. In particular, many scientific questions still remain as to the precise nature of wood-adhesive interactions, and the effect of adhesive penetration on mechanical joint-performance and moisture durability. Answers to these questions require novel, systematic analyses at multi-dimensional scales, and a combination of different analytical techniques. Furthermore, these wood-science challenges necessitate multi-disciplinary solutions, as the answers will undoubtedly be explained through physical, mechanical, chemical, and biological concepts.

The primary role of a wood adhesive is to transfer stresses across the joint interface, or interphase region, and into structurally sound material. Adhesive penetration, no doubt facilitates this stress transfer, and helps reinforce damaged wood cells on the adherend surfaces. Additionally, adhesive penetration increases the total surface area over which wood/adhesive intermolecular associations effectively operate, and once solidified, adhesive polymer entanglements or cured networks, provide mechanical interlocking support to the bondline (Schultz and Nardin 1994). Over-penetration, on the other hand, can result in a starved bondline with poor performance, and be wasteful of expensive adhesive resins. The effects of wood-adhesive penetration on joint performance have been extensively studied (Kamke and Lee 2007); however, to date, there is no clear correlative relationship between penetration depth and bond performance.

One primary reason for these knowledge gaps is due to the many sources of variability and overall complexity in wood-adhesive bondlines. For instance, vast differences can exist between different wood species, between trees of the same species, and between locations within a single tree. As a material, wood is a porous, orthotropic and hygroscopic, bio-composite with multi-scale, hierarchical order (Panshin and De Zeeuw 1980; River et al. 1991; Rowell et al. 2005; Terashima et al. 2009). The majority of wood cells are oriented longitudinally, which provide structural support and conduct fluids vertically along a tree's stem. However, wood also contains radially oriented cells designed for lateral fluid flow. Liquids, of sufficiently low molecular weight, may also move laterally between neighboring cells through interconnecting pits (Kamke and Lee 2007; Panshin and De Zeeuw 1980). Longitudinal cells form concentric, annual growth rings, and each growth ring consists of both thin-walled, wide-diameter, earlywood cells

and thick-walled, small-diameter, latewood cells. Rings closer to the center of a tree, known as heartwood, participate in different physiological functions, and may contain higher concentrations of chemical extractives, than outer rings, known as sapwood. At the microscopic scale, individual wood cell walls are also multi-layer structures, comprised of natural, biopolymers, namely cellulose, hemicelluloses, and lignin. Furthermore, these molecular components are found in different concentrations and orientations in each cell wall layer.

Wood-adhesive systems are also highly variable (Frihart 2005; Rowell et al. 2005; Schultz and Nardin 1994). Fundamental chemical differences separate the general adhesive classes; however, viscosity, morphology, cross-link density, reactivity, and solids content may all be different between formulations of the same adhesive type. Furthermore, adhesive properties change in contact with wood, as they exchange ions and moisture with wood cell walls, and interact with cell wall components through intermolecular associations. Adhesive molecules may exhibit preferential affinity for different cell wall polymers, and depending on molecular weight, can even have small monomers or oligomers infiltrate nano-scale voids in cell walls (Frazier and Ni 1998; Kamke and Lee 2007). Also, different manufacturing operations, such as wood drying, surfacing and thermal treatments, or variable bonding parameters, such as consolidation pressure, temperature and rate, can all have significant effects on wood-adhesive interactions and bond quality.

Another significant reason for lack of better correlations between wood-adhesive penetration and bondline performance relates to how penetration is observed and

quantified. Adhesive penetration is typically measured from 2D microscopy images of the transverse, or cross-section, surface of wood-laminate bondlines, and it is calculated as a perpendicular distance between identified adhesive elements and the adherend interface (Kamke and Lee 2007; Sernek et al. 1999). This approach, however, suffers from two inherent flaws. First, 2D images provide a planar view showing the location of cured adhesive elements, but do not show the 3D connected pathway the adhesive traveled during bonding. This can lead to misinterpretation of results, as information is lost above and below the image-plane. Often adhesive filled lumens are observed far from the bondline, and appear unconnected to other adhesive regions; without the out-of-plane information it is difficult to interpret how such adhesive elements contribute to the bondline performance. The second flaw is that 2D microscopy techniques often necessitate specimen surface preparation, such as water soaking, thin sectioning, or clean-cutting with a microtome. Yet, these are inherently destructive to the wood bondline. Mechanical joint tests are often conducted on matched specimens, or on those from bondlines prepared under similar conditions. In either case, natural variability between different wood specimens tends to complicate quantitative results.

The data collected from traditional mechanical joint tests also obscures the relationship between adhesive penetration and bondline performance. Many conventional joint tests are strength-based, meaning that they measure ultimate failure loads (DeVries and Borgmeier 1994; River 2003; River et al. 1991). Average stresses at failure are subsequently back-calculated based on specimen geometry. However, stress distributions are rarely uniform across wood bondlines, and failures generally originate at stress concentrations around discrete flaws inside the bonded specimens. Furthermore, average

strain may be calculated with strain-gauges or by instrument cross-head displacements.

Though these calculations only account for the displacement at a single, or a few, discrete points, and thus neglect the regions of high strain which may precede failure (Serrano and Enquist 2005).

The present research is part of a broader project to investigate micro-scale, wood-adhesive interactions. The overall project goal is to develop a numerical, computer model to simulate stress-transfer and joint performance in wood bondlines, while quantitatively accounting for the role of adhesive penetration. The model is based on the material point method (MPM), which is a powerful tool in computational mechanics, and offers a significant advantage over finite element models of wood. It is difficult to accurately represent complex wood structures and adhesive penetration patterns in a finite element numerical mesh. However, with MPM, individual pixels from digital images can be directly translated into material points, and assigned distinct properties and boundary conditions (Nairn 2006). Provided sufficient contrast and resolution, digital images of wood-adhesive bondlines can be segmented into the three distinct material phases, air, or voids space in the cell lumens, wood cell walls, and adhesive. Numerical MPM particles, directly based on these phases, thus represent the realistic material structures.

In this work, digital bondline data was collected with non-destructive, 3D, micro X-ray computed tomography (XCT), and reconstructed image-stacks were segmented into the distinct material phases, with simple gray-scale threshold operations. Following XCT analysis, the mechanical joint performance of the same, undamaged wood-bondlines was evaluated with micro-bond, lap-shear tests. Full-field, surface deformations across the

bondline were collected and analyzed using the non-contact, digital image correlation (DIC) technique (Serrano and Enquist 2005). While, true bondline stresses cannot be directly determined from mechanical tests, the DIC technique can calculate the surface strain-fields in the bondline region, with microscopic resolution. These 2D strain-fields can be subsequently compared to ones generated from MPM model simulations of the same specimen and test parameters. Agreement between the simulated and DIC strain maps can be used to validate particular model assumptions through an inverse problem solving approach (Kamke et al. 2014; Muszynski et al. 2014; Nairn et al. 2014). Reproducing this methodology with multiple wood-adhesive/species combinations, which exhibit different anatomical structures, penetration patterns and mechanical properties, can provide a robust sampling for model calibration. Once calibrated and validated, the model will be able to present realistic, 3D stress distributions and concentrations in wood-adhesive bondlines, while quantitatively accounting for the role of adhesive penetration.

1.2 Technical Objectives

This broader, collaborative project was divided into the following experimental tasks:

1. Collect 3D, micro XCT bondline data from laminates prepared with different adhesives and wood species, and which could be quantitatively segmented into the individual material components.
2. Evaluate the mechanical joint performance, in the elastic regime, for the same bondline specimens as scanned with XCT, and measure the 2D, surface strain-fields across the bondline.

3. Develop a 3D, MPM numerical model to predict stress and strain in adhesively-bonded wood joints, using the realistic wood structure and adhesive penetration patterns from segmented micro XCT bondline data.
4. Validate model assumptions through inverse problem solving methodology by comparison between predicted and measured specimen strain-fields
5. Use model to investigate correlations between wood adhesive penetration and mechanical joint performance.

This dissertation presents the complete methods and results on the subject of XCT data collection (Task 1), as well as adhesive formulation, material properties and 3D penetration behavior. The technical objectives directly pertaining to this portion of the project, and the work embodied here in, were as follows:

- 1.1. Develop methods to uniformly tag three different wood adhesives with XCT contrast agents for enhanced x-ray attenuation relative to wood cell walls.
- 1.2. Ensure XCT tag elements remain associated with adhesive polymers throughout bonding.
- 1.3. Determine, and minimize, sources of error, including phase-contrast edge artifacts, in XCT analyses of adhesively-bonded wood materials.
- 1.4. Collect 3D XCT bondline data from multiple replicates of different wood adhesive/species combinations.
- 1.5. Quantify 3D wood-adhesive penetration in the different adhesive/species treatment combinations, and compare results with 2D bondline micrographs.

- 1.6. Demonstrate different sources of variability between and within bondline treatment types and specimen replicates.

1.3 Dissertation Structure

This dissertation is written in manuscript format, meaning that individual chapters are separate publications which either have been, or will be submitted to science journals.

This first chapter presents a general introduction and justification for the completed PhD research project. Chapter 1 also describes how this work was part of a broader research effort to analyze micro-scale wood-adhesive interactions, and quantify the role of adhesive penetration on wood-bondline joint performance. Chapter 2 presents a comprehensive literature review focusing on wood adhesion and x-ray tomographic analysis. Chapter 3 describes a methodology for uniformly tagging a phenol formaldehyde adhesive with iodine, such that it yielded sufficient absorption contrast for quantitative material segmentation in reconstructed XCT bondline data. Chapter 3 was accepted and published in the *Journal of Materials Science* (Paris et al. 2014). Chapter 4 introduces similar iodine-tagging methods for two other wood adhesives, a polymeric diphenylmethane diisocyanate and a hybrid polyvinyl acetate, and presents digital image processing procedures and segmentation criteria for all three adhesive types. This chapter also compares absorption contrast and phase-contrast phenomena in wood XCT analyses. Chapter 4 will be submitted to the journal *Wood Science and Technology*. Chapter 5 was a proceedings paper presented at the 2013 *International Conference on Wood Adhesives*, Toronto, Ontario. It presents some preliminary comparisons in the 3D penetration behavior between the three different adhesive types, and discusses sources of variability

between the different treatments, and within individual specimens. Chapter 6 reports and compares quantitative 3D penetration results for six replicates, from nine different wood-adhesive/species treatment combinations, which were calculated with two different penetration equations. Chapter 6 will be submitted to the *International Journal of Adhesion and Adhesives*. Chapter 7 is a general conclusion, which summarizes the conclusions from chapters 3 – 6.

Two appendices are included at the end of this document. The first is a publication presenting the broader research project methodology in greater detail, and demonstrates the combined XCT, DIC, and MPM numerical modeling techniques. Appendix A was published in *Wood and Fiber Science* (Kamke et al. 2014). Appendix B provides additional figures for the within-treatment, (i.e. individual replicate) penetration results for each wood-adhesive/species combination.

A supplementary document, entitled “3D Photo Montage” is also submitted alongside this dissertation. It includes gray-scale and segmented 3D, sub-volume images from each of the 54 total XCT, wood-adhesive bondline specimens. Table 1-1 provides a list of acronyms and abbreviations used throughout this document. While each acronym is appropriately identified in the body of the document near its use, they are collectively included again here as a quick reference for the reader.

Table 1-1 Acronyms and abbreviations used throughout document

2D	two dimensional	GPC	gel permeation chromatography	PRF	phenol resorcinol formaldehyde
3D	three dimensional	HDPE	high-density polyethylene	PUR	polyurethane
CCD	charged coupled device	HP	Hybrid poplar	PVAc	polyvinyl acetate
CT	computed tomography	IC	ion chromatography	PVC	polyvinylchloride
DCB	dual cantilevered beam	IPN	interpenetrating network	RF	resorcinol formaldehyde
DF	Douglas-fir	KeV	kiloelectron volt	RH	relative humidity
DIC	digital image correlation	MDF	medium density fiberboard	SEM	scanning electron microscopy
DVC	digital volume correlation	MP	maximum penetration	SNR	signal to noise ratio
EDS	energy dispersive microscopy	MPM	material point method	SYP	loblolly pine
EMPA	electron microprobe analysis	MUF	melamine urea formaldehyde	TEM	transmission electron microscopy
EP	effective penetration	NAA	neutron activation analysis	UF	urea formaldehyde
eV	electron volt	NCO	isocyanate functional group	UV	ultraviolet
F:P	formaldehyde to phenol molar ratio	PF	phenol formaldehyde	WP	weighted penetration
FEA	finite element analysis	pMDI	polymeric diphenylmethane diisocyanate	WPC	wood plastic composite
FM	fluorescent microscopy	PP	polypropylene	XCT	x-ray computed tomography

CHAPTER 2. LITERATURE REVIEW

2.1 Wood Adhesion

Wood adhesion is the process of joining two or more wood components, or adherends, by chemical and/or physical forces, through the use of an adhesive (Sellers 1994). Resulting wood composites offer several benefits over solid wood products including randomized defects, greater strength, stiffness or toughness, increased dimensional stability, and more uniform material properties. Moreover, wood composites can utilize greater amounts a tree's wood fiber, and can be manufactured into a variety of shapes and sizes unavailable for solid wood products.

Wood-composite technology has been used and developed throughout human history, with earliest wood-adhesion accounts dating back over 3,000 years to veneer applications in ancient Egyptian societies (Frihart 2005; River 1994). Today, wood-based composites range from panel-type products to engineered lumber and beam components vital to global furniture and construction industries. Composite type, application and performance depend on the nature and quality of the adhesive joint, which is itself a function of both wood and resin properties, as well as manufacturing processes (Frihart 2005). Significant academic and industrial research has been focused on studying wood adhesion and adhesive-interactions. These investigations have led to an increased awareness that wood composites are complex systems based on a natural, and thus highly variable, material, and that wood-adhesive interactions depend on a plethora of intrinsic parameters.

2.1.1 Mechanisms of Adhesion

The purpose of wood adhesion is not to simply bind adherends, but to transfer mechanical stresses effectively from the bulk of one substrate into the sound structure of the second. This requires that both the molecular interactions between the adhesive and wood surfaces (adhesive forces) and those within the bulk of the adhesive (cohesive forces) be greater than or equal to the strength of wood (Sellers 1994). While several bonding mechanisms are important to different materials, wood adhesion is commonly described with four primary theories; yet, debate still surrounds each theory due to the complexity and variability of wood bonding.

The adsorption theory is the most widely accepted explanation of wood adhesion; it suggests that intermolecular forces, i.e. London forces, van der Waals forces, dispersion forces or dipole interactions, exist across adhesive/adherend interface (Frihart 2005; Schultz and Nardin 1994). Hydrogen bonding, a specific dipole-dipole interaction, is particularly important in wood adhesion; wood polymers are extremely polar and strongly attract other polar groups common in amino, phenolic and epoxy resins (River et al. 1991). Although secondary intermolecular forces are weaker than primary chemical bonds, their absolute number summed along an adhesive joint are quite effective (Frihart 2005). Of course, joint quality is still highly dependent on the wood surface characteristics as well as the liquid adhesive surface tension (Vick 2002).

The mechanical interlocking theory suggests that liquid adhesive keying, or penetration, into the wood surface macro voids and pores, followed by resin solidification, physically locks the adherends together (Schultz and Nardin 1994). Several correlations certainly

exist between adhesive penetration and composite joint performance (Ebewele et al. 1986a; White 1977); however, other studies have shown good adhesion between very smooth surfaces, where no significant penetration was observed (Kutnar et al. 2008). Moreover, roughening the substrate surfaces with an abrasive will promote a greater degree of mechanical interlocking (Frihart 2005); however, freshly planed or jointed surfaces are recommended for providing superior bond quality (River et al. 1991). Other criticisms of the mechanical interlocking theory suggest that penetration also increases the surface area over which secondary forces act, transfers stresses into sound wood, and creates a more tortuous path to dissipate energy during fracture (Frihart 2005; Kamke and Lee 2007; Schultz and Nardin 1994). Section 2.2 provides a far more detailed discussion on adhesive penetration; however, the fact remains, the role of adhesive penetration on wood-composite performance is not fully understood (Kamke and Lee 2007). This is a primary focus of the present research.

The interpenetrating network (IPN) theory describes the ability for reactive adhesive monomers, or low molecular weight polymers, to inter-diffuse in the molecular-scale voids between wood cell wall polymers (Frihart 2005; Kamke and Lee 2007). The subsequent curing and bridging between the macro and nano-scale penetration behavior is thought to both bulk up cell wall mechanical properties as well as enhance bond durability (Frazier and Ni 1998). Traditionally, it has been difficult to analytically prove the presence of these nano-scale networks; however, recent high-resolution analyses have shown wood cell wall penetration and possible IPN formation for phenol formaldehyde (PF), phenol resorcinol formaldehyde (PRF) and polymeric diphenylmethane

diisocyanate (pMDI) adhesives (Buckley et al. 2002; Frihart et al. 2010; Gindl et al. 2004a; Gindl et al. 2004b; Jakes et al. 2009; Konnerth et al. 2008).

Lastly, the covalent bonding theory suggests that adhesives containing reactive functionalities can form primary chemical bonds with wood cell wall polymers. Several wood adhesives are certainly capable of forming such bonds; yet, lack of analytical evidence has caused great debate as to their formation under normal bonding conditions (Frazier 2003; Frihart 2005; Yelle et al. 2009). Covalent bonds are much stronger than secondary interactions (Schultz and Nardin 1994); however, their contribution to joint strength may be minimal as the collective secondary forces often already exceed the strength of wood (Frihart 2005). On the other hand, primary bonds are desirable for wood adhesion, as they would likely increase moisture durability (Frihart 2005).

In reality, wood-adhesive joints are complex systems. The adhesion mechanisms are likely a combination of chemical and physical parameters, and may depend on penetration at both the macro and molecular scale (Frihart 2005; Kamke and Lee 2007). Apart from the specific interactions that drive adhesion, it is generally accepted that a good adhesive joint requires the following processes (Brady and Kamke 1988; Frihart 2005; River et al. 1991; Sellers 1994; Vick 2002). First, a sufficient amount of resin must be spread evenly across one or both of the adherend surfaces. Second, the surfaces must then be brought into intimate contact through applied mechanical pressure. This facilitates flow, penetration and wetting, and maximizes the adhesive coverage throughout the joint. Intimate contact requires the resin to be liquid at some point during the bonding process. Powder and hot-melt adhesives are also commonly employed for

wood bonding, though they too, must achieve liquid mobility to attain the required coverage and contact. Third, the adhesive must be set, or cured to a solid state; this can occur through a number of physical or chemical mechanisms including solvent loss, cooling, or polymerization. Sufficient time should be allowed to ensure a rigid adhesive layer. Hot-presses are often used to facilitate joint consolidation, flow and curing. While these processes are necessary for producing a quality adhesive joint, they will not always guarantee one; additional intrinsic wood, resin and manufacturing parameters impact bond performance.

The x-ray computed tomography (XCT) technique described in the present research offers a unique opportunity to view wood adhesive interactions at the micrometer scale in three dimensions. Moreover, the technique is non-destructive, and thus allows one to measure mechanical joint integrity on the same unmodified specimens. Systematic XCT studies of composite joints can help answer the many questions still surrounding wood adhesion mechanisms and parameters involved in developing quality wood bonds.

2.1.2 Wood Adherends

Wood is a complex, organic, hierarchical structure. At the atomic scale, dry wood is primarily 50% carbon, 44% oxygen and 6% hydrogen, with trace amounts of nitrogen and other organics. At the molecular level, these elements make up wood's three classes of polymeric materials, namely cellulose (~50%), hemicelluloses (~20-30%) and lignin (16-30%), as well as various extractives, which vary between species. Lignin is a network polymer of repeating phenyl-propane units which incases or embeds the other two long-chain polysaccharides. The highly ordered arrangements of these three components

define the different levels of the wood cell wall. At the cellular level, dry wood is made of cell wall material and empty, intracellular voids known as lumens. The unique polymeric and cellular arrangements give wood its specific chemical, physical and mechanical properties (Panshin and De Zeeuw 1980; Rowell et al. 2005; Terashima et al. 2009). Each component and property were designed by nature to serve a particular physiological function in the living tree; however, to efficiently utilize wood as an engineering material, man must fully understand how its anatomy and chemistry affect its various uses.

Certainly, wood chemistry and anatomy have considerable impact on the nature of wood adhesion. Moreover, properties differ between hardwoods and softwoods, across species, among trees within a species, along a tree's height, whether samples are juvenile or mature wood, or whether they contain earlywood or latewood (Panshin and De Zeeuw 1980; Rowell et al. 2005). Additionally, wood substrates range in size and shape; they can be individual wood fibers or small particles, thin flakes or strands, sliced or peeled veneers, or even whole boards and structural components. Wood's natural, orthotropic nature is inherent at each level, and thus adherend arrangement and orientation also affect composite performance. Extensive reviews and papers have been published highlighting the behavior of wood as an adherend and the specific contributions of its many native parameters (Ebewele et al. 1980, 1986b; Frihart 2005; Frihart and Hunt 2010; River 2003; River et al. 1991; Sellers 1994). This review will, however, only highlight a select few important wood variables impacting adhesion, namely wood's cellular anatomy and surface energy.

Wood is a porous material; as such, its cellular structure plays a considerable role in influencing adhesive penetration and adherend surface area along a bondline. The majority of wood cells are aligned parallel with a tree's longitudinal axis; cross-sectional, end-grain surfaces offer little surface area for adhesion. Most wood products are face or edge glued along some combination of the radial and tangential planes (River et al. 1991); long composites require scarf or finger joints to prevent weaknesses associated with end gluing.

Liquid adhesive penetration away from the bondline follows the cellular structures originally designed by nature for fluid conduction. Highly ordered and radially aligned longitudinal tracheids represent over 90% of softwood cells (Panshin and De Zeeuw 1980); thus, adhesive penetration in softwoods is generally fairly uniform. However, hardwood anatomy is more complex, and contains large diameter vessel elements surrounded by dense collections of structural fibers (Kamke and Lee 2007; River et al. 1991). Moreover, earlywood cells are generally much broader in softwoods and ring-porous hardwoods than latewood cells. Liquid adhesives follow the path of least resistance during bond formation, and thus penetrate deeper into the more permeable earlywood regions (Kamke and Lee 2007; White et al. 1977). Resin quantities are often adjusted based on wood species to prevent the occurrence of a starved bondline or excessive squeeze out due to over- or under-penetration, respectively (River et al. 1991).

Cellular arrangement also plays a large role in wood bonding. Wood is orthotropic, meaning it exhibits different properties in its three mutually perpendicular directions. Wood-adhesive interactions are also directionally dependent, as cells are arranged

differently and have unique pit formations and frequencies in the longitudinal, radial and tangential directions (Brady and Kamke 1988; Frihart and Hunt 2010; Kamke and Lee 2007; River et al. 1991; Vick 2002).

Lastly, cell connectivity plays a role in wood permeability and thus adhesive flow. Bulk fluid flow between adjacent cells occurs through pits, with effective openings ranging from a few nanometers to a few micrometers (Bowyer et al. 2007; Frihart and Hunt 2010; Panshin and De Zeeuw 1980). Pits naturally restrict the size of particles that may flow from cell to cell; however, manufacturing processes, such as drying, can often further reduce wood permeability (Bowyer et al. 2007; Panshin and De Zeeuw 1980). Softwood bordered pits can potentially become aspirated, a condition where the membrane structure adheres to one side of a pit wall, thus closing off the fluid conduction path. Tyloses represent a similar permeability reduction commonly observed in some hardwood species; in this case, tissue from adjacent parenchyma cells balloons through vessel pits into the broad pore lumens, thus obstructing fluid flow (Bowyer et al. 2007; Panshin and De Zeeuw 1980).

Surface energy is also of great importance in bonding, as it drives the intermolecular adhesive forces and controls wettability. Wetting defines how readily a liquid material will spread across and coat a solid surface. It is often characterized by contact angle measurements in which a liquid of known surface tension is dropped onto a solid substrate. The contact angle is measured between the surface and the droplet's interior edge. Favorable wetting occurs when the angle is less than 90° ; however, angles greater

than 90°, as occur when the droplet beads up on the surface, lead to unfavorable wetting and generally poorer adhesion (Frihart 2005; Frihart and Hunt 2010; River et al. 1991).

Wide-ranging studies have been conducted on wood wettability and its impact on adhesion; specific parameters investigated and reviewed include grain direction, thermal treatments (such as drying), pH, moisture content, age, chemical composition, surface roughness and surface cleanliness (Brady and Kamke 1988; Christiansen 1990, 1991; Frihart and Hunt 2010; Mantanis and Young 1997; River et al. 1991; Shi and Gardner 2001). Additionally, wood extractives greatly affect adherend surface energy and wettability, and vary widely across different wood species (Sellers 1994). For instance, southern pines and Douglas-fir represent two of the most commercially relevant softwoods for structural wood-composites in the United States, yet both are prone to surface deactivation due to their extractive contents (Christiansen 1990, 1991; Frihart and Hunt 2010; Hse 1972; Kamke and Lee 2007; Mantanis and Young 1997; River et al. 1991; Sellers 2001; Shi and Gardner 2001; Shupe et al. 1998). Accordingly, these two species are included in the present research as well. An inert hardwood hybrid poplar species was also studied, offering vastly different surface chemistry, permeability behavior and mechanical properties from the two softwoods.

2.1.3 Wood-Adhesives

Wood-adhesive interactions are as much a function of the adhesive type and variables as they are of the wood. Moreover, many various classes of wood adhesives exist, designed for different performance criteria and environmental exposures. River et al. (1991) describe wood adhesives with the terms “durable” and “permanent”. The former

describes the adhesive's physical characteristics in relation to joint strength and stability when exposed to reversible environmental effects (i.e. temperature, moisture, or physical stress); the latter describes the chemical longevity of an adhesive joint under irreversible environmental effects (River et al. 1991). Durable/permanent adhesives are generally thermoset polymers with reactive functionalities; upon cure they form irreversible, rigid, chemically cross-linked networks that are typically stronger than wood (Frihart 2005; Frihart and Hunt 2010; River et al. 1991). Examples of such structural adhesives include PF, RF, melamine formaldehyde, epoxies or isocyanate resins. Amino resins, such as urea formaldehyde (UF), on the other hand are durable/non-permanent adhesives; they again form cross-linked polymer networks which resist temporary environmental exposure, but degrade chemically overtime in service (Frihart and Hunt 2010; Pizzi 2003b; River et al. 1991). Thermoplastic adhesives are long chain polymers, whose properties are time and temperature dependent; these typically fall into the non-durable category (Frihart and Hunt 2010; River et al. 1991). Resin and composite manufacturers can adjust resin formulations for different joint assemblies. Factors such as solids content, viscosity, molecular weight and polydispersity, polymer morphology (i.e. branched or linear), pH and reactant molar ratios can all contribute to an adhesive's penetration, cure and mechanical behavior (Frihart 2005; Frihart and Hunt 2010; Kamke and Lee 2007; River et al. 1991). Numerous studies and reviews have been conducted on wood adhesives (Frihart 2005; Frihart and Hunt 2010; River et al. 1991; Sellers 1994); however this work will focus on only three different adhesive systems: PF, pMDI and polyvinyl acetate (PVAc).

2.1.3.1 *Phenol Formaldehyde (PF)*

Phenol formaldehyde adhesives, also known as phenolic resins, represent the first commercial synthetic polymers (Pizzi 2003a). PF polymers are the products of condensation reactions between formaldehyde and phenol (Park et al. 2002; Pizzi 2003a). The formaldehyde-to-phenol (F:P) molar ratio drives the final polymer molecular weight and cured state, cross-link density. Novolak resins result when the F:P ratio is less than 1; novolak chains do not contain residual reactive methylol groups, and thus do not cross-link during cure. Resol-type PF resins typically contain a F:P molar ratio between 1.25 and 2.6, and are capable of fully cross-linking to form high molecular weight networks (Park et al. 2002). Resols are the more common PFs used as wood adhesives, and are therefore focused on in this work.

PF resol adhesives are prepared under alkaline conditions, most commonly using sodium hydroxide (Park et al. 2002; Pizzi 2003a); a theoretical PF reaction is provided in Figure 2-1. The reactions typically progress in three phases. First, high alkalinity causes electron delocalization at the ortho (2, 6) or para (4) positions on the phenol ring. Formaldehyde readily reacts with the more reactive phenoxide ions, and attaches to form single, di, or trimethylolphenols. These methylolphenols release water, to form unstable quinone methide intermediaries. In the second phase, polymerization begins and molecular weight increases, as the quinone methides react with other phenol or methylolphenol molecules. The latter (Scheme II, Figure 2-1b) tends to dominate with high F:P molar ratios, resulting in poly-phenols which still contain reactive methylol groups. Methylol phenols may also directly condense with each other as shown in Figure 2-1c to create dimethylene

ether bridges. However, these often release formaldehyde when heated and revert back to the more stable methylene bridges. Polymerization will continue in this second phase to a desired resin molecular weight and viscosity. Adjusting temperatures, reactant concentrations, and the order and time in which reactants are added during the cook process can have a dramatic effect on chain length, polydispersity and polymer morphology, all of which will lead to different adhesive properties (Frihart 2005; Park et al. 2002; Pizzi 2003a; Sellers 1994). Typical plywood PF adhesives have a solids content between 40-45%, a viscosity between 150-1200 cP at 25°C, a molecular weight between a few hundred and 30,000 and a pH between 10 and 13 (Pizzi 2003a; Sellers 1994). The third and final stage is PF cure, when the poly-phenol chains react with each other to gel and form a fully cross-linked thermoset. In wood bonding, this stage typically occurs during hot-pressing which facilitates penetration into the substrate and initiates the curing reaction. Initially, the high temperature lowers the adhesive viscosity, allowing it to flow more easily; however, when the bondline reaches 100°C, water rapidly leaves the adhesive phase, and the cross-linked, solid network forms (Brady and Kamke 1988; Park et al. 2002; Pizzi 2003a). Cured PF adhesives exhibit high moisture durability, and are glassy at room temperature, which results in strong and rigid joints.

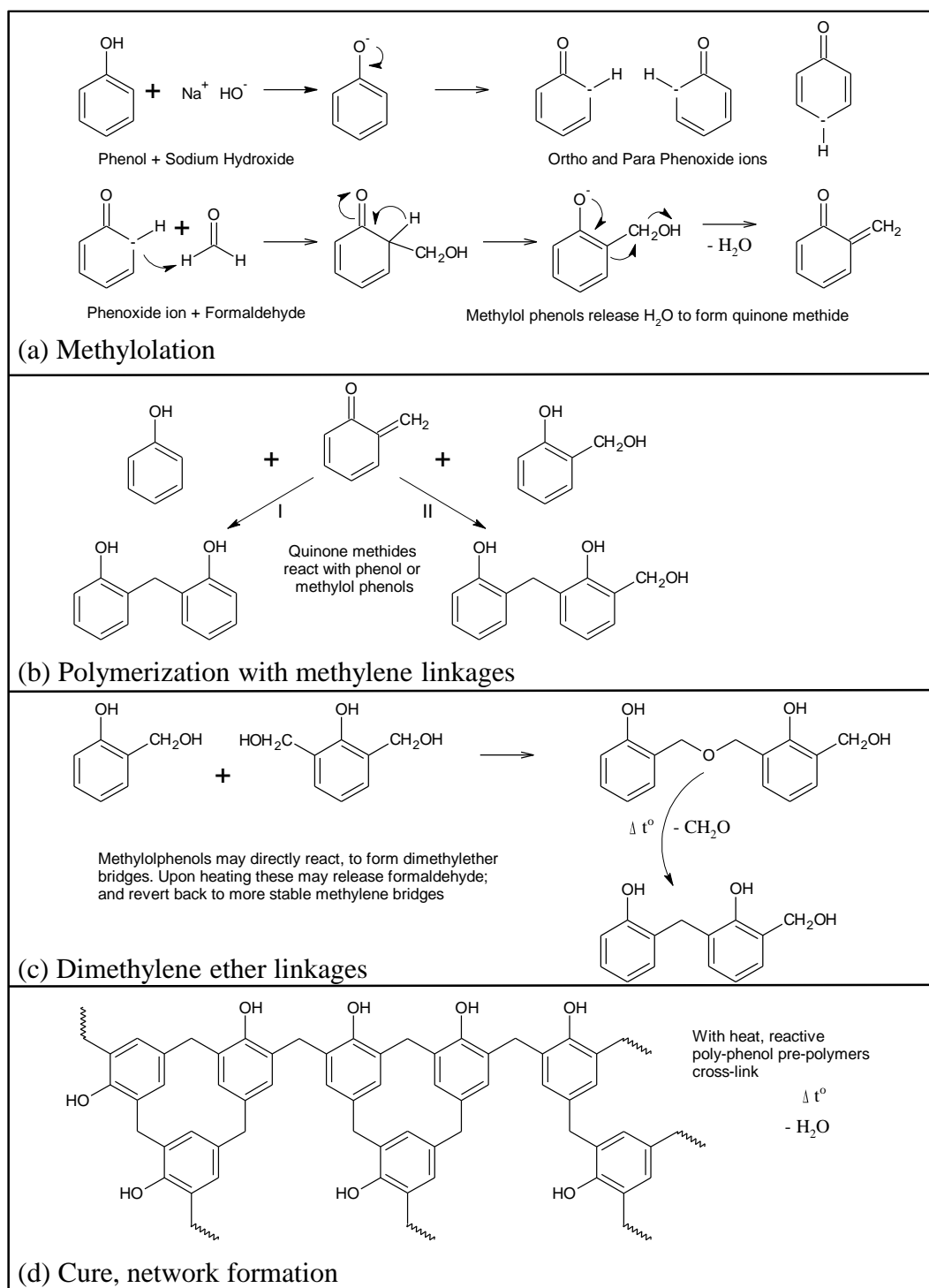


Figure 2-1 Resol phenol formaldehyde resin formulation and representative structures (a) methylation at ortho and para sites, and condensation to quinone methide ions (b) quinone methide polymerization with phenol (I) or methylolphenols (II), (c) direct polymerization between methylol phenols and the release of formaldehyde upon heating, and (d) resin cure where reactive poly-phenol pre-polymers cross-link

2.1.3.2 *Polymeric Diphenylmethane Diisocyanate (pMDI)*

Polymeric isocyanate resins have grown in use as wood adhesives in the past 20 to 30 years, and are now extremely important in many composite panel applications. Like phenolics, pMDI is an organic thermoset capable of forming complex cross-linked structures. However, unlike many water-based adhesives, pMDI has an approximate 100% solids content; the entire liquid phase polymerizes in situ, forming a rigid, glassy network. pMDI synthesis is a complicated, multi-stage process. First, in acidic conditions, aniline is reacted with formaldehyde; resulting methylene-bridged polyanilines are then neutralized and dried. In the second, more dangerous stage known as phosgenation, gaseous chlorobenzene solvents are used to convert the amino groups into isocyanates (NCO). Frazier (2003) provides a far more detailed description regarding MDI synthesis. Industrial pMDI resins are typically low-viscosity mixtures of monomeric MDI molecules and short-chain polyisocyanates with NCO contents between 31 and 32% (Frazier 2003). Additionally, the NCO groups are highly reactive toward a variety of the chemical functionalities found in wood cell walls, including phenols, alcohols and water (Frazier 2003; Frihart 2005). Thus, highly mobile and reactive pMDI adhesives readily wet wood surfaces, and offer superior adhesion upon cure. Figure 2-2 shows one possible MDI monomer, as well as illustrates two possible curing reactions during wood bonding.

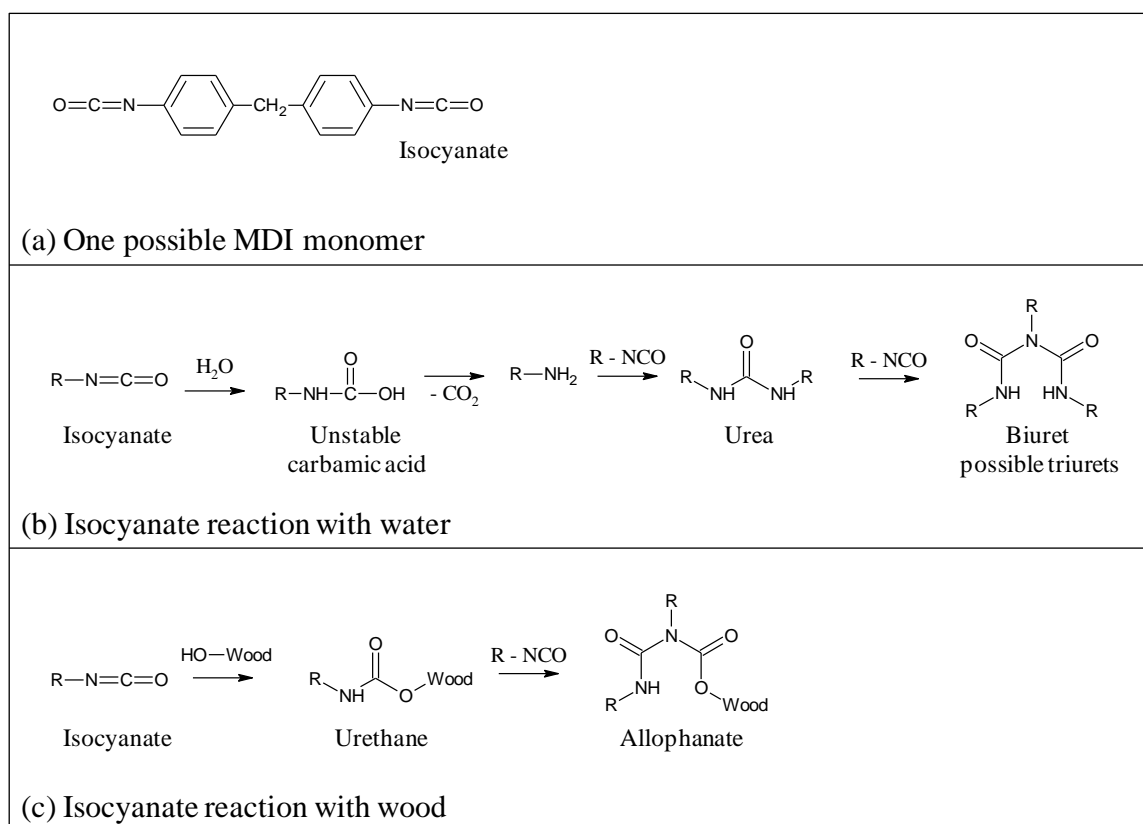


Figure 2-2 (a) One of many potential MDI monomer units, (b) isocyanate reaction with water, representing the common pMDI cure mechanism, (c) possible isocyanate reaction with hydroxyl-rich wood polymers

The pMDI cure process in wood bondlines is still not completely understood. Isocyanate groups readily react with water to form the unstable carbamic acid; this instantly decomposes by releasing carbon dioxide into a more stable amine, as shown in Figure 2-2b. Isocyanate reactions with amines are even faster than with water, and thus polymerization and network formation occurs between MDI units via polyurea, biuret and triuret linkages (Bao et al. 2003; Das et al. 2007; Frazier 2003; Frazier and Ni 1998; Frihart 2005). This is the main bonding pathway (Figure 2-2b), as wood adherends typically have a non-zero moisture content; furthermore, hot pressing helps mobilize

bound water in wood cells toward the bondline. Debate, however, surrounds whether or not pMDI resins covalently bond with wood polymers. Figure 2-2c illustrates that isocyanates certainly do react directly with alcohol-groups to form urethanes and allophanates, and wood cell walls are abundant in hydroxyl groups. However, such reactions with wood are difficult to measure in situ (Frazier and Ni 1998). As previously mentioned covalent bonding is not likely to add to measured joint strength, especially since the abundant polyurea networks have a high propensity for secondary adhesive forces like hydrogen bonding. Additionally, solid-state nuclear magnetic resonance (NMR) results are often complicated due to overlapping peaks (Das et al. 2007; Frazier 2003; Frazier and Ni 1998; Ren 2010). However, recent advancements with solution-state NMR have shown isocyanate-wood urethane formation only occurs in completely dry bonding conditions; the water present in typical wood adherends prevents urethane production under ordinary pMDI bonding conditions (Frihart et al. 2010; Yelle et al. 2009).

The debated urethane presence had offered one possible explanation for the superior moisture durability of wood-pMDI joints (Frazier and Ni 1998). On the other hand, IPN formation by low-molecular weight pMDI components could also add significant moisture durability (Frazier and Ni 1998). Yet, there is still debate about this occurrence, as well. Recent nano-indentation results have shown that pMDI cell wall penetration does effectively bulk up cell wall mechanical properties (Frihart et al. 2010; Jakes et al. 2009); however, chemical-state x-ray microscopy evaluations indicate if pMDI cell wall penetration occurs, it at considerably low concentrations (Buckley et al. 2002). Of course, one must recognize that wood and manufacturing factors will influence IPN formation, as

well as pMDI purity, molecular weight, viscosity and NCO content, which may all be tailored for a particular bonding application (Frazier 2003).

2.1.3.3 *Polyvinyl Acetate (PVAc)*

Unlike PF and pMDI, water-based PVAc adhesives are emulsified thermoplastic polymers. Commonly referred to as white glue, PVAc systems are most popular in paper making, consumer do-it-yourself projects and furniture manufacturing applications.

These polymer emulsions are formed through the linear addition free radical polymerization of vinyl acetate monomers; ethylene may also be added during polymerization to form a more flexible PVAc (Frihart 2005; Geddes 2003). Figure 2-3 shows a representation of the PVAc bonding process and resulting polymer structures.

Geddes (2003) provides a more detailed description regarding PVAc formulation including methods for manipulating chain length and morphology. However, all monomer components are consumed in production, and thus PVAc adhesives are incapable of chemical cross-links. Physical entanglements, however, do occur as the dispersed polymers coalesce during bond formation. Bonding is commonly performed at room temperature; upon application, the water diffuses into the wood substrates and eventually evaporates. As this occurs, the polymer chains crowd together and, provided sufficient mobility (i. e. above their minimum film formation temperature), efficiently pack into a continuous, solid film (Richey and Burch 2002; Wiese 2002).

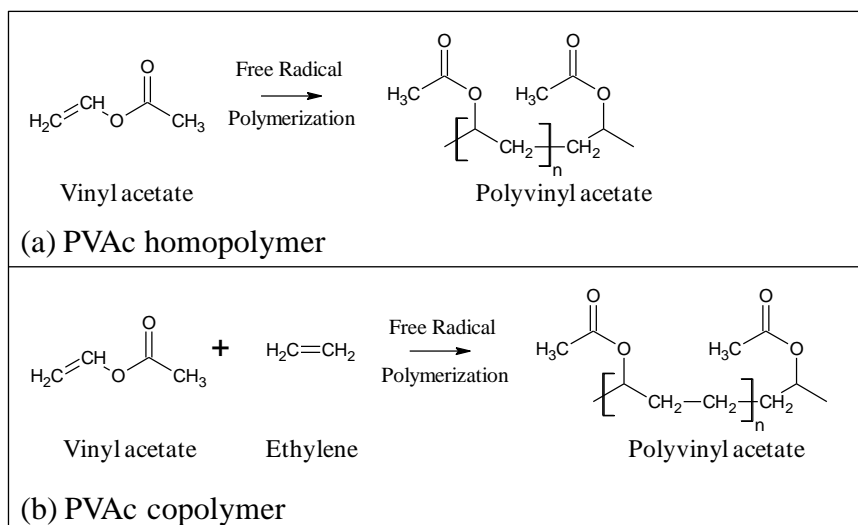


Figure 2-3 PVAc polymerization and resulting (a) homopolymer or (b) a more flexible copolymer with ethylene-bridge

PVAc adhesives often contain roughly 50% solids, and have fairly high viscosity and molecular weight; as such, PVAc penetration is often fairly shallow. However, PVAc polymers have a high propensity for hydrogen bonding and other secondary adhesion forces between its own chains and with the wood polymers (Frihart 2005; Geddes 2003; Lopez-Suevos and Frazier 2005; Lopez-Suevos and Frazier 2008). Additionally, PVAc adhesive films have a low glass transition temperature between 30 - 60°C, depending on specific chemistry, making PVAc adhesive joints more flexible and tough than thermosetting resins (Frihart 2005; Geddes 2003; Lopez-Suevos and Frazier 2005; Lopez-Suevos and Frazier 2008; River 2003). However, as these systems are not ‘cured’, they typically do not perform well in high moisture environments or creep tests (Frihart 2005).

PVAc mechanical properties and durability are often increased with the addition of cross-linking metal catalysts or reactive monomers, such as aluminum chlorides or N-methylolacrylamide, respectively (Frihart 2005; Geddes 2003; Lopez- Suevos and Frazier 2006; Salvini et al. 2009). Similar increases in weather durability, thermal stability and cross-linking have been achieved by adding small amounts of thermosetting PF resins (Lopez- Suevos and Frazier 2006; Lopez-Suevos and Frazier 2006a; Lopez-Suevos and Frazier 2006b). Hybrid adhesive systems are often prepared to exploit preferred properties belonging to the individual components (Cao 2010; Kim and Kim 2006; Zheng et al. 2004). Cao (2010) extensively studied PF/PVAc hybrid wood-adhesive systems; he evaluated resin phase miscibility, pH, viscosity, adhesive penetration, and joint performance all as a function of component ratio. His work showed that a 50:50 mixture generally offered high shear strength, a high percentage of wood failure, a lower viscosity than either independent phase, and effective penetration similar to neat PF resins (Cao 2010). However, Cao did note that the blended system appeared to phase separate. Other hybrid adhesive studies have shown phase immiscibility (Kim and Kim 2006); yet, perhaps joint toughness benefits from some phase separation as it may create a more tortuous path for crack growth (Chowdhury et al. 2011; Ebewele et al. 1986a; River 2003; Unnikrishnan and Thachil 2006). Both pure PVAc and PF/PVAc hybrid adhesives were investigated in the present research.

2.1.4 Joint Performance

Wood-composite joint performance has been assessed by several different criteria; however, testing is primarily of two types, strength-based or energy-based. Strength-

based measurements include internal-bond tests, shear-block tests, and composite bend tests (DeVries and Borgmeier 1994). These methods are fast, easy to replicate, and follow strict standards (ASTM-D-905 2007; ASTM-D-1037 2007); as is the case, the strength methods are often employed by composite and adhesive manufacturers to assess product quality. However, strength tests often stress composite assemblies in wood's two weakest directions, tension perpendicular to grain or shear parallel to grain; many commercial adhesive systems often exceed the strength of wood in these directions. Thus, strength tests fail to describe wood/adhesive interactions, and provide little room for comparison between resins (Gagliano and Frazier 2001; River 2003). Percent wood failure estimates are commonly provided along with recorded joint strengths; however, these too are highly variable and subjective, as several adhesives show little visual contrast to wood. Moreover, strength-based measurements provide average failure stresses; however, the stress distributions across wood joints are rarely uniform due to penetration patterns and anatomical variations (DeVries and Borgmeier 1994; Zink et al. 1996).

Fracture mechanics, on the other hand, determines how much energy is required to extend a crack propagating through a material; this is also referred to as that material's 'toughness'. Fracture testing of wood-adhesives has grown in popularity over the past 30 years as specimen design, real-time crack-assessment techniques and energy-release calculations have been developed and refined (Blackman et al. 1991; Ebewele et al. 1979; Ebewele et al. 1980; Gagliano and Frazier 2001; Nairn 2000; River and Okkonen 1993; Singh et al. 2010; White 1977). One particular method based on mode-I fracture, or opening in cleavage, with the dual cantilevered beam (DCB) specimen has seen considerable use in wood-adhesive joint performance testing. Paris (2010), River (2003),

Gagliano and Frazier (2001) and Blackman et al. (1991) provide more extensive reviews of the development and theory behind mode-I fracture testing.

Results from such studies have yielded intrinsic adhesive and wood/adhesive-interfacial properties independent of adherend strength and modulus. Moreover, DCB specimens can yield numerous data points per test, providing large sample sizes and high statistical power. Mode-I, DCB fracture testing has allowed for the systematic analysis of numerous parameters affecting adhesive joint integrity. Multiple adhesive types (Ebewele et al. 1982; Lopez-Suevos and Frazier 2006a; Paris 2010; Ren and Frazier 2012; River 2003) and inherent adherend properties such as grain angle, moisture content and surface quality have been studied with this method (Ebewele et al. 1980, 1986b; Mijovic and Koutsky 1979). The technique has also been used to study the effects of adhesive layer thickness, fillers and extenders, plasticizers, cross-linkers, coupling agents and weather durability (Ebewele et al. 1979; Ebewele et al. 1986a; Hosen 2010; Lopez-Suevos and Frazier 2006a; Paris 2010; Ren 2010).

Another recent advancement in adhesive performance analyses has been the application of digital image correlation (DIC) techniques with composite-joint tests. DIC provides full-field, surface strain data during specimen loading. Sequential digital images recognize surface features, and tracks their motion as a specimen deforms under stress; reference images acquired prior to loading are used to calculate the strain fields (Pan et al. 2009; Serrano and Enquist 2005; Zink et al. 1995). Speckle patterns are often used to provide numerous discrete points for displacement measurements; this is a significant advantage over traditional single point methods involving LVDTs or strain-gauges (Pan

et al. 2009). Advancements in high resolution optics, rapid-acquisition cameras, correlation algorithms and computer performance have allowed researchers to track in-plane strain development and localized stress concentrations. Out-of-plane deformations can also be accounted for when a second camera system is used in conjunction with more advanced algorithms; this is often necessary for specimens with noticeable Poisson effects or irregular surfaces, or when loading conditions are not in plane with the observed surface (Pan et al. 2009; Serrano and Enquist 2005).

DIC techniques have been applied to various wood-composite systems to better understand wood-adhesive interactions (Blyberg et al. 2012; Gindl et al. 2005; Muller et al. 2005; Muszyński et al. 2002; Serrano and Enquist 2005; Zink et al. 1996). For instance, full-field strain distributions have been observed for shear and compression specimen bondlines, prepared with either a PRF or polyurethane (PUR) adhesive. Results showed high strain values and broad deformation patterns for the compliant PUR system, whereas the rigid PRF showed more efficient load transfer across the joints (Gindl et al. 2005; Muller et al. 2005; Serrano and Enquist 2005). Larger wood composite systems have also been studied with DIC. Laminated veneer lumber, oriented strand board and plywood have been investigated to understand how a larger product, or 'system', responds to bending or moisture-induced shrinking and swelling stresses (Sebera and Muszyński 2011; Zink et al. 1996, 1997).

One great opportunity for DIC technology is its use alongside advanced computer modeling systems, which predict bond performances under simulated loading conditions. Modeling techniques such as finite element analysis (FEA) or the material point method

(MPM), require accurate input data of the various components, including material properties and morphology, as well as appropriate boundary conditions defining the simulated stresses (Muszyński 2009; Nairn 2006). This is complicated for wood, which is orthotropic, opaque and inhomogeneous; composite systems are even more difficult as the adhesive phase flows and interpenetrates throughout the wood matrix (Muszyński 2009; Nairn 2000). Moreover, wood and composite properties have traditionally been measured on a macro-scale; however, properties may be vastly different at the micro level, in the vicinity of the bondline or in regions where adhesive cell wall penetration has occurred. Often property assumptions or theoretical ideal structures are used in model design, and thus model results reflect these imperfect data. However, several studies have demonstrated that DIC can be used to validate model assumptions, as a reverse problem solving method (Blyberg et al. 2012; Gindl et al. 2005; Muller et al. 2005; Muszyński 2009; Muszyński et al. 2002; Nairn 2000; Sebera and Muszyński 2011; Serrano 2001, 2004; Serrano and Enquist 2005). If the surface strain patterns predicted by the FEA or MPM models match the actual test specimens' DIC patterns, then researchers will have more confidence in their assumptions and the model's power.

Significant efforts have also been focused on how to model materials' internal structures more realistically. X-ray computed tomography (XCT) offers a unique opportunity to accurately image these internal structures in 3D. Moreover, XCT is non-destructive, and thus samples are preserved for future mechanical testing, wherein the aforementioned DIC concepts may be employed. Some researchers have even stressed specimens during x-ray tomographic scanning. Digital volume correlation (DVC) techniques can be used to identify strain distributions throughout a specimen's internal 3D structure (Bay 2008;

Bay et al. 1999). Section 2.3.2 provides a fairly comprehensive review of XCT applications to wood and wood-composites; however, little research has yet combined tomographic imaging with mechanical modeling. Forsberg and colleagues used XCT and DCV techniques to study solid wood deformations in 3-point bending experiments. Their results show that the internal anatomical features and cellular arrangement absolutely influence strain developments and concentrations in wood specimens (Forsberg et al. 2008; Forsberg et al. 2010). However, Lech Muszyński and colleagues have proposed, and pursued to a degree, the three fold combination wood-composite XCT data, predictive performance modeling and mechanical testing with DIC to systematically study and understand wood-adhesive interactions (Muszyński 2009; Sebera and Muszyński 2011; Wang 2007). This concept represents one of the primary goals of the present research.

2.2 Adhesive Penetration

As previously discussed in section 2.1, the nature and mechanisms of wood adhesion are influenced by how liquid resins flow and penetrate into the porous wood structure. Moreover, adherend and adhesive characteristics, as well as manufacturing processes all contribute to a joint-system's penetration profile. Additionally, it has been discussed that wood adhesive penetration can occur at two scales: gross penetration refers to resin occupying cell lumens, whereas molecular-scale penetration occurs when smaller adhesive components infiltrate the wood cell walls. Numerous studies and reviews have been conducted to understand which factors control adhesive penetration, and how it influences bondline joint performance (Johnson and Kamke 1992; Kamke and Lee 2007;

Sernek et al. 1999). This section highlights some of the primary penetration detection and quantification methods, as well as some of the correlations between penetration and bond quality.

First, the concept of the wood-adhesive bondline must be clarified. Due to penetration, wood-composite joints often consist of three different 'phases' shown in Figure 2-4.

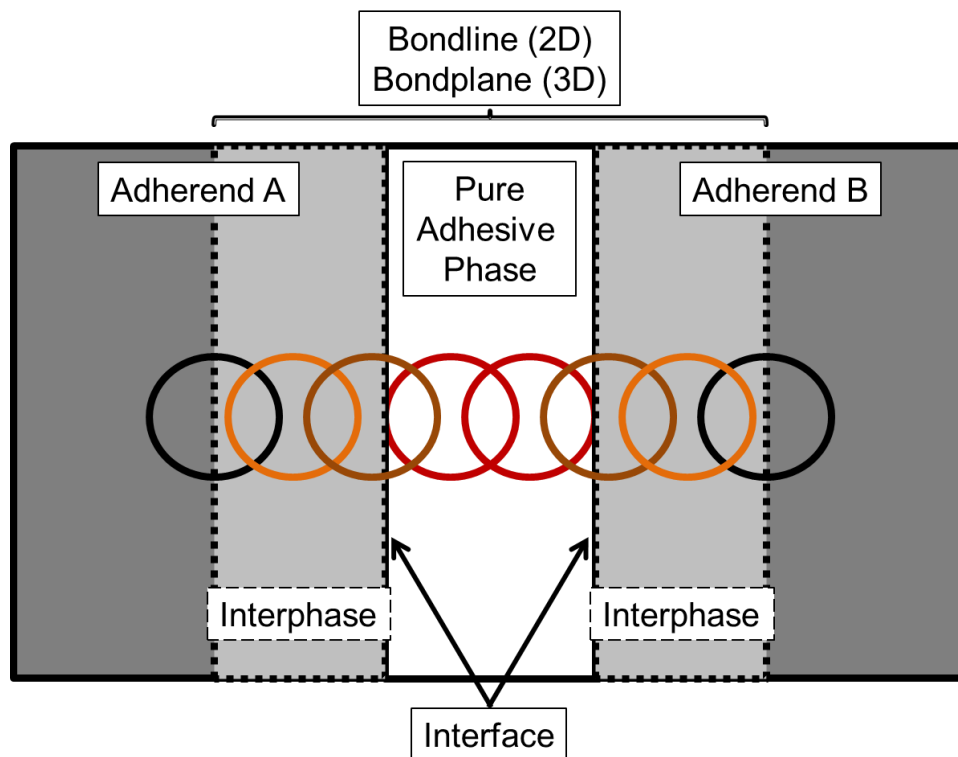


Figure 2-4 Wood-adhesive bondline, dark, grey and white regions represent pure wood phase, wood-adhesive *interphases* and pure adhesive phases, respectively; rings represent the property gradient due to resin penetration

The term 'bondline' collectively refers to the entire wood-adhesive joint. It is actually a misnomer, which has gained in popularity and use, due to the 2D nature of conventional microscopy techniques used for wood-adhesive observation. In reality, the bondline is

actually a 3D “bondplane” or region running the length of the joint. However, throughout this document, the term bondline is used for common reference and convention sake. The pure adhesive layer consists of only the solidified, cross-linked or entangled resin polymers. This pure adhesive may not be present in all wood-adhesive joints, it lies between the two adherend surfaces, and has not penetrated them. The term ‘interface’ by definition refers to the surface boundary between two different materials, and thus is shown as the delineation between the solid adherends and adhesive layer. However, the wood cells at the interface are often damaged due to machining, and thus do not reflect the sound mechanical properties of the bulk adherends. Moreover, both gross and cell wall penetration effectively bulk-up the adherend properties in the ‘interphase’ region. The two-phase (adhesive and wood cell) region exhibits hybrid, and in some cases a gradient of, properties between the pure phases. The overlaid rings, originally proposed by Marra (1992), are intended to indicate how polymer morphology, cure-behavior and mechanical properties may all be influenced and different based on their surrounding material phases (Kamke and Lee 2007; Marra 1992). Therefore, when discussing adhesive penetration and joint performance it is more descriptive and meaningful to refer to the combined bondline and adhesive interphase region, rather than the adhesive ‘interface’.

2.2.1 Measurement

Wood-adhesive penetration measurements are fairly challenging. Gross penetration occurs on a scale of a few microns to millimeters; therefore, microscopes are often the preferred tool for generating sufficient resolution and field of view. Cell wall infiltration

is limited to only a few tens of nanometers, and thus molecular penetration requires even higher magnifications (Frihart 2005; Johnson and Kamke 1992). Visual contrast is also important for identifying penetration. Color, density and chemical composition are often very similar between wood and adhesive polymers making it sometimes difficult to differentiate between the two substances with microscopic or spectroscopic methods (Kamke and Lee 2007). Also, as wood is orthotropic, the penetration pattern will appear surprisingly different depending on which plane is examined. Penetration patterns and depth are most commonly observed on a joint's transverse plane, perpendicular to the bondline (Brady and Kamke 1988; Johnson and Kamke 1992; Kamke and Lee 2007; Sernek et al. 1999); whereas it is more practical to measure adhesive layer thickness along a bondline's longitudinal edge (Paris 2010). All the above difficulties are typically dealt with through very careful and precise specimen preparation, which are both tedious and destructive to the composite specimen (Kamke and Lee 2007). Lastly, penetration has been traditionally studied with various 2D surface techniques. Wood structures, however, are three-dimensional systems; therefore so too is the adhesive penetration and its effects on joint performance. Some 3D techniques have been recently employed for wood-adhesive penetration analyses as well, and represent one of the primary focuses of the present research.

2.2.1.1 2D Observation Techniques

Bright field and fluorescent microscopy are by far the most common methods used to observe gross adhesive penetration (Kamke and Lee 2007). The former requires white light, which contains the spectra of light wavelengths, to be reflected or transmitted

through the wood specimen. Transmitted light generally produces higher contrast and image clarity, but requires the specimen to be a thin section. Moreover, many adhesives, with the exception of dark phenolic resins, show little to no color contrast with surrounding wood structures. Water-soluble dyes are often used to improved contrast, as they will preferentially stain the hygroscopic wood polymers and avoid the hydrophobic adhesive layer. However, greatest contrast is often achieved when stains are used along with fluorescence microscopy (FM) methods. Fluorescence is the photoelectric release of excess energy from excited atoms within a substance. Fluorescent microscopes use a high-power, polychromatic light source and an excitation filter to illuminate a specimen surface with a particular wavelength of light, causing some materials to auto-fluoresce. Different materials, however, will fluoresce to different degrees and with different wavelengths. Emission-filters placed just before the microscope objectives allow only certain wavelengths to pass for detection, thus generating high material contrast (Davidson and Abramowitz 2002; Kamke and Lee 2007). Different filter combinations are often used to tease out various subtle differences between adhesive and wood substances; therefore it is important to report the filter-set and light source along with FM results. Since specimens are illuminated from above and do not require transmission, FM is also a very convenient technique for imaging specimen surfaces, and not just thin sections. Some wood adhesives, such as PVAc will naturally fluoresce at various wavelengths (Cao 2010); however, stains containing fluorescent active agents known as fluorochromes are often used to stain the wood substance. Kamke and Lee (2007) and Cao (2010) both provide very detailed reviews of specific successful FM filter-set/stain/adhesive/wood-species combinations.

Scanning and transmission electron microscopy (SEM and TEM) have also been used to observe wood-adhesive penetration. A coherent electron beam rather than visible light is used as the incident probe energy; the high velocity electrons have significantly smaller wavelengths than photons, and are thus capable of generating images with much higher magnifications and spatial resolutions (Goodhew et al. 2001). However, electrons are also more likely to interact with the material. This means electron transmission, as is the case with TEM, requires ultra-thin specimens less than a micron in thickness. Additionally, both techniques often require organic materials, such as wood, to be coated with a thin carbon or metallic layer to avoid charge build-up on the surface (Goodhew et al. 2001). Resulting grayscale images show little color contrast between wood and adhesive substances. Therefore primarily qualitative penetration data is recorded based on textural differences or the recognition of filled vs. un-filled lumens (Kamke and Lee 2007). Far more quantitative penetration data, however, can be achieved when SEM is used in combination with a chemical-specific, spectroscopic technique such as electron microprobe analysis (EMPA) or energy dispersive spectroscopy (EDS). These techniques can raster-scan specimen surfaces to both image and detect elemental signals related to distinct x-ray emissions from excited atoms (Bolton et al. 1988; Kamke and Lee 2007). However, as adhesives and wood are both organic, these spectroscopic techniques often require the resin to be doped with a heavier tag element to generate contrast. For instance, Modzel (2009) used EMPA to observe the penetration of a PF resin which had been formulated with rubidium hydroxide (Modzel 2009; Modzel et al. 2011). Similarly, Leonard Smith formulated a PF resin using meta-bromophenol rather than phenol, and used EDS to measure its penetration in wood joints and cell walls (Smith and Côté 1971;

Smith 1971). White and colleagues studied the penetration behavior of a similarly meta-brominated PF resin using neutron activation analysis (NAA); however, their interest was not in visualizing the adhesive, but rather observing its concentration at various penetration depths (White 1975, 1977; White et al. 1977).

Molecular penetration into the cell walls has also been extensively studied using multiple other analytical techniques. Infiltration at these scales is below the resolution limits of typical light microscopy techniques, and as previously mentioned SEM and TEM provide low contrast in the absence of elemental tags. Gindl and colleagues studied cell wall penetration with UV microscopy, scanning thermal microscopy and nano-indentation; their results have shown evidence that the low-molecular weight components of melamine-urea-formaldehyde (MUF), UF, PRF, PF and pMDI resins infiltrate cell wall components (Gindl et al. 2002; Gindl et al. 2004a; Gindl et al. 2004b; Konnerth et al. 2008; Stockel et al. 2012). pMDI cell wall infiltration has also been observed with both solution-state and solid-state NMR and chemical-state x-ray microscopy (Buckley et al. 2002; Frazier and Ni 1998; Frihart et al. 2010; Yelle et al. 2009).

Often researchers wish to quantify adhesive penetration to make correlations with joint performance tests (Johnson and Kamke 1992; Kamke and Lee 2007; Paris 2010; Sernek et al. 1999; White 1977). Spectroscopic methods often provide concentration data for cell wall infiltration (Kamke and Lee 2007); however as previously mentioned molecular penetration may have a greater influence on durability than bond-strength or toughness. Gross adhesive penetration data observed from cross-sectional micrographs are most

often used for performance correlations. The two most common calculations are (2-1) maximum penetration and (2-2) effective penetration (Sernek et al. 1999).

2-1

$$MP = \frac{\sum_1^5 (y_i + r_i - y_0)}{5}$$

2-2

$$EP = \frac{\sum_1^n A_i}{X_0}$$

Maximum penetration (MP) measures and compares the average distance to the center of the 5 adhesive objects (y_i) furthest from the bondline to some reference point in the bondline (y_0) while accounting for their radii (r_i). The effective penetration (EP) measurement sums the area of each penetrated adhesive element (A_i), and divides the total area by the maximum image (or object) width (X_0). EP have been considered more practical, and are relatively fast and efficient provided sufficient image contrast and image processing tools can separate the wood and adhesive phases. However, the fact remains that most previous correlations are based on 2D measurements, and yet the system is inherently 3D. Penetration patterns could be wildly different as one moves up or down the bondline, due to imperfect localized spread rates, bonding pressures or wood anatomy. For instance, several researchers have noted significantly different 2D adhesive penetration depths in earlywood vs. latewood cells in the same joint (Brady and Kamke 1988; Paris 2010; White 1977).

2.2.1.2 *3D Observation Techniques*

Some work has been conducted on 3D adhesive penetration analyses. For example, adhesive casting is a process that involves the erosion of wood cell wall substance (Gindl 2001); however, only some cured resins can withstand the harsh chemical treatments. Confocal laser scanning microscopy is a non-destructive method of virtually sectioning different focal planes along a sample's length, and thus allows one to image a volume rather than just a 2D area (Xing et al. 2005). However, this too only offers a limited depth, of a few tens of microns, into the sample. One of the more promising 3D adhesive penetration analyses is x-ray computed tomography (XCT). Researchers have shown that XCT can non-destructively provide high-resolution, internal 3D adhesive penetration data from fairly large ($2 \times 2 \times 2 \text{ mm}^3$) composite joints (Hass et al. 2012; Modzel 2009; Modzel et al. 2011). Though, as with SEM and other spectroscopic techniques, image contrast has been a problem with un-modified adhesive systems. However, Modzel (2009) showed that when adhesive contrast is achieved, one can rapidly calculate an effective bondline thickness (equation 2-2) and penetration depth throughout the entire 3D joint. The present work focuses on improving XCT wood/adhesive contrast, and using XCT analyses to visualize and characterize different adhesive penetration patterns in various wood-composite joints. Section 2.3 describes the fundamentals of x-ray tomography and its previous use in wood and wood-composite analyses.

2.2.2 Impacts on Joint Performance

Several studies have investigated the effects of wood-adhesive penetration on composite joint performance; however, results to date are inconclusive. It is obvious that adhesive

penetration affects joint performance; in fact several of the fundamental adhesion mechanisms cite adequate penetration as a major component in developing bond integrity (Section 2.1.1). However, composite performance and adhesive penetration are highly variable, and depend on adhesive, wood and processing factors.

All wood adherends have surface defects and irregularities caused by machining or drying stresses. Adhesive penetration transfers joint stresses away from the damaged bondline interface (Figure 2-4) into sound wood, and effectively distributes those stresses over a greater area (Frihart 2005; Kamke and Lee 2007). Broader penetration also increases the surface area for the wood-adhesive intermolecular associations and bonding forces (Schultz and Nardin 1994). Over penetration, on the other hand, results in a “starved” bondline, void of any bridging adhesion across the joint (Johnson and Kamke 1992; Kamke and Lee 2007). Excessive penetration is commonly observed with very low viscosity adhesives or highly permeable adherends, and wastes resin, which increases manufacturing costs.

To date, no one knows what represents an optimal penetration depth. For instance, White et al. (1977) noted that joint fracture toughness increased with increasing penetration depth for a RF resin. Ebewele and colleagues (1979) noticed a similar trend; they varied bonding pressures and monitored fracture toughness as a function of adhesive layer thickness. They reported decreases in mechanical performance with increasing thickness (Ebewele et al. 1979); however, this also represents decreasing penetration depths, as adhesive layer thickness and penetration are often inversely related (Ren 2010; White 1977). A similar study noted that increasing PRF resin viscosity decreased both

penetration and fracture energy (Ebewele et al. 1986a). However, some studies show conflicting relationships between penetration depth and joint performance. In 2010, the author observed identical fracture energies for two different adhesive systems; however, these systems exhibited notably different penetration depths. It was unclear whether the adhesive with the shallower penetration was in fact more tough, or whether both systems had merely reached some minimum optimal penetration depth (Paris 2010). Ren (2010) observed a similar result. He was unable to correlate penetration depth with fracture energy for three different PUR adhesives; the adhesive with the least penetration performed the same as one with more than twice its penetration depth (Ren 2010). Shear strength results have also been inconsistent with penetration depth results. For instance, it was found that decreasing the viscosity of a PVAc adhesive (i.e. increasing penetration), resulted in a stronger bond; however, UF resins of different viscosities showed identical shear strengths (Hass et al. 2009).

Adherend variability is one of the primary reasons for such inconclusive correlations. Joint performance measurements and adhesive penetration studies both tend to have large standard deviations (Kamke and Lee 2007; Paris 2010; Ren 2010; White 1977), and yet both analyses are typically conducted on different, albeit, ‘similar’ specimens.

Researchers try to minimize variability by preparing microscopy specimens under identical manufacturing conditions as were used for joint performance specimens. Often, both specimen types are even excised from the same composite, taken within close proximity to each other. However, they are not the very same specimen, and thus the penetration patterns are inherently different. Moreover, microscopy results are 2D, but the joint performance measurements represent volumetric behaviors (Kamke and Lee

2007). For this reason, several researchers have suggested the need for 3D penetration analyses, such as x-ray computed tomography, that preserve specimens for later mechanical joint tests (Hass et al. 2012; Kamke and Lee 2007; Modzel 2009; Muszyński 2009). Combining XCT data and joint testing, along with the predictive power of 3D mechanics modeling and DIC principles can help elucidate the fundamental relationships between adhesive penetration and bond performance. This is the primary focus of the present research.

2.3 X-Ray Computed Tomography

2.3.1 Background and Instrumentation

X-ray computed tomography (XCT) has long been employed as an advanced imaging technique to visualize the internal structures of opaque materials in 3D. It was originally developed by G. N. Hounsfield for use in medical applications where simple 2D radiographs failed to completely identify superimposed structures (Hounsfield 1973). Traditional x-ray radiography produces projection images through an object; denser materials absorb more of the incident x-rays than less dense materials, decreasing x-ray transmission. If two different materials lie in the same path of an incident x-ray beam, their radiographic projections will overlap, providing no positional data along the beams path. One object will shadow or completely block information pertaining to the second, as depicted Figure 2-5.

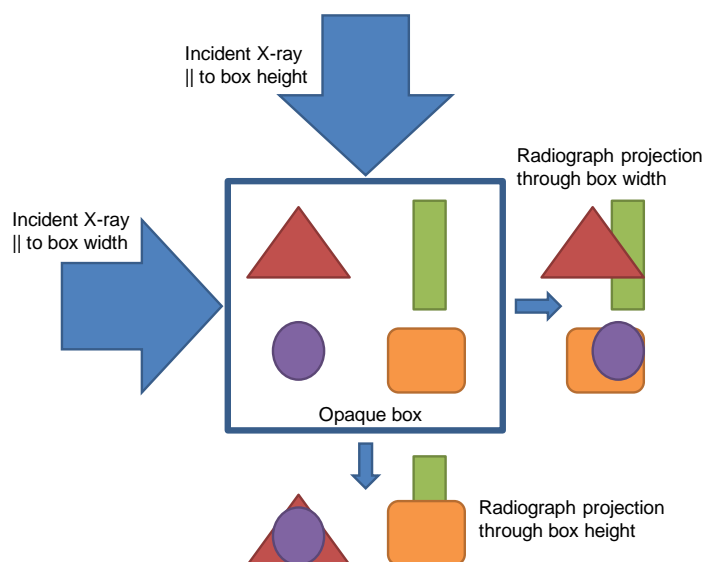


Figure 2-5 Cartoon representation of traditional 2D x-ray radiography

In Figure 2-5, the internal objects' positional information depends on the incident angle of the x-rays; the more angles used, the higher the positional accuracy can be discerned. With X-ray tomography, objects are imaged incrementally throughout a full rotation; the multiple radiographic projections are then reconstructed through mathematical algorithms to provide full internal structure, 3D positional data (Banhart 2008a). The non-destructive, or non-invasive, nature of this technique has not only made it indispensable for medical imaging, but also in materials science, biology, geology, archeology, and engineering disciplines (Hass et al. 2012; Ketcham and Carlson 2001; Mizuno et al. 2010; Modzel et al. 2011; Parkinson et al. 2008; Wildenschild et al. 2002).

2.3.1.1 *X-ray Interactions with Matter*

X-rays are electromagnetic radiation with both wave-like and particle like properties, that traverse along a straight path at frequencies between 10^{16} to 10^{21} Hz. Wavelengths range

between 10^{-8} to 10^{-11} cm, and the x-ray particle, or photon, can have energies ranging between 200 eV - 120 KeV (Banhart 2008b; Wildenschild et al. 2002). X-ray images are produced when photons with high flux, or number per unit area per second, pass through a material. Along their path, x-rays reduce in intensity as they interact with the material's atoms, and while nuclear collisions occur, the most frequent interactions take place with the electrons (Banhart 2008b). These interactions result in three possible outcomes. A photon can be completely absorbed by the electron, transferring to it all its energy and ejecting it from the atom as a photoelectron. It can scatter elastically, retaining its energy but deflected from its trajectory; this is referred to as Rayleigh scattering. Alternatively, it could scatter inelastically, imparting only a portion of its energy to a near-by electron, referred to as Compton scattering (ASTM-E-1441 2011; Banhart 2008b). Photoelectric absorption and Compton scattering are the two most predominant contributors to the reduced intensity, or x-ray absorption, by a material. XCT imaging most often exploits the former, as Compton scattering dominates at high energies, >50-100 KeV (ASTM-E-1441 2011; Ketcham and Carlson 2001).

A material's ability to absorb x-rays is described by its linear attenuation coefficient μ , in units of reciprocal distance. With monoenergetic incident x-rays, μ is easily calculated from the ratio of the transmitted intensity I , to the initial intensity I_0 , through the sample thickness d , according Beer-Lambert's Law (Banhart 2008b; Wildenschild et al. 2002):

2-3

$$\frac{I}{I_0} = e^{(-\mu d)}$$

When a sample consists of multiple different materials, equation 2-3 becomes:

2-4

$$\frac{I}{I_0} = \sum_i e^{(-\mu_i d_i)}$$

where μ_i and d_i are the attenuation coefficients and distances, respectively, for each individual material, i (Ketcham and Carlson 2001). The attenuation coefficient is related to the atoms' absorptive cross-sections, and describes the mean free path a photon can travel into matter before an absorptive or scattering event occurs. As such, μ is dependent on the material's atomic number and weight, Z and A , and electron density ρ_e , as well as the incident photon energy E , described by equation 2-5 (Turner 2004; Wildenschild et al. 2002):

2-5

$$\mu \propto \rho_e \left(\frac{Z^{3.8}}{E^{3.2}} \right)$$

Where ρ_e is calculated using the bulk density ρ , and Avogadro's number N_{Av} as:

2-6

$$\rho_e = \rho \frac{Z}{A} N_{Av}$$

X-ray contrast, or the ability to visualize one material from another in x-ray radiograms and tomograms, depends on their relative density and/or dissimilarities in their atomic compositions. X-ray images are, in fact, maps of intensity values in Hounsfield units (HU), more commonly referred to as CT numbers, after the beam has traversed through the object (Ketcham and Carlson 2001). Softer, less attenuative materials have lower CT

values, such as air at -1000 and water at 0, while denser materials have higher CT values (Ketcham and Carlson 2001).

The attenuation significantly increases when the photon energies correspond to the atom's core electron K, L, and M binding energies (Banhart 2008b). Just above these energies, or absorption edges, the incident photon imparts enough energy into an electron to completely dislodge it from the atom. A higher energy electron will fall down into the resulting vacancy; the difference in energy between the two states is released as a photon. These x-rays are characteristic to their parent element, and are commonly employed in other chemical analyses (Banhart 2008b; Turner 2004). In x-ray imaging, the absorption edge effect is often exploited through the use of elemental tags as contrast agents to discern differences between materials, that when unaltered are indistinguishable (Evans et al. 2010; Iltis et al. 2011; Modzel et al. 2011; Porter and Wildenschild 2010; Wildenschild et al. 2002). Further discussion on contrast agents will follow in section 2.3.2.1.

2.3.1.2 Instrumentation and Data Collection

All x-ray tomographic imaging involves the same basic fundamental procedural steps. X-rays, generated by a conventional x-ray tube or synchrotron particle accelerator, illuminate and traverse linearly through the specimen. The beam can be a single point, fan-shaped, cone-shaped, or highly collimated and parallel. Radiation detectors on the other side of the specimen record transmitted intensity and determine the degree to which the beam was attenuated by the specimen (Ketcham and Carlson 2001). Point-beams, representing the first generation of x-ray tomography systems, used a single point

detector, and the beam-detector pair required translation across the specimen width at every incremental angle. Fan systems were an improvement, using a linear array of detectors; this too required long scan times as only one plane through the material's height could be scanned at a time. Cone and parallel beam sources utilize a 2D detector array, and allow for volumetric tomography and reduced scan times. The most common x-ray detectors consist of scintillating materials which convert the x-ray photons into visible light (Graafsma and Martin 2008). Scintillator size, spacing, and number control the amount of data recorded from each x-ray path and how many x-ray paths can be accounted for simultaneously (Ketcham and Carlson 2001). Secondary photo-detectors known as charged coupled devices, or CCDs convert the visible light into digital intensity data and record it as an image. The CCD camera consists a grid of diodes defining the pixels spacing of the final image; often imaging optics are used in conjunction with the CCD cameras to increase the spatial resolution (Graafsma and Martin 2008; Ketcham and Carlson 2001; Wildenschild et al. 2002). A cartoon illustration depicting the theoretical layout of a conventional tomographic imaging system is provided in Figure 2-6.

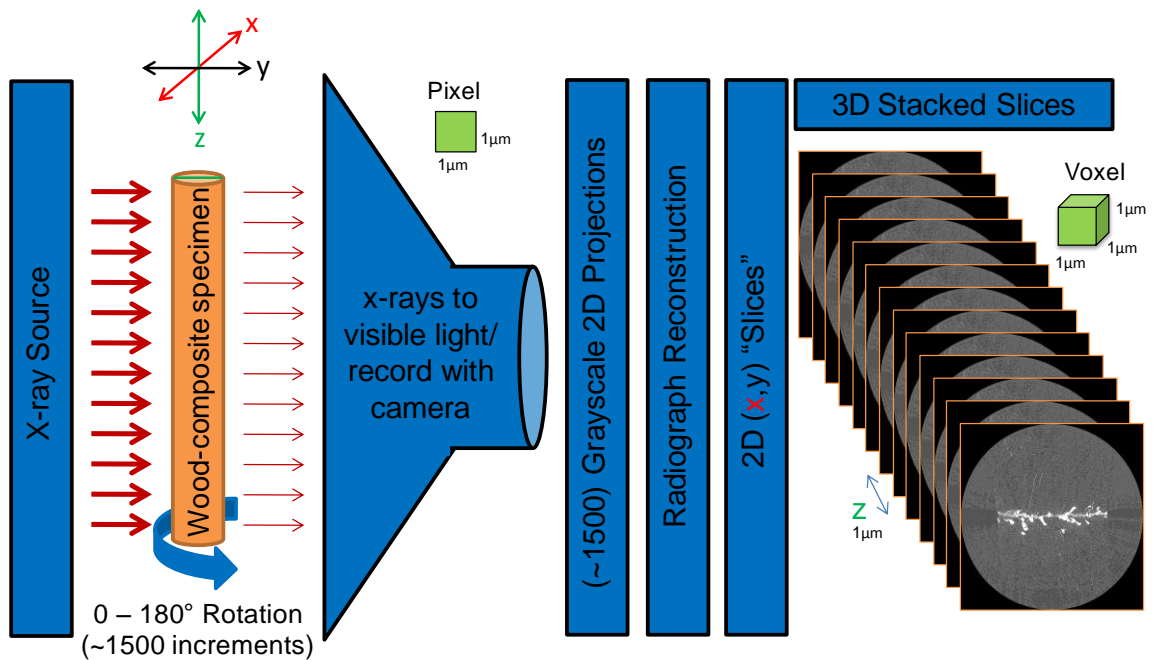


Figure 2-6 Fundamental x-ray tomography imaging system; images correspond to typical tomographic wood-composite specimen from this study

2.3.1.3 Resolution

Resolution is defined as the smallest distance between neighboring objects at which they can be distinctly separated by an imaging system (Banhart 2008a). In digital images, this can be thought of as the original x and y pixel dimensions, as one pixel can exhibit a distinctly different color value than its neighbors. This value is physically limited to the sensor array spacing on the CCD chip and the up-stream magnification optics (Banhart 2008a; Wildenschild et al. 2002). For example, if a 2048 x 2048 pixel CCD camera system with 7.4 $\mu\text{m}/\text{pixel}$ physical spacing was used in conjunction with a 5X optical lens, the pixel resolution would be 1.48 $\mu\text{m}/\text{pixel}$. In 2D, x and y pixels generally correspond to image width and height, respectively, as is the case with the incremental

angular projection radiograms collected in tomographic imaging. However, following image reconstruction, x and y pixels represent specimen width and depth (or thickness), respectively, in the virtual cross-section slices. Vertical stacks of slices define the z-direction, corresponding to specimen height; the slice offset distance is equivalent to the original radiographic y-pixel spacing. The volume-element defining 3D xyz space is the voxel, or the cube of the original analogous 2D pixel (Figure 2-6). Still, the voxel dimensions are an upper limit based on the image system optical hardware; spatial resolution in tomographic imaging is also impacted by the scintillator grid spacing, source divergence from optimal collimation or cone shape, source size and type, signal-to-noise ratio (SNR), and the specimen to source/detector distances (Graafsma and Martin 2008; Kinney and Nichols 1992; Wildenschild et al. 2002). It is common for XCT users to report imaging optics and pixel sizes, but often fine features in the reported resolution range are not identifiable due to partial volume artifacts, which are further discussed in section 2.3.1.5.

Spatial resolution may be improved with the use of higher magnification optics; however, this generally sacrifices specimen field-of-view. Tomographic observation-to-resolution scales are generally accepted as follows: conventional, 10^0 -to- 10^{-3} m; high-resolution, 10^{-1} -to- 10^{-4} m, ultra-high-resolution 10^{-2} -to- 10^{-5} m, and micro tomography 10^{-3} -to- 10^{-6} m (Banhart 2008a; Ketcham and Carlson 2001). The high spatial resolution of micro XCT imaging was, in part, a major reason for its use in this work. While other techniques, such as magnetic resonance imaging (MRI), may also provide non-destructive, 3D images of the internal structures in opaque materials, their spatial resolution limits are on the order of 10^{-3} to 10^{-5} m (Banhart 2008a; Dhondt et al. 2010; Windt et al. 2009).

2.3.1.4 *Reconstruction*

Image reconstruction is the process where the incremental 2D radiographic projections are convoluted and used to form the 3D volumetric tomograms of the object, complete with its internal structure. Mathematical algorithms inversely solve the Beer-Lambert intensity equation (2-4) from each incremental angular radiograph along the appropriate beam path (Wildenschild et al. 2002). The individual slices are thus the line integrals defining the specimen cross-section for a particular x-ray plane through the material. The most common algorithm is the filtered back projection technique, sometimes referred to as the fast filtered back transform (Dowd et al. 1999; Ketcham and Carlson 2001; Kuba and Herman 2008; Wildenschild et al. 2002). An x-ray beam is reduced in intensity to a certain degree, based on the structures through which it traverses, before being detected by the corresponding scintillator/pixel sensors. This results in a single pixel value in a single radiogram. As the specimen rotates, the beam path and detection devices remain the same, but the specimen's internal structures change orientation and position within the beam path. This causes different values for the same pixel location on each consecutive radiogram. The data from each detection point are stacked sequentially according to the scan progression, and stored as sinusoidal waves called sinograms, corresponding to the specimen angular rotation (ASTM-E-1441 2011; Ketcham and Carlson 2001). Sinograms from multiple beam-paths represent multiple equations defining the specimen's internal structures encountered throughout the scan (Stock 2009); however, as long as there are more detection readings, or angles, than paths, a finite solution can be calculated for each internal voxel element (Hounsfield 1973; Kuba and Herman 2008). The reconstructed cross-sections are thus grayscale maps of attenuation

coefficients within an object rather than the reduced intensities; higher voxel values (bright voxels) represent more attenuative materials.

2.3.1.5 Artifacts and Phase-contrast

Like all imaging techniques, tomography can often impart artifacts and noise in the resulting images. These artifacts can range from minor to severe, and can sometimes lead to misinterpretation of results. Common artifacts and sources of error include ring artifacts, beam hardening, partial volume effects, specimen motion, central axis misalignment, general detection noise, and phase-contrast or edge artifacts.

Ring artifacts are circular impressions in the reconstructed slices caused by faulty sensors in the scintillator or CCD devices (Wildenschild et al. 2002). This is generally reduced with a flat-field correction where images are taken of the pure beam, without the sample in the field of view (Haibel 2008). Yet this doesn't always solve the problem entirely; remnant overly bright or completely dark pixels, present in each incremental radiograph, appear as vertical line in the sinograms which are easy to remove during reconstruction (Ketcham and Carlson 2001). Lastly, some remaining ring artifacts in the tomograms may be further removed with image filtering in the Fourier, or frequency, domain post reconstruction (Munch et al. 2009; Ohser and Schladitz 2008).

Beam hardening is a particular problem in tomographic imaging when the source is polychromatic, consisting of a spectrum of x-ray energies and wavelengths. The Beer-Lambert equation, in its simplest form (2-4), assumes the source is monochromatic. The equation can be modified to compensate for polychromatic sources (Wildenschild et al. 2002); however, beam hardening still may occur when lower energy photons are

preferentially absorbed earlier along their path. This is often the case with industrial and medical CT systems, causing the average beam energy to effectively increase as it traverses the object (Kuba and Herman 2008). In reconstructed data, this artifact is manifest as brighter specimen edges, which appear to be more attenuative, even if they are the same material as more centralized structures (Kuba and Herman 2008; Wildenschild et al. 2002). The effect may be reduced by using a pre-hardening screen to filter the low-energy photons prior to specimen imaging, or by imaging thinner specimens (Ketcham and Carlson 2001). However, the effect could be avoided altogether if monochromatic x-rays are used, as is the case with a synchrotron source (Kinney and Nichols 1992).

Partial volume effects are always present in digitized images. This occurs because the area, or volume data as is the case in tomography, is discretely represented by the smallest repeat pixel units. However, when different materials occupy a region smaller than the voxel dimensions, the resulting attenuation value represents their average (Ketcham and Carlson 2001). This also results in blurring at material boundaries, and results in a distribution for each material attenuation value. Ideally, a XCT image of a 2-phase porous object, acquired with a monochromatic source, would result in a grayscale histogram with two separate lines indicating the pure phases. However, there will always be a distribution about the peaks due to partial volume effects, as well as other noise sources, phase uniformity, and material contrast.

Specimen motion during a scan can also cause blurring in reconstructed images. The reconstruction algorithms trace the line beam integrals through the specimen and across

multiple angles; deviation in specimen geometry or position during angular rotation will result in missing information affecting the algorithm accuracy (Haibel 2008). This presents particular problems when imaging dynamic systems such as mobile liquids or specimens being strained; however, if the motion is caused by instrumentation mechanics, repetitive geometric deviations appear in the sinograms which may be corrected during reconstruction (Haibel 2008). Similarly, rotation axis misalignment can cause semi-circular, wispy features to appear in reconstructed images; these however are easily removed by adjusting axis-specific parameters in the construction process (Haibel 2008).

General detection noise can result from mechanical deficiencies or stray radiation during scans. The former often occurs when high energy photons are inefficiently converted to visible light by the scintillating materials (Haibel 2008). Additionally, when x-rays interact with matter, scattering occurs causing source photons to deviate from their projection paths; these can often still reach the detectors causing greater than expected intensity for that point in space (Wildenschild et al. 2002). Additionally, as previously mentioned, new fluorescent photons, not associated with the source, are released by electron excitations occurring above atomic absorption edges (Banhart 2008b). When beam intensity, or photon flux is low, poor counting statistics also represent decreases in signal-to-noise ratios; this is often a problem with conventional cathode-anode x-ray tube sources (Ketcham and Carlson 2001).

Lastly, phase-contrast, also known as edge-enhancement, artifacts are often present in tomographic images. This occurs as a paired over/under designation of CT values at the

interface between two objects with sharp density and refractive index differences, such as solid/air edges (De Witte et al. 2009; Haibel 2008). The phase-contrast mechanism can be either helpful or unfavorable in image analysis, depending on application. Qualitative visual edge detection is certainly enhanced, and often aids in the recognition between low Z materials such as polymers or biological specimens, like wood (Betz et al. 2007; Haibel 2008). In fact, phase-contrast tomography is often used in conjunction with various phase retrieval algorithms which quantify and employ the wave diffraction differences between objects in the reconstruction process (De Witte et al. 2009; Scholz et al. 2010b; Weitkamp et al. 2011); this also serves as a phase-based material segmentation method (Peele and Nugent 2008; Wu et al. 2008). However, the false assignment of CT values at edges also hinders quantitative measurements of component size and connectivity when threshold-based material segmentation methods and absorption contrast reconstruction algorithms are employed (De Witte et al. 2009). The phase-contrast effect can be minimized by positioning the specimen as close as possible to the scintillator screen, which reduces the diffraction pattern spread and inference caused by material edges (Betz et al. 2007; Haibel 2008). Alternatively, large sample to detector distances induce phase-contrast, and are often used in conjunction with the reconstruction algorithms that employ it (Betz et al. 2007; Peele and Nugent 2008; Stock 2009; Wu et al. 2008).

2.3.1.6 *Synchrotron Radiation*

There are two general sources of x-ray radiation, x-ray tubes and synchrotron radiation facilities (Ketcham and Carlson 2001; Kinney and Nichols 1992; Wildenschild et al. 2002). While the former was invaluable in the development of XCT principles and

remains integral in medical and industrial CT imaging, the latter has proven superior and more versatile in materials research, and will be the primary focus of this discussion. Synchrotrons are large particle accelerators, under high vacuum, in which electrons are steered and propelled in a circular orbit by high magnetic fields. The continuous radial change in direction accelerates the particles causing the emission of excess energy as electromagnetic radiation in a tangential direction (Banhart 2008b; Kinney and Nichols 1992). The photon production process is of such high efficiency and flux that a synchrotron facility generally houses multiple tangential research stations known to as beam lines to harness and employ the radiation for numerous experimental analyses (Banhart 2008b). Brilliance, or brightness, is often used to compare the efficiency of x-ray production sources; it is found by dividing the flux by the emission angle and spectral bandwidth of the emitted radiation. Modern synchrotrons produce x-rays with brilliance in excess of 10 orders of magnitude greater than conventional x-ray tubes (Banhart 2008b; Stock 2009).

Synchrotron electromagnetic radiation can consist of a broad spectrum of energies including x-rays as well as infrared light, visible light, microwaves, and radio waves (Wildenschild et al. 2002); however, the brilliance is high enough that the beam is often made monochromatic (Kinney and Nichols 1992; Wildenschild et al. 2002). Discrete, single-energy beams not only increase reconstruction accuracy and efficiency, but also allow element-sensitive imaging just above characteristic chemical absorption edges (Betz et al. 2007). Additionally, placing the beam lines long distances away from the accelerator rings allows for high collimation and small spot-sizes, resulting in extremely coherent beams (Betz et al. 2007; Haibel 2008). Both collimation and making the beam

monochromatic reduce brilliance of typical x-ray tube sources, thus dramatically lowering SNR while increasing scan time to allow for sufficient detection counts. However, this is not the case with synchrotrons; scan times are often two to three orders of magnitude faster than tube-based XCT systems. Additionally, the high brilliance and SNR allows the use of finer gridded scintillators and CCD chips, resulting in finer spatial resolutions in the single digit to sub-micron scales (Betz et al. 2007; Haibel 2008; Kinney and Nichols 1992; Wildenschild et al. 2002).

2.3.2 X-ray Tomography of Wood and Wood-Composites

X-ray computed tomography has been used to study the internal structures of numerous biological materials; however, the focus of this research is XCT application to wood and wood composites. Wood is arguably the most widely employed material throughout human history; still today, novel applications and analyses are being developed to utilize and understand its complex, hierarchical structure more efficiently. Wood anatomy has been studied for centuries to understand structural properties, orthotropicity, fluid conduction, mass transport, molecular composition, tree growth and development, and the particular cellular features unique to different wood species. Traditionally, 2D microscopy has served as the primary analytical tool; however, as previously mentioned, this is destructive to the sample, often requires difficult specimen preparation and fails to fully define what is known to be a three-dimensional network. Several 3D analyses have also been employed such as cast-molding, serial sectioning, confocal scanning microscopy, nuclear magnetic resonance, ultrasonic and microwave imaging, thermal infrared techniques, and other forms of ionizing radiation such as neutrons or gamma rays

(Brashaw et al. 2009; Bucur 2003; Gindl 2001; Mannes et al. 2009a; Mannes et al. 2010; Mannes et al. 2009b; Mannes et al. 2009c; Xing et al. 2005). Each technique is valuable for a particular application, though the non-destructive nature, field-of-view, spatial resolution and material segmentation capabilities associated with XCT proved optimal for this research.

2.3.2.1 *Solid Wood Applications*

XCT is a fairly novel analytical tool for visualizing wood structures, having been employed by only a hand-full of research groups over the past two decades. Few wood species have been studied with this technique. Most commonly, XCT has been used to study beech, *Fagus sylvatica* (Brunetti et al. 2007; De Vetter et al. 2006; Hass et al. 2012; Hass et al. 2010; Mannes et al. 2010; Mannes et al. 2009b; Scholz et al. 2010a; Scholz et al. 2010b; Steppe et al. 2004; Wilkes et al. 2009), Scots pine, *Pinus sylvestris* (De Vetter et al. 2006; Forsberg et al. 2010; Mannes et al. 2010; Scholz et al. 2010a; Scholz et al. 2010b; Van den Bulcke et al. 2010; Van den Bulcke et al. 2008; Walther and Thoemen 2009) and Norway spruce, *Picea abies* (Keunecke et al. 2011; Mannes et al. 2010; Mannes et al. 2009b; Sanabria et al. 2011; Trtik et al. 2007), representing three of the most significant European commercial wood species. Other hardwood studies have included oaks, *Quercus sp.* (Mannes et al. 2010; Modzel et al. 2011; Steppe et al. 2004), hybrid poplar, *Populus deltoides x trichocarpa* (Modzel 2009; Modzel et al. 2011; Standfest et al. 2012), yellow-poplar, *Liriodendron tulipifera* (Modzel 2009), *Eucalyptus sp.* (Mayo et al. 2010), teak, *Tectona grandis* (Mayo et al. 2010) and Padouk, *Pterocarpus soyauxii* (Van den Bulcke et al. 2010). Other softwoods studied with XCT

include Douglas-fir, *Pseudotsuga menziesii* (Mayo et al. 2010; Modzel 2009; Modzel et al. 2011; Standfest et al. 2012), loblolly pine, *Pinus taeda* (Mayo et al. 2010; Modzel 2009), radiata pine, *Pinus radiata* (Evans et al. 2010) and common yew, *Taxus baccata* (Mannes et al. 2010). Voxel dimensions in these studies range from a few dozen microns down to 0.7 μm per side. True spatial resolutions, though, are somewhat less clear due to partial volume effects and other factors which often prevent the identification of the finest features in these voxel ranges (section 2.3.1.5).

One of the primary benefits of XCT analyses is that it allows researchers to rapidly probe reconstructed volumes and identify features in any orthogonal plane or direction, from a single specimen. For example, Mannes et al. used XCT to study a single specimen each of beech, oak, Scots pine, Norway spruce, and yew. In the hardwoods, he was able to identify earlywood and latewood vessels, tyloses, and intervessel pitting, but was unable to discern differences between smaller features such as libriform fibers, fiber-tracheids and axial parenchyma. In the softwoods, thick walled tracheids, ray parenchyma, dentate ray tracheids, spiral thickenings, cross-field pits and even bordered pits were found, though pit margos and tori were below the resolution limits (Mannes et al. 2010). The author also found it peculiar that tyloses and cells of different thicknesses exhibit different grayscale values in the reconstructed data, but argues that their chemical compositions and local densities are likely not different (Mannes et al. 2010). One might also interpret the different pixel values as phase-contrast artifacts or partial volume effects, or both.

Other studies have exploited XCT's 3D nature to analyze the void-space interconnectivity, porosity, and fluid conduction networks within wood samples. Trtik et al. was able to resolve void spaces within spruce small sub-volumes; he showed the connectivity of longitudinal tracheids to each other and to radial cells through their respective pit types (Trtik et al. 2007). Hass et al. identified full vessel networks in beech, and determined that they form in tangential clusters within a growth ring. He also identified that lateral liquid movement across growth-ring boundaries occurs primarily through ray cells (Hass et al. 2010). Similar vessel structures in both teak and eucalyptus samples have also been virtually excised for 3D connectivity display purposes (Mayo et al. 2010). In 2010, Modzel thresholded reconstructed wood XCT sub-volumes, with sufficient grayscale contrast, into their constituent material components; by summing the voxels belonging to the air phase, he quantified the void volume within yellow-poplar, loblolly pine and Douglas-fir specimens (Modzel 2009). Similarly, in 2012, Standfest et al. measured pore sizes in reconstructed Douglas-fir and hybrid poplar sub-volumes before and after a thermo-hygro-mechanical densification process. The researchers were able to observe the modified structures without conventional 2D microscopy specimen preparation procedures that involve water soaking, which would have swelled the compressed wood (Standfest et al. 2012).

The non-destructive nature of XCT has also proven valuable in several wood characterization studies. Archeologists identified structural features in an old wooden mask as belonging to the *Salix* genus, thus helping elucidate its date and place of origin (Mizuno et al. 2010). Steppe et al. investigated juvenile oak and beech wood porosity with XCT, but as the specimens remained undamaged by the analyses the researchers

were able to later microtome slices from the same specimens to compare results to traditional 2D light micrographs. Comparisons between the two techniques, provided they shared similar spatial resolutions, revealed high statistical agreement in vessel size and count (Steppe et al. 2004). Both wood sorption and mechanical testing have also been studied in situ with micro tomography. Derome and colleagues (2011) collected and registered consecutive scans of spruce wood following equilibration to multiple RH environments. The researchers uniquely determined that hysteretic dimensional stability behavior was different between earlywood and latewood regions. In particular, moisture induced strains in earlywood were significantly greater in the tangential direction than the radial; latewood cells, however, exhibited much less directionally dependent moisture movement, and retained their morphology between wet and dry conditions (Derome et al. 2011). As mentioned earlier in section 2.1.4, Forsberg and colleagues demonstrated a procedure that combined XCT and digital volume correlation (DVC) principles to recognize 3D strain development within Scots pine specimens under 3-point bending conditions. Specimens were initially scanned, free of load, to define the DVC grid; three consecutive scans, in which the load was increased step-wise, were then performed and registered with the first. DVC deformation patterns largely demonstrated expected behavior analogous to similar macroscopic measurements, with compression at the top of the specimen and tension below where a brash failure occurred (Forsberg et al. 2008; Forsberg et al. 2010).

XCT can provide both qualitative and quantitative information; the latter, however, often requires material segmentation into an object's various components. In micro-scale analyses of solid wood there are only two different materials present: wood cell wall and

air, filling the void regions. Though the two substances are primarily composed of low-Z atoms, their densities, and thus attenuation coefficients are distinctly different. In theory, reconstruction grayscale histograms should thus consist of two individual peaks, as discussed in section 2.3.1. In practice, material peaks often are broad and overlap one another, primarily due to low SNR levels and artifacts. Organic, cellular materials often contain numerous phase-contrast artifacts, as specimens are full of material edges that produce the paired over/under attenuation estimation values (section 2.3.1.5). Such overly bright/dark edge-outlines are evident in many reconstructed grayscale images throughout the wood XCT literature, and could be interpreted as such artifacts (Forsberg et al. 2008; Hass et al. 2010; Mannes et al. 2010; Modzel 2009; Standfest et al. 2010). Still, researchers have demonstrated successful two-phase wood segmentation is possible with grayscale threshold techniques following parameter optimization, phase-reducing reconstructions, morphological image processing operations and/or median filtering (Hass et al. 2010; Mayo et al. 2010; Modzel et al. 2011; Scholz et al. 2010b; Standfest et al. 2012; Trtik et al. 2007).

Greater challenges arise, however, when quantitative XCT analyses are applied to wood products containing multiple material phases, such as resinous softwoods, adhesively-bonded joints, wood-plastic composites, or wood coatings and sealants. For example, in their Scots pine results, Mannes et al. (2010), found multiple resin canals containing the hardened resin. The substance, having a similar gray-value as the surrounding cell wall material, was qualitatively distinguished based on the authors' prior knowledge of the material rather than grayscale histogram value (Mannes et al. 2010).

Polymeric resins, varnishes, waxes and oils commonly employed to bond or coat wood are organic; additionally, their in-service densities are similar to that of wood cell walls, which is approximately 1.5 g/cm^3 . As is the case, little absorption contrast is often observed between wood and these systems with XCT imaging. There is certainly potential for newer reconstruction or segmentation algorithms to distinguish between materials based on criteria other than absorption contrast and pixel gray value, such as image texture or phase contrast effects (Ohser and Schladitz 2008; Sharma and Aggarwal 2010; Todorovic and Ahuja 2009). However, this work primarily focused on generating sufficient absorption contrast for gray-scale segmentation with modified wood-adhesive resins. Several other researchers have attempted to overcome these difficulties, and apply quantitative tomography to wood-composites and other multi-phase organic systems. Few studies investigated unmodified adhesives and coatings, while several researchers attempted to enhance the grayscale contrast by tagging the resins with different heavy-metal compounds.

2.3.2.2 *Wood-Adhesive Composites*

Composite XCT studies have investigated different joint-assemblies, such as single bondline systems (i.e. between two separate lamina, such as plywood) or those with numerous glue-joints (i.e. particle-based products), as well as many different adhesive types.

In 2011, Van den Bulcke et al. observed multi-layer beech and poplar plywood assemblies bonded with either a PF or MUF resin. At first inspection, reconstructions appear to show bright adhesive layers compared to the surrounding wood structure. This,

however, could also be an artifact due to the low spatial resolution (40 μm per voxel side). At these dimensions, partial volume effects (section 2.3.1.5) might have created two hybrid attenuation values accounting for more macroscopic mixed phases: wood/adhesive in the bondline vicinity and wood/air in the un-penetrated regions. Similar results were found at low resolutions by Sanabria et al. (2011) where they studied spruce timbers bonded with a one-component, moisture-cure PUR adhesive. Fascinatingly, they identified the grayscale values of the bondline region matched those of the latewood; yet, the latewood regions were brighter than the earlywood regions (Sanabria et al. 2011). Both the thick-walled cells, and those with adhesive-filled lumens appear to block more x-rays than the thin-walled, empty-lumen, earlywood regions. This too, however, may be an artifact due to the low spatial resolution; in reality, cell wall density is nearly the same between earlywood and latewood. In both adhesive studies, at this scale, accurate segmentation could not be made between the adhesive, wood and air phases.

At a higher resolution (3.2 $\mu\text{m}/\text{voxel}$), Standfest et al. (2010) studied medium density fiber board (MDF) containing an unmodified UF binder. The authors' primary focus was to measure 3D density and porosity; thus, they did not segment the adhesive or comment on the resin distribution. Yet, it is clear from provided tomograms that no contrast is present between the wood and adhesive phases. The authors do, however, identify contrast between the voids between fiber-bundles and those within fiber lumens, with the latter appearing less attenuative (Standfest et al. 2010). While helpful for characterizing fiber collapse and compaction, this again is more likely a phase-contrast artifact as both void spaces are air. The dark phase-contrast edges within the lumens are likely

overlapping due to their close physical proximity, causing them to appear darker than the broader void spaces between particles.

Philipp Hass and colleagues studied the adhesive penetration behavior of three separate adhesive systems: PUR, UF and PVAc, into beech wood (Hass et al. 2009; Hass et al. 2012; Hass et al. 2010). The researchers provide excellent reasoning for the necessity of 3D penetration characterization techniques, especially in hardwoods where traditional 2D micrographs often show adhesive-filled vessels isolated some distance away from the bondline. The authors demonstrate how 3D micro XCT, with a spatial resolution of 3.7 μm /voxel side, allowed them to rapidly observe penetration patterns at many locations along a specimen's longitudinal axis, providing a more complete representation of the bondline. Additionally, Hass et al. (2011) presented novel wood/adhesive interaction observations, made possible by the micro XCT technique. For instance, virtual slices were excised directly down the length of each bondline region; the planar adhesive layer representations confirmed behavioral trends expected for each adhesive type. The high mobility and reactivity of the PUR system left a patchy adhesive layer, starved in many locations. The glassy, thermoset, UF system resulted in an adhesive layer containing many internal cracks, likely from the differential moduli and dimensional stability behavior compared to the wood adherends. Lastly, the ductile PVAc adhesive layer contained several pores resulting from excessive shrinkage during coalescence and bond formation (Hass et al. 2012). Full-length segmented bondlines, of each adhesive system, are also provided, but the authors acknowledge "strong overlap between the adhesive and wood signals complicated the segmentations" (Hass et al. 2012). They suggest that perhaps a more attenuative dopant or contrast agent may be added to the adhesive phase

to increase the absorption contrast; though, caution is given to potential phase-separation problems often associated with such tagging procedures. Several researchers have, in fact, attempted this tagging approach with varying levels of success.

Walther and Thoemen (2009) tried to segment tagged-UF adhesives, and quantify their distribution, in MDF panels. Barium sulfate and iodine ($Z_{\text{Ba}} = 56$, $Z_{\text{I}} = 53$) were both incorporated into the two resins prior to bonding, with hope for increasing their attenuation values. Scanning electron microscopy (SEM) revealed, that the barium sulfate compound phase-separated and agglomerated randomly along with the fibers. The iodine compound appeared uniformly dispersed throughout the entire MDF matrix, independent of the resin; the authors attributed the iodine behavior to it being water-soluble and therefore more mobile than the UF polymers at the high steam pressures experienced during MDF hot-pressing. The researchers were, therefore, unable to separate the stained adhesive and wood fibers in the resulting XCT reconstructions. The authors suggest a tag agent linked to the adhesive, which does not influence its curing behavior would be beneficial (Walther and Thoemen 2009).

Evans et al. (2010) tagged a MUF resin with copper sulfate ($Z_{\text{Cu}} = 29$) for particle board XCT evaluation. The authors reported enhanced contrast, and used segmented data to quantify resin coverage. Yet, it is peculiar that they display the segmented resin as two different colors; no explanation is provided for this, but this could be evidence of phase separation between the tag and the adhesive. The authors maintain that the copper-II ions remain bound to the urea-formaldehyde component in the resin (Evans et al. 2010); yet, no analytical evidence was provided to support this claim. The authors do cite a patent

(Feng 2002) for justification; though this too, is vague. The specific claim suggests that a water soluble cation, such as Cu(II+) , may be added to liquid resins, and that it would remain associated with the polymers (Feng 2002); however, other research has shown such ions are free to migrate from the adhesive phase when they are not directly linked to the resin polymers (Modzel 2009).

Modzel and colleagues (2009 and 2011) observed the ion migration behavior when they investigated the penetration and moisture durability behavior of a PF adhesive tagged with rubidium ($Z_{\text{Rb}} = 37$). The researchers used rubidium hydroxide to catalyze the phenol/formaldehyde polymerization in substitute of the conventional sodium hydroxide. Yellow-poplar, Douglas-fir and loblolly pine bondlines, prepared with the Rb-PF resin, were scanned at 16 KeV, just above the rubidium K1 electron binding energy. Several resulting tomograms did provide sufficient contrast between the adhesive and wood structures due to the Rb K-edge attenuation; however, these results were inconsistent across multiple replicates (Modzel 2009; Modzel et al. 2011). It was determined that the catalyst, which had been expected to remain associated with the resin was, in fact, not attached to the adhesive polymers, and thus migrated independently during bond formation. Combination of fluorescence microscopy and wavelength dispersive spectroscopy confirmed Rb was not confined to the resin (Modzel 2009; Modzel et al. 2011).

However, Modzel's scans that did exhibit sharp grayscale contrast were segmented, and yielded valuable new details about the PF bondlines and adhesive penetration. For example, virtual cross-section views of Modzel's XCT tomograms showed softwood

penetration patterns are fairly uniform, with adhesive occupying tracheids in the bondline vicinity, and in hardwoods the adhesive is distributed more randomly in the vessel elements. Such penetration patterns are commonly observed with 2D techniques, however, 3D renderings of the isolated adhesive phase revealed the radial pathways traversed by the resin during bond formation (Modzel 2009). These radial connections are often above or below the plane of interest in traditional 2D micrographs, and thus omitted when assumptions are made as to the influence of secluded adhesive-filled cells on bond performance. XCT also allowed Modzel to observe bubbles which formed in 3D adhesive columns, and to evaluate bondline quality before and after cyclic moisture testing (Modzel 2009); traditional 2D microscopy would not have allowed either assessment.

The author also presents an automated approach to measure “effective bondline thickness” which operates on a per-slice basis and counts the pixels segmented into the adhesive phase (Modzel 2009). This method is quantitative, repeatable, and can be applied to the entire bondline volume rapidly, potentially making it more accurate than previously employed techniques. Moreover, the true benefit of this XCT analysis methodology is that undamaged specimens might later be stressed mechanically to better understand the role of penetration on joint performance. This concept, in fact, is one of the primary objectives of the present research, which attempts to push forward the XCT adhesive analyses initiated by Modzel.

2.3.2.3 *Other Multi-phase Wood Systems*

XCT has been used to analyze other multi-phase wood products. While the present research only addresses XCT of wood-adhesive joints, the penetration, tagging and segmentation procedures employed for other organic materials in wood products are certainly relevant. For instance, XCT offers a rapid and non-destructive method to image the particle distribution within wood plastic composites (WPCs) in 3D (Muszyński 2009; Wang 2007; Wang et al. 2007). However, similar material contrast problems arise when one tries to segment the wood filler particles from the polymeric continuous phase.

Wang (2007) investigated WPC tomographic imaging and segmentation for three common matrix plastics, high-density polyethylene (HDPE), polypropylene (PP) and polyvinylchloride (PVC). HDPE and PP polymers contain only carbon and hydrogen, and have densities less than 1 g/cm³. As such, WPC's made with these plastics fail to offer sufficient XCT contrast to the wood filler particles. Wang et al. (2007) added gold micro- and nano-particles ($Z_{Au} = 79$) at 1 wt%, to increase the attenuation of HDPE matrices. While contrast was enhanced, SEM images revealed that the gold particles agglomerated. The gold appeared as separate components in the reconstructed XCT volumes, and thus distinguishing between HDPE and wood still proved difficult (Wang et al. 2007). In fact, the added contrast from the gold particles was not as great, or as consistent, as for WPCs containing PVC matrices.

Chlorine is not as heavy as gold ($Z_{Cl} = 17$); however, it is chemically attached to every PVC polymer repeat unit. This makes PVC polymers extremely uniform, and denser than HDPE or PP. The particular PVC used in this study had a density of 1.4 g/cm³, which is

still similar to that of the wood cell wall. However, at the achieved $6\ \mu\text{m}/\text{voxel}$ spatial resolution, wood cell walls were not differentiated from their lumen spaces, and thus the filler particles exhibited a nominal density lower than the surrounding matrix (Wang 2007).

Wood coatings have also been investigated with XCT techniques; these organic systems also present numerous segmentation difficulties. For example, in 2010 Mannes et al. attempted to visualize the penetration of a water-repellant coating containing silver nanoparticles ($Z_{\text{Ag}} = 47$) into both beech and spruce wood specimens. However, it was determined that the silver-concentration in the preservative was too low to increase its overall attenuation coefficient higher than that of the surrounding wood cells, and thus segmentation was not possible (Mannes et al. 2010). Yet, this again reminds the reader that x-ray contrast is a function of both Z and atoms per unit volume, or density.

In 2010, Scholz et al. used XCT to study wax-impregnated wood. The authors achieved 1.2 and $3.7\ \mu\text{m}/\text{voxel}$ spatial resolutions, for beech and pine wood, respectively, and were able to separate the cell wall, wax, and air signals. The un-tagged, organic waxes, having densities just below $1\ \text{g}/\text{cm}^3$, resulted in attenuation values between those for wood and air (Scholz et al. 2010a; Scholz et al. 2010b), and the grayscale histograms showed well defined minima between the three material peaks. However, this result is in contrast to previous authors, who have shown far greater overlap between wood and air peaks (Modzel 2009; Trtik et al. 2007; Van den Bulcke et al. 2010). Perhaps this is the result of both the high spatial resolution and the authors' use of a phase-contrast reducing algorithm (De Witte et al. 2009; Scholz et al. 2010b).

Van den Bulcke and colleagues used micro XCT analyses to study wood coatings on and in pine and beech wood samples, with 1.2 to 2 $\mu\text{m}/\text{voxel}$ spatial resolutions (Van den Bulcke et al. 2010; Van den Bulcke et al. 2008; Van den Bulcke et al. 2005). The authors' present several three-phase segmented images, and even discuss how the segmentation between the wood and coating phases was cleaner than between the wood and air phases (Van den Bulcke et al. 2010). Unfortunately, there is no discussion of the chemistry or density of the investigated coatings (Van den Bulcke et al. 2010; Van den Bulcke et al. 2008; Van den Bulcke et al. 2005). In 2008, the authors even differentiate and segment between two separate coatings, a top and a base coat, and wood; however, the paper only describes these as a water-borne and solvent borne coating (Van den Bulcke et al. 2008).

Lastly, De Vetter et al. present an XCT investigation of organosilicon compounds in wood. The researchers doped a polydimethylsiloxane coating with 3-bromopropyl-trimethoxysilane and measured its penetration into wood. Both silicone and bromine ($Z_{\text{Si}} = 14$, $Z_{\text{Br}} = 35$) are heavier than the organic atoms in wood polymers, and as such the organosilicon compounds exhibited a significantly brighter attenuation in reconstructed images (De Vetter et al. 2006). However, with only 10 $\mu\text{m}/\text{voxel}$ spatial resolution, wood/air phases could not be cleanly segmented. This paper also describes the use of SEM with EDS to collect 2D maps of the silicon and bromine signals across the wood surface. The combined technique allowed the researchers to determine in-homogeneities in their mixed compounds, as the bromine and silicon signals did not overlap. However, the authors maintain that SEM, EDS and micro XCT can be used as complementary

analyses to track the distribution of various compounds in wood structures (De Vetter et al. 2006).

In summary, x-ray computed tomography applications to solid wood, composites and coatings have been fairly limited. Only a few species and multi-phase systems have been characterized with this 3D technique. Furthermore, segmentation between wood and other organic materials, such as adhesives, is often difficult, and appears to be highly dependent on image quality and resolution. Often partial volume effects lower the theoretical spatial resolutions and cause grayscale overlap near material edges. Several researchers have attempted to increase material contrast for better segmentation by doping resins and coatings with heavier elements, yet these tagging procedures have presented additional difficulties. Many systems phase separated (De Vetter et al. 2006; Modzel et al. 2011; Wang et al. 2007), and in other studies it was unclear how uniformly the tags were dispersed along the organic polymer chains (Evans et al. 2010). Moreover, using the appropriate tag concentration is also important, as both Z and atoms per unit volume, or density, affect attenuation (Mannes et al. 2010). Lastly, it is of crucial importance to recognize that the penetration, durability, mechanical properties and bonding performance of tagged resins may be inherently different than for unmodified systems. Therefore, authors and readers alike cannot always generalize the behavior of a particular coating or adhesive containing a heavy element dopant to be representative of others of its kind.

2.4 References – Introduction and Literature Review

ASTM D 905 - 03 (2007) Standard test method for strength properties of adhesive bonds in shear by compression loading. 15.06 ASTM International, West Conshohocken, PA.

ASTM D 1037 - 06a (2007) Standard test methods for evaluating properties of wood-base fiber and particle panel materials¹. ASTM International, West Conshohocken, PA.

ASTM E1441 (2011) Standard guide for computed tomography (CT) imaging. ASTM International, West Conshohocken, PA.

Banhart, J. 2008a: Introduction. In: Banhart, J., editor, *Advanced Tomographic Methods in Materials Research and Engineering*, Oxford, New York: Oxford University Press, 3-18.

Banhart, J. 2008b: Radiation sources and interaction of radiation with matter. In: Banhart, J., editor, *Advanced Tomographic Methods in Materials Research and Engineering*, Oxford, New York: Oxford University Press, 107-140.

Bao, S. C., Daunch, W. A., Sun, Y. H., Rinaldi, P. L., Marcinko, J. J. and Phanopoulos, C. (2003) Solid state two-dimensional NMR studies of polymeric diphenylmethane diisocyanate (PMDI) reaction in wood. *Forest Products Journal* 53, 6, 63-71.

Bay, B. K. (2008) Methods and applications of digital volume correlation. *Journal of Strain Analysis for Engineering Design* 43, 8, 745-760.

Bay, B. K., Smith, T. S., Fyhrie, D. P. and Saad, M. (1999) Digital volume correlation: Three-dimensional strain mapping using X-ray tomography. *Experimental Mechanics* 39, 3, 217-226.

Betz, O., Wegst, U., Weide, D., Heethoff, M., Helfen, L., Lee, W. K. and Cloetens, P. (2007) Imaging applications of synchrotron X-ray phase-contrast microtomography in biological morphology and biomaterials science. 1. General aspects of the technique and its advantages in the analysis of millimetre-sized arthropod structure. *J. Microsc.-Oxf.* 227, 1, 51-71.

Blackman, B., Dear, J. P., Kinloch, A. J. and Osiyemi, S. (1991) The calculation of adhesive fracture energies from double-cantilever beam test specimens. *Journal of Materials Science Letters* 10, 5, 253-256.

Blyberg, L., Serrano, E., Enquist, B. and Sterley, M. (2012) Adhesive joints for structural timber/glass applications: Experimental testing and evaluation methods. *International Journal of Adhesion and Adhesives* 35, 76-87.

Bolton, A. J., Dinwoodie, J. M. and Davies, D. A. (1988) The validity of the use of SEM/EDAx as a tool for the detection of UF resin penetration into wood cell-walls in particleboard. *Wood Science and Technology* 22, 4, 345-356.

Bowyer, J. L., Shmulsky, R. and Haygreen, J. G. *Forest products and wood science : an introduction.* Blackwell Pub., Ames, Iowa, 2007

Brady, D. E. and Kamke, F. A. (1988) Effects of hot-pressing parameters on resin penetration. *Forest Products Journal* 38, 11-12, 63-68.

Brashaw, B. K., Bucur, V., Divos, F., Goncalves, R., Lu, J. X., Meder, R., Pellerin, R. F., Potter, S., Ross, R. J., Wang, X. P. and Yin, Y. F. (2009) Nondestructive testing and evaluation of wood: A worldwide research update. *Forest Products Journal* 59, 3, 7-14.

Brunetti, A., Mariani, A. and Bidali, S. (2007) X-ray tomography as an estimation technique for wood consolidation by frontal polymerization. *Nuovo Cimento Soc. Ital. Fis. C-Geophys. Space Phys.* 30, 4, 407-413.

Buckley, C. J., Phanopoulos, C., Khaleque, N., Engelen, A., Holwill, M. E. J. and Michette, A. G. (2002) Examination of the penetration of polymeric methylene di-phenyl-di-isocyanate (pMDI) into wood structure using chemical-state x-ray microscopy. *Holzforschung* 56, 2, 215-222.

Bucur, V. (2003) Techniques for high resolution imaging of wood structure: a review. *Measurement Science & Technology* 14, 12, R91-R98.

Cao, Y. 2010: Characterization of PF/PVAc hybrid adhesive-wood interaction and its effect on wood strand composites performance. *Department of Civil and Environmental Engineering*, Washington State University, Pullman, WA.

Chowdhury, S., Yadama, V. and Laborie, M. P. (2011) Reactive maleic anhydride polyolefins (MAPOs) in oriented strand board. Part 1: Dynamic thermomechanical properties of phenol formaldehyde resins blended with two MAPOs. *Holzforschung* 65, 1, 81-87.

Christiansen, A. W. (1990) How overdrying wood reduces its bonding to phenol-formaldehyde adhesives - a critical-review of the literature. 1. Physical responses. *Wood and Fiber Science* 22, 4, 441-459.

Christiansen, A. W. (1991) How overdrying wood reduces its bonding to phenol-formaldehyde adhesives - a critical-review of the literature. 2. Chemical-reactions. *Wood and Fiber Science* 23, 1, 69-84.

Das, S., Malmberg, M. J. and Frazier, C. E. (2007) Cure chemistry of wood/polymeric isocyanate (PMDI) bonds: Effect of wood species. *International Journal of Adhesion and Adhesives* 27, 3, 250-257.

Davidson, M. W. and Abramowitz, M. 2002: Optical Microscopy. In, *Encyclopedia of Imaging Science and Technology*: John Wiley & Sons, Inc.

De Vetter, L., Cnudde, V., Masschaele, B., Jacobs, P. J. S. and Van Acker, J. (2006) Detection and distribution analysis of organosilicon compounds in wood by means of SEM-EDX and micro-CT. *Mater. Charact.* 56, 1, 39-48.

De Witte, Y., Boone, M., Vlassenbroeck, J., Dierick, M. and Van Hoorebeke, L. (2009) Bronnikov-aided correction for x-ray computed tomography. *J. Opt. Soc. Am. A-Opt. Image Sci. Vis.* 26, 4, 890-894.

Derome, D., Griffa, M., Koebel, M. and Carmeliet, J. (2011) Hysteretic swelling of wood at cellular scale probed by phase-contrast X-ray tomography. *Journal of Structural Biology* 173, 1, 180-190.

DeVries, K. L. and Borgmeier, P. R. 1994: Testing of Adhesives. In: Pizzi, A. and Mittal, K. L., editors, *Handbook of adhesive technology*, New York: Marcel Dekker, Inc., 65-91.

Dhondt, S., Vanhaeren, H., Van Loo, D., Cnudde, V. and Inzé, D. (2010) Plant structure visualization by high-resolution X-ray computed tomography. *Trends in Plant Science* 15, 8, 419-422.

Dowd, B. A., Campbell, G. H., Marr, R. B., Nagarkar, V. V., Tipnis, S. V., Axe, L. and Siddons, D. P. (1999) Developments in synchrotron x-ray computed microtomography at the National Synchrotron Light Source. 224-236.

Ebewele, R., River, B. and Koutsky, J. (1979) Tapered double cantilever beam fracture tests of phenolic-wood adhesive joints .Part I. Development of specimen geometry - Effects of bondline thickness, wood anisotropy and cure time on fracture energy. *Wood and Fiber* 11, 3, 197-213.

Ebewele, R. O., River, B. H. and Koutsky, J. A. (1980) Tapered double cantilever beam fracture tests of phenolic-wood adhesive joints .part II. Effects of surface-roughness, the nature of surface-roughness, and surface aging on joint fracture energy. *Wood and Fiber* 12, 1, 40-65.

Ebewele, R. O., River, B. H. and Koutsky, J. A. (1982) Relationship between phenolic adhesive chemistry, cure and joint performance .part I. Effects of base resin constitution and hardener on fracture energy and thermal effects during cure. *Journal of Adhesion* 14, 3-4, 189-217.

Ebewele, R. O., River, B. H. and Koutsky, J. A. (1986a) Relationship between phenolic adhesive chemistry and adhesive joint performance - Effect of filler type on fracture energy. *Journal of Applied Polymer Science* 31, 7, 2275-2302.

Ebewele, R. O., River, B. H. and Koutsky, J. A. (1986b) Wood processing variables and adhesive joint performance. *Journal of Applied Polymer Science* 32, 1, 2979-2988.

Evans, P. D., Morrison, O., Senden, T. J., Vollmer, S., Roberts, R. J., Limaye, A., Arns, C. H., Averdunk, H., Lowe, A. and Knackstedt, M. A. (2010) Visualization and numerical analysis of adhesive distribution in particleboard using X-ray micro-computed tomography. *International Journal of Adhesion and Adhesives In Press, Corrected Proof*.

Feng, M. W. 2002: X-ray measurement of resin distribution in a cellulosic material. In: Office, U. S. P., editor, United States of America, 10. 6,463,120

Forsberg, F., Mooser, R., Arnold, M., Hack, E. and Wyss, P. (2008) 3D micro-scale deformations of wood in bending: Synchrotron radiation μ CT data analyzed with digital volume correlation. *Journal of Structural Biology* 164, 3, 255-262.

Forsberg, F., Sjudahl, M., Mooser, R., Hack, E. and Wyss, P. (2010) Full three-dimensional strain measurements on wood exposed to three-point bending: Analysis by use of digital volume correlation applied to synchrotron radiation micro-computed tomography image data. *Strain* 46, 1, 47-60.

Frazier, C. E. 2003: Isocyanate wood binders. In: Pizzi, A. and Mittal, K. L., editors, *Handbook of Adhesive Technology*, New York: Marcel Dekker, Inc.

Frazier, C. E. and Ni, J. W. (1998) On the occurrence of network interpenetration in the wood-isocyanate adhesive interphase. *International Journal of Adhesion and Adhesives* 18, 2, 81-87.

Frihart, C. R. 2005: Wood adhesion and adhesives. In: Rowell, R. M., editor, *Handbook of Wood Chemistry and Wood Composites*, New York: Taylor & Francis Group.

Frihart, C. R. and Hunt, C. G. 2010: Adhesives with wood materials: bond formation and performance. In: (U.S.), F. P. L., editor, *The Wood Handbook: Wood as an Engineering Material; General Technical Report FPL-GTR-190*, Madison, WI: USDA Forest Service.

Frihart, C. R., Yelle, D. J., Jakes, J. E., Ralph, J. and Stone, D. S. 2010: Use of a new methodology to elucidate isocyanate adhesion to wood. In: Anderson, G., editor *Proceedings of the 33rd Annual Meeting of the Adhesion Society*, Daytona Beach, FL, USA.

Gagliano, J. M. and Frazier, C. E. (2001) Improvements in the fracture cleavage testing of adhesively-bonded wood. *Wood and Fiber Science* 33, 3, 377-385.

Geddes, K. 2003: Polyvinyl and ethylene-vinyl acetates. In: Pizzi, A. and Mittal, K. L., editors, *Handbook of Adhesive Technology*, New York: Marcel Dekker, Inc.

Gindl, W. (2001) SEM and UV-microscopic investigation of glue lines in Parallam((R)) PSL. *Holz Als Roh-Und Werkstoff* 59, 3, 211-214.

Gindl, W., Dessipri, E. and Wimmer, R. (2002) Using UV-microscopy to study diffusion of melamine-urea-formaldehyde resin in cell walls of spruce wood. *Holzforschung* 56, 1, 103-107.

Gindl, W., Schoberl, T. and Jeronimidis, G. (2004a) The interphase in phenol-formaldehyde and polymeric methylene diphenyl-di-isocyanate glue lines in wood. *International Journal of Adhesion and Adhesives* 24, 4, 279-286.

Gindl, W., Schöberl, T. and Jeronimidis, G. (2004b) Corrigendum to "The interphase in phenol-formaldehyde (PF) and polymeric methylene di-phenyl-di-isocyanate (pMDI)

glue lines in wood": [Int. J. Adhes. Adhes. 24 (2004) 279–286]. International Journal of Adhesion and Adhesives 24, 6, 535.

Gindl, W., Sretenovic, A., Vincenti, A. and Muller, U. (2005) Direct measurement of strain distribution along a wood bond line. Part 2: Effects of adhesive penetration on strain distribution. *Holzforschung* 59, 3, 307-310.

Goodhew, P. J., Humphreys, F. J. and Beanland, R. Electron microscopy and analysis. Taylor & Francis, London ; New York, 2001

Graafsma, H. and Martin, T. 2008: Detectors for synchrotron tomography. In: Banhart, J., editor, *Advanced Tomographic Methods in Materials Research and Engineering*, Oxford: Oxford University Press, 277-302.

Haibel, A. 2008: Synchrotron x-ray absorption tomography. In: Banhart, J., editor, *Advanced Tomographic Methods in Materials Research and Engineering*, Oxford, New York: Oxford University Press, 141-160.

Hass, P., Muller, C., Clauss, S. and Niemz, P. (2009) Influence of growth ring angle, adhesive system and viscosity on the shear strength of adhesive bonds. *Wood Material Science & Engineering*, 3-4, 140-146.

Hass, P., Wittel, F., Mendoza, M., Herrmann, H. and Niemz, P. (2012) Adhesive penetration in beech wood: experiments. *Wood Science and Technology* 46, 1-3, 243 - 256.

Hass, P., Wittel, F. K., McDonald, S. A., Marone, F., Stampanoni, M., Herrmann, H. J. and Niemz, P. (2010) Pore space analysis of beech wood: The vessel network. *Holzforschung* 64, 5, 639-644.

Hosen, J. 2010: Fundamental analysis of wood adhesion primers. *Wood Science and Forest Products*, Virginia Tech, Blacksburg, VA.

Hounsfield, G. N. (1973) Computed transverse axial scanning (tomography). *British Journal of Radiology* 46, 552, 1016-1022.

Hse, C. Y. (1972) Wettability of southern pine veneers by phenol formaldehyde wood adhesives. *Forest Products Journal* 22, 1, 51-56.

Iltis, G. C., Armstrong, R. T., Jansik, D. P., Wood, B. D. and Wildenschild, D. (2011) Imaging biofilm architecture within porous media using synchrotron-based X-ray computed microtomography. *Water Resources Research* 47.

Jakes, J. E., Yelle, D. J., Beecher, J. F., Frihart, C. R. and Stone, D. S. 2009: Characterizing polymeric methylene diphenyl diisocyanate reactions with wood: 2. Nano-indentation. In: Frihart, C. R., Hunt, C. G. and Moon, R. J., editors, *Proceedings of the International Conference on Wood Adhesives 2009*, Lake Tahoe, NV, USA: Forest Products Society, 11 p.

Johnson, S. E. and Kamke, F. A. (1992) Quantitative-analysis of gross adhesive penetration in wood using fluorescence microscopy. *Journal of Adhesion* 40, 1, 47-61.

Kamke, F. A. and Lee, J. N. (2007) Adhesive penetration in wood - a review. *Wood and Fiber Science* 39, 2, 205-220.

Kamke, F. A., Nairn, J. A., Muszynski, L., Paris, J. L., Schwarzkopf, M. and Xiao, X. (2014) Methodology for micro-mechanical analysis of an adhesive bond using micro computed x-ray tomography and numerical modeling. *Wood and Fiber Science* 46, 1.

Ketcham, R. A. and Carlson, W. D. (2001) Acquisition, optimization and interpretation of X-ray computed tomographic imagery: applications to the geosciences. *Computers & Geosciences* 27, 4, 381-400.

Keunecke, D., Novosseletz, K., Lanvermann, C., Mannes, D. and Niemz, P. (2011) Combination of X-ray and digital image correlation for the analysis of moisture-induced strain in wood: opportunities and challenges. *European Journal of Wood and Wood Products*, 1-7.

Kim, S. and Kim, H. J. (2006) Study of miscibility of melamine-formaldehyde resin and poly(vinyl acetate) blends for use as adhesives in engineered flooring. *Journal of Adhesion Science and Technology* 20, 2-3, 209-219.

Kinney, J. H. and Nichols, M. C. (1992) X-ray tomographic microscopy (XTM) using synchrotron radiation. *Annu. Rev. Mater. Sci.* 22, 121-152.

Konnerth, J., Harper, D., Lee, S. H., Rials, T. G. and Gindl, W. (2008) Adhesive penetration of wood cell walls investigated by scanning thermal microscopy (SThM). *Holzforschung* 62, 1, 91-98.

Kuba, A. and Herman, G. T. 2008: Some mathematical concepts for tomographic reconstruction. In: Banhart, J., editor, *Advanced Tomographic Methods in Materials Research and Engineering*, Oxford, New York: Oxford University Prss, 19-36.

Kutnar, A., Kamke, F. and Sernek, M. (2008) The mechanical properties of densified VTC wood relevant for structural composites. *Holz Als Roh-Und Werkstoff* 66, 6, 439-446.

Lopez- Suevos, F. and Frazier, C. E. (2006) Rheology of latex films bonded to wood: influence of cross-linking. *Holzforschung* 60, 1, 47-52.

Lopez-Suevos, F. and Frazier, C. E. (2005) Parallel-plate rheology of latex films bonded to wood. *Holzforschung* 59, 4, 435-440.

Lopez-Suevos, F. and Frazier, C. E. (2006a) Fracture cleavage analysis of PVAc latex adhesives: Influence of phenolic additives. *Holzforschung* 60, 3, 313-317.

Lopez-Suevos, F. and Frazier, C. E. (2006b) The role of resol fortifiers in latex wood adhesives. *Holzforschung* 60, 5, 561-566.

Lopez-Suevos, F. and Frazier, C. E. (2008) Wood-adhesive interactions in a PVAc latex. *Holzforschung* 62, 4, 468-471.

Mannes, D., Lehmann, E., Cherubini, P. and Niemz, P. (2009a) Neutron imaging versus standard X-ray densitometry as method to measure tree-ring wood density (vol 21, pg 605, 2007). *Trees-Structure and Function* 23, 5, 1123-1123.

Mannes, D., Marone, F., Lehmann, E., Stampanoni, M. and Niemz, P. (2010) Application areas of synchrotron radiation tomographic microscopy for wood research. *Wood Science and Technology* 44, 1, 67-84.

- Mannes, D., Niemz, P. and Lehmann, E. (2009b) Tomographic investigations of wood from macroscopic to microscopic scale. *Wood Research* 54, 3, 33-44.
- Mannes, D., Sonderegger, W., Hering, S., Lehmann, E. and Niemz, P. (2009c) Non-destructive determination and quantification of diffusion processes in wood by means of neutron imaging. *Holzforschung* 63, 5, 589-596.
- Mantanis, G. and Young, R. (1997) Wetting of wood. *Wood Science and Technology* 31, 5, 339-353.
- Marra, A. Technology of wood bonding: Principles in practice. Van Nostrand Reinhold, New York, 1992
- Mayo, S. C., Chen, F. and Evans, R. (2010) Micron-scale 3D imaging of wood and plant microstructure using high-resolution X-ray phase-contrast microtomography. *Journal of Structural Biology* 171, 2, 182-188.
- Mijovic, J. S. and Koutsky, J. A. (1979) Effect of wood grain angle on fracture properties and fracture morphology of wood-epoxy joints. *Wood Science* 11, 3, 164-168.
- Mizuno, S., Torizu, R. and Sugiyama, J. (2010) Wood identification of a wooden mask using synchrotron X-ray microtomography. *Journal of Archaeological Science* 37, 11, 2842-2845.
- Modzel, G. 2009: Computed X-ray analysis of wood-adhesive bonds. *Wood Science and Engineering*, Oregon State University, Corvallis, OR: 240.

Modzel, G., Kamke, F. A. and De Carlo, F. (2011) Comparative analysis of a wood-adhesive bondline. *Wood Science and Technology* 45, 1, 147-158.

Muller, U., Sretenovic, A., Vincenti, A. and Gindl, W. (2005) Direct measurement of strain distribution along a wood bond line. Part 1: Shear strain concentration in a lap joint specimen by means of electronic speckle pattern interferometry. *Holzforschung* 59, 3, 300-306.

Munch, B., Trtik, P., Marone, F. and Stampanoni, M. (2009) Stripe and ring artifact removal with combined wavelet - Fourier filtering. *Optics Express* 17, 10, 8567-8591.

Muszyński, L. (2009) Imaging wood plastic composites (WPCs): X-ray computed tomography, A few promising techniques, and why we should pay attention. *BioResources* 4, 3, 1210-1221.

Muszynski, L., Kamke, F. A., Nairn, J. A., Schwarzkopf, M. and Paris, J. L. 2014: Integrated method for multi-scale/multi-modal investigation of micro-mechanical wood-adhesive interaction. In: Frihart, C. R., Hunt, C. G. and Yan, N., editors, *Proceedings of the International Conference on Wood Adhesives 2013*, Toronto, Ontario, CAN: Forest Products Society, 16 p.

Muszyński, L., Wang, F. and Shaler, S. (2002) Short-term creep tests on phenol-resorcinol-formaldehyde (PRF) resin undergoing moisture content changes. *Wood and Fiber Science* 34, 4, 612-624.

Nairn, J. A. (2000) Energy release rate analysis for adhesive and laminate double cantilever beam specimens emphasizing the effect of residual stresses. *International Journal of Adhesion and Adhesives* 20, 1, 59-70.

Nairn, J. A. (2006) Numerical simulations of transverse compression and densification in wood. *Wood and Fiber Science* 38, 4, 576-591.

Nairn, J. A., Kamke, F. A., Muszynski, L., Paris, J. and Schwarzkopf, M. 2014: Direct 3D Numerical Simulation of stresses and strains in wood adhesive bondlines based on the actual specimen anatomy from x-ray tomography data. In: Frihart, C. R., Hunt, C. G. and Yan, N., editors, *Proceedings of the International Conference on Wood Adhesives 2013*, Toronto, Ontario, CAN: Forest Products Society, 11 p.

Ohser, J. and Schladitz, K. 2008: Visualization, processing and analysis of tomographic data. In: Banhart, J., editor, *Advanced Tomographic Methods in Materials Research and Engineering*, Oxford, New York: Oxford University Press, 37-105.

Pan, B., Qian, K. M., Xie, H. M. and Asundi, A. (2009) Two-dimensional digital image correlation for in-plane displacement and strain measurement: a review. *Measurement Science & Technology* 20, 6.

Panshin, A. J. and De Zeeuw, C. Textbook of wood technology : structure, identification, properties, and uses of the commercial woods of the United States and Canada. McGraw-Hill, New York, 1980

Paris, J., Kamke, F., Mbachu, R. and Gibson, S. (2014) Phenol formaldehyde adhesives formulated for advanced X-ray imaging in wood-composite bondlines. *Journal of Materials Science* 49, 2, 580-591.

Paris, J. L. 2010: Carboxymethylcellulose acetate butyrate water-dispersions as renewable wood adhesives. *Department of Wood Science and Forest Products*, Virginia Tech, Blacksburg, VA: 169 p.

Park, B.-D., Riedl, B., Yoon Soo, K. and So, W. T. (2002) Effect of synthesis parameters on thermal behavior of phenol–formaldehyde resol resin. *Journal of Applied Polymer Science* 83, 7, 1415-1424.

Parkinson, D. Y., McDermott, G., Etkin, L. D., Le Gros, M. A. and Larabell, C. A. (2008) Quantitative 3-D imaging of eukaryotic cells using soft X-ray tomography. *Journal of Structural Biology* 162, 3, 380-386.

Peele, A. G. and Nugent, K. A. 2008: Phase-contrast and holographic tomography. In: Banhart, J., editor, *Advanced Tomographic Methods in Materials Research and Engineering*, Oxford, New York: Oxford University Press, 161-180.

Pizzi, A. 2003a: Phenolic resin adhesives. In: Pizzi, A. and Mittal, K. L., editors, *Handbook of Adhesive Technology*, New York: Marcel Dekker, Inc.

Pizzi, A. 2003b: Urea-formaldehyde adhesives. In: Pizzi, A. and Mittal, K. L., editors, *Handbook of Adhesive Technology*, New York: Marcel Dekker, Inc.

Porter, M. L. and Wildenschild, D. (2010) Image analysis algorithms for estimating porous media multiphase flow variables from computed microtomography data: a validation study. *Computational Geosciences* 14, 1, 15-30.

Ren, D. 2010: Moisture-cure polyurethane wood adhesives: wood/adhesive interactions and weather durability. *Macromolecular Science and Engineering*, Virginia Tech, Blacksburg, VA.

Ren, D. K. and Frazier, C. E. (2012) Wood/adhesive interactions and the phase morphology of moisture-cure polyurethane wood adhesives. *International Journal of Adhesion and Adhesives* 34, 55-61.

Richey, B. and Burch, M. 2002: Applications for decorative and protective coatings. In: Urban, D. and Takamura, K., editors, *Polymer Dispersions and Their Industrial Applications*, Weinheim: Wiley-VCH, 123-161.

River, B. 2003: Fracture of adhesive-bonded wood joints. In: Pizzi, A. and Mittal, K. L., editors, *Handbook of Adhesive Technology*, New York: Marcel Dekker, Inc.

River, B. H. 1994: Fracture of adhesive-bonded wood joints. In: Pizzi, A. and Mittal, K. L., editors, *Handbook of Adhesive Technology*, New York: Marcel Dekker, Inc., 151-177.

River, B. H. and Okkonen, E. A. (1993) Contoured wood double cantilever beam specimen for adhesive joint fracture tests. *Journal of Testing and Evaluation* 21, 1, 21-28.

River, B. H., Vick, C. B. and Gillespie, R. H. 1991: Wood as an adherend. In: Minford, J. D., editor, *Treatise on Adhesion and Adhesives*, New York: Marcel Dekker, Inc.

Rowell, R. M., Petterson, R., Han, J. S., Rowell, J. S. and Tshabalala, M. A. 2005: Cell wall chemistry. In: Rowell, R. M., editor, *Handbook of Wood Chemistry and Wood Composites*, New York: Taylor & Francis Group.

Salvini, A., Saija, L. M., Finocchiaro, S., Gianni, G., Giannelli, C. and Tondi, G. (2009) A New Methodology in the Study of PVAc-Based Adhesive Formulations. *Journal of Applied Polymer Science* 114, 6, 3841-3854.

Sanabria, S., Wyss, P., Neuenschwander, J., Niemz, P. and Sennhauser, U. (2011) Assessment of glued timber integrity by limited-angle microfocus X-ray computed tomography. *European Journal of Wood and Wood Products* 69, 4, 605-617.

Scholz, G., Van den Bulcke, J., Boone, M., Zauer, M., Baucker, E., Van Acker, J. and Militz, H. (2010a) Investigation on wax-impregnated wood. Part 1: Microscopic observations and 2D X-ray imaging of distinct wax types. *Holzforschung* 64, 5, 581-585.

Scholz, G., Zauer, M., Van den Bulcke, J., Van Loo, D., Pfriem, A., Van Acker, J. and Militz, H. (2010b) Investigation on wax-impregnated wood. Part 2: Study of void spaces filled with air by He pycnometry, Hg intrusion porosimetry, and 3D X-ray imaging. *Holzforschung* 64, 5, 587-593.

Schultz, J. and Nardin, M. 1994: Theories and mechanisms of wood adhesion. In: Pizzi, A. and Mittal, K. L., editors, *Handbook of Adhesive Technology*, New York: Marcel Dekker, Inc., 19-33.

Sebera, V. and Muszyński, L. (2011) Determination of local material properties of OSB sample by coupling advanced imaging techniques and morphology-based FEM simulation. *Holzforschung* 65, 6, 811-818.

Sellers, T. 1994: Adhesives in the wood industry. In: Pizzi, A. and Mittal, K. L., editors, *Handbook of Adhesive Technology*, New York: Marcel Dekker, Inc., 599-614.

Sellers, T. (2001) Wood adhesive innovations and application in North America. (cover story). *Forest Products Journal* 51, 6, 12.

Sernek, M., Resnik, J. and Kamke, F. A. (1999) Penetration of liquid urea-formaldehyde adhesive into beech wood. *Wood and Fiber Science* 31, 1, 41-48.

Serrano, E. (2001) Glued-in rods for timber structures -- a 3D model and finite element parameter studies. *International Journal of Adhesion and Adhesives* 21, 2, 115-127.

Serrano, E. (2004) A numerical study of the shear-strength-predicting capabilities of test specimens for wood-adhesive bonds. *International Journal of Adhesion and Adhesives* 24, 1, 23-35.

Serrano, E. and Enquist, B. (2005) Contact-free measurement and non-linear finite element analyses of strain distribution along wood adhesive bonds. *Holzforschung* 59, 6, 641-646.

Sharma, N. and Aggarwal, L. M. (2010) Automated medical image segmentation techniques. *Journal of medical physics/Association of Medical Physicists of India* 35, 1, 3.

Shi, S. and Gardner, D. (2001) Dynamic adhesive wettability of wood. *Wood and Fiber Science* 33, 1, 58-68.

Shupe, T. E., Hse, C. Y., Choong, E. T. and Groom, L. H. (1998) Effect of wood grain and veneer side on loblolly pine veneer wettability. *Forest Products Journal* 48, 6, 95-97.

Singh, H. K., Chakraborty, A., Frazier, C. E. and Dillard, D. A. (2010) Mixed mode fracture testing of adhesively bonded wood specimens using a dual actuator load frame. *Holzforschung* 64, 3, 353-361.

Smith, L. and Côté, W. (1971) Studies of penetration of phenol-formaldehyde resin into wood cell walls with the SEM and Energy-Dispersive X-ray Analyzer. *Wood and Fiber Science* 3, 1, 56-57.

Smith, L. A. 1971: Resin penetration of wood cell walls - Implications for adhesion of polymers to wood. *College of Forestry*, Syracuse University, SUNY, Syracuse, NY.

Standfest, G., Kranzer, S., Petutschnigg, A. and Dunky, M. (2010) Determination of the microstructure of an adhesive-bonded medium density fiberboard (MDF) using 3-D sub-micrometer computer tomography. *Journal of Adhesion Science and Technology* 24, 8-10, 1501-1514.

Standfest, G., Kutnar, A., Plank, B., Petutschnigg, A., Kamke, F. and Dunky, M. (2012) Microstructure of viscoelastic thermal compressed (VTC) wood using computed microtomography. *Wood Science and Technology*.

Steppe, K., Cnudde, V., Girard, C., Lemeur, R., Cnudde, J. P. and Jacobs, P. (2004) Use of X-ray computed microtomography for non-invasive determination of wood anatomical characteristics. *Journal of Structural Biology* 148, 1, 11-21.

Stock, S. R. *Microcomputed tomography : methodology and applications*. CRC Press, Boca Raton, 2009

Stockel, F., Konnerth, J., Moser, J., Kantner, W. and Gindl-Altmutter, W. (2012) Micromechanical properties of the interphase in pMDI and UF bond lines. *Wood Science and Technology* 46, 4, 611-620.

Terashima, N., Kitano, K., Kojima, M., Yoshida, M., Yamamoto, H. and Westermark, U. (2009) Nanostructural assembly of cellulose, hemicellulose, and lignin in the middle layer of secondary wall of ginkgo tracheid. *Journal of Wood Science* 55, 6, 409-416.

Todorovic, S. and Ahuja, N. 2009: Texel-based texture segmentation. In: *Computer Vision, 2009 IEEE 12th International Conference on: IEEE*, 841-848.

Trtik, P., Dual, J., Keunecke, D., Mannes, D., Niemz, P., Stähli, P., Kaestner, A., Groso, A. and Stampanoni, M. (2007) 3D imaging of microstructure of spruce wood. *Journal of Structural Biology* 159, 1, 46-55.

Turner, J. E. (2004) Interaction of ionizing radiation with matter. *Health Phys.* 86, 3, 228-252.

Unnikrishnan, K. P. and Thachil, E. T. (2006) Toughening of epoxy resins. *Designed Monomers and Polymers* 9, 2, 129-152.

Van den Bulcke, J., Boone, M., Van Acker, J. and Van Hoorebeke, L. (2010) High-resolution X-ray imaging and analysis of coatings on and in wood. *J. Coat. Technol. Res.* 7, 2, 271-277.

Van den Bulcke, J., Masschaele, B., Dierick, M., Acker, J. V., Stevens, M. and Hoorebeke, L. V. (2008) Three-dimensional imaging and analysis of infested coated wood with X-ray submicron CT. *International Biodeterioration & Biodegradation* 61, 3, 278-286.

Van den Bulcke, J., Van Acker, J. and Stevens, M. (2005) Image processing as a tool for assessment and analysis of blue stain discolouration of coated wood. *International Biodeterioration & Biodegradation* 56, 3, 178-187.

Vick, C. B. 2002: Adhesive bonding of wood materials. In: (U.S.), F. P. L., editor, *Wood Handbook, Wood as an Engineering Material*, Ontario: Algrove Publishing Limited, 465.

Walther, T. and Thoemen, H. (2009) Synchrotron X-ray microtomography and 3D image analysis of medium density fiberboard (MDF). *Holzforschung* 63, 5, 581-587.

Wang, Y. 2007: Morphological characterization of wood plastic composite (WPC) with advanced imaging tools : developing methodologies for reliable phase and internal damage characterization. *Wood Science and Engineering*, Oregon State University, Corvallis, OR: 179.

Wang, Y., Muszyński, L. and Simonsen, J. (2007) Gold as an X-ray CT scanning contrast agent: Effect on the mechanical properties of wood plastic composites. *Holzforschung* 61, 6, 723-730.

Weitkamp, T., Haas, D., Wegrzynek, D. and Rack, A. (2011) ANKAphase: software for single-distance phase retrieval from inline X-ray phase-contrast radiographs. *Journal of Synchrotron Radiation* 18, 617-629.

White, M. S. 1975: Influence of resin penetration on the fracture toughness of wood-adhesive bonds. *Forestry*, Virginia Polytechnic Institute and State University, Blacksburg, VA.

White, M. S. (1977) Influence of resin penetration on the fracture toughness of wood adhesive bonds. *Wood Science* 10, 1, 6-14.

White, M. S., Ifju, G. and Johnson, J. A. (1977) Method for measuring resin penetration into wood. *Forest Products Journal* 27, 7, 3.

Wiese, H. 2002: Characterization of aqueous polymer dispersions. In: Urban, D. and Takamura, K., editors, *Polymer Dispersions and Their Industrial Applications*, Weinheim: Wiley-VCH, 41-73.

Wildenschild, D., Hopmans, J. W., Vaz, C. M. P., Rivers, M. L., Rikard, D. and Christensen, B. S. B. (2002) Using X-ray computed tomography in hydrology: systems, resolutions, and limitations. *Journal of Hydrology* 267, 3-4, 285-297.

Wilkes, T. E., Stock, S. R., De Carlo, F., Xiao, X. and Faber, K. T. (2009) X-ray micro-computed tomography of beech wood and biomorphic C, SiC and Al/SiC composites. *Philos. Mag.* 89, 17, 1373-1389.

Windt, C. W., Gerkema, E. and Van As, H. (2009) Most water in the tomato truss is imported through the xylem, not the phloem: a nuclear magnetic resonance flow imaging study. *Plant physiology* 151, 2, 830-842.

Wu, X., Liu, H. and Yan, A. (2008) Phase-contrast X-ray tomography: Contrast mechanism and roles of phase retrieval. *European Journal of Radiology* 68, 3, Supplement 1, S8-S12.

Xing, C., Riedl, B., Cloutier, A. and Shaler, S. M. (2005) Characterization of urea-formaldehyde resin penetration into medium density fiberboard fibers. *Wood Science and Technology* 39, 5, 374-384.

Yelle, D. J., Jakes, J. E., Ralph, J. and Frihart, C. R. 2009: Characterizing polymeric methylene diphenyl diisocyanate reactions with wood: 1. High-resolution solution-state NMR spectroscopy. In: Frihart, C. R., Hunt, C. G. and Moon, R. J., editors, *Proceedings of the International Conference on Wood Adhesives 2009*, Lake Tahoe, NV, USA: Forest Products Society, 5 p.

Zheng, J., Fox, S. C. and Frazier, C. E. (2004) Rheological, wood penetration, and fracture performance studies of PF/pMDI hybrid resins. *Forest Products Journal* 54, 10, 74-81.

Zink, A. G., Davidson, R. W. and Hanna, R. B. (1995) Strain-measurement in wood using a digital image correlation technique. *Wood and Fiber Science* 27, 4, 346-359.

Zink, A. G., Davidson, R. W. and Hanna, R. B. (1996) Strain distributions in adhesive wood joints. *Journal of Adhesion* 56, 1-4, 27-43.

Zink, A. G., Davidson, R. W. and Hanna, R. B. (1997) Effect of composite structure on strain and failure of laminar and wafer composites. *Mechanics of Composite Materials and Structures* 4, 4, 345-359.

CHAPTER 3. PHENOL FORMALDEHYDE ADHESIVES
FORMULATED FOR ADVANCED X-RAY IMAGING IN
WOOD-COMPOSITE BONDLINES

Jesse L. Paris, Frederick A. Kamke, Reginald Mbachu, and Sara K. Gibson

Journal of Material Science

2014, Volume 49, Issue 2

Springer, US

Phenol Formaldehyde Adhesives Formulated for Advanced X-ray Imaging
in Wood-Composite Bondlines

Jesse L. Paris^{a,*}, Frederick A. Kamke^{a,†}, Reginald Mbachu^b, and Sara K. Gibson^b

^a Department of Wood Science & Engineering, Wood-Based Composites Center, Oregon State University, 119 Richardson Hall, Corvallis, OR 97331, USA

^b Arclin Chemical, 475 28th St., Springfield, OR 97477, USA

* Corresponding Author. Tel.: +804 338 4353; Fax +542 737 3385

E-mail address: Jesse.Paris@OregonState.edu (J. L. Paris)

† Secondary Corresponding Author. Tel.: +541 737 8422; Fax +542 737 3385

E-mail address: Fred.Kamke@OregonState.edu (F. A. Kamke)

3.1 Abstract

A phenol formaldehyde (PF) adhesive was uniformly tagged with iodine such that it yielded sufficient x-ray computed tomography (XCT) gray-scale contrast for material segmentation in reconstructed wood-composite bondlines. Typically, untagged adhesives are organic and have a similar solid state density as wood cell walls, and therefore cannot be segmented quantitatively in XCT data. The iodinated PF development involved analysis and comparison of three trial adhesives containing rubidium, bromine or iodine. Adhesive tag efficacy was measured in terms of x-ray absorption contrast enhancement and tag uniformity along the adhesive polymers. Cured adhesive density, tag-element and concentration were each found to significantly impact XCT contrast results, which in turn agreed with theoretical x-ray attenuation predictions for each resin. Ion chromatography confirmed the absence of free iodide in the liquid PF prior to bonding, and fluorescence microscopy and energy dispersive spectroscopy (EDS) showed that iodine tags remained associated with the cured adhesive polymers. XCT and EDS results also demonstrated that when contrast agents are simply mixed into resins, rather than attached to the polymer chains, they are free to migrate independent of the penetrating adhesives during bonding. This then can cause complications with quantitative segmentation and analyses. The iodinated PF yielded consistent and uniform XCT gray-scale contrast; its formulation could be adjusted for other viscosity or molecular weight distribution, which would affect its penetration behavior.

3.2 Introduction

Reducing solid wood into smaller components and reforming them into engineered composite materials via adhesive bonding, extends the resource and randomizes natural variation affording composites more uniform material properties (Pocius 1997). Adhesive penetration, and subsequent solidification in the porous wood structures, increase the surface area over which the intermolecular chemical interactions governing wood adhesion effectively operate, and mechanically interlock the adherends (Schultz and Nardin 1994). Additionally, penetration transfers joint-stresses, past inherent surface irregularities and machining defects, into undamaged wood cells, which is believed to enhance bond strength, toughness, and durability (Ebewele et al. 1982; Frazier and Ni 1998; Pocius 1997; White 1977). However, debate remains as to the quantitative role of adhesive penetration, and what is considered an optimum or sufficient level, in composite joint assemblies. These issues are difficult to ascertain, in part, because adhesive penetration is commonly assessed with various two dimensional (2D) microscopy techniques which are both destructive to the composite specimen and neglect the true three dimensional (3D) bond (Kamke and Lee 2007).

X-ray computed tomography (XCT) is non-destructive, and provides 3D images for the internal structures of materials. XCT is an extremely valuable analytical tool in medical, mechanical engineering and materials-science research disciplines, and within the past decade has grown in application to wood and wood-composites (Banhart 2008a, b; De Vetter et al. 2006; Evans et al. 2010; Haibel 2008; Hass et al. 2012; Hass et al. 2010; Mannes et al. 2010; Mannes et al. 2009; Modzel et al. 2011). While XCT has yielded

detailed, micro-scale 3D wood anatomy data (Bucur 2003; Forsberg et al. 2010; Hass et al. 2010; Mannes et al. 2009; Mayo et al. 2010; Trtik et al. 2007), tracking adhesive infiltration has proven difficult with typical adsorption contrast tomography.

Absorption contrast is achieved when neighboring materials have different linear attenuation coefficients, μ . This value relates to the mean free path of a penetrating x-ray photon in a material before being absorbed or scattered. With highly coherent, mono-energetic x-ray photons, as is the case with synchrotron radiation sources, μ is easily calculated according to Beer-Lambert's law as the ratio of the transmitted, I , to initial, I_0 , radiation intensity through the material's thickness, d (Ketcham and Carlson 2001; Wildenschild et al. 2002).

$$I / I_0 = \exp^{(-\mu d)}$$

The value of the linear attenuation coefficient is a function of both the material's elemental composition and density; dense materials and those with high atomic number (Z), contain more electrons per unit volume, and thus have higher μ values (Banhart 2008b). Wood and phenol formaldehyde (PF) adhesives are both organic, being primarily comprised of carbon, hydrogen and oxygen; moreover, once cured, the PF density is similar to that of the wood cell wall at approximately 1.5 g/cm³. Therefore, wood-composite XCT reconstructions often show minimal gray-scale intensity differences between the wood and adhesive phases at micron-scale resolutions, which makes quantitative material segmentation nearly impossible (Hass et al. 2012; Modzel et al. 2011). Several researchers have attempted to overcome these problems by tagging the adhesive, or matrix phase in the case of wood-plastic composites, with various heavy

metal contrast agents (De Vetter et al. 2006; Evans et al. 2010; Mannes et al. 2010; Modzel et al. 2011; Walther and Thoemen 2009; Wang et al. 2007); however two significant complications have been identified from these tagging methods. First, phase separation and tag mobility is suspect. If tag compounds are not directly attached to the adhesive pre-polymers, they may be free to migrate (Hass et al. 2012; Modzel et al. 2011). Such tag mobility can result in agglomeration, and thus differences in localized attenuation values within the resin phase (Mannes et al. 2010; Walther and Thoemen 2009; Wang et al. 2007). Second, if tags do remain associated with the adhesive phase, it is often unclear how uniform they are distributed along the polymer chains. PF adhesives are typically poly-disperse systems with complex reaction schemes during formulation; one would not expect long and short polymer chains to be tagged to the same degree. This, too, might cause variations in adhesive attenuation coefficients, as resin mobility and penetration depth are, in part, a function of molecular weight. Both complications reduce confidence and accuracy when segmenting wood-composite micro XCT data into the three distinct material phases: air in the lumens, wood cell wall and cured adhesive. This paper demonstrates a method for homogeneously tagging a resin, PF adhesive with iodine (I) to yield sufficient XCT contrast for quantitative material segmentation, with minimal phase overlap. Segmented, bondlines can yield novel and valuable 3D information about adhesive penetration within porous wood structures without damaging specimen joints. Method refinement and development involved the formulation and analysis of two preliminary PF resins, partially tagged with bromine (Br) and I.

3.3 Experimental

3.3.1 Adhesive formulation

Brominated (BrPF), iodinated (IPF1 and IPF2) and control PF resins (1000-2000 g) were prepared with assistance from Arclin, Springfield, Oregon to mimic conventional plywood resins. Meta-bromophenol and meta-iodophenol (98% purity) were included in the BrPF and IPF1 resins at phenol to X-phenol molar ratios of 14.3 and 5.0, respectively; meta-iodophenol accounted for the entire phenol component in IPF2. Formulations were prepared with formaldehyde to phenol-component molar ratios between 1.8 and 2.5 in the presence of a sodium hydroxide (NaOH) catalyst. Reaction temperatures were controlled between 40 °C and 90 °C over an 8 hour period; formulations were considered complete when resin viscosities were between 500 and 600 mPa·s at 25°C. Final adhesives (43% solids, pH ~11.5-12.5) were kept frozen (-10°C) between analyses and bonding.

3.3.2 Gel permeation and ion chromatography

Gel Permeation and Ion Chromatography (GPC and IC, respectively) analyses were conducted by Arclin according to their proprietary analytical procedures. GPC with a Viscotek Triple Detection SEC System and a bank of PLgel columns provided adhesive absolute molecular weight and polydispersity. Analysis for bromide and iodide anions was accomplished with a HP1090 instrument equipped with a Shodex CD-4 detector and Hamilton PRP-100X column.

3.3.3 Powder density, neutron activation analysis, and x-ray radiography

Cured resin samples (1 - 3 g, 125°C, 3 h) were weighed for percent solids (ASTM-D-4426 2006), and ground to a powder in a Wiley Mill (30 mesh, ≤ 0.595 mm). Powder densities were determined according to a modified version of ASTM D 5965, method A (ASTM-D-5965 2007), where the immersion liquid was deionized water.

Br and I concentrations were verified from cured adhesive powder with Neutron Activation Analysis (NAA). BrPF and IPF1 samples (300 - 400 mg) were analyzed with epithermal neutrons at the McMaster Nuclear Reactor in Hamilton, Ontario, Canada, and induced radioactivity (^{80}Br - 617 KeV or ^{128}I - 443 KeV) was collected with a hyper-pure gamma-ray spectrometer. IPF2 samples (100 mg, $n = 3$) were analyzed with thermal neutrons using the TRIGA Mk. II Research Reactor at Oregon State University (OSU), Corvallis, Oregon; subsequent gamma radiation (^{128}I - 526.6 KeV) was collected with a HPGe detector. Calibration, at both facilities was achieved using appropriate sub-standards (Minc 2008).

Adhesive x-ray adsorption contrast was observed as a function of iodine concentration with ground resin mixtures of IPF1 and a PF control. Polyethylene vials (20 mm tall x 9.5 mm diameter) were partially filled with the homogenized powder mixtures, which were tamped down to minimize void-space. Transmission, 2D radiographs of each vial were collected with polychromatic x-rays (25 kVp, 312 μA) on a cone-beam scanner in the School of Mechanical, Industrial and Manufacturing Engineering at OSU. The system consisted of a Feinfocus 160 kVp source and tungsten target, with a 9-inch image intensifier detector (Medelelex HXS-93/PS). Digital gray-scale images were recorded with

a 16-bit CCD camera (Point Grey, GRAS-5055M). A flat-field correction was applied to each radiograph using bright-field and dark-field projections (Haibel 2008). Image processing and analyses were performed with the software package Fiji, which is based on ImageJ (Rasband 1997 - 2012; Schindelin et al. 2012). ‘Flattened’ projections were cropped to a 2 mm wide vertical column in the center of each vial. Mean gray-scale (transmitted intensity) values were compared for the largest possible areas of both pure air and pure resin powder within each column.

3.3.4 Composite specimen preparation

Single-bondline composite laminates were prepared from Douglas-fir (*Pseudotsuga menziesii*, DF), loblolly pine (*Pinus taeda*, SYP) or hybrid poplar (*Populus deltoides* x *Populus trichocarpa*, HP). Individual laminae were conditioned to approximately 12% moisture content, and freshly-planed immediately prior to bonding. Adhesives were applied to laminae tangential-longitudinal planes with a steel roller at 120 g/m² based on resin solids, and bonded in a hot press (185 °C, 8 min, 689.5 kPa). Specimens (2 mm x 2 mm cross-section x 10 mm long) were carefully excised from each laminate using a bandsaw and razor-blade, such that they contained a central, longitudinal bondline.

3.3.5 Fluorescence and scanning electron microscopy (FM and SEM, respectively) and energy dispersive spectroscopy (EDS)

Composite specimens were embedded with Spurr Low-Viscosity ERL 4221 epoxy under a low vacuum (Ellis 2006; Spurr 1969) for easier surface preparation and to minimize charge build-up in empty cell lumens during SEM analysis. Ultra-smooth, cross-section surfaces were prepared with a Leica EM UC7 ultra microtome, and observed with a

Nikon E400 epi-fluorescent microscope, equipped with a high pressure mercury lamp (100W) and UV (300-380 nm excitation “EX”, 400 nm dichromatic mirror “DM”, and 420 nm emission “EM”) or blue-light (420-490 nm EX, 500 nm DM and 515 nm EM) filter sets (Davidson and Abramowitz 2002; Kamke and Lee 2007). Digital FM images were collected with a QImaging MicroPublisher 5.0 RTV CCD camera and QCapture Pro 5.1 image software. The same specimen surfaces were subsequently imaged on a FEI Quanta 3D SEM equipped with EDS after being sputter coated with a thin, conductive layer of a gold/palladium alloy. Elemental maps of carbon, oxygen, nitrogen, sodium, bromine, rubidium, iodine, chlorine, gold and palladium were collected over the same field of view as the FM images with the following parameters: image resolution 512x442 pixels, 16-32 nA beam current, 10-15 kV beam energy, 10.5 mm working distance, 64 frames per map, 200 μ s dwell time, 20-30% dead time, which resulted in approximately 10K - 20K counts/s. Semi-quantitative EDS spectra (100 s) were also collected with the same instrumental parameters from two surface points on each specimen: an adhesive-filled lumen and a cell wall not in contact with PF resin.

Composite (overlaid) elemental maps of oxygen, and the tag element of interest (Br, I, Na or Rb), were prepared with the following processes in Fiji: 1) single element maps were converted from 8-bit color to grayscale images; 2) high intensity outlier pixels were removed with a 1 pixel radius; 3) mean ‘background’ pixel values were subtracted from all image points to remove low-intensity (noise); 4) resulting images were linearly normalized, with 0.4% saturation tolerance, to stretch the pixel intensities over the full 0 - 255 gray-scale range; 5) elemental maps were merged to form RGB composites, with the red and green color channels assigned to the oxygen and tag-signals, respectively.

3.3.6 Synchrotron, micro x-ray computed tomography (XCT)

XCT analyses were performed at two synchrotron, bend-magnet facilities. BrPF and IPF2 composites were scanned on beamline 2-BM-B at the Advanced Photon Source (APS) at the Argonne National Laboratory, Argonne, Illinois. IPF1 specimens were imaged on beamline 8.3.2 at the Advanced Light Source (ALS) at Lawrence Berkeley National Laboratory, Berkeley, California. Experimental parameters are provided in Table 3-1. Both facilities used parallel Si(111) monochromators to image at the specified energies, and LuAG scintillator materials to convert detection signals into visible light. Radiograph projections were then recorded with a 12-bit Roper Scientific CoolSnap K4 HQ CCD camera with 5X objective at the APS, and a 14-bit Cook PCO4000 CCD camera with 10X objective at the ALS. Tomograms from both sources were reconstructed with fast filtered back projection algorithms (Dowd et al. 1999; Haibel 2008), and stored as stacks of floating-point gray-scale slices.

Table 3-1 XCT acquisition parameters for tagged-PF wood composites

Resin	Beam-line	Beam energy [KeV]	Rotation angle [°]	Projections	Exposure time [ms]	Sample to detector distance [mm]	Voxel side length [µm]	Image Stack Slices
Control & BrPF	APS 2-BM-B	14.05	0.12	1504	250	15	1.45	2047
IPF1	ALS 8.3.2	35	0.125	1441	3500	30	0.9	2569
IPF2	APS 2-BM-B	15.3	0.12	1504	250	8	1.45	2047

3.4 Results and Discussion

The three systems discussed in this work, BrPF, IPF1 and IPF2, illustrate the experimental progression undertaken to develop a PF adhesive capable of yielding high gray-scale contrast in micro XCT images of bonded wood-composites. For comparative purposes, information is also provided for a PF adhesive containing rubidium (Rb), which was studied by Modzel and colleagues in 2009, hereafter referred to as RbPF. The RbPF adhesive did provide significantly enhanced micro XCT contrast to wood cell walls (Modzel 2009; Modzel et al. 2011); however, the Rb was added as a RbOH catalyst in the PF formulation, in substitute of the more conventional catalyst, NaOH. Having not been directly bound to the PF polymer chains, Rb ions migrated independent of the adhesive penetration during bonding. This migration was proposed to have caused variations in localized Rb concentrations across composite joints, which helped explain contrast differences observed between specimens prepared and scanned under similar conditions (Modzel 2009).

In the present work, it was paramount to develop a system in which the tag-element was attached to the resin polymers. Yet, it is important to clarify that the adhesives presented here were not intended to represent the bonding behavior and properties of any particular commercially-relevant system. It was recognized that inclusion of contrast-agents, of any type or concentration, would undoubtedly influence adhesive properties, which already vary widely across different PF formulations (Pizzi 2003; Sellers 1994). The primary goal was to prepare a PF system which penetrated the wood upon bonding, transferred bondline stresses once cured, and could be successfully segmented in reconstructed XCT

datasets; nevertheless, the presented systems were prepared based on conventional plywood resin formulations in terms of desired percent solids and viscosity. While BrPF, IPF1 and IPF2 results are all provided together, note that the development of these systems included three separate experiments at synchrotron XCT sites (Table 3-1), with increasing success in tag efficacy and afforded image contrast. Figure 3-1 provides example XCT cross-section images of composite specimens bonded with each experimental adhesive; in each case, two sub-areas from the same reconstructed slice are provided with their corresponding gray-scale histograms. The first area shows only wood cells and empty lumens, while the second shows the bondline region with adhesive filled or coated lumens. Comparison of the histogram shapes within, and between, each specimen helps illustrate both the adhesive development and some of the image noise and artifacts encountered, and overcome, throughout this study.

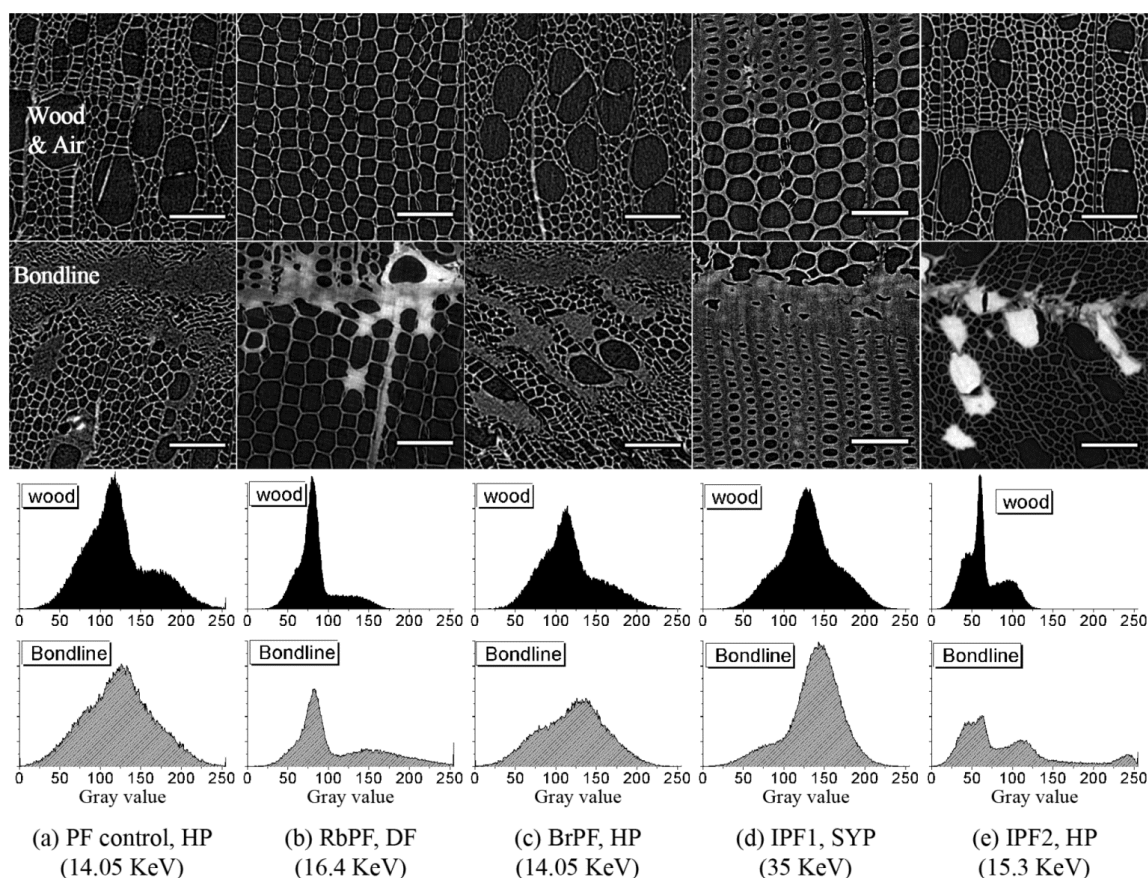


Figure 3-1 Cross-section XCT slices of each specimen type with indicated scan energy. Sub-areas of wood and air only (top row), and region containing a horizontal bondline (bottom row) were selected from the same reconstructed image (scale bars = 100 μm). Parent images were first normalized to utilize the full 256 bit gray-scale range. Gray-scale histograms correspond to the respective sub-areas, and each histogram pair has the same area under the curve (vertical axis = pixel count)

Initially, Br was chosen as the tag element because it has similar atomic mass to Rb ($Z_{\text{Br}} = 35$, $Z_{\text{Rb}} = 37$), and meta-bromophenol has previously shown to support PF polymerization (Smith and Côté 1971; White et al. 1977). During the synthesis of PF resins, methylation of phenol typically occurs at the ortho and para positions of the ring. The attachment of bromine at the meta position of the ring was not expected to prevent polymerization. The polymerization reaction progressed as expected; however,

BrPF failed to yield any noticeable x-ray absorption contrast in the bonded specimens (Figure 3-1c, bottom). APS beamline scientists suggested iodine might be a more effective contrast agent, as it is significantly heavier than bromine ($Z_I = 53$). Thus, IPF1 was prepared using meta-iodophenol and at a higher molar ratio to un-substituted phenol, effectively increasing the tag mass and concentration from the BrPF resin. Yet, IPF1 XCT data suffered from increased image noise, and yielded limited, and inconsistent, contrast between the wood and adhesive phases. Moreover, in a few instances, adhesive occupying lumens far from the bondline appeared brighter than adhesive directly at the joint interface (Figure 3-1d, bondline). It was suspected that during formulation the phenol and I-tagged phenol reactants likely polymerized at different rates, were incorporated into different chain lengths, and perhaps yielded different degrees of branching and cross-linking. Certainly, one would expect the mobility and reactivity of a halogen-substituted phenol to be different relative to an un-substituted phenol. Consequently Br and I distributions on the PF adhesive chains were likely heterogeneous, which resulted in different localized tag concentrations in bonded joints. The third adhesive, IPF2, was formulated entirely with meta-iodophenol to ensure uniform iodine distribution across all PF polymers, independent of molecular weight or morphology. This also significantly raised the overall wt% I in the cured resin. IPF2 did provide sufficient XCT image contrast for 3D material segmentation, as depicted in Figure 3-2. This paper details the properties of each resin, and why IPF2 was successful compared to the first two trials.

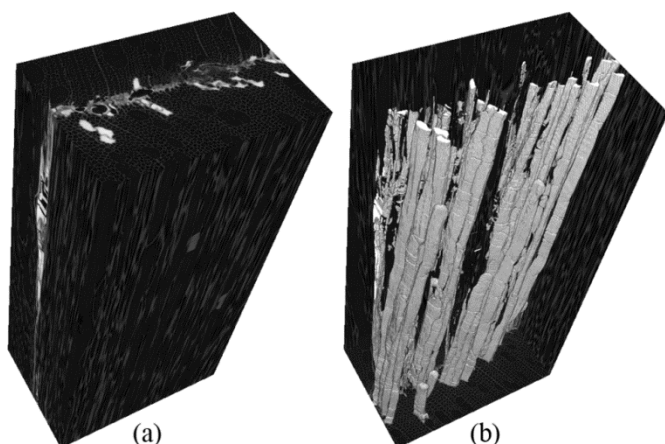


Figure 3-2 XCT sub-volume (1.71 mm^3) virtually excised from the same HP, IPF2 specimen in Figure 3-1e. (a) Solid 3D volume; (b) segmented, adhesive phase not including the wood material occupying the same internal space

3.4.1 Adhesive properties

Table 3-2 provides the collective physical properties and tag concentrations for each experimental PF adhesive. Viscosity and molecular weight were measured just after formulation, while density and percent solids were measured from cured samples of each adhesive, with the exception of RbPF; its percent solids, molecular weight and viscosity were reported elsewhere (Modzel 2009). The RbPF density of 1.3 g/cm^3 was assigned as a conservative estimate, which neglected any added Rb mass, but was in the typical range of cured PF adhesives (Sellers 1994; Umemura et al. 1998). Tag concentrations were first predicted for each adhesive using the percent solids value and known formulation reactant quantities (Modzel 2009), and then measured directly with NAA. Each system resulted in similar solids content and viscosity, as intended. Molecular weight increased with tag mass and quantity; however, each system had a similar polydispersity index (PDI), or ratio between weight average and number average molecular weights. IPF1 was

the only exception, with slightly lower viscosity and PDI; its viscosity was expected to advance slightly between formulation and bonding. Curiously, BrPF had a noticeably reduced powder density than the control PF. Perhaps the meta-Br presence resulted in the formation of more linear polymer chains with lower potential cross-linking than the un-substituted PF morphologies; in turn, this may have reduced the polymer packing efficiency upon resin cure. The higher GPC Mark-Houwink coefficients of the BrPF and IPF resins relative to the control lend credence to this view. The added void-volume may have offset the added mass from the heavier Br atoms, which were, after all, only present at 3.3 wt% in that system. Similar, polymer morphologies likely formed in the IPF1 and IPF2 resins, though the higher tag concentrations and masses were able to overcome any excess void-volume effects, and thus increase the overall cured density in these systems. In each resin, the calculated and measured concentrations agreed very closely, indicating that little to no tag material was liberated during formulation or cure.

Table 3-2 Adhesive material properties. Molecular weight data includes number average (Mn), weight average (Mw) and PDI (Mw:Mn). Standard deviation in parentheses (n=3). BrPF and IPF NAA results are from a single replicate. RbPF results were adopted from another report (Modzel 2009); RbPF density was estimated

Adhesive	Solids	Powder density	Viscosity	Molecular weight			Cured resin tag concentration	
	[%]	[g/cm ³]	[mPa·s]	Mn	Mw	PDI	Calculated [wt%]	Measured [wt%]
Control PF	43.2	1.43 (0.06)	600	3110	5920	1.90	-	-
BrPF	43.8	1.28 (0.06)	700	9180	16570	1.81	3.3	3.2
IPF1	44.0	1.57 (0.03)	515	14420	16360	1.13	12.1	12.2
IPF2	44.1	2.24 (0.06)	600	11800	22380	1.90	41.1	39.5 (0.2)
RbPF	47.0	1.3	750	1987	-	-	25.7	-

3.4.2 Adhesive x-ray attenuation

X-ray absorption contrast depends on the relative difference in linear attenuation coefficient, μ , between neighboring materials; in turn, μ depends on material density and molecular formula (Ketcham and Carlson 2001). To better understand why the RbPF system yielded good contrast, and to explain the results of the presented experimental resins, theoretical attenuation length was determined for each adhesive (Henke et al. 1993). Attenuation length describes the depth an incident photon will penetrate into a material before its probability of being absorbed or scattered becomes $1/e$; μ is the inverse of attenuation length with units of reciprocal distance (Ketcham and Carlson 2001). Theoretical attenuation lengths were calculated for the various materials in the XCT wood-composite specimens; observed differences in the theoretical μ values were expected correlate with and elucidate observed gray-scale contrasts. Cellobiose was chosen to represent wood cell wall polymers, and was assigned a density equal to that of the cell wall substance, approximately 1.54 g/cm^3 . Figure 3-3a shows a representative cellobiose repeat unit. Cured adhesive formulae were calculated using the known formulation reactants and quantities, the measured solids content, and a theoretical PF dimer repeat-unit. Figure 3-3b shows two phenol units which were first fully methylolated at the para and ortho positions, then polymerized linearly via a dimethylene ether linkage, common for resol-type PF adhesives at synthesis temperatures below 150°C (Frihart 2005; Park et al. 2002; Pizzi 2003). While it is likely that different morphologies also formed during polymerization and cure, this structure was assumed a good approximation for the attenuation calculation. IPF2 provided an opportunity to check this assumption, as each phenol unit should have exactly one iodine substituent.

Accordingly, the IPF2 molecular formula based on the provided structure should have an iodine stoichiometric coefficient of two. The calculated iodine coefficient was 1.85, which was determined sufficiently close to mass balance considering the calculation contained additional variability in the solids and reagent quantities.

Figure 3-3c is a plot of log attenuation coefficient as a function of beam energy; the figure key provides the density and molecular formula used for each material in the calculation (Henke et al. 1993). Cellobiose attenuation closely matched theoretical wood results presented elsewhere (Mannes et al. 2010). It is clear that with similar molecular formulae and density there is no discernible difference in attenuation between the control PF and cellobiose within the provided photon energy range. As a result, XCT reconstructions of wood-composites bonded with control PF adhesives failed to provide enough image contrast for material segmentation (Figure 3-1a, bondline). Just above the Rb k-shell electron binding energy (k-edge = 15.3 KeV), the calculated RbPF attenuation coefficient is 24 times greater than for cellobiose. RbPF yielded sufficient image contrast (Figure 3-1b, bondline) in this energy range, yet quantitative segmentation suffered from tag mobility complications (Modzel 2009). BrPF, scanned just above the Br k-edge (13.7 KeV), yielded a theoretical attenuation coefficient only three and a half times more than cellobiose; this clearly was not enough for sufficient contrast (Figure 3-1c, bottom). The predicted IPF1 attenuation is about seven times greater than for cellobiose within the range studied; however, IPF1 specimens were scanned above the I k-edge (33.2 KeV), which was beyond the attenuation calculation range (Henke et al. 1993). Nevertheless, a sharp increase in attenuation was expected above the k-edge, similar to the Br and Rb

species. However, the increased energy also significantly reduced the cellobiose attenuation, which increased image noise.

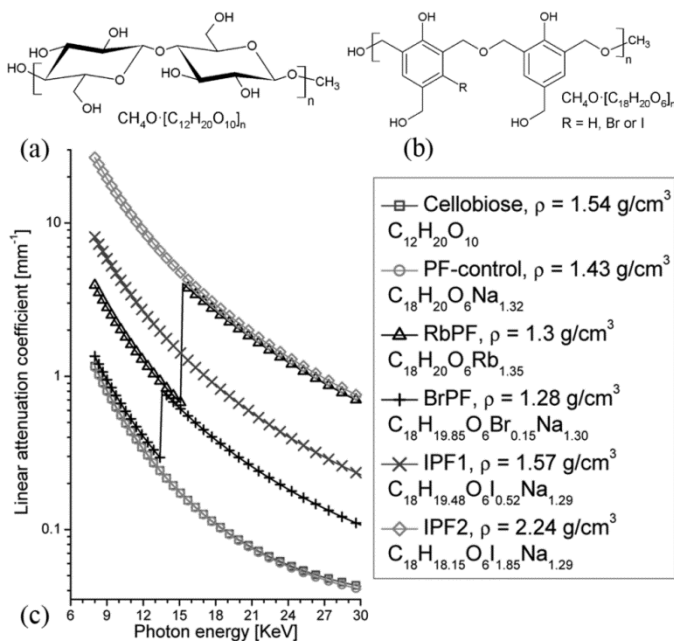


Figure 3-3 Repeat units and molecular formulae for (a) cellobiose and (b) cured resol-PF adhesive polymers used to calculate theoretical attenuation coefficients for each material as a function of beam energy (c); plot key indicates specific molecular formulae and density values used for each attenuation prediction

Scintillator detectors assign photon intensities to specific gray levels ranging from pure black to pure white, with a floating point value. Quantitative phase segmentation with simple gray-scale threshold operations requires clearly defined valleys between material peaks; furthermore, segmentation confidence increases with decreasing peak overlap. The bondline histograms in Figure 3-1 illustrate this concept. Composite specimen b exhibits two clear peaks, which can be segmented with a threshold centered in the valley separating them; for specimen e, three material phases could be quantitatively segmented as there are two clear valleys (Figure 3-1). Image processing procedures, such as edge-

preserving median filters, can further decrease phase overlap and improve segmentation confidence (Hass et al. 2010; Mayo et al. 2010; Standfest et al. 2012; Trtik et al. 2007); however, some initial contrast is still necessary. Wood-based composites contain three separate material phases, air, wood and adhesive; an optimal histogram for quantitative segmentation would thus consist of three isolated peaks distributed along the gray-scale range, as observed in Figure 3-1e. Peak height represents pixel count for a particular gray value, while peak breadth relates to how confidently one can assign a peak to a particular material. Broader peaks represent low signal-to-noise levels and/or overlaps in material gray values. The tallest peak in each histogram represents air; the brighter peak (high gray-scale value), or shoulder when there is little contrast, immediately to the right of the air peak represents wood cell walls. The darker peak (low gray-scale value), or shoulder, left of the air peak is an artifact caused by large differences in density and refractive index at the interface of dissimilar materials (Betz et al. 2007; Haibel 2008; Modzel 2009). With a fixed gray-scale range, simply maximizing the attenuation difference between any two phases could reduce the achievable contrast for the third. For example, Figure 3-1d shows the greatest overlap between the air and wood peaks, and these specimens were scanned at the highest energy.

X-ray radiographs of control PF and IPF1 adhesive powders were collected to determine if absorption contrast could be enhanced with increasing wt% I, even below the iodine k-edge. Figure 3-4 compares the mean gray-scale pixel intensity from regions containing air-space and ground resin in each projection image. Note that the response variable in this figure is transmission intensity, which is opposite from XCT gray-scale intensity. In radiographic projections, high pixel intensities correspond with high photon transmission

through the material (i.e. low absorption); with XCT high pixel intensities relate to high attenuation (i.e. low transmission). Air intensity was uniform in each projection, while adhesive transmission intensity decreased significantly from zero to 12.2 wt% I. Bulk, or apparent, density (ρ_{bulk}) was checked as a confounding factor since x-ray attenuation is influenced by density and composition (Ketcham and Carlson 2001). The void volume fraction (v_a) in the powder column is inversely proportional to ρ_{bulk} . Despite cured IPF1 being denser than control PF, ρ_{bulk} and v_a did not correlate with the observed intensity behavior (Figure 3-4).

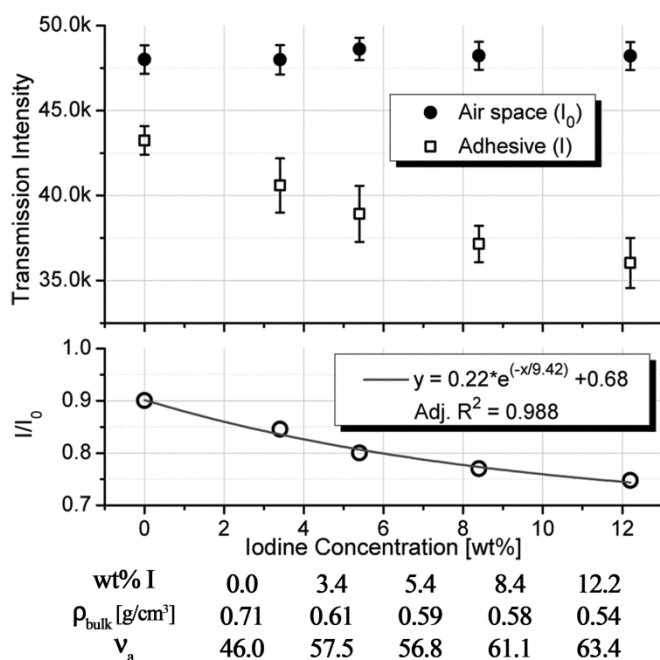


Figure 3-4 (top) Mean x-ray transmission (gray-scale) intensity through air and adhesive powder with increasing wt% iodine, error bars indicate ± 1 standard deviation; (bottom) mean intensity ratio, I/I_0 , and fitted regression line; measured wt% I, apparent densities and void-volume fractions are also provided

In both air-space and adhesive filled regions, the transmitted x-rays passed through both container walls and the internal material. The relationship between adhesive intensity (I)

and airspace intensity (I_0) was expected to follow the Beer-Lambert attenuation law, and an exponential fit to the ratio data showed a high adjusted R^2 of 0.988. The significance of the relationship showed that even below the iodine k-edge, and independent of bulk density, increasing iodine concentration would further reduce transmission intensity, resulting in greater XCT contrast.

IPF2 was prepared based on the results from both BrPF and IPF1. Meta-iodophenol made up the entire phenol component in IPF2, to maximize the achievable iodine concentration with the presented method and ensure all resin polymers were substituted to the same degree, regardless of chain length. Cured IPF2 contained 39.9 wt% I, and had a density of 2.24 g/cm³ (Table 3-2). Accordingly, IPF2 showed the highest theoretical attenuation of all adhesives including RbPF (Figure 3-3c). Subsequent XCT data, collected below the iodine k-edge, yielded significantly enhanced adhesive contrast. The bondline image in Figure 3-1e shows dark void spaces in empty lumens, light-gray cell walls and bright adhesive at the bond interface and in several vessels; these phases correspond to the three primary peaks in the IPF2 bondline histogram. Also, the IPF2 adhesive gray value is more consistent than the other systems, as evident by the clear, rightmost peak in the bondline histogram (Figure 3-1e). This observation is intuitive because all IPF2 polymer chains contained the same degree of iodine substitution. In Figure 3-1b, RbPF appears less consistent; the brightest regions likely indicate higher Rb concentrations (Modzel 2009). Consequently, the RbPF bondline histogram shows no clear distinction between wood and adhesive peaks; rather, they form one broad peak which extends farther along the gray-scale range than the shoulder in the wood-only histogram. As was the case,

RbPF could not be segmented. The IPF2 system, however, was segmented (Figure 3-2) with gray-scale thresholds in the valleys between each peak.

The above results indicate that density, molecular formula, tag uniformity and signal-to-noise ratio all impact adhesive x-ray contrast. Wood and adhesives are complex, organic systems with similar density; x-ray absorption contrast between the two materials requires ample difference in attenuation coefficients. Perhaps, an adhesive consisting entirely of meta-bromophenol would achieve similar results as IPF2 if it were scanned just above the Br k-edge; however, its density would likely be lower than IPF2. Similarly, one might argue that contrast might be even greater for IPF2 if it were imaged above the I k-edge; yet, this would increase image noise since beam attenuation in wood is drastically decreased at such high beam energies.

3.4.3 Tag mobility assessment

Quantitative segmentation of a tagged adhesive requires the contrast agent to remain attached and uniformly distributed along the polymers throughout both the formulation and bonding processes. Initially, there was concern that the Br and I tags, attached at the meta position of the phenol reactants, might be released from the aromatic rings when exposed to the high temperature and pH reaction environments during adhesive cook. However, IC results showed no free bromide or iodide ions in any of the experimental adhesives following formulation. Composite specimens were bonded at still higher temperatures than formulation. NAA results confirmed that resin powders contained the same tag concentrations as predicted (Table 3-2); yet, it was unclear whether the Br and I were, in fact, still attached to the cured PF polymers. Fluorescent micrographs and EDS

elemental maps were used to determine if observed adhesive locations corresponded with tag spectra. Figure 3-5 compares the FM and EDS images from the same surfaces of specimens bonded with each resin. In each FM image, dark PF adhesive shows clear contrast to surrounding, light-colored cells. In EDS images, the oxygen elemental signal, shown in red, most clearly represented the wood structure, as the embedding epoxy had a lower oxygen concentration than the surrounding cell walls. Tag-element maps, shown in green, are overlain on the oxygen maps. EDS spectra include the cumulative detected fluorescent counts from 64 scans for each element of interest. Raw images exhibited a uniform level of background noise from low intensity pixels only detected in a single or few scans; however, this was easily removed with simple image processing.

Figure 3-5b shows Rb contamination in cell walls far from the RbPF specimen bondline and around cell lumens void of adhesive; this supports earlier evidence that the Rb ions moved independent of the adhesive polymers (Modzel 2009; Modzel et al. 2011). The EDS images of BrPF, IPF1 and IPF2 (Figures 3-4d, f and h, respectively) show tag signals directly correspond with the adhesive locations in the matching FM images. For BrPF and IPF1, only a portion of the phenol reactants were substituted. Tag concentration in these systems were likely heterogeneous across different polymer molecular weight, and thus polymer mobility was effected; this might explain the observed non-uniformity in tag-signal intensity. However, iodine intensity in IPF2 appears consistent at all adhesive locations. Additionally, semi-quantitative point spectra of the Br and I-tagged composite specimens showed there were no measurable traces of tags on cell wall edges far from the bondline and not in contact with adhesive.

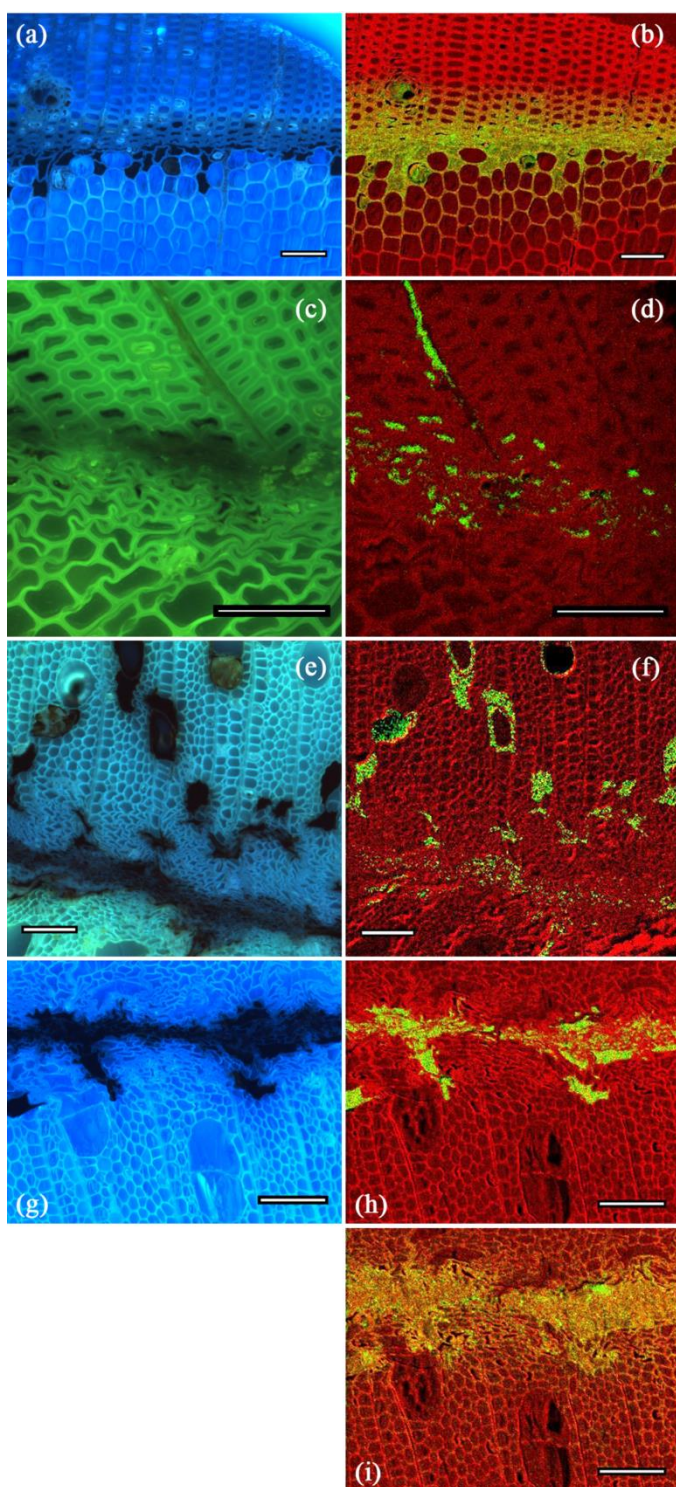


Figure 3-5 FM images (left) and EDS elemental maps (right) of the same specimen surface for composites bonded with RbPF (a & b, DF), BrPF (c & d, SYP), IPF1 (e & f, HP) and IPF2 (g - i, HP). BrPF FM image (c) acquired with 'blue' filterset and (a, e & g) acquired with UV filterset. EDS red phase represents oxygen signal and green indicates tag-element of interest: Rb (b), Br (d), I (f & h) and Na (i). Scale bars = 100 μ m

Rb ions were included as an alkaline catalyst during the RbPF adhesive formulation (Modzel et al. 2011); the conventional catalyst system, NaOH was used in formulation of the BrPF and IPF resins. Figure 3-5i shows the Na elemental map for the IPF2 specimen. As with Rb (Figure 3-5b), the Na signal intensity appears non-uniform in the bondline region, and Na ions migrated far from the bond interface. However, unlike the Rb ions, sodium appeared indiscriminately in both cell walls and epoxy-filled lumens. This is not surprising as Na is much smaller and more reactive than Rb, affording it greater mobility. Na ions distributed throughout the wood cells after adhesive cure were likely remobilized by the liquid epoxy embedding media before it hardened. Several studies have shown similar migration and agglomeration behavior for ions or metal-particles dispersed in liquids designed to penetrate wood structures (De Vetter et al. 2006; Mannes et al. 2010; Matsunaga et al. 2009; Matsunaga et al. 2004; Walther and Thoemen 2009; Wang et al. 2007). Often wood's heterogeneous chemical and anatomical structures magnify these separation effects. Charged ions may be preferentially absorbed into different cell wall layers, and micro- or nano-sized metallic particles can often be size excluded from penetration by small pit structures (Matsunaga et al. 2009; Matsunaga et al. 2004). Therefore, if contrast agents are required to quantify the penetration behavior of an adhesive or solution into wood structures, consideration must be given to chemical or physical phase separation.

The collective IC and EDS results indicate that the halogen substituents remained attached to the phenol reactants throughout formulation and bonding. Furthermore, the

IPF2 tag concentration appeared uniform across the polymer molecular weight distribution, since it consisted entirely of meta-iodophenol; this observation is consistent with the uniform XCT gray-scale intensity in Figure 3-1e. It is true that one would not expect a PF resin prepared with a substituted phenol to polymerize in the same manner as one containing only phenol. However, the goal of this work was to develop an adhesive system which could be confidently segmented from wood-composite XCT data. The BrPF and IPF adhesives presented here were formulated according to one particular recipe. This of course could be adjusted for different desired molecular weight distribution, viscosity, solids content or cross-linking potential, all of which in turn would affect adhesive penetration and performance behavior.

3.5 Conclusions

A resol-type, phenol formaldehyde adhesive formulated with meta-iodophenol yielded sufficient and consistent micro x-ray computed tomography image contrast in bonded wood-composites. Air, wood and adhesive phases could all be segmented from reconstructed 3D datasets with simple histogram thresholds centered between the three material gray-scale peaks. Preliminary adhesives containing lower concentrations of iodine or bromine were also presented, and compared, with a control and rubidium-labeled adhesive. X-ray absorption contrast improved with increasing tag mass and concentration and cured adhesive density; however, image quality and segmentation confidence suffered at high beam energies when signal-to-noise levels were low. X-ray results for wood and adhesives agreed with theoretical attenuation behavior predicted for each material as a function of beam energy. Tag efficacy and mobility were also accessed

with multiple chemical and visual analyses including ion chromatography, neutron activation analysis, fluorescent microscopy and energy dispersion spectrometry. The iodine and bromine tags, originally covalently bonded to the formulation reactants, remained associated with the liquid and cured adhesive polymers. Sodium and rubidium, which were merely mixed into the liquid adhesives as polymerization catalysts, retained high mobility, and migrated independent of the adhesive polymers during bonding. The presented formulation could be modified to achieve different viscosity, solids content, or molecular weight distribution, which would in turn influence penetration behavior and joint performance. The afforded x-ray tomography contrast and segmentation confidence with these tagged adhesives can help improve fundamental understanding of wood adhesion and the role of adhesive penetration.

3.6 Acknowledgements

Use of the Advanced Photon Source was supported by the U. S. Department of Energy, Office of Science, Office of Basic Energy Sciences, under Contract No. DE-AC02-06CH11357. The Advanced Light Source is supported by the Director, Office of Science, Office of Basic Energy Sciences, of the U.S. Department of Energy under Contract No. DE-AC02-05CH11231. Financial support was provided by the Wood-Based Composites Center, a National Science Foundation Industry/University Cooperative Research Center. Resin formulation and technical assistance were provided by Arclin, in Springfield, Oregon.

3.7 References

ASTM D 4426-01 (2006) Standard test method for determination of percent nonvolatile content of liquid phenolic resins used for wood laminating. ASTM International, West Conshohocken, PA.

ASTM B 5965 - 02 (2007) Standard test method for specific gravity of coating powders. ASTM International, West Conshohocken, PA.

Banhart, J. 2008a: Introduction. In: Banhart, J., editor, *Advanced Tomographic Methods in Materials Research and Engineering*, Oxford, New York: Oxford University Press, 3-18.

Banhart, J. 2008b: Radiation sources and interaction of radiation with matter. In: Banhart, J., editor, *Advanced Tomographic Methods in Materials Research and Engineering*, Oxford, New York: Oxford University Press, 107-140.

Betz, O., Wegst, U., Weide, D., Heethoff, M., Helfen, L., Lee, W. K. and Cloetens, P. (2007) Imaging applications of synchrotron X-ray phase-contrast microtomography in biological morphology and biomaterials science. 1. General aspects of the technique and its advantages in the analysis of millimetre-sized arthropod structure. *J. Microsc.-Oxf.* 227, 1, 51-71.

Bucur, V. (2003) Techniques for high resolution imaging of wood structure: a review. *Measurement Science & Technology* 14, 12, R91-R98.

Davidson, M. W. and Abramowitz, M. 2002: Optical Microscopy. In, *Encyclopedia of Imaging Science and Technology*: John Wiley & Sons, Inc.

De Vetter, L., Cnudde, V., Masschaele, B., Jacobs, P. J. S. and Van Acker, J. (2006) Detection and distribution analysis of organosilicon compounds in wood by means of SEM-EDX and micro-CT. *Mater. Charact.* 56, 1, 39-48.

Dowd, B. A., Campbell, G. H., Marr, R. B., Nagarkar, V. V., Tipnis, S. V., Axe, L. and Siddons, D. P. (1999) Developments in synchrotron x-ray computed microtomography at the National Synchrotron Light Source. 224-236.

Ebewele, R. O., River, B. H. and Koutsky, J. A. (1982) Relationship between phenolic adhesive chemistry, cure and joint performance .part I. Effects of base resin constitution and hardener on fracture energy and thermal effects during cure. *Journal of Adhesion* 14, 3-4, 189-217.

Ellis, E. (2006) Solutions to the problem of substitution of ERL 4221 for vinyl cyclohexene dioxide in Spurr low viscosity embedding formulations. *Microscopy Today* 14, 4, 32-33.

Evans, P. D., Morrison, O., Senden, T. J., Vollmer, S., Roberts, R. J., Limaye, A., Arns, C. H., Averdunk, H., Lowe, A. and Knackstedt, M. A. (2010) Visualization and numerical analysis of adhesive distribution in particleboard using X-ray micro-computed tomography. *International Journal of Adhesion and Adhesives* 30, 8, 754-762.

Forsberg, F., Sjodahl, M., Mooser, R., Hack, E. and Wyss, P. (2010) Full three-dimensional strain measurements on wood exposed to three-point bending: Analysis by use of digital volume correlation applied to synchrotron radiation micro-computed tomography image data. *Strain* 46, 1, 47-60.

Frazier, C. E. and Ni, J. W. (1998) On the occurrence of network interpenetration in the wood-isocyanate adhesive interphase. *International Journal of Adhesion and Adhesives* 18, 2, 81-87.

Frihart, C. R. 2005: Wood adhesion and adhesives. In: Rowell, R. M., editor, *Handbook of Wood Chemistry and Wood Composites*, New York: Taylor & Francis Group.

Haibel, A. 2008: Synchrotron x-ray absorption tomography. In: Banhart, J., editor, *Advanced Tomographic Methods in Materials Research and Engineering*, Oxford, New York: Oxford University Press, 141-160.

Hass, P., Wittel, F., Mendoza, M., Herrmann, H. and Niemz, P. (2012) Adhesive penetration in beech wood: experiments. *Wood Science and Technology* 46, 1-3, 243 - 256.

Hass, P., Wittel, F. K., McDonald, S. A., Marone, F., Stampanoni, M., Herrmann, H. J. and Niemz, P. (2010) Pore space analysis of beech wood: The vessel network. *Holzforschung* 64, 5, 639-644.

Henke, B. L., Gullikson, E. M. and Davis, J. C. (1993) X-ray interactions - photoabsorption, scattering, transmission, and reflection at E=50-30,000 EV, Z=1-92. *Atom. Data Nucl. Data Tables* 54, 2, 181-342.

Kamke, F. A. and Lee, J. N. (2007) Adhesive penetration in wood - a review. *Wood and Fiber Science* 39, 2, 205-220.

Ketcham, R. A. and Carlson, W. D. (2001) Acquisition, optimization and interpretation of X-ray computed tomographic imagery: applications to the geosciences. *Computers & Geosciences* 27, 4, 381-400.

Mannes, D., Marone, F., Lehmann, E., Stampanoni, M. and Niemz, P. (2010) Application areas of synchrotron radiation tomographic microscopy for wood research. *Wood Science and Technology* 44, 1, 67-84.

Mannes, D., Niemz, P. and Lehmann, E. (2009) Tomographic investigations of wood from macroscopic to microscopic scale. *Wood Research* 54, 3, 33-44.

Matsunaga, H., Kiguchi, M. and Evans, P. D. (2009) Microdistribution of copper-carbonate and iron oxide nanoparticles in treated wood. *Journal of Nanoparticle Research* 11, 5, 1087-1098.

Matsunaga, H., Matsumura, J. and Oda, K. (2004) X-ray microanalysis using thin sections of preservative-treated wood - Relationship of wood anatomical features to the distribution of copper. *Iawa Journal* 25, 1, 79-90.

Mayo, S. C., Chen, F. and Evans, R. (2010) Micron-scale 3D imaging of wood and plant microstructure using high-resolution X-ray phase-contrast microtomography. *Journal of Structural Biology* 171, 2, 182-188.

Minc, L. D. 2008: Neutron Activation Analysis. In: Pearsall, D. M., editor *Encyclopedia of Archaeology*, New York: Academic Press, 1669 - 1683.

Modzel, G. 2009: Computed X-ray analysis of wood-adhesive bonds. *Wood Science and Engineering*, Oregon State University, Corvallis, OR: 240.

Modzel, G., Kamke, F. A. and De Carlo, F. (2011) Comparative analysis of a wood-adhesive bondline. *Wood Science and Technology* 45, 1, 147-158.

Park, B.-D., Riedl, B., Yoon Soo, K. and So, W. T. (2002) Effect of synthesis parameters on thermal behavior of phenol-formaldehyde resol resin. *Journal of Applied Polymer Science* 83, 7, 1415-1424.

Pizzi, A. 2003: Phenolic resin adhesives. In: Pizzi, A. and Mittal, K. L., editors, *Handbook of Adhesive Technology*, New York: Marcel Dekker, Inc.

Pocius, A. V. Adhesion and adhesives technology: an introduction. Hanser Publishers; Hanser/Gardner Publications, Munich, New York; Cincinnati, Ohio, 1997

Rasband, W. S. 1997 - 2012: ImageJ. In: *U. S. National Institutes of Health*, <http://imagej.nih.gov/ij/>, Bethesda, Maryland, USA.

Schindelin, J., Arganda-Carreras, I., Frise, E., Kaynig, V., Longair, M., Pietzsch, T., Preibisch, S., Rueden, C., Saalfeld, S. and Schmid, B. (2012) Fiji: an open-source platform for biological-image analysis. *Nature Methods* 9, 7, 676-682.

Schultz, J. and Nardin, M. 1994: Theories and mechanisms of wood adhesion. In: Pizzi, A. and Mittal, K. L., editors, *Handbook of Adhesive Technology*, New York: Marcel Dekker, Inc., 19-33.

Sellers, T. 1994: Adhesives in the wood industry. In: Pizzi, A. and Mittal, K. L., editors, *Handbook of Adhesive Technology*, New York: Marcel Dekker, Inc., 599-614.

Smith, L. and Côté, W. (1971) Studies of penetration of phenol-formaldehyde resin into wood cell walls with the SEM and Energy-Dispersive X-ray Analyzer. *Wood and Fiber Science* 3, 1, 56-57.

Spurr, A. R. (1969) A low-viscosity epoxy resin embedding medium for electron microscopy. *Journal of ultrastructure research* 26, 31-43.

Standfest, G., Kutnar, A., Plank, B., Petutschnigg, A., Kamke, F. and Dunky, M. (2012) Microstructure of viscoelastic thermal compressed (VTC) wood using computed microtomography. *Wood Science and Technology*.

Trtik, P., Dual, J., Keunecke, D., Mannes, D., Niemz, P., Stähli, P., Kaestner, A., Groso, A. and Stampanoni, M. (2007) 3D imaging of microstructure of spruce wood. *Journal of Structural Biology* 159, 1, 46-55.

Umemura, K., Takahashi, A. and Kawai, S. (1998) Durability of isocyanate resin adhesives for wood - I: Thermal properties of isocyanate resin cured with water. *Journal of Wood Science* 44, 3, 204-210.

Walther, T. and Thoemen, H. (2009) Synchrotron X-ray microtomography and 3D image analysis of medium density fiberboard (MDF). *Holzforschung* 63, 5, 581-587.

Wang, Y., Muszyński, L. and Simonsen, J. (2007) Gold as an X-ray CT scanning contrast agent: Effect on the mechanical properties of wood plastic composites. *Holzforschung* 61, 6, 723-730.

White, M. S. (1977) Influence of resin penetration on the fracture toughness of wood adhesive bonds. *Wood Science* 10, 1, 6-14.

White, M. S., Ifju, G. and Johnson, J. A. (1977) Method for measuring resin penetration into wood. *Forest Products Journal* 27, 7, 3.

Wildenschild, D., Hopmans, J. W., Vaz, C. M. P., Rivers, M. L., Rikard, D. and Christensen, B. S. B. (2002) Using X-ray computed tomography in hydrology: systems, resolutions, and limitations. *Journal of Hydrology* 267, 3-4, 285-297.

CHAPTER 4. X-RAY COMPUTED TOMOGRAPHY OF WOOD-
ADHESIVE BONDLINES: ATTENUATION AND PHASE
CONTRAST EFFECTS

Jesse L. Paris, Frederick A. Kamke, and Xianghui Xiao

To be submitted for publication in *Wood Science and Technology*

X-ray Computed Tomography of Wood-Adhesive Bondlines:
attenuation and phase-contrast effects

Jesse L. Paris^{a,*}, Frederick A. Kamke^{a,†}, and Xianghui Xiao^b

^a Department of Wood Science & Engineering, Wood-Based Composites Center, Oregon State University, 119 Richardson Hall, Corvallis, OR 97331, USA

^b Advanced Photon Source, Beamline 2-BM-B, Argonne National Laboratory, Argonne, IL 60439, USA

* Corresponding Author. Tel.: +804 338 4353; Fax +542 737 3385

E-mail address: Jesse.Paris@OregonState.edu (J. L. Paris)

† Secondary Corresponding Author. Tel.: +541 737 8422; Fax +542 737 3385

E-mail address: Fred.Kamke@OregonState.edu (F. A. Kamke)

4.1 Abstract

Micro-scale X-ray computed tomography (XCT) is discussed as a technique for identifying 3D adhesive distribution in wood-adhesive bondlines. Visualization and material segmentation of the adhesives from the surrounding cellular structures requires sufficient gray-scale contrast in the reconstructed XCT data. Commercial wood adhesive polymers have similar chemical characteristics and density to wood cell wall polymers, and therefore do not provide good XCT attenuation contrast in their native form. Here, three different adhesive types, namely phenol formaldehyde, polymeric diphenylmethane diisocyanate, and a hybrid polyvinyl acetate, are tagged with iodine such that they do yield sufficient x-ray attenuation contrast. However, even with significant x-ray attenuation, phase-contrast effects at material edges can still complicate image quality and segmentation in XCT data reconstructed with conventional filtered back projection absorption contrast algorithms, if unaccounted for. One dataset is also reconstructed with a quantitative phase retrieval algorithm, which isolates and removes the phase-contrast effect. The article discusses importance for consideration and balance between x-ray acquisition parameters, material attenuation and phase-contrast effects in all quantitative XCT analyses of wood-adhesive bondlines.

4.2 Introduction

X-ray computed tomography (XCT) is a non-destructive imaging technique capable of providing 3D data of the internal structures in opaque materials. Achievable XCT image resolution ranges from the millimeter to nanometer scale depending on equipment, experimental parameters, and the size and volume of the imaged specimen (Chen et al.

2011; Graafsma and Martin 2008; Ketcham and Carlson 2001; Kinney and Nichols 1992). The technique was first developed in the early 1970's for medical imaging, and has since been refined and applied in numerous engineering, biological and materials science research arenas (Banhart 2008; Hounsfield 1973; Ketcham and Carlson 2001; Wildenschild et al. 2002). More recently, there have been numerous applications of XCT for wood and wood-based composite analyses (Hass et al. 2012; Hass et al. 2010; Kamke et al. 2014; Mannes et al. 2010; Mannes et al. 2009a; Mannes et al. 2009b; Mayo et al. 2010; Modzel 2009; Modzel et al. 2011; Muszyński 2009; Paris et al. 2014; Standfest et al. 2012; Steppe et al. 2004; Trtik et al. 2007); this is the primary focus of the present work.

The basic XCT technique involves the illumination of a specimen with penetrating x-ray radiation; after traversing through the specimen, the x-rays are then converted to visible light with a scintillation film and recorded as a digital image with a camera. The resulting projection, or radiograph, represents the apparent 2D density map of the specimen with respect to the orientation of the x-ray beam. If the specimen or source/detector optics are rotated, and a series of radiographs are incrementally collected, through a full 180 degrees, 3D positional data is recorded (Banhart 2008; Ketcham and Carlson 2001). As the photons pass through the specimen, they interact with matter and are reduced in intensity and/or diffracted from their initial trajectory. The extent of these interactions are material dependent. When different materials are present in the same volume, they can be distinguished from each other if the spatial resolution is fine enough to identify clear material edges, and if there is sufficient contrast in the reconstructed image.

Two primary contrast mechanisms are employed in XCT material analyses. The most common mechanism is absorption contrast, which exploits differences in material linear attenuation coefficients, μ , or the ability for that material to absorb or scatter penetrating x-rays. The value of μ depends on the energy of the incident x-rays, and is proportional to material atomic number (Z) and density (Banhart 2008; Ketcham and Carlson 2001; Paris et al. 2014; Wildenschild et al. 2002). With absorption tomography, gray-scale reconstructed tomograms are 3D maps of relative attenuation coefficients (Banhart 2008; Ketcham and Carlson 2001; Wildenschild et al. 2002). The second mechanism, which is growing in popularity, understanding and effectiveness, is known as phase-contrast tomography. The basic principle in phase-contrast tomography is that a coherent beam of incident photons will undergo a phase shift, or Fresnel diffraction, at the interface between two materials with different refractive indices (Betz et al. 2007; Cloetens et al. 1997; Peele and Nugent 2008). In reconstructed tomograms, the phase-contrast effect results in paired, light/dark fringes at material edges, and the intensity of the effect will increase with distance between the specimen and detector, due to free space propagation of the out-of-phase photon waves (Betz et al. 2007; Cloetens et al. 2002; Cloetens et al. 1997).

Phase-contrast tomography is particularly useful for differentiation between low Z materials, such as soft biological tissues, where there is little adsorption contrast (Betz et al. 2007; De Witte et al. 2009; Peele and Nugent 2008). However, application of this phenomena can be either qualitative or quantitative. The former occurs when radiographic projections are reconstructed with conventional XCT algorithms, and the edge enhancement effect helps researchers identify material boundaries. Quantitative

applications of phase-contrast tomography involve the reconstruction of XCT data using various phase retrieval algorithms, where the phase shift is identified, and resulting tomograms represent maps of relative refractive indices (Betz et al. 2007; Cloetens et al. 2002; De Witte et al. 2009; Weitkamp et al. 2011; Wu et al. 2008). Phase retrieval algorithms, however, are highly sensitive to the nature of the incident x-rays, and often require a highly coherent, parallel and monochromatic photon beam. Synchrotron x-ray sources are ideal for quantitative phase retrieval (QPR) XCT analyses. Initial QPR algorithms required a sample to undergo multiple scans at varied specimen-to-detector distances or at multiple beam energies to isolate the phase-contrast effect (Cloetens et al. 2002; Gureyev et al. 2001; Peele and Nugent 2008). More recently, however, advanced algorithms have been introduced which can utilize one, 'defocused' XCT dataset from a single scan, which significantly cuts down on scan time and specimen damage due to prolonged exposure to ionizing radiation (Mayo et al. 2003; Mayo et al. 2010; Paganin et al. 2002; Weitkamp et al. 2011).

To date, the majority of wood XCT studies have used conventional reconstruction methods, such as the filtered back projection algorithm, and relied on absorption contrast for material identification and differentiation (Hass et al. 2010; Mannes et al. 2010; Modzel et al. 2009, 2011; Paris et al. 2014; Trtik et al. 2007). In micro scale analyses, absorption contrast is typically adequate for studying anatomical cellular features in solid wood, as only two materials, air and wood cell wall, are present. At low XCT energies (< 10 KeV), the linear attenuation coefficient of wood cell wall material is sufficiently greater than that of air (Mannes et al. 2010; Paris et al. 2014). Additionally, a small degree of phase-contrast effects, such as those generated with small specimen-to-detector

distances are tolerable, as dark fringe effects can be counted in the empty lumens and bright edge effects may be segmented as part of the wood signal. However, absorption contrast is far more challenging in micro XCT analyses of wood-composites, where multiple materials, such as adhesives, are present in the volume of interest. Wood-adhesives are typically organic, and have a cured density similar to that of wood cell walls, and therefore do not generate sufficient absorption contrast for simple gray-scale segmentation (Hass et al. 2012; Modzel et al. 2011; Paris et al. 2014). Several attempts have been made to increase adhesive attenuation properties by incorporating inorganic, heavy metal, tags as contrast agents into the liquid adhesives (Evans et al. 2010; Modzel et al. 2011; Walther and Thoemen 2009); however, independent tag mobility, particle agglomeration, and phase separation between tag and adhesive molecules is a common complication with this approach.

The present study is part of a broader project to quantify 3D adhesive penetration in wood-adhesive bondlines using synchrotron-based micro XCT, and then assess mechanical joint performance from the same, undamaged XCT specimens (Kamke et al. 2014; Paris et al. 2013). In a previous publication, the authors demonstrated a method for successfully tagging a phenol formaldehyde (PF) wood adhesive with iodine for quantitative XCT material segmentation, while avoiding tag migration complications (Paris et al. 2014). In this paper, two other common wood adhesive types, polyvinyl acetate (PVAc) and polymeric diphenylmethane diisocyanate (pMDI), were tagged with iodine and imaged with absorption contrast micro XCT. However, this paper also discusses the impacts of phase-contrast effects on wood-adhesive XCT material segmentation.

4.3 Experimental

4.3.1 Adhesive formulation and bonding

The iodinated PF adhesive (IPF) was formulated according to a similar procedure as is used for commercial plywood adhesives (44 % solids); however, 100 % of the phenol component was replaced with meta-iodophenol (Kamke et al. 2014; Paris et al. 2014). A control PF was prepared with the same procedure, which contained no iodophenol.

A neat emulsion PVAc (54 % solids) was used in the preparation of a 50:50 mixture with the above IPF resin, similar to one described elsewhere (Cao 2010). Both the neat PVAc and IPF resins were first diluted, individually, to 25 % solids with deionized water, and then the two dilutions were vigorously hand-mixed until the resulting adhesive appeared homogeneous.

The iodinated pMDI (IpMDI) was prepared from a commercial pMDI resin (Huntsman, Rubinate 1840). The neat resin isocyanate (NCO) content (30.5 %) was first determined according to ASTM D 5155, Method C, where the titrant was 1 N hydrochloric acid, and 200 mL instead of 100 mL anhydrous methanol was used to avoid solution turbidity (ASTM-D-5155 2010). A neat pMDI sample was then reacted with 2,4,6 triiodophenol (TIP, 97 % purity, purchased from Alfa Aesar) to convert approximately 10 % of the known NCO groups to iodine-substituted urethanes according to the following procedure: (1) 10.92 g TIP was dissolved in 15.11 g (17 mL) anhydrous tetrahydrofuran (THF, purchased from EMD Millipore) and stirred at room temperature for 1 hour (a small amount of insoluble material caused the resulting solution to appear hazy; however, this was assumed negligible compared to the majority of TIP which went into solution

instantaneously), (2) the TIP/THF solution was added to 30.08 g of neat pMDI in a separate, round-bottom flask and reacted for 24 hours at 50 °C under inert nitrogen (N₂) gas. To avoid unwanted moisture exposure, chemical and solution additions were all done with needle transfer techniques under N₂, and all glassware was completely clean and flamed dry prior to use. In a preliminary pMDI tagging trial, attempt was made to remove the THF solvent with vacuum distillation. However, this caused steep viscosity increase, which was impractical for wood adhesive application, penetration and bonding. Therefore, the THF solvent was allowed to remain in the final version of the liquid IpMDI adhesive.

Adhesives were applied at a common, resin-solids spread-rate of 122 g/m² to the tangential-longitudinal surfaces of freshly-planed, 12 mm thick, Douglas-fir (*Pseudotsuga menziesii*, DF), loblolly pine (*Pinus taeda*, SYP) or hybrid poplar (*Populus deltoides* x *Populus trichocarpa*, HP) lamina. Specific bonding conditions varied between each adhesive type; however, the initial consolidation pressure for all treatments was 690 kPa. All PF composites were bonded in a 185 °C hot press for 8 min. The hybrid PVAc and IpMDI specimens were first compressed using the desired force and then clamped between steel plates. The clamped assembly was then placed in an oven for complete cure (hybrid PVAc at 150 °C for 3 h; IpMDI at 50 °C for 14 h followed by 103°C for an additional 1 h).

4.3.2 Adhesive cure and elemental analysis

The tagged adhesives were analyzed to assess percent solids, powder density and, in the case of hybrid PVAc, film morphology. PF resins and the hybrid IPF/PVAc samples were

cured in an oven at 125 °C and 150 °C, respectively, for 3 hours (Paris et al. 2014). Neat pMDI specimens, which require moisture to initiate the curing reaction (Frazier 2003), were placed in a desiccator with a beaker of deionized water, and the whole assembly was placed in a 103 °C oven for 48 hours. The desiccator vacuum inlet remained open for steam and CO₂ to slowly vent, but still created a high temperature and humidified environment for pMDI cure. For IpMDI samples, the oven was first set to 50 °C for 48 hours, which allowed bulk THF to slowly evaporate before increasing to 103 °C for an additional 48 hours. The percent solids was determined by weight loss after curing. Cured specimens were ground into fine powders, and their specific gravity was measured according to a modified version of ASTM D-5965, described elsewhere (ASTM-D-5965 2007; Paris et al. 2014).

Iodine concentrations for the cured adhesive powders were verified with neutron activation analysis (NAA) using the TRIGA Mk II Research Reactor at Oregon State University; reactor and NAA procedural details are provided elsewhere (Paris et al. 2014).

Iodine tag mobility was investigated in the bondlines. Specimens excised from bonded laminates were embedded in Spurr Low-Viscosity epoxy resin (Ellis 2006; Paris et al. 2014; Spurr 1969), and the cross-section (4 mm²) was microtomed to an ultra-smooth surface. Bondline fluorescence micrographs (FM) were collected for each specimen surface using a Nikon E400 epi-fluorescent microscope under UV light (Paris et al. 2014). The same specimen surfaces were then coated with a gold/palladium alloy and analyzed in a scanning electron microscope equipped with energy dispersive

spectroscopy (EDS) elemental mapping (Paris et al. 2014). EDS images, which were overlain elemental signatures of oxygen and iodine, provided good contrast between wood cell structure and adhesive locations. These images were then scaled and registered with the FM images for qualitative comparison (Paris et al. 2014).

4.3.3 Micro X-ray Computed Tomography

XCT scans were collected on beamline 2-BM-B at the Advanced Photon Source (APS), at the Argonne National Laboratory, Argonne, IL. A total of 1504 radiographic projections were collected over 0.12° angular increments at 15.3 KeV and a 250 millisecond exposure time. The specimen-to-scintillator distance for the majority of the APS scans was 8 mm; however, one of the SYP IpMDI specimens was scanned a second time at a distance of 30 mm. Tomograms were reconstructed with a conventional fast filtered back projection (FBP) algorithm (Dowd et al. 1999; Paris et al. 2014). The 30 mm SYP IpMDI specimen data was also reconstructed with the ANKAphase QPR algorithm (Mayo et al. 2003; Paganin et al. 2002; Weitkamp et al. 2011). All reconstructed data sets were stored as longitudinal stacks of floating-point (32-bit) gray-scale, cross-section images with voxel side-lengths of $1.45\ \mu\text{m}$. All additional XCT beamline details, acquisition parameters, and optical equipment are reported elsewhere (Kamke et al. 2014; Paris et al. 2014).

All image processing operations, for both XCT tomogram data and FM/EDS images, were done using the ImageJ-based software package Fiji, which contains several preloaded analysis plugins (Rasband 1997 - 2012; Schindelin et al. 2012). Specific processing steps for preparing composite EDS images are described in detail elsewhere

(Paris et al. 2014); while XCT image processing and segmentation methods followed a modified procedure to that previously presented by the authors (Kamke et al. 2014). Specific modifications are as follows: (1) cropped sub-volumes, 500 - 750 voxels (725 - 1087 μm , radial) x 750 voxels (1087 μm , tangential) x 1500 slices (2175 μm , longitudinal), were digitally excised from the center of the scanned-specimens, as to contain no machining defects or artifacts associated with the specimen geometry; (2) directly following the normalization operation with a 0.4 % saturation tolerance, image stack gray-scale histograms were carefully inspected, and the lower bound, gray-scale limit was shifted slightly lower than the histogram peak that represents air, then the image stack was converted from 32-bit to 8-bit, which distributed the gray-values for materials of interest over the full 0 - 2^8 gray level range (Betz et al. 2007) (in other words, all voxel values darker than air were forced to a value of zero); and (3) specific criteria, rather than constant threshold values, were used to segment the sub-volumes into the various material phases. These criteria were adhesive-system dependent, as each adhesive had different attenuation characteristics, and in the case of IPF and IpMDI, some low molecular weight components were believed to penetrate, at the nano-scale, into the wood cell walls (Frazier and Ni 1998; Jakes et al. 2013; Paris et al. 2013; Stockel et al. 2012). The specific criteria for determining the material threshold were as follows: (1) “air-to-cell wall” – the 1st derivative of the histogram curve crossed zero (i.e. a minimum between histogram peaks); (2) “cell wall-to-pure adhesive” – 1st derivative curve crossed zero, when possible; however, if no minima was detected above the pure wood peak, and rather a shallow-sloping curve continued along the remainder of the gray-scale range, the threshold value was chosen when the 5-point moving-average 2nd derivative curve fell

below 0.01 % of the full 1st derivative value range; and (3) if cell wall penetration was believed present (i.e. a gradient of gray-values or plateau was observed between the pure adhesive or pure cell wall peaks) the threshold value was taken where the 5-point average 2nd derivative value fell below 0.05% for the 1st derivative value range. The chosen threshold values are arbitrary, but confirmed by visual observation, and then held constant for each adhesive type.

4.4 Results and Discussion

In previous publications, the authors explained the numerous achievable benefits for using non-destructive, 3D XCT for analysis of adhesive bonds in wood (Kamke et al. 2014; Paris et al. 2014; Paris et al. 2013). In addition, a detailed study was provided on how to formulate a phenol formaldehyde adhesive tagged with iodine, such that it yielded sufficient x-ray absorption contrast (Paris et al. 2014). The conceptual findings from that study of how to generate necessary absorption contrast, and ensure tag molecules do not migrate independently from adhesive polymers during bonding and cure, were applied here to two additional adhesive types. Iodinated hybrid PVAc and pMDI adhesives were prepared because they would offer significantly different penetration, cure and mechanical performance characteristics from the IPF system. These modified adhesives will undoubtedly have different properties than their control, untagged forms. However, the broader project goal was to develop three adhesive systems which met the following criteria: (1) formed bonds which could be mechanically tested, (2) could be imaged with micro XCT and segmented from wood cell walls, and (3) had unique flow and mechanical properties from each other to offer variable datasets for the development and

validation of a model to relate wood adhesive penetration with composite joint performance (Kamke et al. 2014; Muszynski et al. 2014; Nairn et al. 2014; Paris et al. 2014; Paris et al. 2013; Schwarzkopf et al. 2014).

4.4.1 Tag efficacy and adhesive X-ray attenuation

Directly synthesizing emulsified PVAc polymers to contain a high iodine concentration was undesired. Cao (2010) had previously demonstrated compatible hybrid adhesive with various PF:PVAc ratios. A 50:50 mixture of the IPF and PVAc system was prepared as it offered high concentration of iodine and yet maintained flow and mechanical properties different from the pure IPF system. It was observed that upon mixing the two systems, the viscosity raised much higher than both pure systems, even at the reduced solids content (25 %). Additionally, the resulting hybrid adhesive had poor dry-out resistance, and thus needed to be bonded within several minutes of mixing. This behavior was different than previously observed (Cao 2010), but was believed to be due to large pH differences between the pure systems or polymer entanglements, as IPF had a very high molecular weight (Cao 2010; Paris et al. 2014). In spite of these odd liquid-state properties, cured samples of the hybrid PVAc system showed excellent film-formation and coalescence, with no evidence of phase separation or polymer incompatibility.

The IpMDI adhesive was prepared by reacting a sample of a commercial pMDI with 2,4,6 triiodophenol. Isocyanate groups readily react with phenol molecules to form urethane linkages (Frazier 2003), and with triiodophenol three iodine atoms could be attached for each displaced isocyanate. In this case, the addition of 24 wt% iodine reduced the isocyanate content from 31 to 20 %, which is still well above that for

commercial polyurethane wood adhesives, so adequate bond performance was still to be expected (Hosen 2010; Ren 2010). Theoretically, only 10% of the initial NCO groups were converted to the modified urethane structures; however, as the liquid resin mass increased, the final NCO content was a lower percentage of the total liquid adhesive mass. Furthermore, the liquid adhesive in this case contained THF as a delivery solvent for the triiodophenol and pMDI polymers, as well as to promote a random and homogeneous distribution of the modified polymers in the presence of the untagged MDI molecules. Early attempts to remove THF from the liquid adhesive caused sharp increases in the modified system viscosity, likely because the remaining isocyanate molecules could further react with the modified urethanes (Frazier 2003). It was expected that the THF would diffuse away during the bonding process, where under bond-consolidation pressure, the viscosity increases would not be an issue. The presence of THF likely had a large impact on how the modified adhesive penetrated and bonded relative to conventional pMDI adhesives, but that was not a concern in the present project where the model development was the main focus (Kamke et al. 2014; Muszynski et al. 2014; Nairn et al. 2014).

It was vital to ensure the iodine tags remained uniformly associated with the modified adhesive polymers throughout bonding and cure. Figure 4-1 shows paired images of the same specimen surfaces for SYP samples boned with the hybrid PVAc and IpMDI adhesives, acquired with FM and EDS elemental analysis. In both FM images (Figure 4-1a and b), the cell walls appear light blue, and embedding epoxy in the cell lumens appears darker blue. The adhesive in both cases is dark reddish-brown.

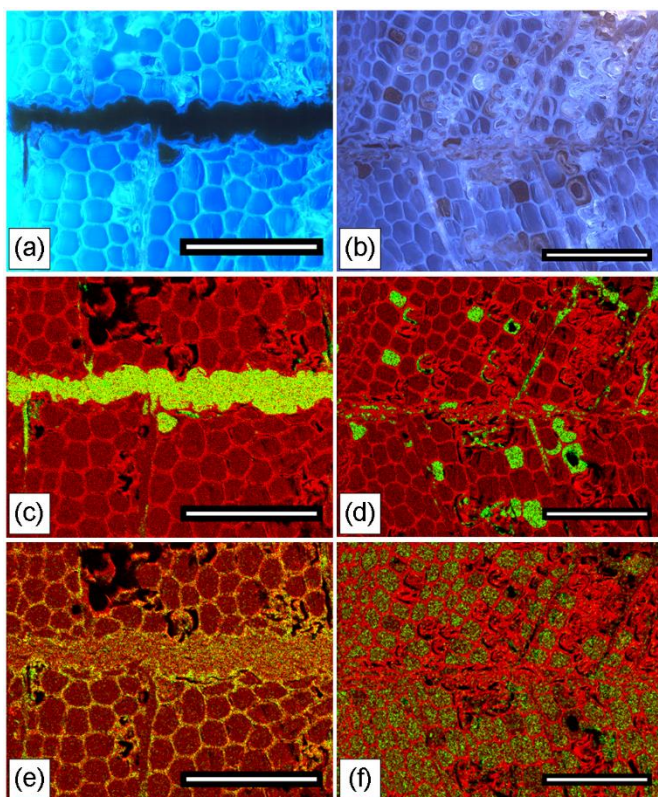


Figure 4-1 Hybrid PVAc (a, c, e) and IpMDI (b, d, f) bondlines in wood paired by FM (a - b) and EDS (c - f) images; adhesive appears dark in FM images; EDS elemental signal for oxygen shown in red, element of interest in green (c & d – iodine, e – sodium, and f – chlorine); scale bars = 200 μ m

Directly comparing images 4-1a to c, and 4-1b to d, it is clear that the iodine tags appear uniformly distributed in the same locations as the adhesive in the FM images.

Furthermore, there is no evidence of phase separation between the IPF and PVAc polymers in either image 4-1a or c. In Figure 4-1e it is clear that sodium migrated away from the bond, and moved freely through the wood structure. This was previously observed for the pure IPF adhesive (Paris et al. 2014); although, the previous research revealed more of the sodium remained in the bondline than observed here. Perhaps the hybrid system, which had higher water content, caused the sodium hydroxide ions in the

PF catalyst to more strongly disassociate in the presence of the more acidic PVAc polymers.

The contrast in the IpMDI FM image (Figure 4-1b) is not as great as for the hybrid PVAc system; yet, the iodine signal still appears uniformly distributed in the darkest adhesive locations. The lower contrast, in the IpMDI image is due to heterogeneous and incomplete epoxy embedding; the brightest locations in the FM image are damaged cell wall material which folded into cell lumens during microtoming. This is evident by comparing the chlorine signal (Fig 4-1f) with the FM image (Fig 4-1b); there was no chlorine detected in these spots, and the oxygen signal was high.

Modified and control adhesive solids content, powder density and iodine content are provided in Table 4-1. The iodine content measured with NAA is compared to a theoretical value calculated for each cured adhesive based on the known formulation components and solids content. The IpMDI solids value was higher than the expected value of 69% based on the initial amount of THF in the liquid resin, and the solids content of neat pMDI. Perhaps some residual THF did not diffuse from the samples as they were being cured, or some of the initial 27 wt% THF evaporated during the resin formulation (24 h, 50°C, under low flowing N₂).

Table 4-1 Average cured adhesive solids content, powder density, and iodine content; n = 3, standard deviation in parentheses

Adhesive	Solids [wt%]	Powder density [g/cm ³]	Cured I content [wt% I]	
			Calculated	Measured
Control PF	43.2 (1.3)	1.43 (0.06)	-	-
IPF	44.1 (0.9)	2.24 (0.06)	41.1	39.5 (0.2)
Neat pMDI	92.5 (0.1)	1.18 (0.09)	-	-
IpMDI	78.3 (0.1)	1.41 (0.06)	22.0	24.0 (0.6)
Neat PVAc	53.7 (0.1)	1.24 (0.03)	-	-
Hybrid IPF/PVAc	24.1 (0.5)	1.59 (0.09)	21.3	23.9 (0.3)

Cured powder density increased for all modified resins compared to controls, and IPF had significantly greater wt% iodine compared to IpMDI and the hybrid PVAc, which were approximately the same.

The linear x-ray attenuation coefficient for each adhesive can be estimated based on density and molecular structure over a broad range of possible XCT photon energies (Henke et al. 1993; Paris et al. 2014). These theorized structures and attenuation estimates are provided in Figure 4-2. The structure for cellobiose is provided elsewhere and used here as an analog for the wood cell wall. The IPF structure has been refined from that which was previously presented (Paris et al. 2014). Dimethylene ether bridges tend to release formaldehyde upon cure and revert to the more stable methylene monomer linkage (Figure 4-2a) (Park et al. 2002). This change did not have a significant impact on the calculated IPF attenuation behavior. Additionally, the theoretical repeat unit provided for the hybrid PVAc system is a stoichiometric combination of the IPF and PVAc dimer formulae based on the mixing ratio. Each phenol unit in the IPF adhesive contained the iodine tags, and therefore, every IPF molecule should have the same iodine

concentration, independent of molecular weight. For IpMDI and the hybrid PVAc systems this was not the case. In both of these systems, the tag distribution depended on liquid resin mixing efficiency, and any phase separation effects that could have occurred during bonding. However, there was no evidence of inhomogeneity in these adhesives seen in either the NAA or EDS results.

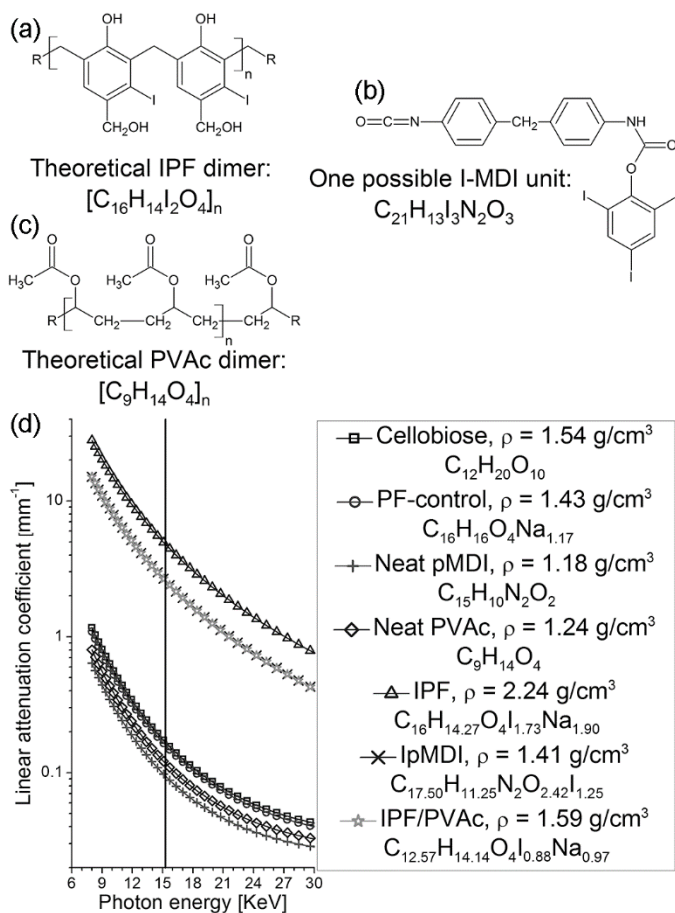


Figure 4-2 (a - c) theoretical dimer repeat units for each modified adhesive system, and (d) calculated x-ray attenuation coefficients for each cured adhesive; the legend provides the specific molecular formula and density (ρ) values used in the calculation; the vertical line at 15.3 KeV indicates the XCT scan energy

It is readily apparent that there is not a great difference between the attenuation coefficient traces for any of the control resins compared with cellobiose over this range of photon energy. IPF clearly has the greatest attenuation behavior, which is understandable as it had the greatest iodine content and density (Table 4-1). However, both the hybrid PVAc and IpMDI attenuation traces are at least an order of magnitude greater than cellobiose, and are nearly indistinguishable from each other. This is not surprising as they both have similar density and iodine content. At the indicated scan energy, 15.3 KeV, the three modified adhesives were predicted to offer sufficient x-ray absorption contrast to the surrounding wood cell walls. While the coefficient traces appear to maintain reasonable separation to still higher scan energy, the cellobiose attenuation becomes exceedingly small, indicating the wood material would be almost transparent to the harder x-rays. With the overall goal to segment three materials, air, wood and adhesive, higher beam energy would force greater overlap between the air and wood signals on a fixed gray-scale range (i.e. 2^8 distinct gray levels).

4.4.2 Adhesive absorption contrast

Figures 4-3, 4-5 and 4-6 show reconstructed sub-volumes, as well as their corresponding gray-scale histograms and threshold values, for specimens bonded with IPF, IpMDI, and the hybrid PVAc adhesives, respectively. These particular specimens were chosen as they show distinctly different gray-scale histograms, and thus threshold values, within the same adhesive type. Two different specimens, but same adhesive, are shown in each figure. The variability between each image pair is thus due to differences in wood anatomy. Each figure depicts a solid, gray-scale, sub-volume; the darkest regions are air

and the lightest regions are adhesive. The mid-range gray values are cell walls. The trimmed histograms show the distribution of the gray values, denoted as ϵ , across the approximate 0.5 – 0.8 billion voxels in each sub-volume. The 1st and 5-point, moving-average 2nd derivatives of the histogram, ϵ' and ϵ'' , respectively, are also plotted, as these values were used to quantitatively determine the threshold levels indicated by the vertical lines. Three threshold levels were used when adhesive was detected in cell walls.

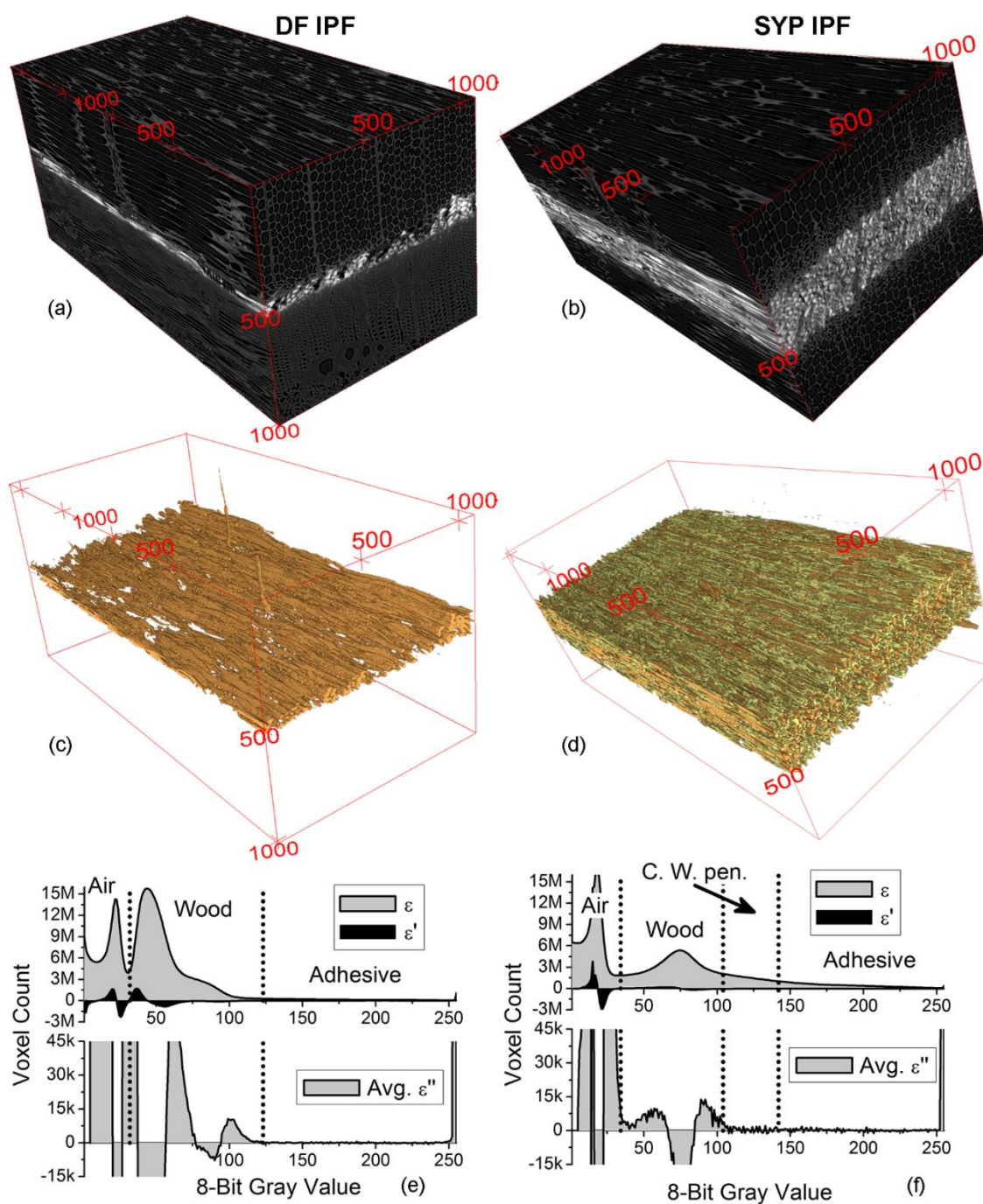


Figure 4-3 IPF bonded wood shown as XCT gray-scale sub-volumes (a - b), segmented adhesive (c - d), and "trimmed" 8-bit gray-scale histograms (top - gray value and 1st derivative, bottom -average 2nd derivative); species (Left - DF, right - SYP); sub-volume bounding box dimensions in μm

In Figure 4-3, the DF specimen contains earlywood on one side of the bondline and latewood on the other, whereas the SYP specimen has earlywood on both sides. In fact, the initial laminates for the SYP specimens were carefully controlled to only have earlywood at the interface. Though the spread rate and lamination pressure were the same for both species, the SYP specimen shows a far greater amount of adhesive in the bondline region. The adhesive, in the DF specimen, readily flowed into the large earlywood cells, but not into the small diameter, latewood cells. Perhaps the excess adhesive flowed laterally, to more easily penetrated regions of the bondline, outside of this particular field-of-view. It is also apparent, that the SYP bondline is highly crushed, indicating the thin-walled earlywood cells collapsed under the consolidation pressure. The presence of the denser latewood regions, must have prevented this collapse in the DF specimen. The greater amount of adhesive and more air volume in the SYP IPF specimen is also evident by the relative size of the material peaks in the histograms. The air peak in the DF histogram is shorter than in the SYP specimen, and the opposite is true for the wood peak. Additionally, the wood peaks appear to be centered at different gray values in each histogram (~ 40 in DF, and 75 in SYP); however, this is an artifact caused by phase-contrast effects at the cell wall edges.

The shoulder to the right of the DF wood peak is a bright phase-contrast effect. Paired light/dark fringes appear at the interface between materials with different index of refraction (Betz et al. 2007; Cloetens et al. 1997; Gureyev et al. 2001; Mayo et al. 2003). Figure 4-4 shows an earlywood and latewood region on a slice from the DF IPF specimen in Figure 4-3a; the top images were collected after histogram normalization, and the

bottom after having been trimmed. The plots in 4b show the gray-scale value along the corresponding line segments in each image.

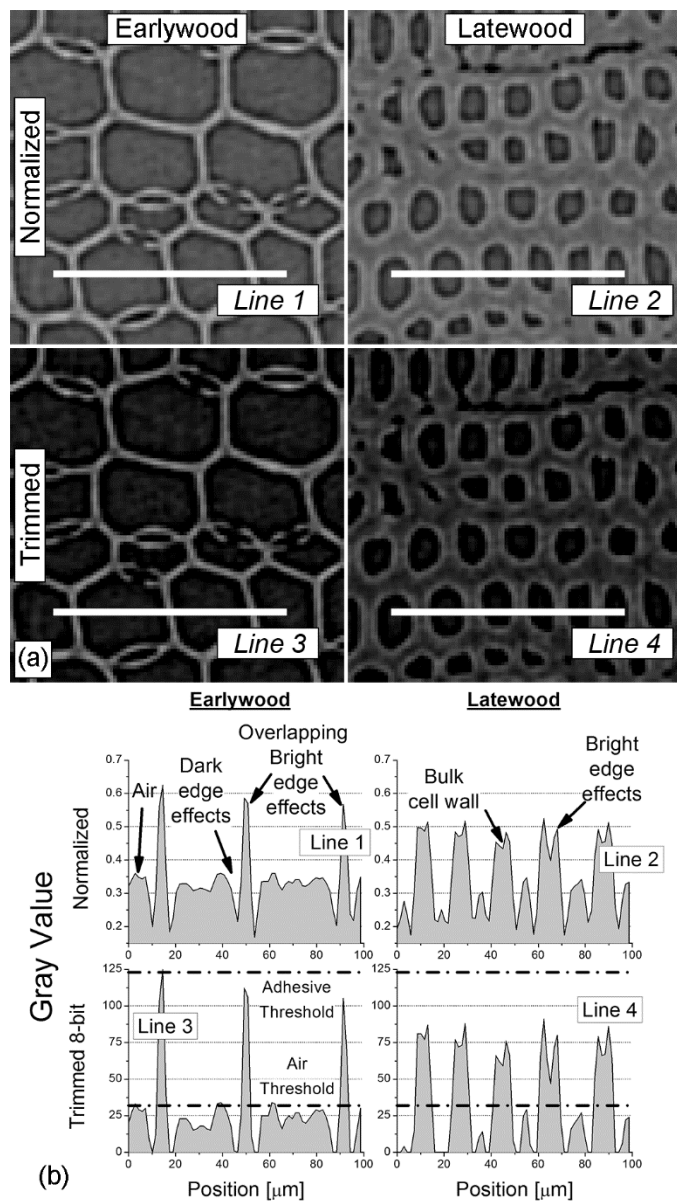


Figure 4-4 (a) Cross-section slice from DF IPF sub-volume in Figure 4-3 showing earlywood (left) and latewood (right), after histogram normalization (top) and trimming (bottom), and (b) gray value plots corresponding to the 100 μm line segments in (a)

The phase-contrast effects appear as an overly-dark ring of pixels just to the inside, or lumen side, and as an overly bright ring on the extreme edges, of a double cell wall. Histogram trimming forces the dark ring effects in the cell lumens to a zero gray value, and allows them to be included with the ‘air’ gray value, but the bright rings are still present on the cell edges. In earlywood regions these bright rings overlap across the entire thickness of the double cell wall. Latewood cell edges are much thicker, and so there are still a large number of voxels in the center of a double cell wall edge that do not show the phase-contrast effect. The lower gray value voxels, in the center of the cell edges, are hereafter referred to as bulk cell wall. Both sides of the SYP sub-volume in Figure 4-3b are earlywood, and so there is no discernable peak for bulk cell wall material in the corresponding histogram. The entire ‘wood’ peak in Figure 4-3f is comprised of over-lapping phase-contrast effects (gray value ~75). The ‘wood’ peak in the DF laminate, however, shows both bulk cell wall (tall peak at gray value ~40) and phase-contrast effects (right shoulder at gray value ~75). The IPF, IpMDI, and hybrid PVAc adhesives were formulated to exhibit reconstructed gray levels above both the bulk cell wall and the bright phase-contrast edge effects, for the reported experimental parameters. A preliminary IPF resin, containing only 12 wt% iodine, provided a low degree of absorption contrast to the bulk cell wall, but its gray level overlapped with the bright edge effects on earlywood cell walls (Paris et al. 2014).

The DF and SYP histograms in Figure 4-3 also differ to the right of the bulk cell wall/bright phase-contrast, compound ‘wood’ peak(s). The SYP histogram gradually decreases over the remaining gray levels (75 to 255), while the DF histogram flattens out at a near zero voxel count level for the remaining gray-scale range. This is because cell

wall penetration was detected in the SYP sample. The observed gradient of voxel gray levels is due to partial volume effects, which occur when two materials occupy the same pixel (Ketcham and Carlson 2001). The 1.45 μm per voxel-side spatial resolution is too coarse to differentiate adhesive and wood polymers inside the cell wall, but when both are present in the same voxel, the assigned gray value represents an average. The segmented image in Figure 4-3d shows both pure adhesive voxels (orange) and the voxels containing both adhesive and cell wall, which are collectively grouped as cell wall penetration (yellow). Similar cell wall penetration was not observed in the DF IPF specimen. This is not to say it did not occur, but rather was not detected based on the chosen threshold level criteria.

Lastly, it is also interesting to note the DF IPF gray-scale sub-volume shows 3 latewood resin canals (Figure 4-3a). The density and chemical nature of these natural resins are similar to that of the untagged adhesives, and thus they could not be separated from the cell walls due to lack of absorption contrast.

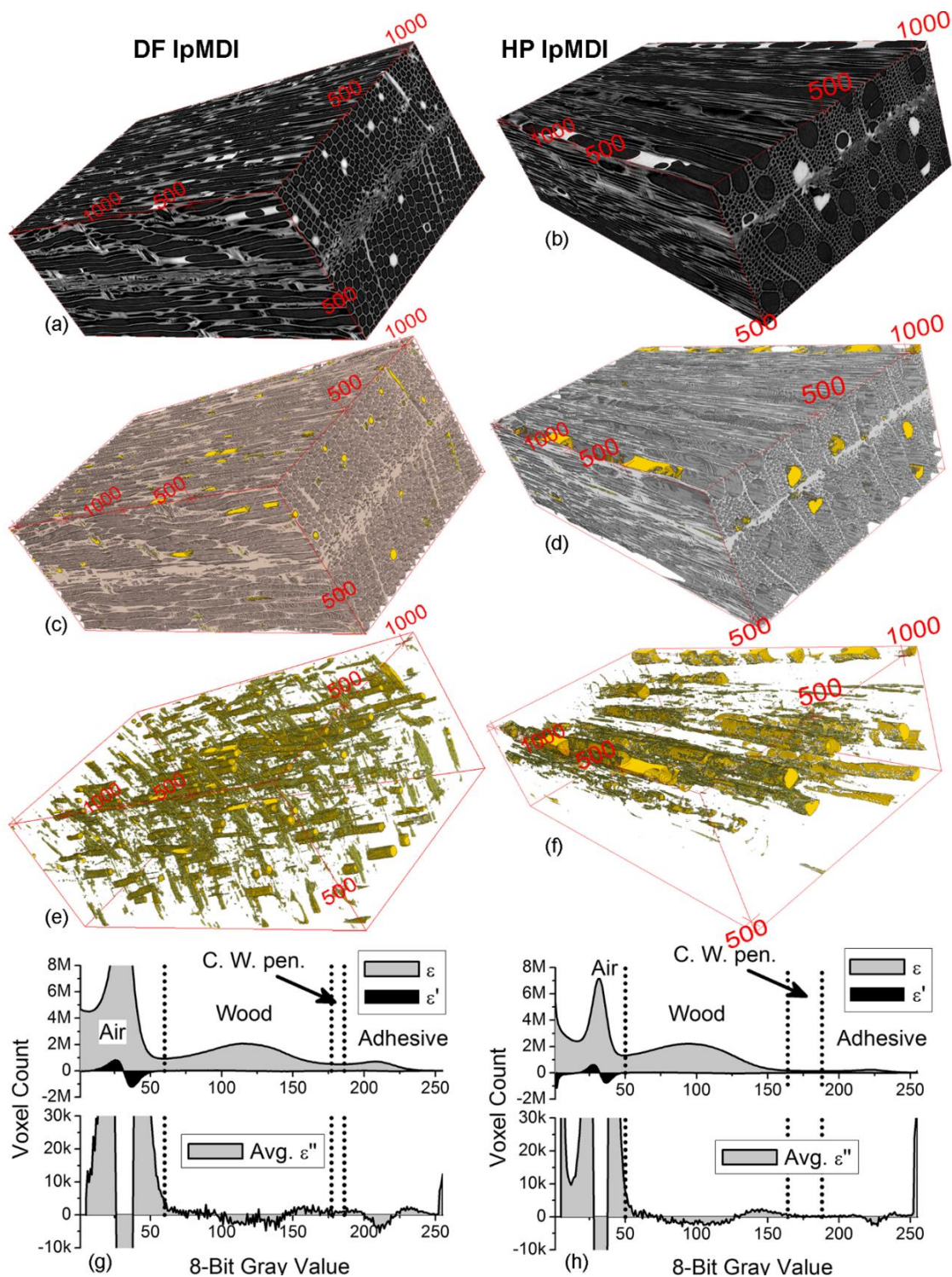


Figure 4-5 IpMDI bonded wood shown as XCT gray-scale sub-volumes (a - b), segmented wood and adhesive (c - d), segmented adhesive (e - f), and "trimmed" 8-bit gray-scale histograms (top - gray value and 1st derivative, bottom -average 2nd derivative); species (Left - DF, right - HP); sub-volume bounding box dimensions in μm

The IpMDI bondlines in Figure 4-5 are DF and HP, and neither contain latewood zones or have extensive crushing at the interface between the two lamina. IpMDI had lower density, lower iodine content, and consequently, lower predicted attenuation coefficient compared to IPF (Table 4-1 & Figure 4-2d). The gray-scale histograms show the three material peaks evenly distributed across the 256 gray levels. Increasing the relative difference in absorption contrast between the cell wall and adhesive compromises relative differences between cell wall and air, on a fixed gray-scale range. Phase-contrast effects are also observed in the IpMDI specimens. The breadth of the central peak in each histogram is the result of limited spatial resolution and partial volume effects where some air, cell wall, and phase contrast effects are all present in individual voxels, which causes a gradient of gray-scale values. The partial volume effect is also evident in regions where adhesive has penetrated the cell wall. Nevertheless, segmentation of pure adhesive (yellow) and IpMDI in the cell walls (green) was achieved (Figure 4-5e and f) when the moving-average 2nd derivative fell below the 0.05 % criteria.

A segmented view of the wood structure and pure adhesive is shown in Figures 4-5c and d. It appears as if there is no adhesive connecting the wood on either side of the bondline. If this were truly the case, the two halves would not remain bonded together. These IpMDI joints were capable of transferring stresses across the bondline. Therefore, adhesive must have been present between the two lamina, even if it was not detected. One possible explanation is that the IpMDI coated the cells at this interface, and the coating thickness is below the 1.45 μm per voxel XCT resolution. If this was the case, perhaps the criteria for differentiating cell wall infiltration was too strict at 0.05 %.

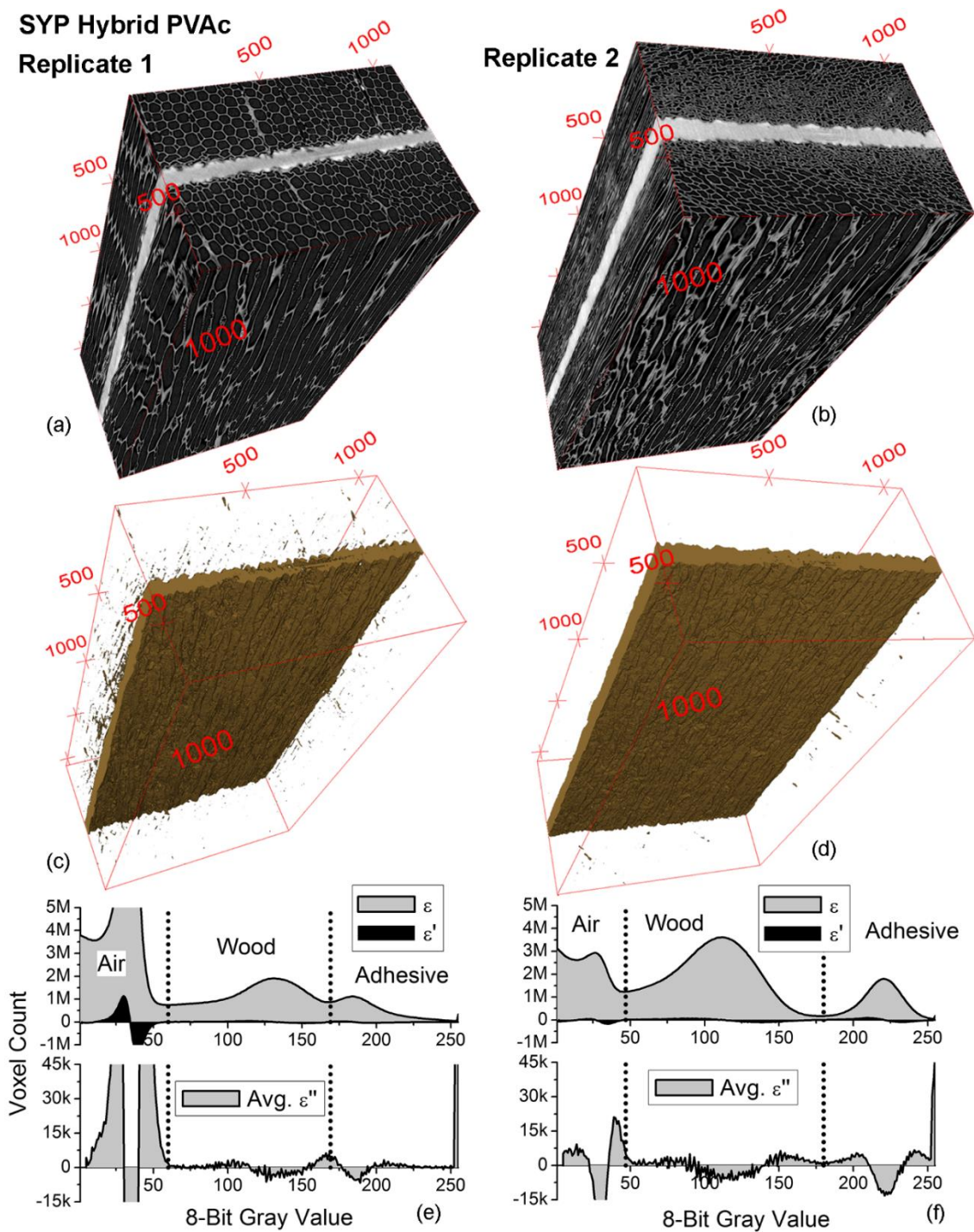


Figure 4-6 Hybrid IPF/PVAc bonded SYP XCT gray-scale sub-volumes (a - b), segmented adhesive (c - d), and "trimmed" 8-bit gray-scale histograms (e - f; top - histogram and 1st δ , bottom - true and 5X moving average 2nd δ); sub-volume bounding box dimensions in μm

The hybrid PVAc adhesive was predicted to exhibit similar attenuation behavior as IpMDI (Figure 4-2d). Figure 4-6 shows two replicate SYP composite sub-volumes bonded with this hybrid system. The corresponding histograms show the material peaks are fairly evenly distributed along the 256 gray-value range. However, the hybrid PVAc histograms are considerably different from each other, even though they are the same wood species, adhesive, and both show only earlywood. The difference is due to the high degree of crushing near the wood/adhesive interfaces in replicate 2. The histogram for this specimen shows a shorter air peak and broader wood peak, centered at approximately 110, compared to the same wood peak in replicate 1, centered at approximately 130. The crushing forced more wood cell material into the sub-volume at the expense of air-space in the crushed cell lumens. Many of the collapsed cell walls near the bondline were in direct contact with each other. This effectively reduced the phase shift responsible for the bright edge effects seen in the other earlywood regions. One notable impact of this reduced edge-brightening, phase-contrast effect, is there was less overlap between the wood and adhesive material peaks in replicate 2 than replicate 1; which consequently resulted in less noise in the segmented adhesive phase. The bright edge effects in replicate 1 caused several of the cells, far from the true adhesive interface, to be included in the adhesive segmentation due to the material peak overlap (Figure 4-6c). The overlap and threshold also appeared to cut off a portion of the adhesive in the center of the pure adhesive layer. Why the middle of the adhesive layer had a lower gray value than the edges is not entirely clear. Perhaps this is an indication of phase separation between the IPF and PVAc polymers; however, there was no evidence of this in neat hybrid PVAc films or in either the FM or EDS composite bondline images. This could also be the

result of phase-contrast effects between wood and adhesive, which were not observed in the other resins. Other samples showed phase contrast effects between wood and air, but not between wood and adhesive.

4.4.3 Quantitative Phase Retrieval

The adhesives, experimental parameters and segmentation criteria used in this work were able to tolerate the observed phase-contrast effects. Similar phase-contrast edge effects have been observed in several other XCT analyses of wood. One author noted that tyloses in oak appeared to have a greater gray-scale value than thick cell walls, and argued that this was not likely due to chemical or density variations in the anatomical features (Mannes et al. 2010). This is analogous to the gray-scale differences between earlywood and latewood. In another XCT study of medium density fiberboard, air inside collapsed wood fibers had a darker gray value than larger pockets of air between fiber bundles (Standfest et al. 2010). This was most likely due to dark phase-contrast fringes overlapping in the smaller voids; however, histogram trimming can alleviate these effects (Figure 4-4). It is also known that phase-contrast effects become stronger with larger specimen-to-detector distances (Betz et al. 2007; Cloetens et al. 2002; Cloetens et al. 1997). Modzel observed this influence in XCT scans of wood-adhesive bondline specimens, and concluded that decreasing specimen-to-detector distance resulted in a better signal-to-noise ratio (Modzel 2009). The present authors agree with this conclusion, when the data is reconstructed with conventional filtered back projection algorithms, which exploit absorption contrast effects. However, if quantitative phase retrieval algorithms are used, which capture and utilize the Fresnel phase shift effects,

larger distances may be tolerated and even preferred. Figure 4-7 shows three views of the same location in a SYP IpMDI composite, scanned and reconstructed different ways. The specimen was scanned twice at different specimen-to-scintillator distances (8 mm and 30 mm), and reconstructed with a conventional FBP algorithm and an experimental, phase-contrast QPR algorithm (Weitkamp et al. 2011).

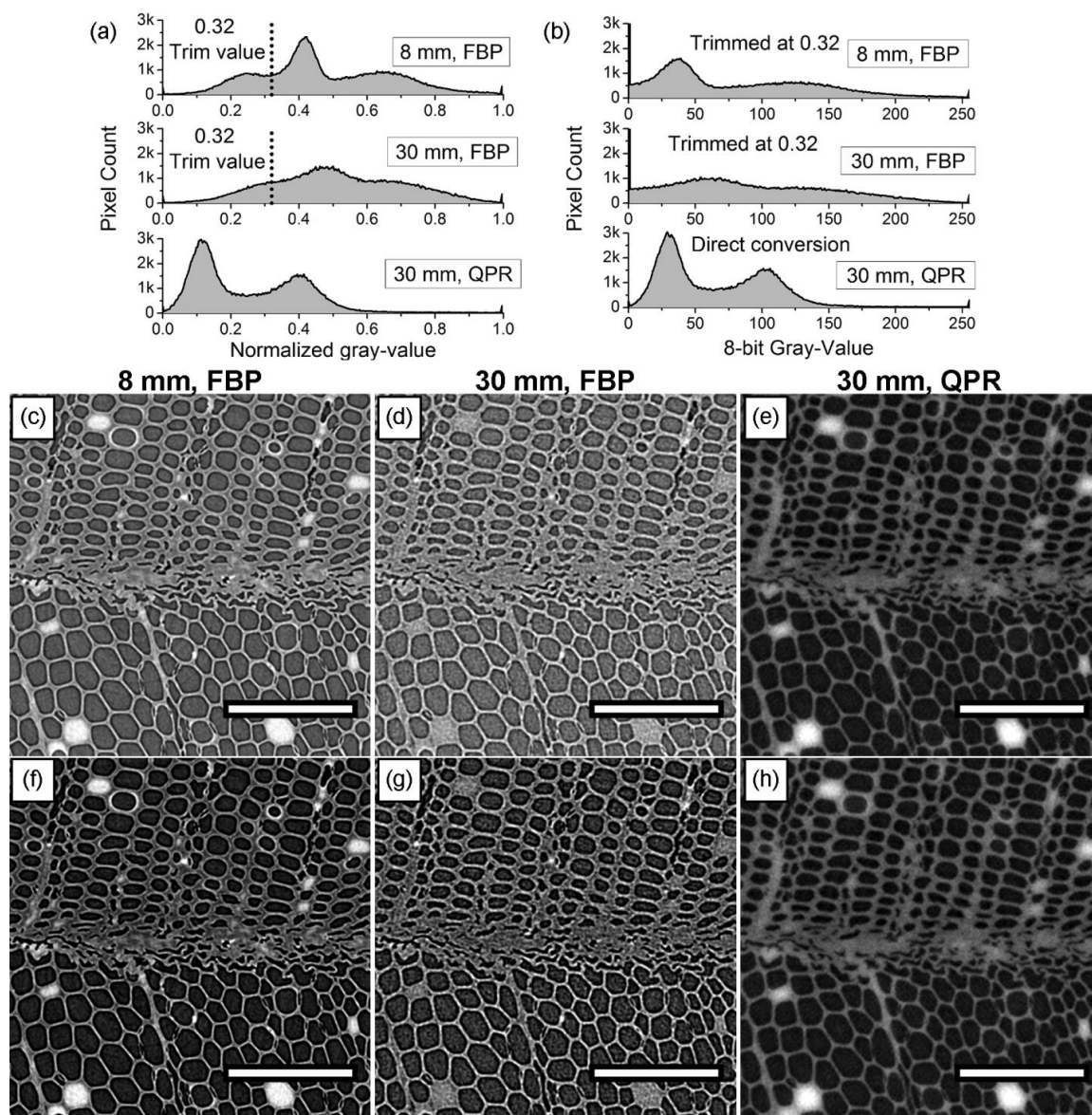


Figure 4-7 Gray-scale histograms and corresponding SYP IpMDI composite XCT slice (same specimen view) scanned at 8 or 30 mm specimen-to-scintillator distances, and reconstructed with an FBP or QPR algorithm; histograms: (a) normalized, and (b) trimmed at the specified value and converted to 8-bit data; images: (c - e) normalized, and (f - h) 8-bit; scale bars = 200 μm

The normalized histograms for the two FBP reconstructions show three peaks, a tall central peak and two, almost balanced lower peaks, or shoulders, on either side. The material covering the greatest area, or pixel count, is air in the cell lumens, which is the

tall central peak. The next most abundant material is the cell wall, and this corresponds to the lighter-gray (higher attenuation) peak or shoulder to the right. However, every double cell wall has two zones of dark phase-contrast effects in the lumens on either side of the edge. These dark zones add up, and form the left peak or shoulder, darker than air. This specimen contains only earlywood, and so all the cells have thin walls. This causes the bright edge effects to overlap, and very little of the true (bulk) wood attenuation signal is observed. Therefore, the histogram side peaks, or shoulders, appear somewhat balanced. The histogram for the 30 mm scan in Figure 4-7a clearly shows greater peak overlap than the 8 mm specimen. This is because the effect of the x-ray phase-shift is stronger with greater free-space propagation after traversing through the specimen (Betz et al. 2007; Cloetens et al. 1997). With the FBP absorption contrast algorithm, the phase contrast effect can be recognized, and trimmed away. However, differentiating between the wood and air is far more difficult. On the other hand, the phase retrieval algorithm uses the phase-contrast effect in the original data reconstruction. Notice how the phase effects are eliminated in the QPR histograms, and only two peaks are observed. The 8 mm, FBP images look less noisy and show good gray-contrast between air, wood and adhesive, compared to the 30 mm, FBP images. However, simply reconstructing the 30 mm data with the QPR algorithm recaptures the material gray-scale contrast. The 30 mm, QPR images appear defocused compared to the 8 mm, FBP images, but the histogram peaks (Figure 4-7b) are narrower and show less overlap. Additionally, these images have not been filtered, and median filtering would help with image sharpness and clarity while preserving material edges (Mayo et al. 2010; Paris et al. 2014).

Phase retrieval algorithms are still relatively new, compared to conventional absorption contrast reconstruction algorithms, and are still being developed for various soft-tissue XCT applications (Cloetens et al. 2002; De Witte et al. 2009; Paganin et al. 2002; Peele and Nugent 2008; Weitkamp et al. 2011). Some studies have already demonstrated their effectiveness at generating contrast in various wood and fiber tomography analyses (Betz et al. 2007; Mayo et al. 2003; Mayo et al. 2010). One recent study was even able to segment air, wood and a low density, un-tagged wax in wood lumens from XCT data reconstructed with a phase retrieval algorithm (De Witte et al. 2009; Scholz et al. 2010). The QPR data shown in Figure 4-7 was only a preliminary attempt to utilize this algorithm for wood-adhesive XCT data, and the IpMDI adhesive was intentionally designed for enhanced absorption contrast to wood. However, perhaps with further algorithm development, and a greater understanding of the experimental trade-offs between absorption and phase-contrast phenomena, phase retrieval algorithms may allow for quantitative segmentation of un-tagged wood-adhesive XCT data.

4.5 Conclusions

In a previous study the authors introduced necessary considerations for tagging a phenol formaldehyde adhesive such that it yielded sufficient absorption contrast for quantitative material segmentation in micro x-ray computed tomography data. Here two other adhesive types, a polymeric diphenylmethane diisocyanate and a hybrid polyvinyl acetate, were tagged with iodine for similar x-ray imaging success. A combination of elemental mapping and fluorescent microscopy of wood-adhesive bondlines confirmed the tags were uniformly distributed in these adhesives; while theoretical attenuation

coefficients, calculated for each adhesive based on cured resin density and tag concentration, were used to help predict and explain observed absorption contrast. Quantitative segmentation was demonstrated with several examples of reconstructed bondlines, and their subsequent gray-scale histograms. However, it was observed that phase-contrast effects, commonly detected at material edges, have a significant impact on wood XCT data, as wood is full of cellular edges. Material attenuation differences and segmentation methods must tolerate these phase-contrast effects if XCT data are reconstructed with conventional absorption contrast algorithms. However, phase retrieval algorithms, which identify and eliminate phase-contrast effects, could potentially offer greater segmentation confidence, and perhaps even identify material contrast in untagged wood-adhesive bondlines.

4.6 Acknowledgements

Use of the Advanced Photon Source was supported by the U. S. Department of Energy, Office of Science, Office of Basic Energy Sciences, under Contract No. DE-AC02-06CH11357. Financial support was provided by the Wood-Based Composites Center, a National Science Foundation Industry/University Cooperative Research Center; project code A-04-KA.

4.7 References

ASTM D 5155 - 10 (2010) Standard test methods for polyurethane raw materials: Determination of the isocyanate content of aromatic isocyanates. ASTM International, West Conshohocken, PA.

ASTM B 5965 - 02 (2007) Standard test method for specific gravity of coating powders. ASTM International, West Conshohocken, PA.

Banhart, J. 2008: Introduction. In: Banhart, J., editor, *Advanced Tomographic Methods in Materials Research and Engineering*, Oxford, New York: Oxford University Press, 3-18.

Betz, O., Wegst, U., Weide, D., Heethoff, M., Helfen, L., Lee, W. K. and Cloetens, P. (2007) Imaging applications of synchrotron X-ray phase-contrast microtomography in biological morphology and biomaterials science. 1. General aspects of the technique and its advantages in the analysis of millimetre-sized arthropod structure. *J. Microsc.-Oxf.* 227, 1, 51-71.

Cao, Y. 2010: Characterization of PF/PVAc hybrid adhesive-wood interaction and its effect on wood strand composites performance. *Department of Civil and Environmental Engineering*, Washington State University, Pullman, WA.

Chen, H.-H., Chien, C.-C., Petibois, C., Wang, C.-L., Chu, Y. S., Lai, S.-F., Hua, T.-E., Chen, Y.-Y., Cai, X. and Kempson, I. M. (2011) Quantitative analysis of nanoparticle internalization in mammalian cells by high resolution X-ray microscopy. *Journal of Nanobiotechnology* 9, 1, 14.

Cloetens, P., Ludwig, W., Boller, E., Helfen, L., Salvo, L., Mache, R. and Schlenker, M. 2002: Quantitative phase contrast tomography using coherent synchrotron radiation. In: *Proc. SPIE*, 82-91.

Cloetens, P., Pateyron-Salomé, M., Buffière, J. Y., Peix, G., Baruchel, J., Peyrin, F. and Schlenker, M. (1997) Observation of microstructure and damage in materials by phase sensitive radiography and tomography. *Journal of Applied Physics* 81, 9, 5878-5886.

De Witte, Y., Boone, M., Vlassenbroeck, J., Dierick, M. and Van Hoorebeke, L. (2009) Bronnikov-aided correction for x-ray computed tomography. *J. Opt. Soc. Am. A-Opt. Image Sci. Vis.* 26, 4, 890-894.

Dowd, B. A., Campbell, G. H., Marr, R. B., Nagarkar, V. V., Tipnis, S. V., Axe, L. and Siddons, D. P. (1999) Developments in synchrotron x-ray computed microtomography at the National Synchrotron Light Source. 224-236.

Ellis, E. (2006) Solutions to the problem of substitution of ERL 4221 for vinyl cyclohexene dioxide in Spurr low viscosity embedding formulations. *Microscopy Today* 14, 4, 32-33.

Evans, P. D., Morrison, O., Senden, T. J., Vollmer, S., Roberts, R. J., Limaye, A., Arns, C. H., Averdunk, H., Lowe, A. and Knackstedt, M. A. (2010) Visualization and numerical analysis of adhesive distribution in particleboard using X-ray micro-computed tomography. *International Journal of Adhesion and Adhesives* 30, 8, 754-762.

Frazier, C. E. 2003: Isocyanate wood binders. In: Pizzi, A. and Mittal, K. L., editors, *Handbook of Adhesive Technology*, New York: Marcel Dekker, Inc.

Frazier, C. E. and Ni, J. W. (1998) On the occurrence of network interpenetration in the wood-isocyanate adhesive interphase. *International Journal of Adhesion and Adhesives* 18, 2, 81-87.

Graafsma, H. and Martin, T. 2008: Detectors for synchrotron tomography. In: Banhart, J., editor, *Advanced Tomographic Methods in Materials Research and Engineering*, Oxford: Oxford University Press, 277-302.

Gureyev, T. E., Mayo, S., Wilkins, S. W., Paganin, D. and Stevenson, A. W. (2001) Quantitative In-Line Phase-Contrast Imaging with Multienergy X Rays. *Physical Review Letters* 86, 25, 5827-5830.

Hass, P., Wittel, F., Mendoza, M., Herrmann, H. and Niemz, P. (2012) Adhesive penetration in beech wood: experiments. *Wood Science and Technology* 46, 1-3, 243 - 256.

Hass, P., Wittel, F. K., McDonald, S. A., Marone, F., Stampanoni, M., Herrmann, H. J. and Niemz, P. (2010) Pore space analysis of beech wood: The vessel network. *Holzforschung* 64, 5, 639-644.

Henke, B. L., Gullikson, E. M. and Davis, J. C. (1993) X-ray interactions - photoabsorption, scattering, transmission, and reflection at E=50-30,000 EV, Z=1-92. *Atom. Data Nucl. Data Tables* 54, 2, 181-342.

Hosen, J. 2010: Fundamental analysis of wood adhesion primers. *Wood Science and Forest Products*, Virginia Tech, Blacksburg, VA.

Hounsfield, G. N. (1973) Computed transverse axial scanning (tomography). *British Journal of Radiology* 46, 552, 1016-1022.

Jakes, J. E., Gleber, S.-C., Vogt, S., Hunt, C. G., Yelle, D. J., Grigsby, W. and Frihart, C. R. 2013: New synchrotron-based technique to map adhesive infiltration in wood cell walls. In: *Proceedings of the 36th Annual Meeting of the Adhesion Society*, Datona Beach, FL, USA, 3 p.

Kamke, F. A., Nairn, J. A., Muszynski, L., Paris, J. L., Schwarzkopf, M. and Xiao, X. (2014) Methodology for micro-mechanical analysis of an adhesive bond using micro computed x-ray tomography and numerical modeling. *Wood and Fiber Science* 46, 1.

Ketcham, R. A. and Carlson, W. D. (2001) Acquisition, optimization and interpretation of X-ray computed tomographic imagery: applications to the geosciences. *Computers & Geosciences* 27, 4, 381-400.

Kinney, J. H. and Nichols, M. C. (1992) X-ray tomographic microscopy (XTM) using synchrotron radiation. *Annu. Rev. Mater. Sci.* 22, 121-152.

Mannes, D., Marone, F., Lehmann, E., Stampanoni, M. and Niemz, P. (2010) Application areas of synchrotron radiation tomographic microscopy for wood research. *Wood Science and Technology* 44, 1, 67-84.

Mannes, D., Niemz, P. and Lehmann, E. (2009a) Tomographic investigations of wood from macroscopic to microscopic scale. *Wood Research* 54, 3, 33-44.

Mannes, D., Sonderegger, W., Hering, S., Lehmann, E. and Niemz, P. (2009b) Non-destructive determination and quantification of diffusion processes in wood by means of neutron imaging. *Holzforschung* 63, 5, 589-596.

Mayo, S., Davis, T., Gureyev, T., Miller, P., Paganin, D., Pogany, A., Stevenson, A. and Wilkins, S. (2003) X-ray phase-contrast microscopy and microtomography. *Optics Express* 11, 19, 2289-2302.

Mayo, S. C., Chen, F. and Evans, R. (2010) Micron-scale 3D imaging of wood and plant microstructure using high-resolution X-ray phase-contrast microtomography. *Journal of Structural Biology* 171, 2, 182-188.

Modzel, G. 2009: Computed X-ray analysis of wood-adhesive bonds. *Wood Science and Engineering*, Oregon State University, Corvallis, OR: 240.

Modzel, G., Kamke, F. A. and De Carlo, F. 2009: Investigation of PF adhesive penetration in wood by x-ray micro-tomography. In: Frihart, C. R., Hunt, C. G. and Moon, R. J., editors, *Proceedings of the International Conference on Wood Adhesives 2009*, Lake Tahoe, NV, USA: Forest Products Society, 5 p.

Modzel, G., Kamke, F. A. and De Carlo, F. (2011) Comparative analysis of a wood-adhesive bondline. *Wood Science and Technology* 45, 1, 147-158.

Muszyński, L. (2009) Imaging wood plastic composites (WPCs): X-ray computed tomography, A few promising techniques, and why we should pay attention. *BioResources* 4, 3, 1210-1221.

Muszynski, L., Kamke, F. A., Nairn, J. A., Schwarzkopf, M. and Paris, J. L. 2014: Integrated method for multi-scale/multi-modal investigation of micro-mechanical wood-adhesive interaction. In: Frihart, C. R., Hunt, C. G. and Yan, N., editors, *Proceedings of the International Conference on Wood Adhesives 2013*, Toronto, Ontario, CAN: Forest Products Society, 16 p.

Nairn, J. A., Kamke, F. A., Muszynski, L., Paris, J. and Schwarzkopf, M. 2014: Direct 3D Numerical Simulation of stresses and strains in wood adhesive bondlines based on the actual specimen anatomy from x-ray tomography data. In: Frihart, C. R., Hunt, C. G. and Yan, N., editors, *Proceedings of the International Conference on Wood Adhesives 2013*, Toronto, Ontario, CAN: Forest Products Society, 11 p.

Paganin, D., Mayo, S. C., Gureyev, T. E., Miller, P. R. and Wilkins, S. W. (2002) Simultaneous phase and amplitude extraction from a single defocused image of a homogeneous object. *Journal of Microscopy* 206, 1, 33-40.

Paris, J., Kamke, F., Mbachu, R. and Gibson, S. (2014) Phenol formaldehyde adhesives formulated for advanced X-ray imaging in wood-composite bondlines. *Journal of Materials Science* 49, 2, 580-591.

Paris, J. L., Kamke, F., Nairn, J. A., Schwarzkopf, M. and Muszynski, L. 2013: Wood-adhesive penetration: non-destructive, 3D visualization and quantification. In: Frihart, C. R., Hunt, C. G. and Yan, N., editors, *Proceedings of the International Conference on Wood Adhesives 2013*, Toronto, Ontario, CAN: Forest Products Society, 13 p.

Park, B.-D., Riedl, B., Yoon Soo, K. and So, W. T. (2002) Effect of synthesis parameters on thermal behavior of phenol-formaldehyde resol resin. *Journal of Applied Polymer Science* 83, 7, 1415-1424.

Peele, A. G. and Nugent, K. A. 2008: Phase-contrast and holographic tomography. In: Banhart, J., editor, *Advanced Tomographic Methods in Materials Research and Engineering*, Oxford, New York: Oxford University Press, 161-180.

Rasband, W. S. 1997 - 2012: ImageJ. In: *U. S. National Institutes of Health*, <http://imagej.nih.gov/ij/>, Bethesda, Maryland, USA.

Ren, D. 2010: Moisture-cure polyurethane wood adhesives: wood/adhesive interactions and weather durability. *Macromolecular Science and Engineering*, Virginia Tech, Blacksburg, VA.

Schindelin, J., Arganda-Carreras, I., Frise, E., Kaynig, V., Longair, M., Pietzsch, T., Preibisch, S., Rueden, C., Saalfeld, S. and Schmid, B. (2012) Fiji: an open-source platform for biological-image analysis. *Nature Methods* 9, 7, 676-682.

Scholz, G., Zauer, M., Van den Bulcke, J., Van Loo, D., Pfriem, A., Van Acker, J. and Militz, H. (2010) Investigation on wax-impregnated wood. Part 2: Study of void spaces filled with air by He pycnometry, Hg intrusion porosimetry, and 3D X-ray imaging. *Holzforschung* 64, 5, 587-593.

Schwarzkopf, M., Muszynski, L. and Nairn, J. 2014: Stereoscopic optical method for the assessment of load transfer patterns across the adhesive bond interphase. In: Frihart, C. R., Hunt, C. G. and Yan, N., editors, *Proceedings of the International Conference on Wood Adhesives 2013*, Toronto, Ontario, CAN: Forest Products Society, 12 p.

Spurr, A. R. (1969) A low-viscosity epoxy resin embedding medium for electron microscopy. *Journal of ultrastructure research* 26, 31-43.

Standfest, G., Kranzer, S., Petutschnigg, A. and Dunky, M. (2010) Determination of the microstructure of an adhesive-bonded medium density fiberboard (MDF) using 3-D sub-micrometer computer tomography. *Journal of Adhesion Science and Technology* 24, 8-10, 1501-1514.

Standfest, G., Kutnar, A., Plank, B., Petutschnigg, A., Kamke, F. and Dunky, M. (2012) Microstructure of viscoelastic thermal compressed (VTC) wood using computed microtomography. *Wood Science and Technology*.

Steppe, K., Cnudde, V., Girard, C., Lemeur, R., Cnudde, J. P. and Jacobs, P. (2004) Use of X-ray computed microtomography for non-invasive determination of wood anatomical characteristics. *Journal of Structural Biology* 148, 1, 11-21.

Stockel, F., Konnerth, J., Moser, J., Kantner, W. and Gindl-Altmutter, W. (2012) Micromechanical properties of the interphase in pMDI and UF bond lines. *Wood Science and Technology* 46, 4, 611-620.

Trtik, P., Dual, J., Keunecke, D., Mannes, D., Niemz, P., Stähli, P., Kaestner, A., Groso, A. and Stampanoni, M. (2007) 3D imaging of microstructure of spruce wood. *Journal of Structural Biology* 159, 1, 46-55.

Walther, T. and Thoemen, H. (2009) Synchrotron X-ray microtomography and 3D image analysis of medium density fiberboard (MDF). *Holzforschung* 63, 5, 581-587.

Weitkamp, T., Haas, D., Wegrzynek, D. and Rack, A. (2011) ANKAphase: software for single-distance phase retrieval from inline X-ray phase-contrast radiographs. *Journal of Synchrotron Radiation* 18, 617-629.

Wildenschild, D., Hopmans, J. W., Vaz, C. M. P., Rivers, M. L., Rikard, D. and Christensen, B. S. B. (2002) Using X-ray computed tomography in hydrology: systems, resolutions, and limitations. *Journal of Hydrology* 267, 3-4, 285-297.

Wu, X., Liu, H. and Yan, A. (2008) Phase-contrast X-ray tomography: Contrast mechanism and roles of phase retrieval. *European Journal of Radiology* 68, 3, Supplement 1, S8-S12.

CHAPTER 5. WOOD-ADHESIVE PENETRATION: NON-
DESTRUCTIVE, 3D VISUALIZATION AND
QUANTIFICATION

Jesse L. Paris, Frederick A. Kamke, John Nairn, Lech Muszyński, and Matthew

Schwarzkopf

Proceedings of the *International Conference on Wood Adhesives 2013*

Forest Products Society

Toronto, Ontario, CAN

Wood-Adhesive Penetration:
non-destructive, 3D visualization and quantification

Jesse L. Paris^{*}, Frederick A. Kamke[†], John Nairn, Lech Muszyński and Matthew
Schwarzkopf

Department of Wood Science & Engineering, Wood-Based Composites Center, Oregon
State University, 119 Richardson Hall, Corvallis, OR 97331, USA

^{*} Corresponding Author. Tel.: +804 338 4353; Fax +542 737 3385

E-mail address: Jesse.Paris@OregonState.edu (J. L. Paris)

[†] Secondary Corresponding Author. Tel.: +541 737 8422; Fax +542 737 3385

E-mail address: Fred.Kamke@OregonState.edu (F. A. Kamke)

5.1 Abstract

Wood-composite structural performance is directly influenced by adhesive penetration away from the joint interface and into the porous wood structure. Shallow penetration may result in poor stress-transfer and reduced dimensional stability; while over-penetration can yield a starved bondline. Furthermore, penetration depth is highly dependent on multiple adhesive and wood characteristics, as well as material processing and bonding conditions. Thus, the complex relationship between adhesive penetration and composite joint performance has been difficult to define quantitatively. This is, in part, because adhesive penetration is often observed with various 2D microscopy techniques, which are destructive to bonded specimens and fail to define the full volumetric adhesive distribution in composite joints. X-ray computed tomography (XCT), however, is a non-destructive technique capable of providing micro-scale, 3D bondline and adhesive distribution data.

In this work, internal, 3D wood anatomy and adhesive penetration XCT data were collected for multiple bonded specimens prepared from three wood species: Douglas-fir (*Pseudotsuga menziesii*), loblolly pine (*Pinus taeda*) and a hybrid poplar (*Populus deltoides x Populus trichocarpa*), and three common wood adhesive types: phenol formaldehyde, polymeric diphenylmethane diisocyanate and polyvinyl acetate. Iodine tags were attached to the organic adhesives for enhanced XCT gray-scale contrast relative to wood for quantitative material segmentation. Novel views of 3D wood-adhesive penetration inside wood-composite joints are presented, along with data quantifying

penetration depth. These results provide a unique view into the highly complex and variable nature of wood-adhesive penetration.

5.2 Introduction

Wood adhesive penetration has long been studied in an effort to understand the mechanisms of wood adhesion. Findings have helped elucidate influencing parameter relationships for a variety of factors governing wood-adhesive penetration, including wood species, moisture content and surface energy, adhesive type, viscosity and molecular weight, and bonding conditions such as temperature and pressure (Frazier and Ni 1998; Frihart 2005; Jakes et al. 2013; Johnson and Kamke 1992; Kamke and Lee 2007). However, the majority of wood-adhesive penetration studies to-date have used 2D microscopy techniques, where transverse, or cross-section, surfaces or sections of composite bondlines were observed. While vast amounts of valuable data have been generated from such techniques, 2D analyses suffer from a few inherent flaws. First, researchers may be able to determine where cured adhesives reside on a wood-composite cross-section, but the planar views provide little information about the 3D flow path the adhesive traveled during bonding. Often microscopy images may show isolated adhesive elements in cell lumens which appear unconnected to the bondline; interpretation of such elements is often a challenge because the true connectivity would lie outside the image plane. Additionally, some adhesives cure *in-situ* by releasing carbon dioxide causing bubbles to form in adhesive columns within wood cell lumens (Frazier 2003); a cross-section view through one of these bubbles would appear as if the adhesive were merely coating a wood cell, rather than filling it. Furthermore, intense surface preparation,

soaking, sectioning and staining are often necessary for quality microscopy images, which are inherently destructive to the composite specimens (Jakes et al. 2013; Kamke and Lee 2007; Paris et al. 2014). Matched specimens are typically used in attempts to correlate composite performance with adhesive penetration, which introduces additional variability.

Micro X-ray computed tomography (XCT), on the other hand, is a non-destructive 3D imaging technique capable of providing detailed, 3D, wood-adhesive penetration data (Hass et al. 2012; Kamke et al. 2014; Modzel et al. 2011; Paris et al. 2014). The technique has been invaluable for many years in materials science and medical imaging disciplines, and has only recently been adopted for wood products evaluations. An early challenge thus far for wood-adhesive XCT analyses has been generating sufficient X-ray absorption contrast to allow differentiation between the wood and adhesive phases (Evans et al. 2010; Hass et al. 2012; Modzel et al. 2011). However, Paris et al. (2014) demonstrated a method for tagging a phenol formaldehyde (PF) resin with iodine, such that it yielded sufficient gray-scale contrast in reconstructed composite tomograms for quantitative material segmentation. In this research, the XCT technique is applied to three different wood-composite joints. The presented specimens were prepared with three different wood species, Douglas-fir (*Pseudotsuga menziesii*, DF) loblolly pine (*Pinus taeda*, SYP) and a hybrid poplar (*Populus deltoides* x *Populus trichocarpa*, HP), which presented different anatomical structures for penetrating adhesives. Similarly, composites were bonded with three different adhesive types exhibiting different morphology, flow and cure characteristics. These adhesives included the aforementioned iodinated PF

(IPF), and two other adhesive types similarly tagged with iodine, polyvinyl acetate (hybrid PVAc) and polymeric diphenylmethane diisocyanate (IpMDI).

Adhesive penetration can occur at both the microscopic scale, where the adhesives coat and or fill wood cell lumens, and on the nanometer scale, where low-molecular weight adhesive components can infiltrate cell walls (Frazier and Ni 1998; Frihart 2005; Kamke and Lee 2007). Penetration at both scales likely influences composite joint performance and bond durability. Nano-scale XCT resolutions are achievable, but there is a trade-off between resolution and field-of-view (Chen et al. 2011; Ketcham and Carlson 2001). The XCT data reported here had micrometer-scale spatial resolution over a few millimeters field-of-view; thus bulk adhesive penetration is presented. However, evidence of cell wall infiltration was also identified, but material segmentation at this scale was below the resolution limits. Bulk material segmentation, offered 3D visualization of adhesive distribution inside the composite joints, and penetration depths were easily calculated on the segmented digital data sets. Multiple calculations have been presented for quantifying adhesive penetration into wood (Kamke and Lee 2007; Paris 2010; Sernek et al. 1999); however, there is still debate over which best describes the phenomena and most closely correlates with performance. Non-destructive XCT imaging provides a unique opportunity for researchers to not only run multiple calculations simultaneously on reconstructed data-sets, but also allows one to still conduct joint performance tests on the very same, undamaged composite specimens (Kamke et al. 2014).

5.3 Materials and Methods

5.3.1 Composite specimen preparation

Adhesives' solids content, viscosity and cure characteristics were modeled after three general wood-adhesive classes, but were modified to contain 20-40 wt% iodine. The IPF formulation and tagging procedure are described in detail elsewhere (Paris et al. 2014). Hybrid PVAc was a hybrid adhesive prepared with equal parts of a common emulsion PVAc and IPF. IpMDI tagging was done by substituting a portion of the isocyanate groups on a commercial pMDI adhesive with triiodophenol. Complete descriptions of the hybrid PVAc and IpMDI adhesive preparations will be submitted in a later publication. Adhesives were applied to the tangential-longitudinal (30-70 cm²) faces of freshly planned DF, SYP, or HP wood laminates with a resin-solids spread rate of 120 g/m². Composite assemblies were bonded under the following conditions: 690 kPa (DF and SYP) or 420 kPa (HP), 185°C for 8 minutes (IPF), 150 °C for 3 hours (hybrid PVAc), and 50°C for 14 hours (IpMDI). XCT specimens, approximately 2 mm x 2 mm x 15 mm (radial x tangential x longitudinal) were excised from the laminated assemblies.

5.3.2 Synchrotron, micro X-ray computed tomography (XCT)

XCT specimens were scanned on beamline 2-BM-B at the Advanced Photon Source (APS) at the Argonne National Laboratory, Argonne, Illinois. Specific beamline hardware are described elsewhere (Kamke et al. 2014). Radiographic projections (1504 images) were collected every 0.12° through a 180° rotation; the beam energy, exposure time and sample-to-detector distance were 14.05 KeV, 250 ms and 8 mm, respectively. A fast filtered back projection algorithm was used for tomographic reconstruction (Dowd et

al. 1999). Reconstructed tomograms were stored as stacks of 2048 sequential, floating-point, gray-scale, cross-section images, representing virtual slices along the longitudinal direction. The full XCT field-of-view volume was approximately $3 \times 3 \times 3 \text{ mm}^3$, with voxel side lengths of $1.45 \mu\text{m}$.

5.3.3 Image processing and penetration analysis

XCT image processing was done using Fiji, a bundled software package of ImageJ, Java and several digital image analysis plug-in toolkits (Schindelin et al. 2012). Image stacks were imported into the program, and central, sub-volume regions-of-interest (ROI), with dimensions 750 voxels (1.09 mm, tangential) x 500 voxels (0.73 mm, radial) x 1500 voxels (2.18 mm, longitudinal), and containing a vertical bondline, were digitally excised (cropped) from each specimen. Image processing is described elsewhere (Kamke et al. 2014). The first and second derivative curves of the processed ROI gray-scale histograms were used to determine the global-threshold segmentation values. Specific segmentation criteria depended on adhesive type, as each system caused a different degree of X-ray attenuation. Air and pure-wood phases were always thresholded at the minimum in the valley separating the two clear material peaks, where the first derivative crossed zero; this was also the case for segmenting pure adhesive. However, when histograms exhibited broad and extended valleys between pure-wood and pure-adhesive peaks, cell wall penetration was believed present, and thus segmented as a fourth material phase. Cell wall penetration threshold values were chosen when the moving-average (5X) second derivative curve fell below 0.01% (IPF) or 0.05% (IpMDI) of the first derivative curve's

total range; this indicated the change in slope of the pure-wood histogram peak's upper tail was negligible.

Once segmented, adhesive elements, 10 voxels or greater, were counted for each virtual image-stack slice with the Fiji 'analyze particles' plug-in. Isolated agglomerations less than 10 voxels were considered noise, and ignored. Effective (EP) and weighted penetration (WP) depths into each wood-adherend were calculated with the following two methods:

$$EP = \frac{\sum A_i}{X_{image}} \quad WP = \sqrt{\left[\frac{\sum Y_i^2 A_i}{\sum A_i} \right]}$$

where A_i is the area of an identified adhesive element in voxels², X_{image} is the width of the image (750 voxels), and Y_i is the distance of the centroid for each A_i object from the plane defining the surface of the penetrated wood-adherend. When a thick adhesive layer existed between laminates, as with hybrid PVAc, two wood-surface planes were identified, one for each adherend; adhesive material between these planes was not counted as it had not penetrated into either wood laminate.

5.4 Discussion

The results offer novel information regarding the 3D adhesive penetration behavior in three different wood-composite types. The intent of this paper is to introduce the capabilities of XCT for wood-composite joint analyses. Only one replicate per treatment type is provided, and the analyzed sub-volume ROIs were relatively small (1.71 mm³). Readers should not interpret the following penetration behavior as characteristic of the

presented wood species or adhesive types. It is, however, important to recognize the many sources and types of variability, between and within, the different composite treatments. The following discussion will highlight some of the notable comparisons and information afforded with XCT analyses, previously unavailable with typical 2D microscopy.

5.4.1 XCT material segmentation

Full reconstructed image stacks consisted of 2048 virtual cross-section slices, with dimensions of 2048 x 2048 pixels resulting in over 8.5 billion voxels, and approximately 35GB, per specimen. Sub-volume ROIs consisting of approximately 0.5 billion voxels were more manageable data-sets for analysis. As these ROIs were digitally excised from the center of each image stack, they were also free of noise associated with edges of non-cylindrical specimens (Haibel 2008; Ketcham and Carlson 2001). After additional filtering and conversion to 8-bit format, remaining voxels in each ROI had a gray-scale value ranging from 0 (black) representing low attenuation to 255 (white) indicating a material which caused high X-ray attenuation. Wood-composite joints contain three primary material components, namely air, wood cell walls and the adhesive. Air, occupying cell lumens and void spaces, has the lowest density, and thus resulted in the darkest voxel elements. Conversely, the adhesives had the greatest x-ray attenuation and brightest voxel values, as they were tagged with iodine to afford sufficient contrast to the surrounding wood cell walls.

Figure 5-1 shows examples of gray-scale histograms, along with the first derivative curves and lines indicating the gray-scale threshold values. The tallest, leftmost, peak in

each image corresponds to air; this is also the narrowest of the material peaks, as the air phase is the most uniform material present (i.e. presents lowest spread of possible attenuation values). Voxels to the left of the air peak result from phase contrast artifacts, which cause overly dark values near material edges (Betz et al. 2007; Haibel 2008); these voxels occurred to the inside of all wood cell edges so they were included in the air phase. The central peak in each histogram represents wood cell walls. The variable breadth of this peak is due to multiple factors, including partial volume effects from the thin and numerous cell wall edges (Haibel 2008; Wildenschild et al. 2002), as well as the relative attenuation differences of the tagged adhesive phases. For example, compare the wood peaks in Figure 5-1b and c; adhesive IPF contained twice as much iodine as IpMDI (40 vs. 20 wt%), and had a greater density. Thus, IPF attenuation was much greater than IpMDI. Air and wood cell wall properties were similar in both specimens, but the wood cell wall peak appears narrower in the IPF specimen because it was forced further to the left when all three materials were normalized to the 8-bit gray-scale range. Lastly, the rightmost peak in each histogram, at high gray-scale values, is the adhesive phase which contains the iodine tags.

There is always concern in image analyses, when contrast-agent tagging is necessary, that there may be phase separation between the tag-marker and the material in question. Such difficulties have occurred, and complicated quantitative results, in several wood-adhesive XCT studies (Modzel et al. 2011; Walther and Thoemen 2009; Wang et al. 2007). Paris et al. (2014) used energy dispersive spectroscopy (EDS) to confirm that the iodine tags remained with adhesive IPF throughout bonding and resin cure. The same EDS technique was applied to hybrid PVAc and IpMDI composite bondlines, and confirmed the iodine

tags remained uniformly associated with those adhesives as well; that data will be published in a later manuscript. The significance of this finding, however, is that one can have confidence that brightest voxels in the Figure 5-1 histograms are indeed adhesive.

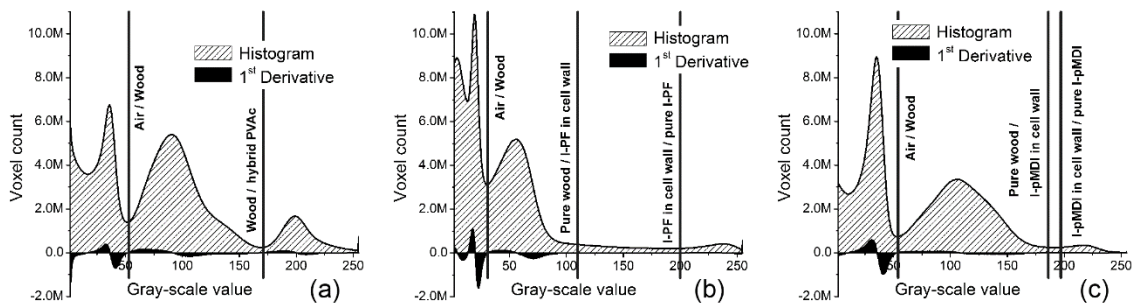


Figure 5-1 Gray-scale histogram and first derivative curves for processed ROIs with lines indicating the material segmentation threshold values (a) DF_hybrid PVAc, (b) HP_IPF and (c) SYP_IpMDI (voxel count in millions)

Quantitative segmentation is simple with global thresholds when histogram material peaks are separated by clear valleys; and segmentation confidence increases with decreasing phase overlap. The histogram for specimen DF_hybrid PVAc shows air-to-wood and wood-to-adhesive thresholds at approximate gray-scale values 55 and 170 (Figure 5-1a). The other two specimens also show clear air-to-wood thresholds at gray-scale values 30 and 55 for HP_IPF and SYP_IpMDI, respectively. However, these specimens' histograms show a much broader valley between the wood and adhesive peaks. These are voxels believed to indicate where IPF and IpMDI adhesives have infiltrated the wood cell walls. PF and pMDI adhesives often have low molecular-weight polymer components, which have been demonstrated to penetrate wood cell walls (Frazier and Ni 1998; Jakes et al. 2013; Stockel et al. 2012; Yelle et al. 2009). Cell wall penetration occurs at a nanometer scale; thus it would be impossible to separate

individual material components within a single voxel at the 1.45 μm per voxel resolution in the current study. Rather, penetrated cell wall voxels would show gray-scale values between the two pure phases, which would increase in value with increasing degree of adhesive infiltration.

Figures 5-2, 5-3 and 5-4 show an orthogonal view of the reconstructed ROIs for DF_hybrid PVAc, HP_IPF and SYP_IpMDI, respectively. Each image series shows the gray-scale XCT sub-volume, directly corresponding to the respective histogram in Figure 5-1, as well as segmented views resulting from the thresholds, as indicated.

Notice first that the gray-scale XCT views for the hybrid PVAc and IpMDI bonded specimens are much lighter than the IPF composite. This reflects the earlier comment that, because IPF had the highest iodine concentration, its adhesive attenuation affect was greater relative to the wood and air phases in that composite joint. Thus, the air and wood phases were forced to darker gray-values along the 0-255 range.

The segmented composite views (Figures 5-2b, 5-3b and 5-4b) show the same ROIs after having removed the air space; here individual wood cells are visible along with the artificially-colored adhesive bondline regions. Yet, the composite views still only provide surface or 2D information. However, when the wood material is removed, as in the third image of each series, the volumetric adhesive distribution inside the wood composite joints is visible. This 3D view inside the composite joint offers novel information into adhesive penetration behavior along a specimen joint that is unavailable with conventional 2D microscopy techniques. Furthermore, XCT imaging, and all post

reconstruction processing operations, are non-destructive and do not involve intensive specimen preparation.

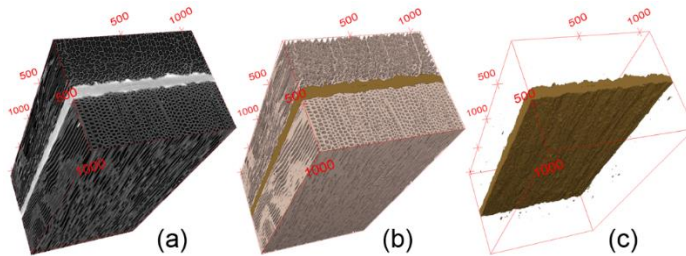


Figure 5-2 ROI for specimen DF_hybrid PVAc (1.71 mm^3 , bounding box dimensions in μm); (a) gray-scale XCT view corresponding to the histogram in Figure 5-1a, (b) segmented composite and (c) segmented hybrid PVAc adhesive

Figures 5-3 and 5-4 show the further separated pure adhesive and region of apparent cell wall penetration in specimens HP_IPF and SYP_IpMDI, respectively. Image ‘e’ in both figures shows only the voxels between the pure wood and adhesive peaks in both respective Figure 5-1 histograms. While the gross-penetration patterns appear significantly different for IPF and IpMDI, the region of suspected nano-scale cell wall penetration looks as if it were a shell around both adhesives’ pure material components. In other words, gray-scale voxel values between pure wood and adhesive phases were always adjacent to cell lumens containing adhesive, thus further supporting the claim of cell wall infiltration.

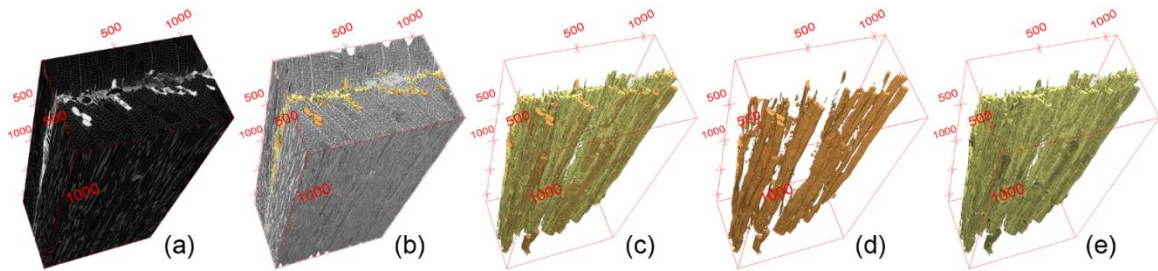


Figure 5-3 ROI for specimen HP_IPF (1.71 mm^3 , bounding box dimensions in μm); (a) gray-scale XCT view corresponding to the histogram in Figure 5-1b, (b) segmented composite, (c) segmented total adhesive phase, (d) segmented pure IPF and (e) segmented IPF in wood cell walls

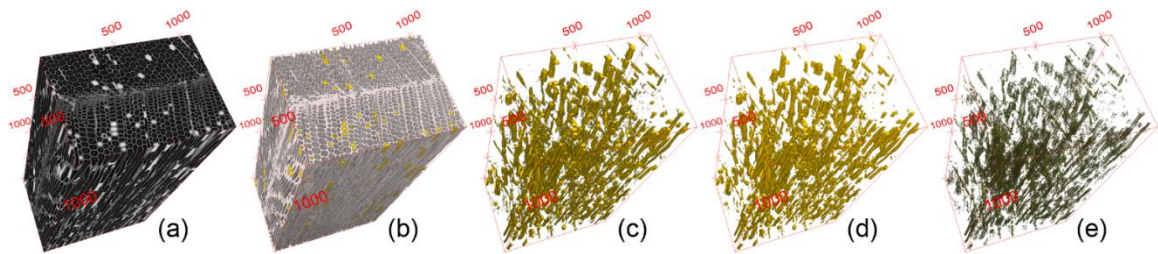


Figure 5-4 ROI for specimen SYP_IpMDI (1.71 mm^3 , bounding box dimensions in μm); (a) gray-scale XCT view corresponding to the histogram in Figure 5-1c, (b) segmented composite, (c) segmented total adhesive phase, (d) segmented pure IpMDI and (e) segmented IpMDI in wood cell walls

5.4.2 Comparison of 3D adhesive penetration behavior

Gross, or bulk lumen, wood-adhesive penetration has been calculated in a variety of ways and described in detail for multiple factors in previous studies (Johnson and Kamke 1992; Kamke and Lee 2007; Paris 2010; Sernek et al. 1999). However, traditional penetration studies investigated 2D composite surfaces or sections, and thus failed to capture penetration variability along the length of a bonded specimen. Digital, 3D XCT images, on the other hand, can provide quantitative penetration data throughout segmented ROI sub-volumes, using relatively simple image analysis counting operations.

Figure 5-5 shows the effective (EP) and weighted penetration (WP) results for the three composite specimens described above. Measurements were made for every virtual cross-section slice in each image stack. Distinctions were made for penetration into either side of the bondline, as indicated; while the box-plots labeled ‘mean’ indicate the average penetration for both lamina. Again, these results reflect the behavior for a single replicate per treatment, and are not meant to represent typical behavior for a species or adhesive class. However, the plot can help illustrate some of the variability revealed with non-destructive volumetric penetration analyses.

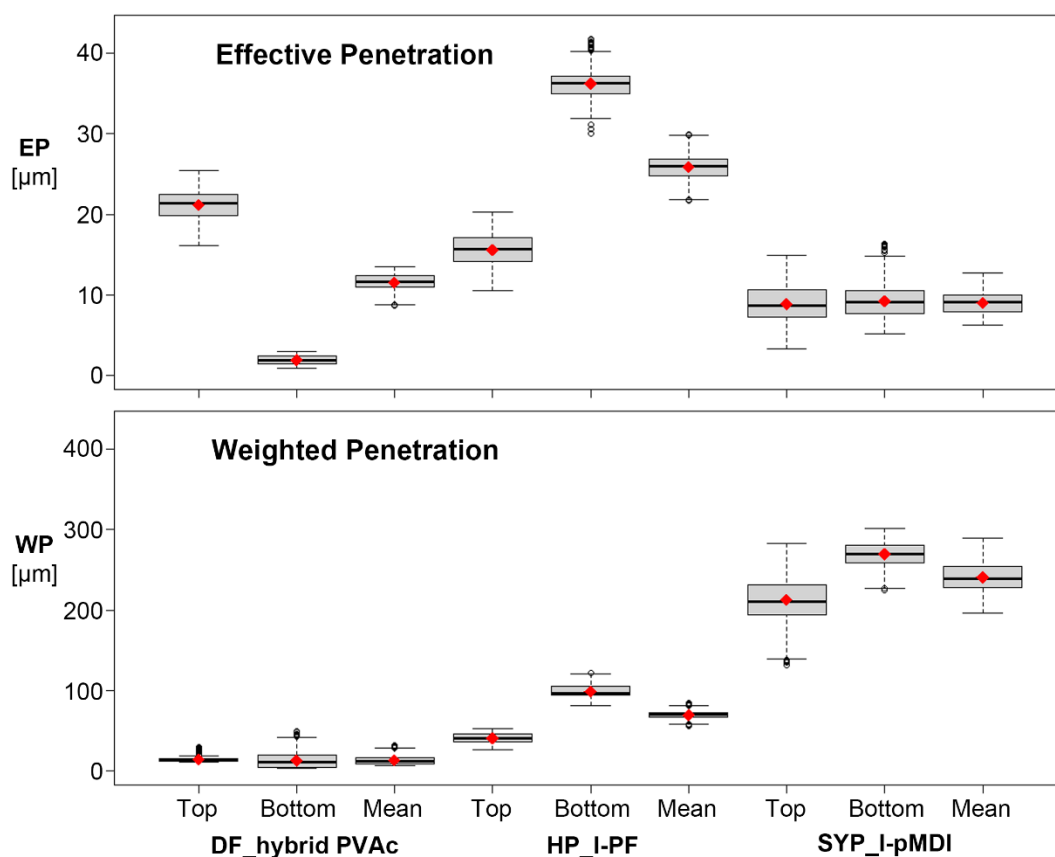


Figure 5-5 EP and WP box plots for DF_hybrid PVAc, HP_IPF and SYP_IpMDI; measured values represent the total adhesive area, including cell wall penetration; plots include the median (center line) and mean (bold diamond) for each distribution; ‘Top’ and ‘Bottom’ correspond to the respective top or bottom laminate as shown in Figures 5-2 to 5-4, while ‘Mean’ refers to the average penetration between the top and bottom laminates

First, compare the difference between the two calculations. The WP scale is an order of magnitude greater than EP. With the EP measurement, the greatest observed differences in penetration are no more than 20-30 μm , while for WP differences are as much as 200 to 300 μm between hybrid PVAc and IpMDI adhesives. The EP calculation accounts for the total adhesive area divided by the image width (tangential), while the WP measurement takes into account the radial distance of each adhesive element into the substrate. Comparing Figures 5-2a, 5-3a and 5-4a, the total adhesive area, or number of white surface voxels, are nearly the same, and the width of the image stacks are each 750 voxels. However, the adhesive distribution is vastly different across the three treatments. Consequently, the WP calculation appears to better illustrate the pattern of the penetrated adhesives, as observed in Figures 5-2c, 5-3c and 5-4c. It is still unclear which calculation correlates best with performance results; however, as this is a non-destructive, in-situ imaging technique, performance analyses can easily be performed on the very same undamaged specimens. Such comparisons are currently under investigation, and those results will be released in a later manuscript.

Figure 5-5 also allows one to compare the penetration differences in each lamina. For example, SYP_IpMDI appears to have fairly balanced EP and WP on both sides of the bondline, and this is visually consistent with what is seen in Figure 5-4c. However, for HP_IPF, penetration into the bottom laminate appears to be greater than into the top. A close look at Figure 5-3b reveals that this is because there were more vessels in the bottom laminate at the joint interface; whereas the top laminate's bonding surface appeared to have more small-diameter fibers exposed than the broader vessels. A similar

analysis of specimen DF_hybrid PVAc (Figure 5-2a and b) shows latewood on the bottom laminate and earlywood on the top, explaining the unbalanced EP behavior seen in Figure 5-5.

Lastly, one can see how penetration varies along the length of a bonded joint. For instance, the WP ‘mean’ box-plots for DF_hybrid PVAc and HP_IPF have narrow upper and lower quartile limits; while the range for SYP_IpMDI is fairly broad. Figures 5-2c and 5-3c show that the shape and depth of the penetrated adhesive phase in these specimens changes little along the specimen height. Yet the lower half of the Figure 5-4c ROI appears to have a greater number, or density, of segmented adhesive elements, A_i 's, than the upper portion of the same bondline. If traditional 2D microscopy techniques had been used to analyze this specimen, results may have been considerably different depending on whether it was sectioned in the upper or lower half.

5.5 Conclusions

Micro X-ray computed tomography is a powerful tool for 3D wood-adhesive penetration analyses. A challenge to-date has been generating sufficient X-ray gray-scale contrast for quantitative material segmentation; however, the presented adhesives were tagged with iodine to overcome such issues. Three different wood species and adhesive types were studied with this technique. Reconstructed tomogram image stacks were segmented into wood and adhesive material components using simple histogram threshold image-processing operations. Gray-scale histograms also revealed evidence of cell wall penetration for tagged phenol-formaldehyde and polymeric isocyanate resins, which both contained some low-molecular weight components. Once segmented, volumetric

adhesive penetration and distribution calculations are simple with digital image analysis counting operations. Such calculations can provide high statistical power, and offer novel insight into the variability of adhesive penetration along the length of wood-composite bondlines. Lastly, as X-ray tomography is non-destructive, undamaged specimens are preserved for future joint-performance studies where an investigator knows the true in-situ adhesive distribution in the composite joint. Such combined analyses could lead to better correlations linking adhesive penetration with wood-composite performance.

5.6 Acknowledgements

Use of the Advanced Photon Source was supported by the U. S. Department of Energy, Office of Science, Office of Basic Energy Sciences, under Contract No. DE-AC02-06CH11357. Financial support was provided by the Wood-Based Composites Center, a National Science Foundation Industry/University Cooperative Research Center.

5.7 References

Betz, O., Wegst, U., Weide, D., Heethoff, M., Helfen, L., Lee, W. K. and Cloetens, P. (2007) Imaging applications of synchrotron X-ray phase-contrast microtomography in biological morphology and biomaterials science. 1. General aspects of the technique and its advantages in the analysis of millimetre-sized arthropod structure. *J. Microsc.-Oxf.* 227, 1, 51-71.

Chen, H.-H., Chien, C.-C., Petibois, C., Wang, C.-L., Chu, Y. S., Lai, S.-F., Hua, T.-E., Chen, Y.-Y., Cai, X. and Kempson, I. M. (2011) Quantitative analysis of nanoparticle internalization in mammalian cells by high resolution X-ray microscopy. *Journal of Nanobiotechnology* 9, 1, 14.

Dowd, B. A., Campbell, G. H., Marr, R. B., Nagarkar, V. V., Tipnis, S. V., Axe, L. and Siddons, D. P. (1999) Developments in synchrotron x-ray computed microtomography at the National Synchrotron Light Source. 224-236.

Evans, P. D., Morrison, O., Senden, T. J., Vollmer, S., Roberts, R. J., Limaye, A., Arns, C. H., Averdunk, H., Lowe, A. and Knackstedt, M. A. (2010) Visualization and numerical analysis of adhesive distribution in particleboard using X-ray micro-computed tomography. *International Journal of Adhesion and Adhesives* 30, 8, 754-762.

Frazier, C. E. 2003: Isocyanate wood binders. In: Pizzi, A. and Mittal, K. L., editors, *Handbook of Adhesive Technology*, New York: Marcel Dekker, Inc.

Frazier, C. E. and Ni, J. W. (1998) On the occurrence of network interpenetration in the wood-isocyanate adhesive interphase. *International Journal of Adhesion and Adhesives* 18, 2, 81-87.

Frihart, C. R. 2005: Wood adhesion and adhesives. In: Rowell, R. M., editor, *Handbook of Wood Chemistry and Wood Composites*, New York: Taylor & Francis Group.

Haibel, A. 2008: Synchrotron x-ray absorption tomography. In: Banhart, J., editor, *Advanced Tomographic Methods in Materials Research and Engineering*, Oxford, New York: Oxford University Press, 141-160.

Hass, P., Wittel, F., Mendoza, M., Herrmann, H. and Niemz, P. (2012) Adhesive penetration in beech wood: experiments. *Wood Science and Technology* 46, 1-3, 243 - 256.

Jakes, J. E., Gleber, S.-C., Vogt, S., Hunt, C. G., Yelle, D. J., Grigsby, W. and Frihart, C. R. 2013: New synchrotron-based technique to map adhesive infiltration in wood cell walls. In: *Proceedings of the 36th Annual Meeting of the Adhesion Society*, Datona Beach, FL, USA, 3 p.

Johnson, S. E. and Kamke, F. A. (1992) Quantitative-analysis of gross adhesive penetration in wood using fluorescence microscopy. *Journal of Adhesion* 40, 1, 47-61.

Kamke, F. A. and Lee, J. N. (2007) Adhesive penetration in wood - a review. *Wood and Fiber Science* 39, 2, 205-220.

Kamke, F. A., Nairn, J. A., Muszynski, L., Paris, J. L., Schwarzkopf, M. and Xiao, X. (2014) Methodology for micro-mechanical analysis of an adhesive bond using micro computed x-ray tomography and numerical modeling. *Wood and Fiber Science* 46, 1.

Ketcham, R. A. and Carlson, W. D. (2001) Acquisition, optimization and interpretation of X-ray computed tomographic imagery: applications to the geosciences. *Computers & Geosciences* 27, 4, 381-400.

Modzel, G., Kamke, F. A. and De Carlo, F. (2011) Comparative analysis of a wood-adhesive bondline. *Wood Science and Technology* 45, 1, 147-158.

Paris, J., Kamke, F., Mbachu, R. and Gibson, S. (2014) Phenol formaldehyde adhesives formulated for advanced X-ray imaging in wood-composite bondlines. *Journal of Materials Science* 49, 2, 580-591.

Paris, J. L. 2010: Carboxymethylcellulose acetate butyrate water-dispersions as renewable wood adhesives. *Department of Wood Science and Forest Products*, Virginia Tech, Blacksburg, VA: 169 p.

Schindelin, J., Arganda-Carreras, I., Frise, E., Kaynig, V., Longair, M., Pietzsch, T., Preibisch, S., Rueden, C., Saalfeld, S. and Schmid, B. (2012) Fiji: an open-source platform for biological-image analysis. *Nature Methods* 9, 7, 676-682.

Sernek, M., Resnik, J. and Kamke, F. A. (1999) Penetration of liquid urea-formaldehyde adhesive into beech wood. *Wood and Fiber Science* 31, 1, 41-48.

Stockel, F., Konnerth, J., Moser, J., Kantner, W. and Gindl-Altmutter, W. (2012) Micromechanical properties of the interphase in pMDI and UF bond lines. *Wood Science and Technology* 46, 4, 611-620.

Walther, T. and Thoemen, H. (2009) Synchrotron X-ray microtomography and 3D image analysis of medium density fiberboard (MDF). *Holzforschung* 63, 5, 581-587.

Wang, Y., Muszyński, L. and Simonsen, J. (2007) Gold as an X-ray CT scanning contrast agent: Effect on the mechanical properties of wood plastic composites. *Holzforschung* 61, 6, 723-730.

Wildenschild, D., Hopmans, J. W., Vaz, C. M. P., Rivers, M. L., Rikard, D. and Christensen, B. S. B. (2002) Using X-ray computed tomography in hydrology: systems, resolutions, and limitations. *Journal of Hydrology* 267, 3-4, 285-297.

Yelle, D. J., Jakes, J. E., Ralph, J. and Frihart, C. R. 2009: Characterizing polymeric methylene diphenyl diisocyanate reactions with wood: 1. High-resolution solution-state

NMR spectroscopy. In: Frihart, C. R., Hunt, C. G. and Moon, R. J., editors, *Proceedings of the International Conference on Wood Adhesives 2009*, Lake Tahoe, NV, USA: Forest Products Society, 5 p.

CHAPTER 6. QUANTITATIVE WOOD-ADHESIVE PENETRATION
WITH X-RAY COMPUTED TOMOGRAPHY

Jesse L. Paris and Frederick A. Kamke

To be submitted for publication in the *International Journal of Adhesion and Adhesives*

Quantitative Wood-Adhesive Penetration with X-ray Computed Tomography

Jesse L. Paris* and Frederick A. Kamke†

Department of Wood Science & Engineering, Wood-Based Composites Center, Oregon State University, 119 Richardson Hall, Corvallis, OR 97331, USA

* Corresponding Author. Tel.: +804 338 4353; Fax +542 737 3385

E-mail address: Jesse.Paris@OregonState.edu (J. L. Paris)

† Secondary Corresponding Author. Tel.: +541 737 8422; Fax +542 737 3385

E-mail address: Fred.Kamke@OregonState.edu (F. A. Kamke)

6.1 Abstract

Micro X-ray computed tomography (XCT) was used to analyze the 3D adhesive penetration behavior of different wood-adhesive bondlines. Three adhesives, a phenol formaldehyde (PF), a polymeric diphenylmethane diisocyanate (pMDI), and a hybrid polyvinyl acetate (PVA), all tagged with iodine for enhanced x-ray attenuation, were used to prepare single-bondline laminates in two softwoods, Douglas-fir and loblolly pine, and one hardwood, a hybrid polar. Adhesive penetration depth was measured with two separate calculations, and results were compared with 2D fluorescent micrographs. A total of 54 XCT scans were collected, representing six replicates of each treatment type; each replicate, however, consisted of approximately 1500 individual, cross-section slices stacked along the specimen length. Clear penetration differences were observed between each adhesive type, and between wood species bonded with both the PF and pMDI adhesives. Individual specimen comparisons showed multiple levels and sources of variability in wood-adhesive bondlines, and digitally segmented 3D adhesive phases offered unique, in-situ views of the cured adhesive structures.

6.2 Introduction

Wood-based composites represent a broad class of materials which are critically important to residential construction, timber engineering and furniture manufacturing industries. The performance of all adhesively-bonded materials, including wood products, depends on the ability for the adhesive to transfer mechanical stresses across the joint interface. As wood is a natural, porous material, the nature of this interface is highly variable, and liquid adhesives can flow and penetrate the cellular substrate during

bonding. In discussions of wood adhesion, the word “interface” is often replaced with the term “interphase”, which includes the region of adhesive penetration and transition between pure and mixed material properties (Kamke and Lee 2007; Marra 1992).

Adhesive penetration occurs at multiple scales in this interphase region. Bulk, or micro-scale, penetration describes flow into and between cell lumens and voids. However, some adhesives containing low-molecular weight components may penetrate the wood cell walls, at the molecular level, or nanometer scale. Bulk penetration transfers bondline stresses into sound wood to avoid stress concentrations around damaged cells caused during surface preparation prior to bonding. High stress zones might also occur at abrupt boundaries between the adhesive and adherend(s) when they have different elastic moduli, but bulk penetration can provide a smoother material-property gradient in the interphase region (Frihart 2005). Furthermore, bulk flow increases the surface area over which the intermolecular forces and chemical associations governing adhesion effectively operate, and once cured, solidified adhesives provide mechanical interlocking resistance to hold the substrates together (Schultz and Nardin 1994). Molecular scale penetration can increase cell wall modulus and dimensional stability, which can ultimately affect bondline moisture durability (Frazier and Ni 1998; Jakes et al. 2009). Over penetration, on the other hand, can result in a starved bondline, where too little adhesive remains in the bondline for efficient load transfer (River et al. 1991). Furthermore, composite manufactures wish to avoid excessive penetration, which is wasteful of expensive resin materials.

While the influence of adhesive penetration on wood-composite joint performance has been extensively studied (Ebewele et al. 1986; Frihart 2005; Gindl et al. 2005; Kamke

and Lee 2007; Paris 2010; River et al. 1991; White 1977), there is still no clear consensus as to what represents an optimal penetration depth. This is, in part, due to the high variability between different adhesive types and formulations, wood anatomy and chemistry, and manufacturing parameters, all of which influence penetration behavior (Frihart 2005; Kamke and Lee 2007). Yet, another primary reason for the lack of stronger depth-to-performance correlations is that adhesive penetration is traditionally observed and quantified with various 2D microscopy techniques, which have two inherent flaws. First, bondline photomicrographs show where an adhesive has penetrated, but not the 3D path it followed to get there. Information is often lost above and below the image-plane that describes the true connectivity of the cured adhesive network. Second, microscopy specimen preparation often requires soaking and/or sectioning, which are inherently destructive to the wood-adhesive bondlines (Cao 2010; Johnson and Kamke 1992; Kamke and Lee 2007; Paris 2010; Sernek et al. 1999). Researchers often rely on matched specimens, or ones prepared under similar conditions, to correlate mechanical performance and penetration results, but natural anatomical variations can be fairly drastic even for matched specimens.

Micro X-ray computed tomography (XCT) offers a unique solution to both challenges. Several researchers have demonstrated the power of non-destructive, micro XCT for studying 3D wood anatomy (Hass et al. 2010; Mannes et al. 2009; Mayo et al. 2010; Standfest et al. 2012; Steppe et al. 2004; Trtik et al. 2007). XCT analyses of wood-adhesive bondlines, on the other hand, have been more challenging due to the lack of x-ray absorption contrast between wood cell walls and adhesive polymers (Hass et al. 2012). Some studies have tried doping adhesives with heavy metal particles or ions to

improve the adhesive x-ray attenuation relative to wood (Evans et al. 2010; Mannes et al. 2010; Modzel et al. 2011; Standfest et al. 2010; Walther and Thoemen 2009); however, quantitative results were often complicated by independent tag mobility and agglomeration, which lead to heterogeneous adhesive x-ray properties.

Recently, the authors presented methods for uniformly tagging three different adhesives, a phenol formaldehyde (PF), a hybrid polyvinyl acetate (PVAc) mixed with PF, and a polymeric diphenylmethane diisocyanate (pMDI), with iodine, such that they could be quantitatively segmented with absorption-contrast, micro XCT (Kamke et al. 2014; Paris et al. 2014a; Paris et al. 2013; Paris et al. 2014b). These adhesives, hereafter referred to as IPF, hybrid PVAc, and IpMDI, respectively, were used to bond laminates of Douglas-fir (*Pseudotsuga menziesii*, DF), loblolly pine (*Pinus taeda*, SYP) and a hybrid poplar (*Populus deltoides* x *Populus trichocarpa*, HP) (Paris et al. 2014a; Paris et al. 2013; Paris et al. 2014b). The broader goal of this work was to use digital, segmented wood and adhesive volumes as inputs in a 3D, numerical model to assess the relationship between adhesive penetration and bondline mechanical performance (Kamke et al. 2014; Nairn 2006; Nairn et al. 2014). The same, undamaged, XCT specimens were subsequently mechanically tested with various micro-bond tests, in parallel to the model simulations (Muszynski et al. 2014; Nairn et al. 2014; Schwarzkopf et al. 2014). Comparisons between the simulated and actual results were then used to calibrate and validate the model based on a reverse problem solving methodology, including the true composite anatomy and penetration profile (Kamke et al. 2014; Muszynski et al. 2014; Nairn et al. 2014).

In total, 54 specimens, representing six replicates per adhesive/adherend treatment, were scanned with micro XCT. In addition to providing a robust sampling for the model development, this work also represents one of the largest, if not the largest, digital collections of micro-scale, 3D wood-adhesive penetration data, to date. Segmented wood cell wall and adhesive material phases in these specimen volumes offer novel 3D views of the full interconnectivity and adhesive distribution in the wood bondline interphase (Paris et al. 2013; Paris et al. 2014b). Furthermore, the 3D perspectives provide unique, qualitative information about the in-situ structure and morphology of the cured adhesives. Additionally, cell wall penetration was observed in several of the IPF and IpMDI bondlines (Paris et al. 2013; Paris et al. 2014b). While material segmentation in a cell wall was below the resolution limits in this study, averaged adhesive/wood x-ray gray values were observed in cell walls adjacent to lumens filled with these adhesives.

In this paper, adhesive penetration depth, calculated along the length of each specimen, are presented and compared with 2D photomicrographs of specimens excised from the same bonded laminates. Two separate penetration depth calculations are used. The first, effective penetration (EP), has been previously used in several wood-adhesive studies (Cao 2010; Ren 2010; Sernek et al. 1999; Zheng 2002; Zheng et al. 2004). The second, weighted penetration (WP), is proposed here, and is similar to the second moment of area calculation often used in mechanical engineering disciplines (Onouye and Kane 2007). The WP calculation accounts for both the area and perpendicular distance an adhesive object has penetrated, and is proposed to offer a better representation of the adhesive penetration and distribution than the EP calculation. With these penetration results,

effects of adhesive type, wood species, and variability in wood anatomy between and within replicates are compared.

6.3 Materials and Methods

XCT adhesive bondlines were scanned and reconstructed at the Advanced Photon Source, at the Argonne National Laboratory in Argonne, Illinois. Tomogram resolution was 1.45 μm per voxel side length. The presented adhesive penetration results and subsequent discussion refer to sub-volume regions of interest, which were digitally excised from the central region of each XCT specimen. Sub-volume dimensions were approximately 500 to 750 voxels (725 – 1080 μm , radial or perpendicular to the bondline) x 750 voxels (1087 μm tangential or parallel to the bondline) x 1500 slices (2175 μm longitudinal or along the bondline length). Specific methodology regarding adhesive formulation, bonding, XCT scanning procedures, 3D tomogram reconstruction, and material segmentation in XCT sub-volumes is described in detail elsewhere (Kamke et al. 2014; Paris et al. 2014a; Paris et al. 2013; Paris et al. 2014b).

6.3.1 Viscosity determination

Adhesive viscosity was measured on an AR2000 rheometer with steady-state flow (1 – 500 s^{-1}) and a stainless steel, cone-and-plate geometry (40 mm, 1:59°, 52 μm gap, 25°C). Three replicates were collected per adhesive type, and used to prepare average flow curves. The hybrid PVAc adhesive had a short pot life, and thus three separate batches were prepared for viscosity determination (Paris et al. 2014b).

6.3.2 Fluorescent microscopy (FM) and image analysis

Bondline microscopy specimens were excised from neighboring locations in the same initial laminates as the XCT specimens. Cross-section surfaces were prepared with a glass knife on a Leica EM UC7 ultra microtome, and imaged with a Nikon E400 epifluorescent microscope with a 100 Watt mercury lamp and a UV filter set (300 – 380 nm excitation, 400 nm dichromatic mirror, and 420 nm emission). Specimens bonded with IPF and the hybrid PVAc adhesive were embedded in Spurr low-viscosity epoxy resin prior to sectioning and imaging (Ellis 2006; Paris et al. 2014a; Paris et al. 2014b; Spurr 1969). IpMDI specimens, however, were not embedded, and were stained with a 0.5 % Safranin solution after microtoming. Resulting IPF and hybrid PVAc images showed blue cell walls and blue epoxy-filled lumens, and the adhesive phase was dark reddish-brown to black. IpMDI micrographs had red cell walls, dark empty lumens, and blue adhesive. FM images were collected from three replicate specimen surfaces for each adhesive/species treatment combination (i.e. 27 total FM images). FM image resolution was 0.34 μm per pixel side length.

All image analyses were done in Fiji, a bundled software package of ImageJ, containing several preloaded plugins (Rasband 1997 - 2012; Schindelin et al. 2012). Adhesives were segmented from FM, color images according to the following procedure, which is also illustrated with a SYP hybrid PVAc specimen in Figure 6-1: (1) images were split into the individual red (R), green (G) and blue (B) color channels, each of which provided an 8-bit, gray-scale image, whose intensity corresponded with the original RGB color intensity; (2) for hybrid PVAc and IpMDI specimens, the B and G images were

added, and then the R channel was subtracted to yield a gray-scale image with the greatest adhesive contrast (Figure 6-1b); in the case of IPF, the blue channel provided sufficient contrast, and thus the R and G channels were discarded; (3) three successive iterations of an edge-preserving median filter, with a 1-pixel radius, were applied to the gray-scale image; (4) a global gray-level threshold was applied to the filtered image at the minimum in the 10-point (IPF and hybrid PVAc) or 5-point (IpMDI) moving-average gray-level histogram, ε , (i.e. where the of corresponding average 1st derivative, ε' , crossed zero), as shown in Figure 6-1c; (5) high intensity, outlier pixels were removed from the resulting binary image (Figure 6-1d) with a 1-pixel radius; (6) to check segmentation accuracy, the final difference was taken between the original and final binary images (Figure 6-1e).

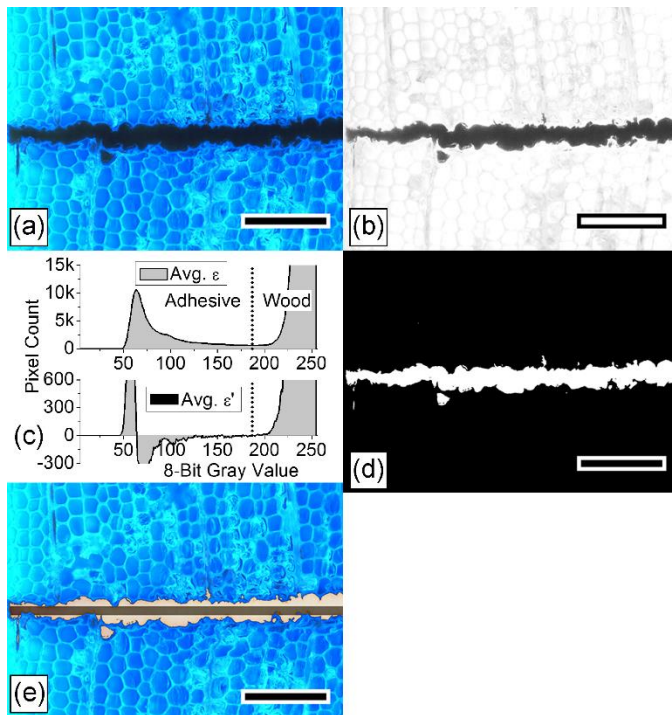


Figure 6-1 FM adhesive segmentation of a hybrid PVAc bondline: (a) original RGB image; (b) result of 'B' + 'G' - 'R' color channels; (c) moving average histogram and 1st derivative from 'b'; (d) binary adhesive; (e) adhesive overlain on original image, pure adhesive layer (dark) and penetrated adhesive (light); scale bars = 200 μ m

6.3.3 Measurement of adhesive penetration

Adhesive penetration depth was collected for each FM image, and from each slice in the 54 XCT, sub-volume image-stacks. Images were initially rotated such that the bondline was horizontal across the transverse image-plane; XCT sub-volumes were subsequently tilted so that the bondplane was parallel along the image-stack height. Even though laminate surfaces were planed prior to bonding, resulting bonded wood-lamina interface(s) were rarely a perfect line, or plane, across the area, or through the volume of interest, due to anatomical variability and cell crushing during consolidation (Kamke et al. 2014; Paris et al. 2014a; Paris et al. 2014b). A best-fit line, or plane in 3D, was used to

define the wood-lamina interface, as a common, y-coordinate reference for quantifying penetration depth. When a pure adhesive layer separated the laminates, two, parallel, ‘best-fit’ bondlines/bondplanes were defined; this was always the case for the hybrid PVAc adhesive (Figure 6-1e). A ‘best-fit’ bondline minimized the y-coordinate, positional error between ten manually-selected points, evenly spaced along the wood surface, as shown in Figure 6-2. In an XCT sub-volume, 12 points were chosen; four were placed at the lamina corners on the top and bottom slices, and the remaining eight were evenly spaced both across the stack width (x) and height (z).

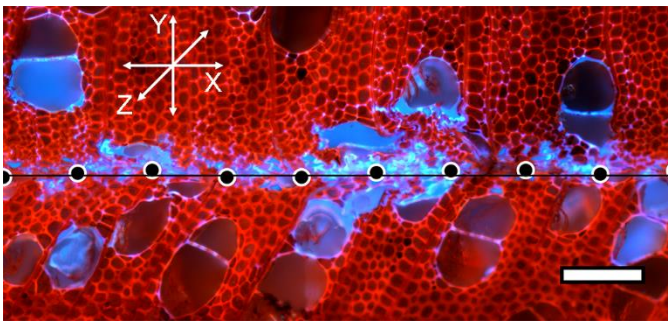


Figure 6-2 FM image of HP IpMDI bondline; black line = defined wood-lamina interface, and minimizes y-coordinate position error between the ten, equally-spaced, black points across the image; scale bar = 100 μm

Area and position (x, y, z or slice) were recorded for each adhesive element identified in segmented (i.e. binary) adhesive-phase images (Figure 6-1d), using the “Analyze Particles” operation in Fiji. Only adhesive elements four (FM) or ten (XCT) pixels or greater were counted in each image/slice (i.e. smaller, unconnected pixel elements were ignored, as these were likely noise and their total area had negligible effects on the

penetration calculations). Both pure adhesive and adhesive identified in wood cell walls were collectively grouped in the penetration calculations.

Adhesive penetration depth, into each wood laminate, was calculated with the following EP and WP calculations:

$$EP = \frac{\sum A_i}{X_{image}}$$

$$WP = \sqrt{\left[\frac{\sum Y_i^2 A_i}{\sum A_i} \right]}$$

where A_i is the area of a counted adhesive ‘particle’ in pixels, X_{image} is the image width in pixels, and Y_i is perpendicular distance, in pixels, from the centroid of each A_i particle to the defined ‘best-fit’ bondline/bondplane. Each value was then converted to μm dimensions based on the appropriate image resolution. Separate penetration depths were collected into each side of the bondline, and account for some of the observed variability within each specimen (Paris et al. 2013). However, the results presented here show the average depth for both lamina in each slice. Pure adhesive layers, existing between wood lamina, were not counted in penetration measurements, but were included in a separate measurement of the total adhesive area.

All statistical analyses were done using RStudio (ver. 0.97.551, Boston, Massachusetts). A two-factor analysis of variance (ANOVA) was used to determine the XCT penetration differences between adhesive and species, and check for an adhesive/species interaction. The ANOVA test was modified to allow for unequal treatment variances (weighted least

squares), as this traditional assumption was not met. Separate analyses were conducted using the replicate means (i.e. $n = 6$) versus an analysis where the random variation related to each slice was included as a nested factor (Zuur 2009). Significance was defined with an alpha level of 0.05.

6.4 Results and Discussion

Results presented here describe the 3D flow and penetration behavior for three different wood adhesives in three wood species. These adhesives were uniformly tagged with iodine for enhanced x-ray attenuation, and thus gray-scale contrast for quantitative image segmentation in reconstructed micro XCT datasets (Paris et al. 2014a; Paris et al. 2014b). The reported penetration depths are thus restricted to these particular adhesives, and are not meant to represent the behavior of the broader PF, PVAc, and pMDI adhesive classes. Furthermore, these results are a product of the particular gray-level segmentation criteria and image processing operations used throughout this work (Kamke et al. 2014; Paris et al. 2014a; Paris et al. 2013; Paris et al. 2014b). Nonetheless, the following discussion does present one of the largest collections of 3D wood-adhesive bondline data, to date. Penetration measurements are compared with adhesive viscosity, adhesive type, wood species, replicates and laminates within a treatment, calculation method, and with 2D fluorescence microscopy results.

6.4.1 Adhesive viscosity

Average steady-state viscosity flow curves are plotted in Figure 6-3. IPF, control pMDI, and IpMDI adhesives exhibited Newtonian flow over the provided shear range, with viscosity of approximately 1300, 500, and 50 centipoise (cP), respectively. pMDI resins

contain low molecular weight (MW) monomers and oligomers, which easily flow past one another, until reaction conditions cause them to chemically react. The IPF resin also had some low MW molecules, but its overall weight-average MW was fairly high, at 22,380 previously reported elsewhere (Paris et al. 2014a). Higher MW polymers exhibit greater resistance to flow. In addition, the liquid IpMDI adhesive contained approximately 27 wt% tetrahydrofuran (THF), which was included as solvent for the iodine addition reaction (Paris et al. 2014b). The presence of the THF likely caused the significant viscosity decrease in the IpMDI relative to the control pMDI.

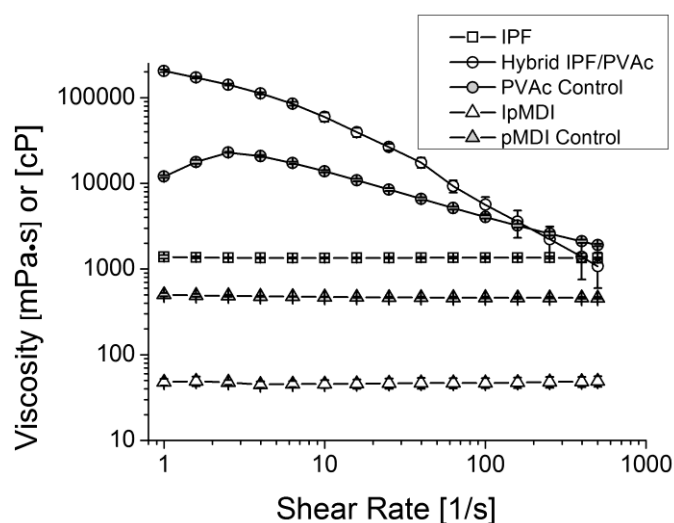


Figure 6-3 Average ($n = 3$) steady-state viscosity flow curves for the iodine-tagged and control adhesives, bars = ± 1 standard deviation

Both control and hybrid PVAc adhesives showed shear-dependent viscosity behavior. The neat PVAc appeared to thicken at low shear rates, but then shear-thinned from 12,000 cP to 2,000 cP; while the hybrid PVAc decreased from 200,000 cP to 1,000 cP over the entire experimental range. Over the majority of the shear range, the hybrid PVAc

is consistently more viscous than the neat system; however, at high shear rates, the hybrid-PVAc viscosity becomes highly variable, and the two traces appear to cross. This high shear-rate behavior is likely an artifact due to the cone and plate viscosity measurement method, where the small gap between the cone and plate (52 μm) influences the flow of the polymer dispersion. Large particles, or entangled polymer chains in the case of the mixed IPF/PVAc adhesive, were displaced by centrifugal force from the cone and plate assembly, rather than untangled and allowed to flow in the dispersion. Similar particle-size effects have been observed in other water-based polymer dispersions (Paris 2010). There, the extreme slope in the flow curves at high shear rates was lessened by using a concentric cylinder instrument geometry with a wider, and more uniform gap. Still, it is unclear which behavior is more closely related to what occurs in a wood-adhesive bondline during consolidation. Perhaps, wood anatomy imposes similar particle size separation effects during bonding. It is well known that only small molecular weight adhesive components can infiltrate wood cell walls (Frazier and Ni 1998; Jakes et al. 2013; Jakes et al. 2009; Kamke and Lee 2007); analogous particle size effects likely hinder bulk penetration as well, as most softwood tracheid lumens are approximately 50 μm or smaller (Panshin and De Zeeuw 1980).

Generally, low viscosity adhesives penetrate deeper than high viscosity adhesives (Kamke and Lee 2007); however, caution is given to making direct correlations between viscosity and penetration results, for multiple reasons. For instance, flow behavior during consolidation is highly dynamic and non-uniform. Interactions also occur between the wood and adhesives, such as moisture and ion exchange with the wood cell walls. Additionally, the temperature is not constant if laminates are being hot-pressed. And

lastly, it is difficult to predict what shear rate(s) adhesives are exposed to during bonding, which will have an impact on the viscosity of shear dependent systems. Crude shear-rate estimations can be made based on fluid mechanics, consolidation pressure and rate, and assumptions of wood cell geometry (Darby 2001; Paris 2010); however these assumptions often neglect the aforementioned dynamic changes that occur during bonding and inherent wood variability.

6.4.2 3D wood-adhesive penetration

Table 6-1 gives the 3D XCT penetration and adhesive area results; Figure 6-4 shows this same data, plotted in comparison to 2D FM measurements. Additional XCT gray-scale and segmented images of these different adhesive/species treatment combinations may be found elsewhere (Kamke et al. 2014; Paris et al. 2014a; Paris et al. 2013; Paris et al. 2014b). It is apparent that the WP and EP calculations yield different results. EP is simply a measure of the total adhesive area identified divided by the image width. While the end result has units of length, EP cannot adequately represent the complex pattern of penetration into the wood substrate. Ignoring magnitude, the trends of the EP and adhesive area charts in Figure 6-4 are nearly identical. The only difference occurred for the hybrid PVAc system, where the pure adhesive layer was counted in the area calculation; this was excluded in the EP calculation, as it represented adhesive that had not penetrated into the wood.

EP calculations have been useful for comparing various versions of the same adhesive type, where the flow behavior is relatively consistent (Modzel 2009; Paris 2010; Ren 2010; Sernek et al. 1999; Zheng et al. 2004). When investigating actual penetration

depths and distributions, the WP calculation perhaps offers a better comparison. For example, with the exception of SYP IPF, the mean EP results for all other treatments only ranges between 7 and 20 microns (Table 6-1), which is less than the diameter of a softwood, earlywood tracheid. Statistically, these treatments were not significantly different from each other. And yet, the XCT images showed vastly different penetration behavior between the adhesive types, and the IPF and IpMDI resins each showed adhesive-filled lumens several cells deep into the wood laminates. The similar EP results are partly explained because adhesive resin-solids spread rates were kept uniform for all treatment types. Thus, the total adhesive area, and therefore EP, was expected to be uniform between each treatment; any expected differences would be due to possible resin squeeze out, adhesive layer thickness, or the segmentation method and sensitivity to detect all the adhesive in the digital images. The larger EP values in the SYP IPF treatment are due to extensive wood crushing around the bondline in these specimens, as well as a high degree of cell wall penetration, which was identified according to the specified segmentation criteria. Greater discussion on both SYP IPF phenomena are provided elsewhere (Paris et al. 2014b). Nevertheless, the WP calculation, does show significant differences between each adhesive type, and between wood species within the IPF and IpMDI adhesives. Therefore, the remaining discussion will primarily focus on the WP results.

Table 6-1 XCT mean adhesive penetration results and coefficient of variation (COV) for each wood adhesive/species treatment

Species	Adhesive	WP	COV WP	EP	COV EP	Area	COV Area
		[μm]	[%]	[μm]	[%]	[mm^2]	[%]
DF	IPF	24.4	34.1	10.4	25.2	2.26×10^{-2}	25.2
HP	IPF	44.8	50.1	19.6	31.1	4.27×10^{-2}	31.1
SYP	IPF	42.5	37.6	42.8	40.5	9.30×10^{-2}	40.5
DF	hybrid PVAc	15.8	35.8	9.08	35.4	7.02×10^{-2}	29.1
HP	hybrid PVAc	27.2	24.3	11.4	23.0	6.23×10^{-2}	14.3
SYP	hybrid PVAc	18.4	33.3	9.13	49.3	7.43×10^{-2}	19.5
DF	IpMDI	154	13.9	14.4	32.9	3.13×10^{-2}	33.0
HP	IpMDI	104	24.6	7.44	18.0	1.60×10^{-2}	19.2
SYP	IpMDI	229	4.85	8.16	63.3	1.76×10^{-2}	64.2

Adhesive type and wood species were both significant factors in the WP results. Furthermore, a significant adhesive x species interaction was identified, meaning the magnitude of the species effect depended on which adhesive was used. Also, WP ANOVA results were consistent between the analysis only using the replicate means, and the analysis including the random error between each slice, as a nested factor.

One expects the adhesive types to influence penetration depth, as they have different chemistry, MW distribution, and were bonded under different conditions (Paris et al. 2014a; Paris et al. 2013; Paris et al. 2014b). The adhesive effect also appears to loosely correlate with viscosity, insofar as IpMDI had the lowest viscosity (Figure 6-3) and resulted in the deepest WP (Table 6-1 and Figure 6-4a). However, it is challenging to quantify the penetration dependence on viscosity. For the IPF and hybrid PVAc systems the relationship is less clear. WP results were not statistically different between the DF IPF and hybrid PVAc resins (Figure 6-4). Furthermore, hybrid PVAc flow curves (Figure 6-3) showed shear thinning and possible particle size effects. Without knowing the shear

rate during bonding, or the extent of the particle size effects, it is difficult to directly relate the penetration results to viscosity.

Penetration differences between species, within a given adhesive type, are perhaps more interesting, as all laminates were bonded under similar conditions. DF and SYP are both softwoods, which consist of highly ordered, and radially-aligned, longitudinal tracheids, of relatively uniform size. HP, on the other hand, is a diffuse porous hardwood, with a more random arrangement of both small-diameter fibers and large-diameter vessels.

Adhesive penetration patterns directly reflect these anatomical differences. Previous researchers noticed fairly uniform penetration patterns in softwoods, and more random adhesive distributions in hardwood vessels (Kamke and Lee 2007; Modzel 2009; Sernek et al. 1999). In the XCT data, HP penetration was also predominately observed in vessel elements (Paris et al. 2014a; Paris et al. 2013; Paris et al. 2014b), and quantitative WP results were noticeably different from the DF and SYP treatments for a given adhesive type. For instance, HP boxplots have a wider interquartile range than the softwoods for each adhesive (Figure 6-4a). In other words, the middle 50 % of HP penetration depths were spread over a broader range, which is a reflection of the more random and complex hardwood anatomy. Additionally, for IpMDI, which had the greatest WP results, HP penetration was significantly less than in the softwoods. This behavior was not the same with the IPF and hybrid PVAc systems. On the contrary, the IPF adhesive penetrated deeper into HP compared to DF. Yet, within-group variability was too large to observe significant differences in mean WP depths between HP and SYP IPF treatments, or between any of the species bonded with hybrid PVAc.

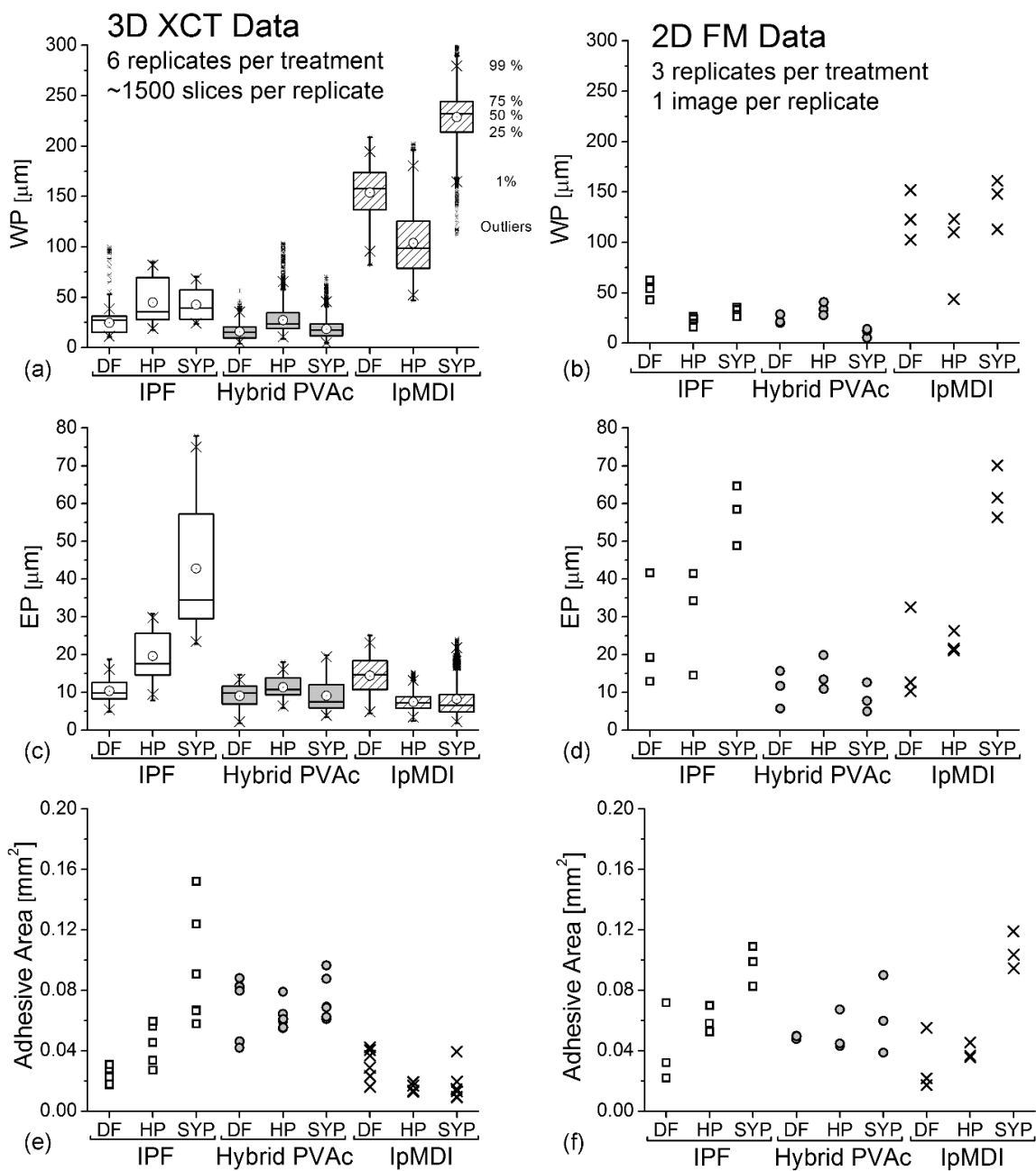


Figure 6-4 XCT (left) and FM (right) adhesive penetration results for each wood adhesive/species treatment; (a – b) WP; (c – d) EP; and (e – f) total adhesive area; results are the average from both sides of the bondline; boxplots (a and c) each contain ≈ 9000 data points (1500 slices \times 6 replicates) per treatment, center circles = treatment means; stacked data points (b, d, e, and f) = replicate means (6 for XCT, and 3 for FM)

Penetration results from 2D FM images appear to agree well with those collected from XCT sub-volumes (Figure 6-4). While the mean WP magnitudes may appear different between the two techniques, the three FM data points are generally within the range of the XCT results for each treatment. One exception to this observation is for SYP IpMDI. The FM data points, for this treatment, are considerably below the majority of the XCT data. SYP IpMDI also shows EP and adhesive area differences between XCT and FM measurements (Figures 6-4c v. d and 6-4e v. f). Figure 6-5 helps to illustrate this difference.

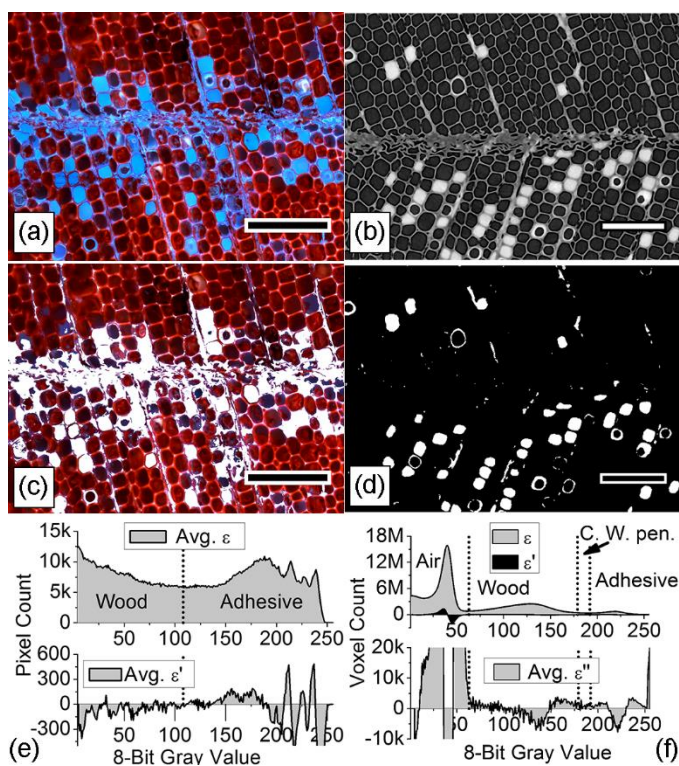


Figure 6-5 SYP IpMDI FM (left) vs. XCT (right) comparison; (a – b) original images, (c) segmented adhesive, overlain on original image, (d) binary bulk adhesive + cell wall penetration, and (e – f) 8-bit gray-scale histograms indicating threshold values (vertical lines); scale bars = 100 μ m

The two images in Figures 6-5a and b are from different specimens; however, they both show fairly similar IpMDI penetration distributions in the SYP laminates, and both were segmented at the minima in the corresponding gray-scale histograms. The difference between the measured penetration results is due to the amount of adhesive and cell wall penetration detected directly spanning across the wood lamina interface. The XCT image in Figure 6-5d shows almost no adhesive in this region; while the FM images in Figures 6-5a and c show a lot of adhesive near the interface. It was discussed elsewhere (Paris et al. 2014b) that IpMDI must have been present in this region of the XCT specimens, or else they would not have been capable of transferring stresses across the joint. It was suggested that the XCT resolution was too coarse to identify adhesive coating the cell walls in this region, and that the criteria for determining adhesive penetration in the cell walls may have been too strict (Paris et al. 2014b). In the XCT data, cell wall penetration was identified when both adhesive and cell wall occupied the same voxel space, and thus the gray-value for that voxel represented the average of both pure material attenuation signals. Detection of adhesive and cell wall penetration in the IpMDI FM data, on the other hand, was fundamentally different, and depended on the adsorption of Safranin stain into the wood cell walls. Perhaps the amount of adhesive present in the cell walls, at the interface, was below the XCT resolution limit and segmentation criteria, but was still enough to inhibit the Safranin absorption in the FM specimens. In consequence, more adhesive was detected at the joint interface in the FM images than the XCT images. EP and adhesive area results were thus greater for the FM specimens (Figure 6-4). The WP measurements, on the other hand, were lower because the added adhesive area was

adjacent to the wood lamina interface, and thus had a greater impact in the denominator of the WP equation than in the numerator.

XCT results showed SYP IpMDI specimens had the greatest overall mean WP and one of the largest ranges of WP values, compared to all other treatments (Table 6-1 and Figure 6-4a). Figure 6-6a shows the within and between replicate variability for all six SYP IpMDI replicates. Replicates 1 – 3 were excised from one original laminate, while 4 – 6 were excised from a second laminate. There appears to be no significant difference between replicates or laminates; rather, the majority of the treatment variability is due to differences between the individual slices within each replicate. Furthermore, these sub-volume data stacks were only approximately 2 mm in the longitudinal direction. This shows penetration data can vary considerably above and below a single 2D image-plane, as in traditional microscopy analyses. Within-specimen variability could also result from unbalanced penetration from one half of the bondline to the other, as discussed elsewhere (Paris et al. 2013); however, the penetration results here show the average of both lamina in each slice.

Figure 6-6b shows WP results for each SYP IPF replicate, and in this treatment there appears to be very little within specimen variability. Instead, each individual specimen has a different mean WP depth, and moreover, there appears to be a strong difference between the two individual laminates. Replicates 4 – 6 all have higher WP values than replicates 1 – 3, which indicates that even matched specimens, prepared with the same manufacturing parameters, can still show considerable variability.

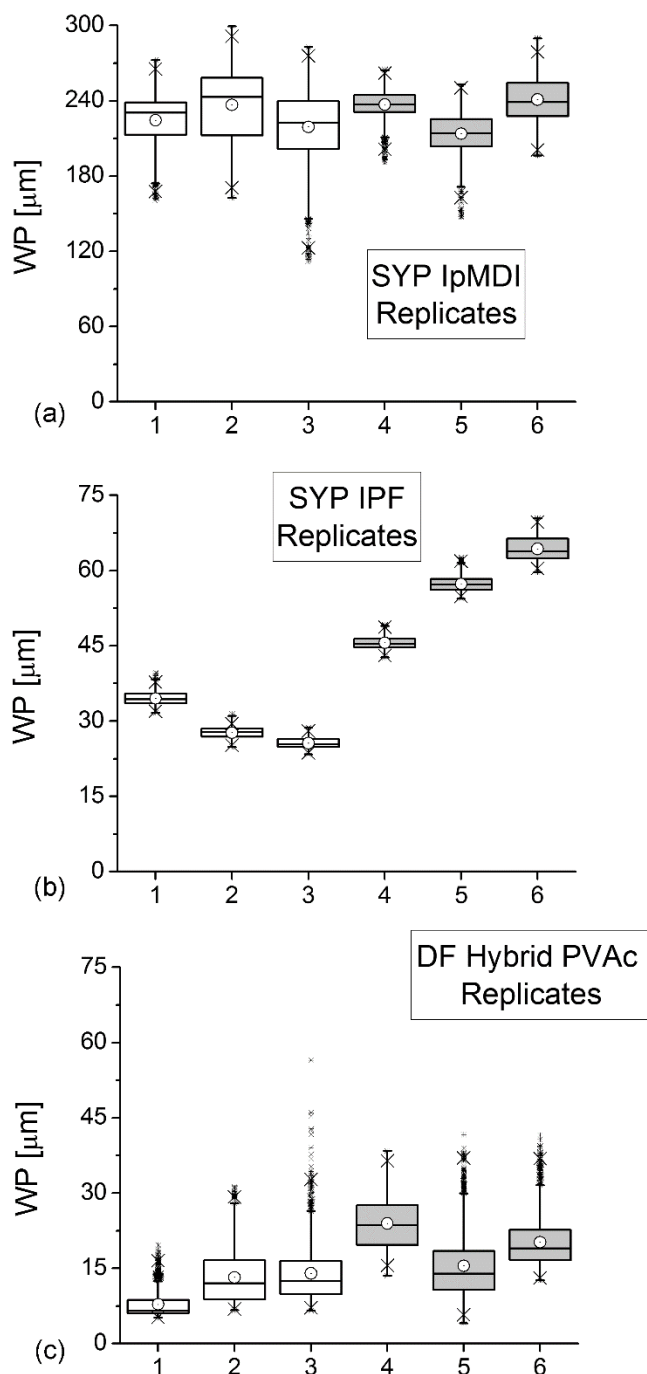


Figure 6-6 Adhesive XCT WP results (average of both bondline sides) by replicate for (a) SYP IpMDI, (b) SYP IPF, and (c) DF hybrid PVAc; $n \approx 1500$ slices per replicate; center circles = specimen means; replicates 1 – 3 and 4 – 6 were excised from 2 separate original laminates

DF hybrid PVAc replicates, in Figure 6-6c, show relatively uniform within-specimen variability, and do not exhibit significant differences between laminates. Replicate 4, however, has greater WP results than the other replicates. With XCT, it is easy to rapidly scan through the image stacks, and view the 3D replicate sub-volumes from multiple angles to investigate the source of any observed differences. Figure 6-7 shows several views of the DF hybrid PVAc replicate 4 sub-volume, and it is readily apparent that one side of the bondline had a significant slope-of-grain. The radial-longitudinal (RL) plane, in Figure 6-7a, shows how adhesive can easily flow into open tracheids at the wood lamina interface, and travel long distances in the cell lumens. A single cross-section slice through this region (Figure 6-7c) shows adhesive-filled cell lumens not connected to the bondline, or to each other. Without the additional RL view, it would be difficult to know how the adhesive got to these locations, or how they were subsequently impacting mechanical joint performance. The RL views in Figure 6-7a and b also show lateral adhesive flow in ray cells. Figure 6-7b in particular, shows the effect of a lateral resin canal, in the center of a row of ray cells, known as a fusiform ray (identified with white arrows). The cross-section slice in Figure 6-7d runs directly through the center of this fusiform ray, and the tangential-longitudinal (TL) view in Figure 6-7e looks directly down its length. Figure 6-7f shows the full segmented adhesive phase in this sub-volume region of replicate 4. It is clear in this 3D view how factors such as slope-of-grain and different anatomical features can have a dramatic effect on the wood-adhesive penetration behavior.

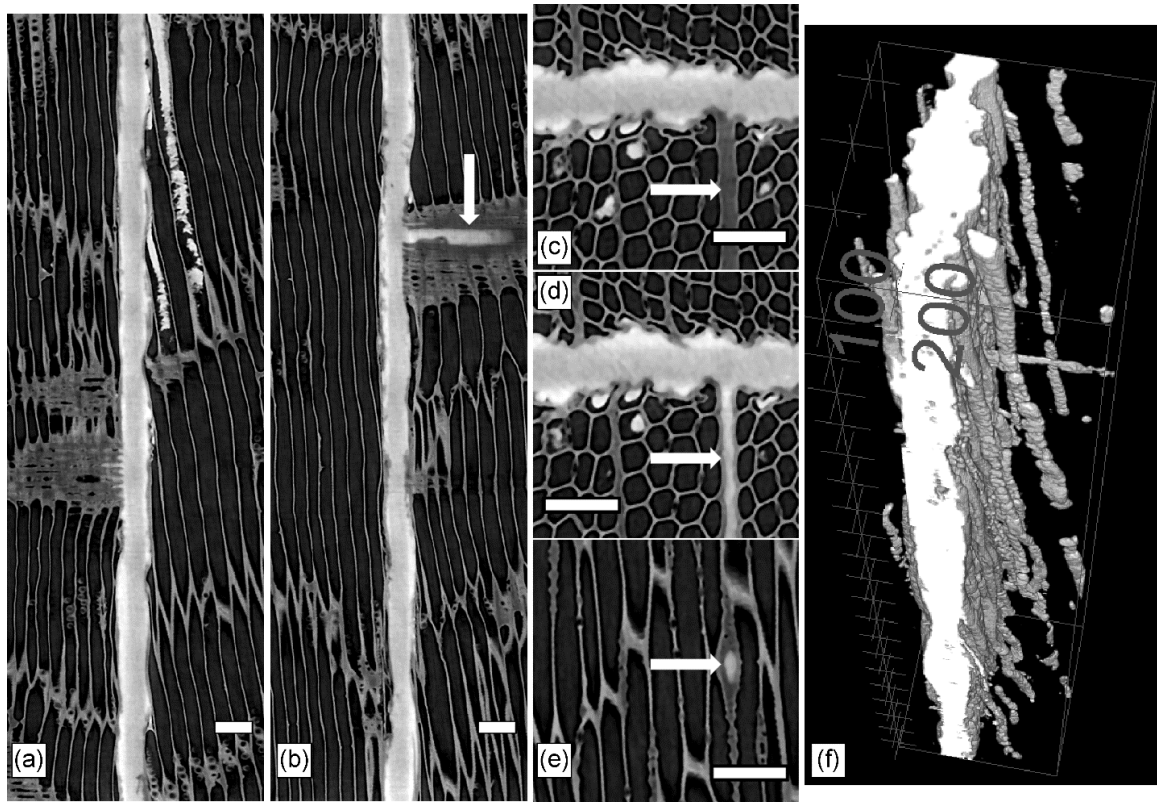


Figure 6-7 DF hybrid PVAc replicate 4 sub-volume: (a - b) RL planes show effects of grain angle, ray cells and a fusiform ray (arrows) on penetration, (c - d) transverse planes, 23 μm apart, above and in fusiform ray, (e) TL view into fusiform ray, and (f) 3D adhesive sub-volume (μm box dimensions); scale bars = 100 μm (a - e)

XCT offers other unique information about the in-situ cure behavior and resin structures in wood-adhesive bondlines. For instance, isocyanate resins release carbon dioxide (CO_2) during cure in the presence of moisture (Frazier 2003), and pMDI wood adhesives are known to react with bound water in wood cell walls (Yelle et al. 2009). It is also known that the CO_2 can cause bubbles to form in neat films of cured isocyanate adhesives (Ren 2010; Zheng 2002). However, bubbles were also clearly visible in IpMDI bondlines

imaged with XCT, as shown in Figure 6-8. The cross-section view in Figure 6-8a shows a HP vessel containing cured IpMDI, and it appears the adhesive merely coated the inner lumen surfaces. Such behavior has been previously reported as typical for pMDI resins, and that pMDI wicks along the cell lumen surfaces (Buckley et al. 2002; Zheng 2002). However, bulk flow occurred with the IpMDI adhesive used here, and the appearance of coating the inner lumen surface was an artifact of the 2D image-plane transecting a bubble. Further down the same vessel column (Figure 6-8b), cured adhesive completely fills the lumen space. The RL and 3D views of this vessel, in Figures 6-8c and d, show the distinct oval and concave impressions made by the CO₂ bubbles during adhesive cure. Similar bubble formations were also clearly seen in DF and SYP IpMDI 3D bondlines (Paris et al. 2013; Paris et al. 2014b).

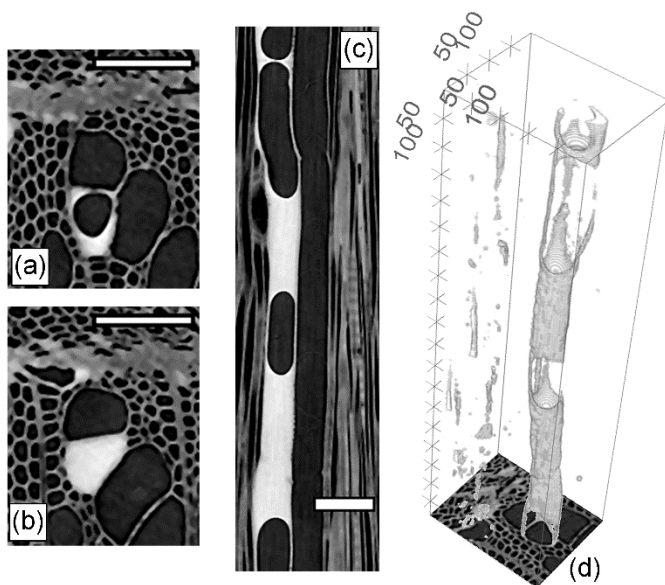


Figure 6-8 IpMDI bubbles in HP vessel; (a) sub-volume top slice, (b) 400 μm below top ($\sim 1/3$ length), (c) RL plane through vessel, and (d) segmented adhesive column (μm box dimensions); scale bars = 100 μm (a – c)

3D reconstructions of IPF bondlines also showed interesting in-situ adhesive cure behavior. Distinct horizontal cracks were observed along the length of pure IPF adhesive columns, as shown in Figure 6-9a. Cross-linked PF adhesives are often brittle, and perhaps these cracks formed due to restrained resin shrinkage during resin cure, or cooling following laminate hot pressing. Similar cracks were observed in 3D micro XCT analyses of wood laminates bonded with urea formaldehyde, another brittle wood adhesive (Hass et al. 2012). It is yet to be determined how cracks like these might impact bond performance. Perhaps the effect will not be significant, as pure IPF columns were typically surrounded by regions of cell wall penetration (Figure 6-9b), which may distribute stress concentrations around these cracks into the wood cell walls. Answering such questions in the past would have been fairly difficult using conventional 2D microscopy and matched specimens for mechanical testing. However, non-destructive XCT bondline analyses, paired with the 3D numerical model currently in development (Kamke et al. 2014; Muszynski et al. 2014; Nairn et al. 2014), could be useful in understanding the relationships between adhesive penetration and structure and mechanical joint performance.

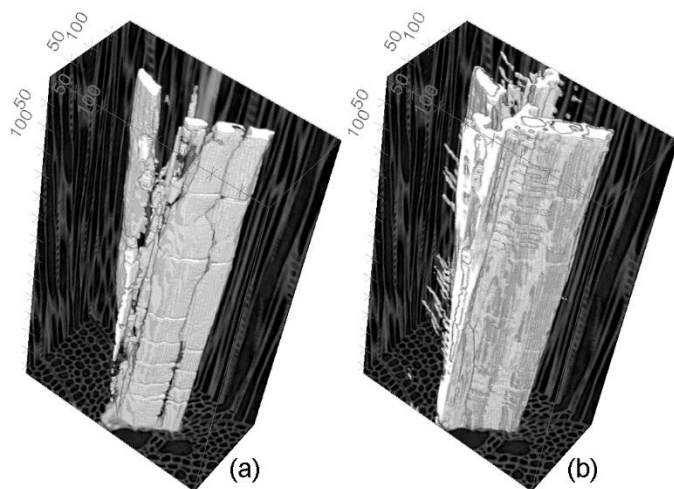


Figure 6-9 IPF cured adhesive cracks in HP vessels; (a) segmented bulk adhesive, and (b) total adhesive including cell wall penetration (μm box dimensions)

6.5 Conclusion

Micro XCT was used to analyze the 3D penetration and distribution behavior of three wood adhesives in bondlines prepared from three different wood species. Penetration depth was calculated with two separate equations, namely effective penetration and a weighted penetration calculation, introduced here. The adhesives, which were all tagged with iodine for greater X-ray attenuation, had different chemistry, molecular weight, viscosity, and cure mechanisms, and were therefore expected to result in different penetration depths. Indeed, reconstructed sub-volumes exhibited vastly different adhesive distribution profiles between the different treatment types. However, effective penetration results, which divide the total adhesive area identified in an image by the image width, were unable to identify many treatment differences. The weighted penetration calculation, on the other hand, which accounts for the area of an identified adhesive element as well as the perpendicular distance it penetrated into a wood laminate, was able

to discern clear differences between adhesive type, and between species bonded with a particular adhesive. Moreover, weighted penetration results from XCT specimens agreed with those from specimens imaged with 2D fluorescent microscopy. Replicate comparisons within a particular adhesive/species treatment showed penetration results can be highly variable between laminates bonded with the same experimental conditions, between specimens excised from the same initial laminates, and along the length of an individual specimen. Furthermore, digital XCT image-stacks of wood-adhesive bondlines allow for rapid assessment of adhesive penetration from multiple view-points and specimen orientations. Lastly, segmented 3D adhesive phases in XCT sub-volumes provided novel views at the in-situ, cured resin structures.

6.6 Acknowledgements

Financial support was provided by the Wood-Based Composites Center, a National Science Foundation Industry/University Cooperative Research Center.

6.7 References

Buckley, C. J., Phanopoulos, C., Khaleque, N., Engelen, A., Holwill, M. E. J. and Michette, A. G. (2002) Examination of the penetration of polymeric methylene di-phenyl-di-isocyanate (pMDI) into wood structure using chemical-state x-ray microscopy. *Holzforschung* 56, 2, 215-222.

Cao, Y. 2010: Characterization of PF/PVAc hybrid adhesive-wood interaction and its effect on wood strand composites performance. *Department of Civil and Environmental Engineering*, Washington State University, Pullman, WA.

Darby, R. Chemical engineering fluid mechanics. Marcel Dekker, New York, 2001

Ebewele, R. O., River, B. H. and Koutsky, J. A. (1986) Relationship between phenolic adhesive chemistry and adhesive joint performance - Effect of filler type on fracture energy. *Journal of Applied Polymer Science* 31, 7, 2275-2302.

Ellis, E. (2006) Solutions to the problem of substitution of ERL 4221 for vinyl cyclohexene dioxide in Spurr low viscosity embedding formulations. *Microscopy Today* 14, 4, 32-33.

Evans, P. D., Morrison, O., Senden, T. J., Vollmer, S., Roberts, R. J., Limaye, A., Arns, C. H., Averdunk, H., Lowe, A. and Knackstedt, M. A. (2010) Visualization and numerical analysis of adhesive distribution in particleboard using X-ray micro-computed tomography. *International Journal of Adhesion and Adhesives* 30, 8, 754-762.

Frazier, C. E. 2003: Isocyanate wood binders. In: Pizzi, A. and Mittal, K. L., editors, *Handbook of Adhesive Technology*, New York: Marcel Dekker, Inc.

Frazier, C. E. and Ni, J. W. (1998) On the occurrence of network interpenetration in the wood-isocyanate adhesive interphase. *International Journal of Adhesion and Adhesives* 18, 2, 81-87.

Frihart, C. R. 2005: Wood adhesion and adhesives. In: Rowell, R. M., editor, *Handbook of Wood Chemistry and Wood Composites*, New York: Taylor & Francis Group.

Gindl, W., Sretenovic, A., Vincenti, A. and Muller, U. (2005) Direct measurement of strain distribution along a wood bond line. Part 2: Effects of adhesive penetration on strain distribution. *Holzforschung* 59, 3, 307-310.

Hass, P., Wittel, F., Mendoza, M., Herrmann, H. and Niemz, P. (2012) Adhesive penetration in beech wood: experiments. *Wood Science and Technology* 46, 1-3, 243 - 256.

Hass, P., Wittel, F. K., McDonald, S. A., Marone, F., Stampanoni, M., Herrmann, H. J. and Niemz, P. (2010) Pore space analysis of beech wood: The vessel network. *Holzforschung* 64, 5, 639-644.

Jakes, J. E., Gleber, S.-C., Vogt, S., Hunt, C. G., Yelle, D. J., Grigsby, W. and Frihart, C. R. 2013: New synchrotron-based technique to map adhesive infiltration in wood cell walls. In: *Proceedings of the 36th Annual Meeting of the Adhesion Society*, Datona Beach, FL, USA, 3 p.

Jakes, J. E., Yelle, D. J., Beecher, J. F., Frihart, C. R. and Stone, D. S. 2009: Characterizing polymeric methylene diphenyl diisocyanate reactions with wood: 2. Nano-indentation. In: Frihart, C. R., Hunt, C. G. and Moon, R. J., editors, *Proceedings of the International Conference on Wood Adhesives 2009*, Lake Tahoe, NV, USA: Forest Products Society, 11 p.

Johnson, S. E. and Kamke, F. A. (1992) Quantitative-analysis of gross adhesive penetration in wood using fluorescence microscopy. *Journal of Adhesion* 40, 1, 47-61.

Kamke, F. A. and Lee, J. N. (2007) Adhesive penetration in wood - a review. *Wood and Fiber Science* 39, 2, 205-220.

Kamke, F. A., Nairn, J. A., Muszynski, L., Paris, J. L., Schwarzkopf, M. and Xiao, X. (2014) Methodology for micro-mechanical analysis of an adhesive bond using micro computed x-ray tomography and numerical modeling. *Wood and Fiber Science* 46, 1.

Mannes, D., Marone, F., Lehmann, E., Stampanoni, M. and Niemz, P. (2010) Application areas of synchrotron radiation tomographic microscopy for wood research. *Wood Science and Technology* 44, 1, 67-84.

Mannes, D., Niemz, P. and Lehmann, E. (2009) Tomographic investigations of wood from macroscopic to microscopic scale. *Wood Research* 54, 3, 33-44.

Marra, A. Technology of wood bonding: Principles in practice. Van Nostrand Reinhold, New York, 1992

Mayo, S. C., Chen, F. and Evans, R. (2010) Micron-scale 3D imaging of wood and plant microstructure using high-resolution X-ray phase-contrast microtomography. *Journal of Structural Biology* 171, 2, 182-188.

Modzel, G. 2009: Computed X-ray analysis of wood-adhesive bonds. *Wood Science and Engineering*, Oregon State University, Corvallis, OR: 240.

Modzel, G., Kamke, F. A. and De Carlo, F. (2011) Comparative analysis of a wood-adhesive bondline. *Wood Science and Technology* 45, 1, 147-158.

Muszynski, L., Kamke, F. A., Nairn, J. A., Schwarzkopf, M. and Paris, J. L. 2014: Integrated method for multi-scale/multi-modal investigation of micro-mechanical wood-adhesive interaction. In: Frihart, C. R., Hunt, C. G. and Yan, N., editors, *Proceedings of*

the International Conference on Wood Adhesives 2013, Toronto, Ontario, CAN: Forest Products Society, 16 p.

Nairn, J. A. (2006) Numerical simulations of transverse compression and densification in wood. *Wood and Fiber Science* 38, 4, 576-591.

Nairn, J. A., Kamke, F. A., Muszynski, L., Paris, J. and Schwarzkopf, M. 2014: Direct 3D Numerical Simulation of stresses and strains in wood adhesive bondlines based on the actual specimen anatomy from x-ray tomography data. In: Frihart, C. R., Hunt, C. G. and Yan, N., editors, *Proceedings of the International Conference on Wood Adhesives 2013*, Toronto, Ontario, CAN: Forest Products Society, 11 p.

Onouye, B. and Kane, K. *Statics and strength of materials for architecture and building construction*. Pearson Prentice Hall, Upper Saddle River, N.J.,2007

Panshin, A. J. and De Zeeuw, C. *Textbook of wood technology : structure, identification, properties, and uses of the commercial woods of the United States and Canada*. McGraw-Hill, New York,1980

Paris, J., Kamke, F., Mbachu, R. and Gibson, S. (2014a) Phenol formaldehyde adhesives formulated for advanced X-ray imaging in wood-composite bondlines. *Journal of Materials Science* 49, 2, 580-591.

Paris, J. L. 2010: Carboxymethylcellulose acetate butyrate water-dispersions as renewable wood adhesives. *Department of Wood Science and Forest Products*, Virginia Tech, Blacksburg, VA: 169 p.

Paris, J. L., Kamke, F., Nairn, J. A., Schwarzkopf, M. and Muszynski, L. 2013: Wood-adhesive penetration: non-destructive, 3D visualization and quantification. In: Frihart, C. R., Hunt, C. G. and Yan, N., editors, *Proceedings of the International Conference on Wood Adhesives 2013*, Toronto, Ontario, CAN: Forest Products Society, 13 p.

Paris, J. L., Kamke, F. A. and Xiao, X. (2014b) X-ray Computed Tomography of Wood-Adhesive Bondlines: attenuation and phase-contrast effects. *Wood Science and Technology To Be Submitted*.

Rasband, W. S. 1997 - 2012: ImageJ. In: *U. S. National Institutes of Health*, <http://imagej.nih.gov/ij/>, Bethesda, Maryland, USA.

Ren, D. 2010: Moisture-cure polyurethane wood adhesives: wood/adhesive interactions and weather durability. *Macromolecular Science and Engineering*, Virginia Tech, Blacksburg, VA.

River, B. H., Vick, C. B. and Gillespie, R. H. 1991: Wood as an adherend. In: Minford, J. D., editor, *Treatise on Adhesion and Adhesives*, New York: Marcel Dekker, Inc.

Schindelin, J., Arganda-Carreras, I., Frise, E., Kaynig, V., Longair, M., Pietzsch, T., Preibisch, S., Rueden, C., Saalfeld, S. and Schmid, B. (2012) Fiji: an open-source platform for biological-image analysis. *Nature Methods* 9, 7, 676-682.

Schultz, J. and Nardin, M. 1994: Theories and mechanisms of wood adhesion. In: Pizzi, A. and Mittal, K. L., editors, *Handbook of Adhesive Technology*, New York: Marcel Dekker, Inc., 19-33.

Schwarzkopf, M., Muszynski, L. and Nairn, J. 2014: Stereoscopic optical method for the assessment of load transfer patterns across the adhesive bond interphase. In: Frihart, C. R., Hunt, C. G. and Yan, N., editors, *Proceedings of the International Conference on Wood Adhesives 2013*, Toronto, Ontario, CAN: Forest Products Society, 12 p.

Sernek, M., Resnik, J. and Kamke, F. A. (1999) Penetration of liquid urea-formaldehyde adhesive into beech wood. *Wood and Fiber Science* 31, 1, 41-48.

Spurr, A. R. (1969) A low-viscosity epoxy resin embedding medium for electron microscopy. *Journal of ultrastructure research* 26, 31-43.

Standfest, G., Kranzer, S., Petutschnigg, A. and Dunky, M. (2010) Determination of the microstructure of an adhesive-bonded medium density fiberboard (MDF) using 3-D sub-micrometer computer tomography. *Journal of Adhesion Science and Technology* 24, 8-10, 1501-1514.

Standfest, G., Kutnar, A., Plank, B., Petutschnigg, A., Kamke, F. and Dunky, M. (2012) Microstructure of viscoelastic thermal compressed (VTC) wood using computed microtomography. *Wood Science and Technology*.

Steppe, K., Cnudde, V., Girard, C., Lemeur, R., Cnudde, J. P. and Jacobs, P. (2004) Use of X-ray computed microtomography for non-invasive determination of wood anatomical characteristics. *Journal of Structural Biology* 148, 1, 11-21.

Trtik, P., Dual, J., Keunecke, D., Mannes, D., Niemz, P., Stähli, P., Kaestner, A., Groso, A. and Stampanoni, M. (2007) 3D imaging of microstructure of spruce wood. *Journal of Structural Biology* 159, 1, 46-55.

Walther, T. and Thoemen, H. (2009) Synchrotron X-ray microtomography and 3D image analysis of medium density fiberboard (MDF). *Holzforschung* 63, 5, 581-587.

White, M. S. (1977) Influence of resin penetration on the fracture toughness of wood adhesive bonds. *Wood Science* 10, 1, 6-14.

Yelle, D. J., Jakes, J. E., Ralph, J. and Frihart, C. R. 2009: Characterizing polymeric methylene diphenyl diisocyanate reactions with wood: 1. High-resolution solution-state NMR spectroscopy. In: Frihart, C. R., Hunt, C. G. and Moon, R. J., editors, *Proceedings of the International Conference on Wood Adhesives 2009*, Lake Tahoe, NV, USA: Forest Products Society, 5 p.

Zheng, J. 2002: Studies of PF resole/isocyanate hybrid adhesives. Virginia Polytechnic Institute and State University.

Zheng, J., Fox, S. C. and Frazier, C. E. (2004) Rheological, wood penetration, and fracture performance studies of PF/pMDI hybrid resins. *Forest Products Journal* 54, 10, 74-81.

Zuur, A. F. Mixed effects models and extensions in ecology with R. Springer, New York, NY, 2009

CHAPTER 7. SUMMARY AND CONCLUSIONS

7.1 Summary

Wood-adhesive penetration plays an important role in bond performance and durability; however, traditional methods for analyzing penetration depth and distribution involve damaging specimen preparation and results in 2D surface data. It is often difficult to interpret the penetration/performance relationship from 2D bondline photomicrographs, as critical adhesive connectivity and distribution information is lost above and below the image-plane. Furthermore, matched specimens are often used for penetration and mechanical testing in parallel, and correlations are made between the two sets of results. Yet, wood is a porous, heterogeneous and orthotropic material, and significant variability can exist between matched specimens. In this work, micro x-ray computed tomography (XCT) was used to visualize 3D, adhesive penetration in wood bondlines. As XCT is a non-destructive imaging technique, the same specimens were preserved for subsequent mechanical testing, thus eliminating variability between matched specimens.

Additionally, digital XCT datasets were used as direct input to a numerical model to simulate mechanical performance and stress distribution in adhesively-bonded wood joints, while quantitatively accounting for the role of adhesive penetration. These three separate analyses, XCT, mechanical testing and numerical modeling, were all part of a broader, collaborative project to study micro-scale wood/adhesive interactions. The bulk of this dissertation, however, focused on XCT imaging, adhesive physical and chemical properties that effect x-ray attenuation, and 3D penetration depth and variability.

Three adhesive systems, with different flow behavior, cure mechanisms, and mechanical properties, were used to bond wood laminate specimens prepared from three different wood species with unique anatomical features. The adhesives, phenol formaldehyde (IPF), polymeric diphenylmethane diisocyanate (IpMDI), and a hybrid polyvinyl acetate (hybrid PVAc), were uniformly tagged with iodine to provide sufficient x-ray absorption contrast for quantitative material segmentation from wood cell walls in reconstructed XCT datasets. The wood species included two softwoods, Douglas-fir (DF) and loblolly pine (SYP), as well as one hardwood, hybrid poplar (HP).

Combined elemental analyses and fluorescence microscopy (FM) images were used to confirm that iodine tags remained associated with the adhesive polymers throughout bonding. Additionally, cured density and theoretical polymer repeat unit structures were used to calculate and predict adhesive x-ray attenuation behavior relative to wood cell walls. Preliminary x-ray radiographs and XCT scans provided important benchmark results to assist in adhesive formulation and XCT parameter optimization.

Once the appropriate adhesive systems and procedures were established, 54 bondline specimens, representing six replicates from the nine different adhesive/species combinations were scanned at the Advanced Photon Source synchrotron at the Argonne National Laboratory, in Argonne, Illinois. The resulting radiographs were reconstructed into a 3D image dataset with an absorption contrast, filtered back projection algorithm. Specimen scan volumes were approximately 8 mm³, and had voxel side lengths of 1.45 μm. Centralized, sub-volumes, approximately 0.725 mm thick (radial, perpendicular to bondline) x 1.09 mm wide (tangential, parallel to bondline) x 2.18 mm tall (longitudinal,

along the bondline), were digitally excised from the full datasets, and separated into wood and adhesive material components with gray-scale, threshold operations. Segmented adhesive volumes showed novel views of the 3D distribution patterns and cured network structures, and were used to calculate penetration depth with two separate equations. Pairwise results comparisons showed different treatment effects owing to both adhesive type and wood species, and provided a detailed view of the inherent anatomical variability in wood bondlines. XTC penetration results were also compared to those from 2D fluorescence bondline micrographs of matched specimens. While the two sets of results showed good agreement, it was obvious that the 3D measurement provided a broader view of the penetration variability.

7.2 Conclusions

Three adhesive systems were prepared that provided sufficient x-ray absorption contrast for quantitative material segmentation in reconstructed XCT wood-bondline datasets. Cured IPF, IpMDI, and hybrid PVAc adhesives contained between 20 – 40 wt% iodine, which was confirmed by neutron activation analysis. Energy dispersive spectroscopy (EDS) elemental mapping and FM confirmed iodine remained associated with cured adhesive polymers in the wood bondlines, and did not migrate independently during bonding. Preliminary x-ray experiments and attenuation calculations showed adhesive absorption contrast, relative to wood, improved with increased cured resin density and iodine concentration. However, gray-scale threshold segmentation between three material phases, air, wood and adhesive, required a balance in material contrast to minimize overlap between any two material gray-value histogram peaks. This balance was partially

accomplished by using an x-ray beam energy of 15.3 KeV, which was below the iodine k-edge. A higher beam energy might have improved the wood/adhesive contrast, but would have caused a greater overlap between the wood and air gray-level values.

The effect of phase-contrast edge enhancement fringes must also be accounted for in quantitative XCT analyses of wood. Excessively dark and bright voxels are manifested to the air and cell wall sides, respectively, of the edge of an empty cell lumen. The dark fringes can be segmented collectively with the air phase, but the bright fringes can obscure the material signals between wood and adhesive. The relative extent of these effects can be reduced with small specimen-to-scintillator detector distances; however, phase-contrast effects may be all together eliminated if XCT data is reconstructed with quantitative phase retrieval algorithms.

Partial volume artifacts can cause material gray-level peak broadening and overlap, which in turn reduces segmentation confidence. This effect is particularly common at edges, where two different materials exist within the same voxel space, and the assigned gray value represents an average. However, partial volume effects also showed evidence of cell wall penetration for IPF and IpMDI, which both contained low molecular weight pre-polymer adhesive molecules. Pure material segmentation within the cell walls was below the resolution limits in this study, and cell wall penetration was not observed for the hybrid PVAc adhesive system.

Segmented 3D, adhesive sub-volumes also showed unique cure behavior for the IPF and IpMDI systems. Distinct transverse cracks were observed in cured IPF columns in penetrated lumens; which were likely the result of differential shrinkage and thermal

expansion behavior between the brittle adhesive and wood cell wall. Additionally, the impressions of gas bubbles, which formed during resin cure, were clearly visible in 3D IpMDI adhesive columns, filling wood cell lumens. Cross-section 2D photomicrographs through similar bubbles have misled previous researches to conclude that isocyanate resins penetrate via wicking along wood cell walls rather than by bulk flow.

Penetration results were considerably different between two separate equations. Effective penetration, which is merely a function of adhesive area rather than a perpendicular penetration distance to the bondline, showed few differences between the adhesive treatments. This is understandable as adhesive spread rate based on solids content was constant between all treatment types. Weighted penetration (WP), on the other hand, which accounted for the distance and area of identified adhesive elements, was a better descriptor of adhesive distribution. WP results depended on adhesive type, wood species and local anatomical features in the vicinity of the bondline. Additional variability was identified between replicates of the same treatment type, along the length of individual specimens, and between different sides of the bondline in individual XCT image slices. IpMDI showed the deepest WP results, and had the lowest liquid adhesive viscosity. The hybrid PVAc adhesive resulted in shallowest WP depth; however, these results were not as easily correlated with viscosity as the hybrid PVAc adhesive exhibited shear thinning behavior. Moreover, both the viscosity and penetration behavior for the hybrid PVAc system may have been influenced by particle size effects due to molecular entanglements.

The primary technical objectives of this research were achieved. Methods were developed to identify 3D wood-adhesive penetration with non-destructive XCT,

quantitatively segmenting the data into individual material components for future analyses.

7.3 Limitations and Future Work

This work was part of a broader and ongoing project. The XCT datasets are being used as realistic-structure material points for numerical modeling. Results from the broader project will help to quantify the relationship between wood-bondline joint performance and 3D wood-adhesive penetration behavior. However, the methods and adhesive formulations described in this work are directly transferable to future research, as well.

One limitation determined in this work relates to tagging efficacy and uniformity. In poly-disperse and pre-polymeric liquid adhesives, it is suggested that tagging the initial monomer units will result in the most uniform tag distribution, and thus segmentation confidence. This was the case for the IPF adhesive. For IpMDI, a commercial pMDI resin was reacted to substitute only a portion of the available isocyanate groups with iodine, and for the hybrid PVAc, a neat emulsion PVAc was blended with the IPF adhesive. In each case, no evidence of independent tag migration or phase separation was detected, and XCT adhesive gray-values appeared uniform across all images. However, caution is given to always check for tag uniformity in research efforts where adhesives require modifying for analytical detection, as such inhomogeneity could result in misinterpretation of results.

Certainly, the described IPF adhesive, and various formulations of it, can be readily used in various wood-adhesion studies. Specific effects of individual factors known to influence bond performance, such as adhesive spread rate, different wood species, wood

surface energy and treatments, or consolidation pressure, temperature and rate, can be systematically investigated with new advanced analytical methods, like XCT and other elemental analyses. One project, which just began, involves new specimens bonded with different molecular weight formulations of the IPF adhesive. New bondline specimens will be scanned with micro XCT, before and after accelerated weathering, to assess the role of cell wall penetration on bond durability. Another aspect of that project is to use nano-XCT, and similar material segmentation procedures for separate wood cell wall polymers and adhesive material in penetrated cell walls, in an attempt to correlate cell wall penetration results with resin molecular weight.

Another novel research idea would be to use 3D XCT analyses and pairwise numerical modeling to investigate the effects of viscosity and many other dynamic factors on bulk adhesive flow during wood bonding. Adhesive viscosity undoubtedly plays a role in adhesive penetration, but it is hard to draw strong correlations due to multiple sources of variability. Many wood adhesives show shear dependent behavior, but it is difficult to determine the nature of the shear forces and the shear rates experienced during bond consolidation. Furthermore, multiple additional physical factors effect adhesive penetration during bonding, such as variable temperature and pressure, cellular anatomy, and preferential water absorption. These dynamic forces and factors could be simulated with the right numerical model, and XCT analyses of segmentable adhesives could help validate such a model.

The need for iodine tags to generate sufficient adhesive contrast was, in itself, another project limitation. It is true that these adhesives did, and will, perform differently than

their unmodified controls, and thus these adhesive penetration and the subsequent performance results are not directly representative of commercial systems. However, XCT instrumentation and reconstruction algorithms continue to evolve and improve. A quantitative phase retrieval algorithm was demonstrated here, which identified x-ray phase shifts in the source beam, as it traversed through materials with different index of refraction. Perhaps future algorithm refinement, or different algorithms all together, may be able to provide XCT bondline data that can be quantitatively segmented without relying on material absorption contrast. Alternatively, such image segmentation techniques may rely on phase contrast retrieval algorithms or perhaps image texture properties.

Lastly, one other limitation of this work relates to partial volume effects and the discretization of digital image information to single-value pixels. The size of pixels, or voxels in 3D, is a function of camera or detector grid spacing and image magnification optics. Features smaller than the pixel size cannot be clearly resolved, and if multiple materials occupy the same pixel space, the value represents an average. This was a noticeable issue with XCT and EDS data for IpMDI-bonded specimens. Adhesive, or iodine signals, could not be clearly resolved at the interface between the two sides of the bondline. Bondline FM images, on the other hand, did appear to show adhesive along the interface. It was discussed that disagreement was because all three methods detected fundamentally different physical signals, representing adhesive. FM images depended on stain adsorption into wood cell walls, while EDS depended on iodine signal counts, and XCT images were formed based on x-ray attenuation. Pixels and voxels at the laminate interface likely contained a greater amount of cell wall than adhesive, and thus the

assigned gray-values and iodine signals were closer to that of pure wood. Perhaps, though, even a small amount of IpMDI sufficiently hindered stain adsorption in cell walls along the interface, and thus FM images appeared to detect adhesive. Higher resolution XCT or EDS scans, directly along this interface, could likely help elucidate these issues.

APPENDIX A. METHODOLOGY FOR MICRO-MECHANICAL
ANALYSIS OF WOOD-ADHESIVE BONDS USING
XCT AND NUMERICAL MODELING

Frederick A. Kamke, John Nairn, Lech Muszyński, Jesse L. Paris, Matthew Schwarzkopf,
and Xianghui Xiao

Wood and Fiber Science

2014, Volume 46, Issue 1

Society of Wood Science and Technology

Methodology for Micro-Mechanical Analysis of Wood-Adhesive Bonds Using XCT and
Numerical Modeling

Frederick A. Kamke^{a,*†}, John A. Nairn^{a,†}, Lech Muszyński^{a,†}, Jesse L. Paris^a, Matthew
Schwarzkopf^a and Xianghui Xiao^b

^a Department of Wood Science & Engineering, Wood-Based Composites Center, Oregon
State University, 119 Richardson Hall, Corvallis, OR 97331, USA

^b Advanced Photon Source, Beamline 2-BM-B, Argonne National Laboratory, Argonne,
IL 60439, USA

* Corresponding Author. Tel.: +541 737 8422; Fax +542 737 3385
E-mail address: Fred.Kamke@OregonState.edu (F. A. Kamke)

† Member Society of Wood Science and Technology (SWST)

A.1 Abstract

The structural performance of wood-adhesive bonds depends on their ability to transfer stress across an interface of dissimilar materials, namely cell wall substance and cured polymeric adhesive. The interphase region of the bond consists of cell wall substance, voids, and voids filled with adhesive. An integrated method to numerically model the micro-mechanical behavior of this system is described. The method includes micro x-ray computed tomography (XCT) to define the three-dimensional (3D) structure of the bond on a micron scale. Tomography data was used as direct input to a micro-mechanics model. The model provided a 3D representation of equivalent strain and equivalent stress of the adhesive bond under load, and furthermore, integrated the microstructure of the interphase region into the solution. The model was validated using lap-shear test results from the same specimens that were scanned for XCT. Optical measurement and digital image correlation techniques provided full-field displacement data of the surface of the lap-shear specimens under load. Model simulation results compared favorably with measured surface displacements with spatial resolution in the micron range. The main advantage of the methodology is the accurate representation of the 3D microstructure of wood, and penetrating adhesive system, in the numerical model.

A.2 Introduction

The structural performance of wood-adhesive bonds depends on their ability to transfer stress across an interface of dissimilar materials, namely cell wall substance and cured polymeric adhesive. The “interface” of the bondline is actually part of an “interphase” region comprised of cell wall substance, voids, and voids filled with the cured adhesive

system (Kamke and Lee 2007) . Furthermore, the pre-polymeric adhesive may penetrate the cell wall during bond formation. The scale of the interphase region corresponds to the scale of the wood ultra-structure, and is thus defined on the micron level. This system of cell walls, cured synthetic polymer, and void space is remarkably small, complex, and variable.

Although conceptual models have been proposed to explain the effect of adhesive penetration on the bond performance, to-date no direct evidence of such correlation has been provided. Frihart (2009) postulated the difference in bond performance between *in situ* polymerized systems, which become cross-linked and tend to be rigid, and the pre-polymerized adhesive systems that are more ductile (Frihart 2009). Stress in the region of the bond interphase depends on the nature and degree of adhesive penetration into the substrate. Penetration of *in situ* polymerized systems has been demonstrated to change cell wall and bulk wood properties (Furuno et al. 2004; Gindl et al. 2004; Gindl and Gupta 2002; Jakes et al. 2009; Miroy et al. 1995). Regardless of the extent of adhesive penetration into the cell lumens, cell wall, or both, the influence of penetration on adhesive bond performance is largely unknown.

Müller et al. (2005) measured the two-dimensional (2D) strain field of single-lap bonded wood assemblies in shear by tension loading using interferometry with spatial resolution of 0.1 micron. Results were used to calculate shear moduli of the interphase region of specimens bonded with phenol-resorcinol-formaldehyde (PRF) or polyurethane (PU) adhesive. The shear moduli of the PRF specimens were more than seven times greater than the PU specimens. An optical measurement method based on the digital image

correlation (DIC) principle has been used to measure 2D strain fields of bonded wood assemblies (Serrano and Enquist 2005). Like the interferometer technique, DIC requires a clear view of the edge of the specimen. The spatial resolution of the DIC method is controlled by the optics associated with the camera system and must be balanced against the desired field of view. The authors reported a spatial resolution of 0.2 mm. Similar to (Muller et al. 2005), Serrano and Enquist (2005) reported distinctly different strain behavior, but nearly identical ultimate strength for PRF and PU bonded specimens. None of these reports provided information concerning adhesive penetration.

Müller et al. (2005) and Serrano and Enquist (2005) modeled lap-shear bond behavior using finite element analysis (FEA). For the purpose of these studies the properties of the adhesives were estimated from previous work and assumptions were made on the thickness of the “bondline” in the FEA model. It is unclear if bondline thickness referred to pure adhesive at the idealized interface between the adherents, or to an interphase region (including the region of penetration of adhesive). In both studies the trends simulated by FEA compared well to the full-field strain measurements. One promising way to approach micromechanical analysis in heterogeneous materials of this level of complexity is integration of multi-scale and multi-modal advanced imaging techniques, numerical modeling and elements of inverse problem methodology (Muszyński and Launey 2010).

X-ray computed tomography (XCT) is a useful tool for three-dimensional (3D) mapping of porous wood structures and adhesive penetration in wood (Hass et al. 2012; Kamke et al. 2010; Kamke and Lee 2007; Modzel 2009; Modzel et al. 2011). To-date, XCT has not

demonstrated the ability to distinctly separate penetration of adhesive in a cell wall from adhesive in the cell lumen. While XCT provides excellent visual characterization of 3D pathways for penetration, the challenge still remains to quantitatively relate penetration to bond performance. In addition, XCT requires micron-level spatial resolution to differentiate thin cell walls from the cured adhesive polymer. The x-ray attenuation of organic adhesives is nearly the same as cell wall substance. Consequently, material contrast is generally poor without the addition of a contrast agent (Modzel 2009).

The objective of the current study was to develop an integrated method for quantitative assessment and numerical simulation of the elastic behavior of bonded wood systems that could capture the effects of adhesive penetration into cell lumens and the complex nature of the micro-morphology of wood. Penetration of adhesive in cell walls was beyond the scope of this work. The present report describes the methodology from adhesive formulation to computer simulation results, as well as validation by micro-bond testing. Subsequent reports will compare the bond behavior of several adhesive types in three wood species.

A.3 Materials and Methods

The research project was divided into three phases. First, the wood-adhesive system was defined using micro XCT. The outcome of this phase was 3D representation of the physical system, with near micron resolution, allowing separation of the three principle components – wood cell wall, adhesive, and voids. With one micron resolution individual pits and thin cell walls could be clearly represented in the 3D digital tomogram. Second, numerical modeling using the material point method (MPM) was selected such that

tomogram data could be directly implemented into a numerical model, and thus accurately represent the physical system. The numerical model is necessary to visualize the internal stress distribution in the bond interphase, which by principle cannot be measured. Finally, a micro-mechanical, lap-shear, bond test (Figure A-1) was designed such that the same specimen that was scanned for XCT was used for mechanical testing. The optical measurement system employed the DIC principle to measure surface displacements and strain maps on one side of the adhesive bond. The measured surface displacements and strain maps could be directly indexed to the tomogram data and MPM simulation results. The test protocol allowed a direct comparison, and thus validation, of the MPM model results.

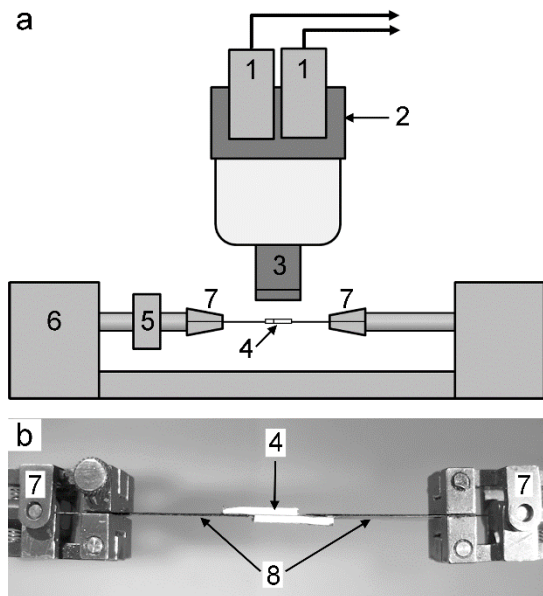


Figure A-1 (a) Universal test machine showing lap-shear specimen and DIC optical measurement system; (b) Example of a lap-shear specimen with ends bonded to graphite-epoxy tabs for attachment to test machine; 1 cameras, 2 beam splitter, 3 microscope objective, 4 specimen, 5 load cell, 6 test frame, 7 grip, 8 graphite-epoxy tab

To illustrate the experimental method, an example of hybrid poplar (*Populus trichocarpa* \times *Populus deltoides*) wood bonded with PF adhesive is described. Poplar is a hardwood species that has vessel cells (approx. 100 micron diameter) that are uniformly dispersed throughout the growth ring. The vessels are approximately 500 to 800 micron in length and are connected via simple perforation plates (no membrane) arranged end-to-end in the longitudinal direction. Most of the other cells are longitudinal fibers, which have thicker cell walls (approx. 3 micron) with lumens about 15 micron in diameter and 1 mm in length. Fluid transport between longitudinal fibers occurs via pits that contain a membrane, which presents a high resistance to flow. Consequently, nearly all fluid flow in the longitudinal direction in poplar occurs through vessels.

To enhance the x-ray attenuation contrast, the PF adhesive was formulated using 100 percent 3-iodophenol (IPF) with a synthesis procedure similar to the manufacture of a commercial plywood adhesive. The resulting resin contained 39.5 weight-percent iodine. Iodine has an atomic mass of 126.9, and thus created an adhesive with an x-ray attenuation coefficient approximately 30 times greater than wood substance. The weight-average molecular weight (MW) was approximately 22,000, which is greater than a typical plywood PF resin. However, the polydispersity was 1.9, which is about the same as a plywood PF resin. The viscosity at 25°C was 930 cP. Although the fluid properties and cure characteristics of the experimental resin may differ from a commercial PF resin, the objective of the project, which is modeling the bond behavior, was not compromised.

Adhesive bonds were formed by applying 61 g/m² PF solids per face to the tangential surface of 15 mm thick wood lamina. The assembly was pressed at 185 °C, at 0.48 N/mm², for 8 minutes. After cooling and conditioning to a constant moisture content at 20°C and 65% relative humidity, the bonds were isolated by cutting to 2 mm x 2 mm x 15 mm specimens. The specimens were cut on the radial-longitudinal plane with a microtome to create a clean surface that clearly exposed the anatomical structure of the wood (Figure A-2e). Finally, a notch was cut on both ends of the specimen to create a lap-shear specimen with overlapping area of approximately 2 mm x 6 mm (Figure A-1b).

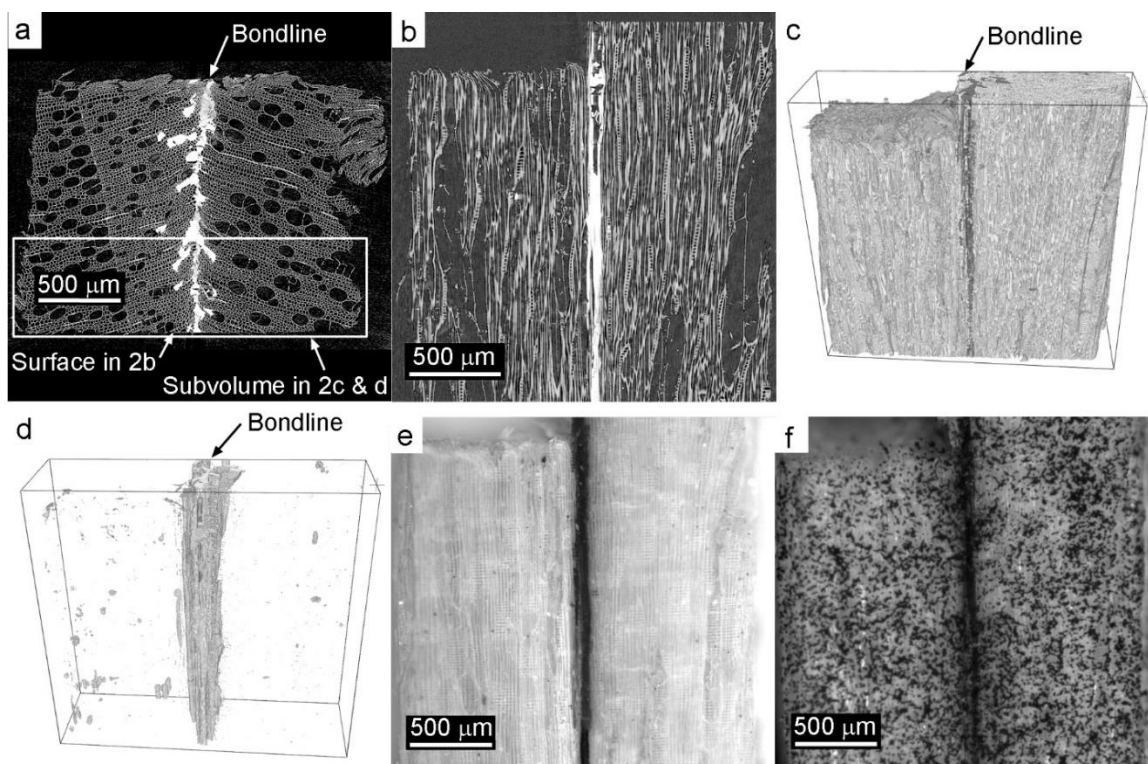


Figure A-2 Poplar and IPF lap-shear specimen; a) Transverse view of reconstructed tomogram; b) Radial slice from (a) showing microtomed surface; c) Segmented sub-volume from (a, box) showing adhesive phase; d) Segmented sub-volume from (c) showing adhesive phase; e) UV fluorescence micrograph of microtomed surface; f) Same surface as (e) with speckle pattern applied for DIC displacement measurement

Micro XCT was performed on beamline 2-BM-B at the Advanced Photon Source (APS) at Argonne National Laboratory. Synchrotron radiation was desired for its high energy, parallel, monochromatic beam. Synchrotron radiation provides rapid scanning, which reduces the chance for biological specimens to change moisture content during the scan, and provides the best image quality. Scanning was performed at 15.3 keV and 250 ms exposure time per radiograph. The distance between the scintillator screen and the specimen was 8 mm, which is a critical parameter that affects the degree of phase contrast due to x-ray interference after free-space propagation (Wilkins et al. 1996). Radiograph projections on the scintillator screen were captured by a 12-bit camera (Photometrics CoolSnap k4) with a 5x microscope objective lens. During the XCT scan, the specimen was rotated in 0.12 degree increments over 180 degrees. The raw radiogram data was used to reconstruct the 3D image using a fast-filtered back-projection algorithm on a dedicated computing system at the APS. The reconstructed data sets consisted of 2048 digital images in 32-bit (floating point) format, with 1.45 microns per voxel side and a total field of view volume of $2.97 \times 2.97 \times 2.97 \text{ mm}^3$. A minimum of two neighboring pixels is needed to define the shape of an object, and thus the imaging system intrinsic spatial resolution, or smallest resolvable identifiable object, is 2.90 microns.

Digital processing of the tomogram data was done using Fiji, a bundled software package of ImageJ 1.45i (NIH 2013), including several preloaded 3D image analysis plug-in modules. Reconstructed image stacks (sequentially numbered images representing virtual transverse slices along the length of the specimen) were imported into the program with an HDF-reader plug-in supplied by the APS beamline staff (Tieman 2007). XCT data sets

were then cropped to sub-volumes approximately 2 mm (L) x 650 μm (R) x 2 mm (T), isolating the microtomed, radial-longitudinal surface with the centered adhesive bondline (Figure A-2). Image stacks were then subject to the following processes: 1) normalization, with 0.4% saturation tolerance, to stretch the stack gray values over the full 0 - 2^{32} gray-scale range; 2) conversion to an 8-bit image stack with 0 - 2^8 gray-scale range; 3) a 3D median filter, with a 3x3x3 voxel neighborhood, was applied in 3 consecutive iterations, to smooth the sub-volume data while preserving material edges; 4) gray-scale threshold values were used to segment the volume into three material phases - cell wall, adhesive and voids (Figure A-6); and 5) a binary noise removal filter, with a 1 voxel radius, eliminated singular, unconnected voxels. Processed, binary sub-volumes were saved as bitmap image-stacks to be directly imported into the modeling software.

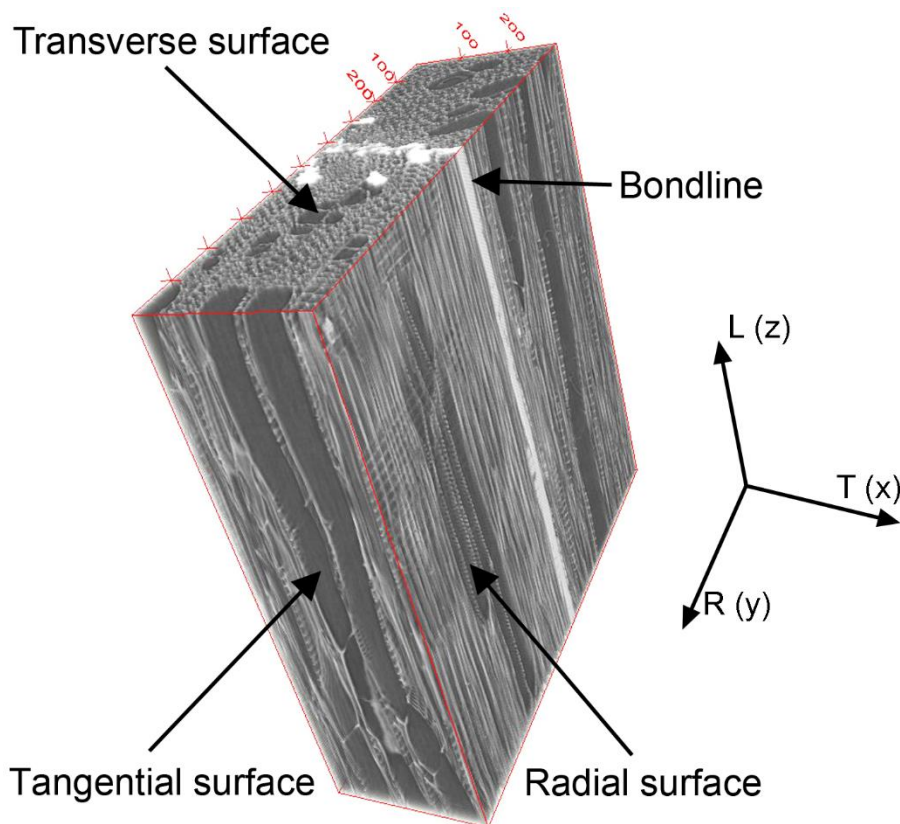


Figure A-3 Example of tomogram of poplar bonded with IPF (0.3 mm x 1 mm x 1 mm). Reference planes are shown for transverse (end-grain), radial, and tangential surfaces; Reference directions, relative to anatomy of wood, indicated at right: longitudinal (L), radial (R), tangential (T)

The bonded assemblies were too small for the grips in the universal test machine.

Consequently, a graphite-epoxy tab was bonded to each end of the lap-shear specimen as shown in Figure A-1b. To serve as a reference, a digital image of the microtomed surface was captured using a fluorescence microscope (Figure A-2e), where UV illumination proved good color contrast between the PF and wood. To enhance optical measurement, laser-printer toner was used to apply a speckle pattern on the microtomed surface (Figure A-2f). The speckle pattern provides unique reference targets needed for DIC analysis.

The lap-shear specimens were loaded in tension with a small universal test machine

(Instron Electropuls E1000), with loading rate of 0.5 N/min and the load was monitored with an Instron 100 N static load cell (Figure A-1a). The optical measurement system (Vic-Micro 3D™ by Correlated Solutions, Inc.), consisting of a stereo microscope and two digital cameras, was positioned to monitor deformation of the microtomed surface with speckle pattern. An image was captured every second. The spatial resolution was 1.27 $\mu\text{m}/\text{pixel}$. The DIC measurement analysis was performed for reference targets spaced at 8.92 μm (5 pixels) intervals. The displacement of each reference target was determined with precision of $\pm 0.037 \mu\text{m}$, which translated to ± 68.2 linear microstrain. One limitation was the coarse appearance of the finest available speckle pattern under high magnifications used in this study. The field of view for the DIC data included the notch (overlap) on one end of the specimen, which provided a clear reference point for spatial indexing of tomograms, DIC data, and modeling results.

Modeling the adhesive bond was accomplished using finite element analysis (FEA) and the material point method (MPM). The high degree of spatial resolution needed to represent the entire cellular structure of the lap-shear specimen for 3D MPM modeling was not feasible. Instead, a two-step modeling procedure was applied. First, 2D FEA was used to model the entire lap-shear specimen. The FEA results were used to define the boundary conditions for a sub-volume of the specimen defined from the tomography data. Finally, a 3D MPM model was used to simulate the linear elastic deformation of the sub-volume.

The challenge for the numerical modeling was to discretize the structure determined by tomography and then to model the stress and strain encountered in the micro-bond

testing. The preferred method is a particle-based method, rather than a finite element method. In particle-based methods, one can go directly from voxels in the tomogram to a numerical model without any need for constructing a finite element mesh. A custom MPM code (Nairn 2011) was used for this task. The code has previously been shown to work well for modeling realistic 2D wood structures (Nairn 2006).

A full 3D simulation of the entire specimen using the finest spatial resolution of the tomogram had 9 billion voxels; that problem size was well beyond the capabilities of the available MPM software. The following strategy was adopted. A sub-volume was carved out of the tomogram data in a region that included the surface mapped by the micro-bond experiments. The reduced region covered the full width of the specimen (y-direction, radial, ~ 2 mm), a length along the bondline to encompass expected stress concentrations (z-direction, longitudinal, ~ 2 mm), but only a partial depth (x-direction, tangential, ~ 650 μm). The resulting tomogram structure is shown in Figure A-2. This subset was converted to 1430 bmp files along the z-axis. Each bmp file was a transverse slice of the specimen with x and y direction having 450 and 1522 pixels, respectively. The sub-volume had about 0.98 billion isotropic 1.45 μm voxels.

Due to practical computer limitations, the system model was scaled down further by coarse graining each slice to fewer particles. The simulations presented here used x and y of 200 by 676 pixels in each slice for a resolution of 3.25 μm per particle. Figure A-4a shows one slice from tomogram data at resolution of 1.45 μm per pixel, while Figure A-4b shows the MPM model by directly translating this slice into particles in the model. The full 3D model was then constructed by similarly mapping a series of slices along the

z-direction of the specimen. Again, it was not possible to include all slices. Because the structure of wood varies much more significantly in the transverse plane than in the axial plane, the modeling procedure assumed that less resolution was needed in the z-direction. The results in this paper were derived from simulations performed at two spatial resolutions - $14.5 \mu\text{m}$ and $5.8 \mu\text{m}$ per particle in the z-direction. The resulting simulations had approximately 8 million or 20 million particles depending on the selected spatial resolution, and computation time was 11 hours and 38 hours, respectively, in multi-core parallel code using 12 cores.

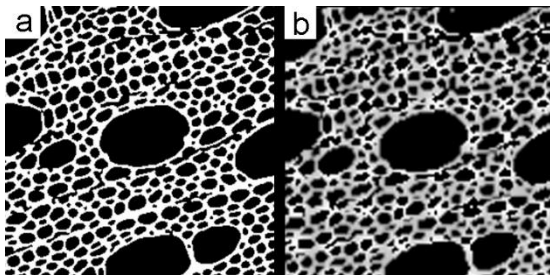


Figure A-4 (a) One slice of tomogram data at a resolution of $1.45 \mu\text{m}$ per pixel; (b) The computer representation of this same slice in an MPM model with $3.25 \mu\text{m}$ per particle. These images show only the wood components. The adhesive component has been removed and was supplied to the computer model by superposing adhesive images with wood images

Because the computer model was only for a portion of the full specimen, the choice of boundary conditions was crucial. Two methods were used. First, the micro-bond tests measured full displacement fields on the y-z surface plane. Experimental displacements were extracted in the z and y directions on the top ($z = 0 \text{ mm}$) and bottom ($z = 2.068 \text{ mm}$) of the modeled sub-volume. Those results were fit to functions of y along each edge, and

then applied as displacement boundary conditions to the ends of the 3D modeled region. While this worked, it gave only one specific result and would not be an acceptable approach for anticipated future work that will conduct virtual experiments on the role of bondline properties. Because anticipated virtual materials will not match the actual resin, the experimental boundary conditions would not be appropriate for such simulations. Therefore, a global-local approach was developed for selecting boundary conditions. The global analysis was to run a 2D finite element analysis (FEA) on the entire micro-bond specimen, including the carbon tabs. Next, for the MPM region being modeled, the FEA y and z displacements on the ends (boundary) were extracted, and they were fit to functions of position y along each edge. The derived functions were applied as displacement boundary conditions to the 3D modeled sub-volume. The final boundary condition was to set displacement in the x-direction to be zero on the back surface of the sub-volume, which is the interior plane opposite of the microtomed surface.

The numerical modeling also needed material properties. These initial simulations assumed linear elastic materials. The resin was assumed to be isotropic with modulus of 1000 MPa and Poisson's ratio of 0.33, which are typical for thermosetting polymer resins (Umemura et al. 1998). However, the modulus for the IPF was estimated to be at the lower end of the range because the presence of iodine will reduce cross-linking. The wood components were assumed to be transversely isotropic with high modulus in the longitudinal direction and isotropic properties in the radial-tangential plane. The global FEA calculations used properties for solid wood. The MPM simulations needed cell wall properties. The longitudinal modulus of the cell wall was estimated by extrapolating typical wood properties to cell wall density (Gibson and Ashby 1997). The other values

were estimated. The simulations would be improved with measured cell wall properties, but this information was not available. All wood properties used for the simulations are listed in Table A-1.

Table A-1 Mechanical properties assumed for global FEA and local MPM simulations

Material	Property	Direction	FEA	MPM
Bulk wood	Normal modulus (MPa)	z	7,500	-
Bulk wood	Normal modulus (MPa)	x, y	900	-
Bulk wood	Shear modulus (MPa)	z-x, z-y	500	-
Bulk wood	Poisson ratio	z-x, z-y	0.23	-
Bulk wood	Poisson ratio	x-y	0.33	-
Cell wall	Normal modulus (MPa)	z	-	30,000
Cell wall	Normal modulus (MPa)	x, y	-	3,000
Cell wall	Shear modulus (MPa)	z-x, z-y	-	3,000
Cell wall	Poisson ratio	z-x, z-y	-	0.2
Cell wall	Poisson ratio	x-y	-	0.33
Adhesive	Normal modulus (MPa)	isotropic	1,000	1,000
Adhesive	Poisson ratio	isotropic	0.33	0.33

A.4 Results and Discussion

The preliminary results presented here are proof of concept for the integrated procedure.

The results are not intended to represent the behavior of all PF adhesive bonds.

Comparison of adhesive bond performance among other wood species and other adhesive types will be presented in a future publication.

A.4.1 Micro-XCT

An example of processed 3D tomographic data is shown in Figure A-2a-d. The ends of the lap-shear specimen are not shown. The bondline is oriented vertically on the x-y plane in Figure A-2a, and vertically on the y-z plane in Figure A-2b. Due to greater x-ray attenuation than cell wall, the IPF adhesive appears white in the reconstructed tomogram. As seen on transverse surface (Figure A-2a), the microtomed edge is at bottom. Figure A-2b shows a 1.45 μm thick virtual surface that corresponds to the microtomed edge. In this view only one slice from the tomogram is shown. Figure A-2c is a 3D rendering of the same specimen, with microtomed surface in the foreground, but segmented based on the gray-scale intensity of the voxels. In Figure A-2c the adhesive phase was assigned a dark color for illustration. Figure A-2d shows the same sub-volume as Figure A-2c with just the adhesive phase shown. As expected, most of the adhesive penetrated the relatively large diameter vessel cells, which are oriented in the longitudinal direction (z-direction).

Figures A-3 and A-5 illustrate the spatial resolution achieved in the tomograms. The reference planes are defined in Figure A-3 in relation to the orientation of the bondline. Note that the orientation of the long axis of the vessel cells is in the longitudinal direction, and the bondline is approximately parallel to the tangential surface (longitudinal-tangential plane). The double cell wall (walls of two adjacent cells), pits in vessel walls, and pits in longitudinal fibers can be distinguished. Individual walls of adjacent cells cannot be separated. Figure A-5 illustrates an example of the radial surface of the wood, with the longitudinal direction in a vertical orientation. The images in Figure A-5 have not been filtered. The image at left (Figure A-5) shows vessel cells, inter-vessel

pitting (lower left), and a portion of a ray (upper left). When the region indicated by the square is magnified 10x (center image), and 20x (right image), the limit of feature identification is revealed. The image at right (Figure A-5) shows a double cell wall (vertical white region) with three inter-vessel pits.

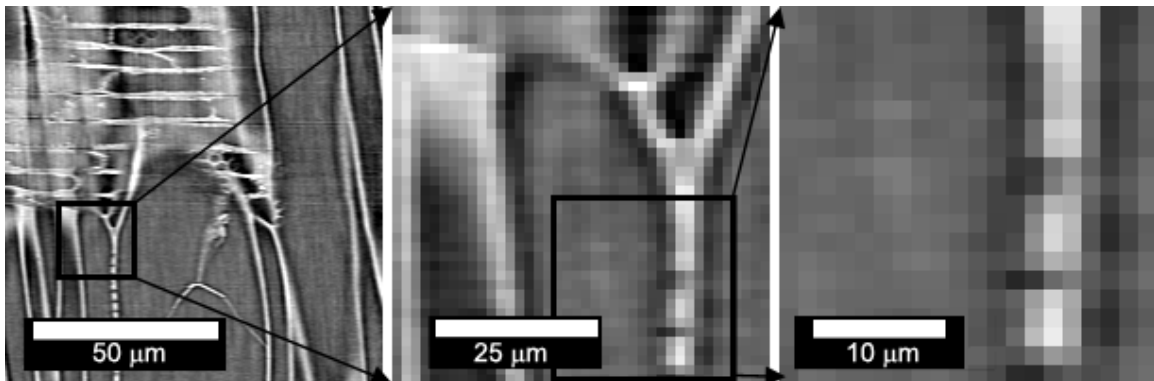


Figure A-5 Tomogram images showing radial surface to illustrate the spatial resolution and feature recognition; pixel size = 1.45 μm

The adhesive phase can be separated from the cell walls based on the gray-scale value of the voxels. For the 8-bit gray-scale images there are 256 levels of gray (0 = black, 255 = white). As shown in Figures A-2a, A-2b, and A-3, white and black voxels represent the highest and lowest x-ray attenuation, respectively. The corresponding gray-scale intensity histogram is shown in Figure A-6, where peaks and valleys in the distribution correspond to the gray-scale values used for segmentation. If the specimen contains materials with distinctly different x-ray attenuation coefficients, the phases can be separated based on gray-scale intensity. While a histogram plot of the gray-scale intensity is helpful to decide which voxels should be assigned to adhesive, cell wall, or voids, the overlapping of the

tails of the distributions make the exact separation of phases impossible. Figure A-2d illustrates the result of such an approximate segmentation process when only the gray-scale values assigned to adhesive are displayed. Overlap of material phases occurs where adhesive penetrates the cell wall, which is approximately in the gray-scale range of 140 to 190 as shown in Figure A-6.

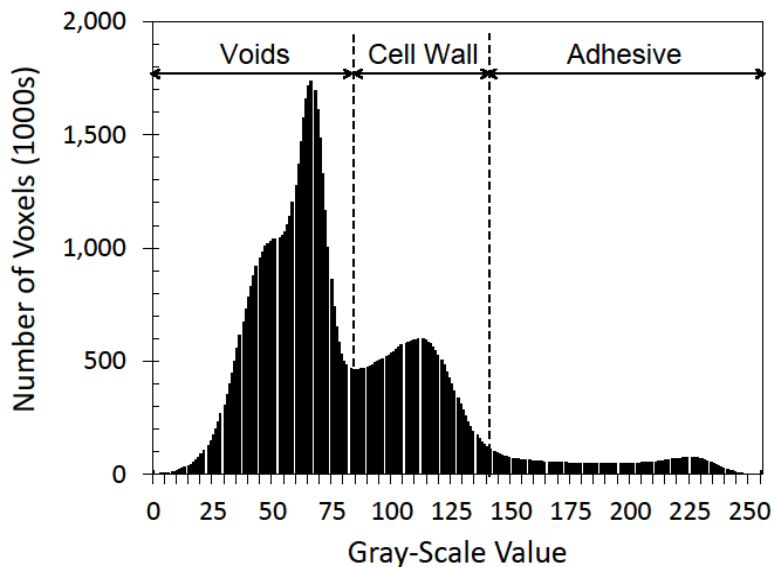


Figure A-6 Histogram plot of gray-scale values for a sub-volume of a tomogram. Gray-scale values have been linearly normalized from 0 to 255. Voxels, with gray-scale values indicated, have been assigned to represent voids (0 - 83), cell wall (84 - 141) and adhesive (142 - 255)

A.4.2 Micro-Bond Testing

The set of shear strain maps recorded on the microtomed surface of the lap-shear specimen, at four stages of the micro-bond test, yielded results expected for a lap-shear specimen (Figure A-7). As the tensile load was increased, a distinct axial shear strain

concentration developed in the region of the notch bottom. This is in accord with the knowledge gained through analytical and numerical simulations, but is rarely measured with reasonable precision. However, the pattern of shear strain development is not a smooth gradient, as one would expect for a homogeneous material. Discontinuity in the pattern of shear strain is a consequence of the heterogeneous nature of the wood structure. The scale of the interphase region of the adhesive bond is similar to the scale of the dominant anatomical features of the wood – namely the vessel cells in hardwood species. Therefore, the observed deformation of the lap-shear specimen is influenced by the pattern of adhesive penetration, the nature of the adhesion between polymer and cell wall, and the mechanical properties of the polymer. Empty vessels behave as voids, which do not offer much resistance to load and result in high strain areas. Vessels filled with adhesive transfer stress differently than empty vessels. This phenomenon is clearly illustrated in Figure A-7, where the high strain region depicted in red corresponds to the location of empty vessel cells at the surface of the specimen.

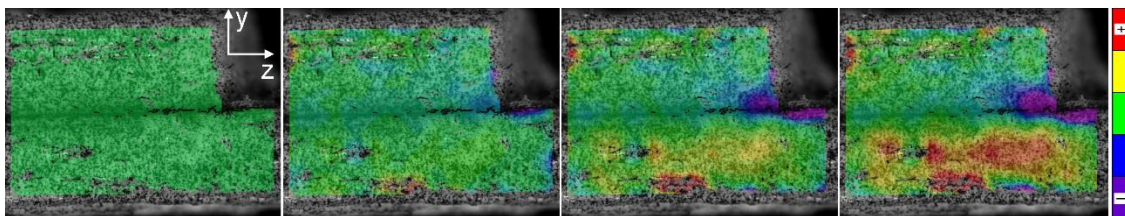


Figure A-7 Progression of shear strain development during tension loading in half of a lap-shear specimen (notch at right) as calculated from DIC measurement; a) 0 N, b) 10 N, c) 20 N, d) 30 N

A.4.3 Computer Simulation Modeling

The validity of the global-local method to select boundary conditions for the MPM model is demonstrated in Figure A-8, where experimental micro-bond displacements are compared to displacements calculated by global FEA. The two methods had similar displacements, which validates the FEA option for choosing boundary conditions.

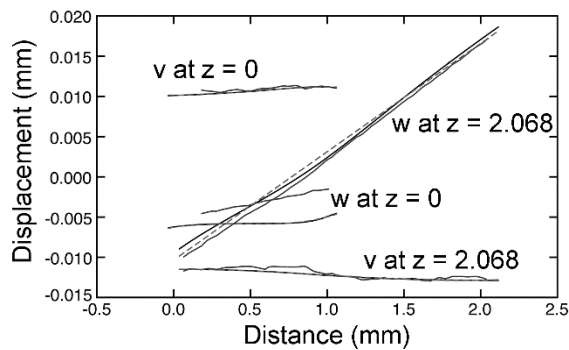


Figure A-8 The displacements in the z direction (w) and y direction (v) on the top ($z = 0$) and bottom ($z = 2.068$) of the modeled subvolume; Gray lines are experimental results by DIC; Black lines are FEA calculations; Dotted lines are fits to FEA results that provided functions to input for MPM boundary conditions

Figure A-9 compares displacements in the z-direction measured with the DIC optical method to those calculated by the MPM model. The good agreement between the results was expected because FEA displacements, which are close to the measured displacements, were used as the boundary conditions for the MPM analysis. The agreement between the model and the measurement may be better evaluated by looking at strain maps. Figure A-10 compares simulated surface strain in the z-direction and shear strain (y-z plane) to the strains measured with the DIC optical system at the highest strain

level used in the micro-bond test. Again, the model and experiments show similar patterns.

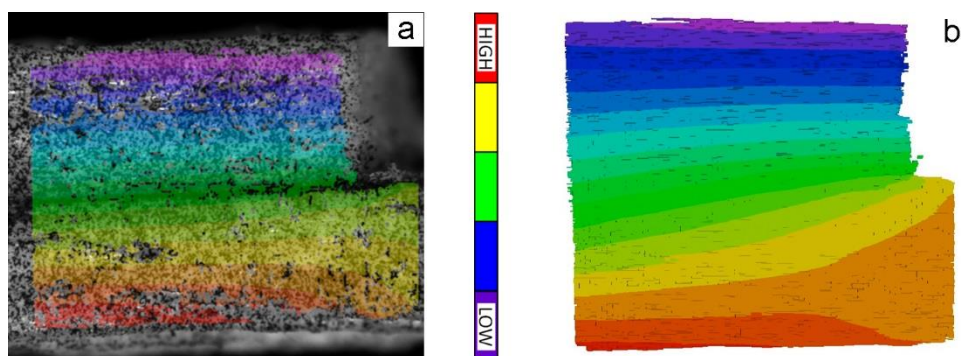


Figure A-9 (a) Experimental DIC results for displacements in z-direction (horizontal); (b) The same displacements estimated by the MPM model

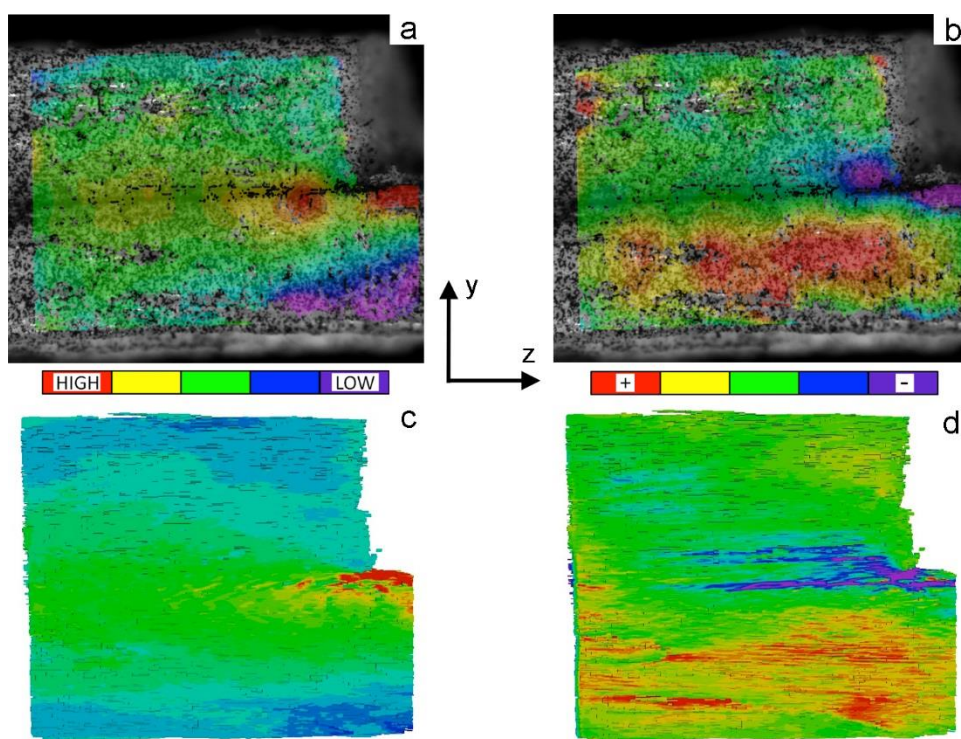


Figure A-10 (a) Normal strain in z-direction, and (b) shear strain measured by DIC; (c) Normal strain in z-direction, and (d) shear strain from MPM results

With the MPM model validated it then becomes possible to examine the results of the 3D simulation with a measurable level of confidence. The goal is to gain new insight into adhesive bond performance. Two examples are given here. Figure A-11 shows equivalent strain and stress (also known as octahedral strain and stress) for a virtual cross-section of the specimen close to the notch. These terms were chosen because they are invariants of the strain and stress tensors. For isotropic materials these invariants are often associated with shear failures. Although this approach may not provide the best indicators for anisotropic materials like wood, this analysis still provides some insight. Future work will seek to predict wood failure using anisotropic failure criteria. In Figure A-11, the equivalent strain is high at the bondline and decreases as a function of distance into either wood substrate. The rate of change of the strain might be a useful metric for bond performance. In contrast, the equivalent stress is low in the adhesive and high in the wood near the bondline, with high stress regions extended around the thin-walled, large-diameter vessel cells in the wood. These observations are consistent with the assignment of material properties, where the modulus of the adhesive is less than the modulus of the cell wall in the longitudinal direction (Table A-1). These high stress regions are the likely location for initiation of bond failure.

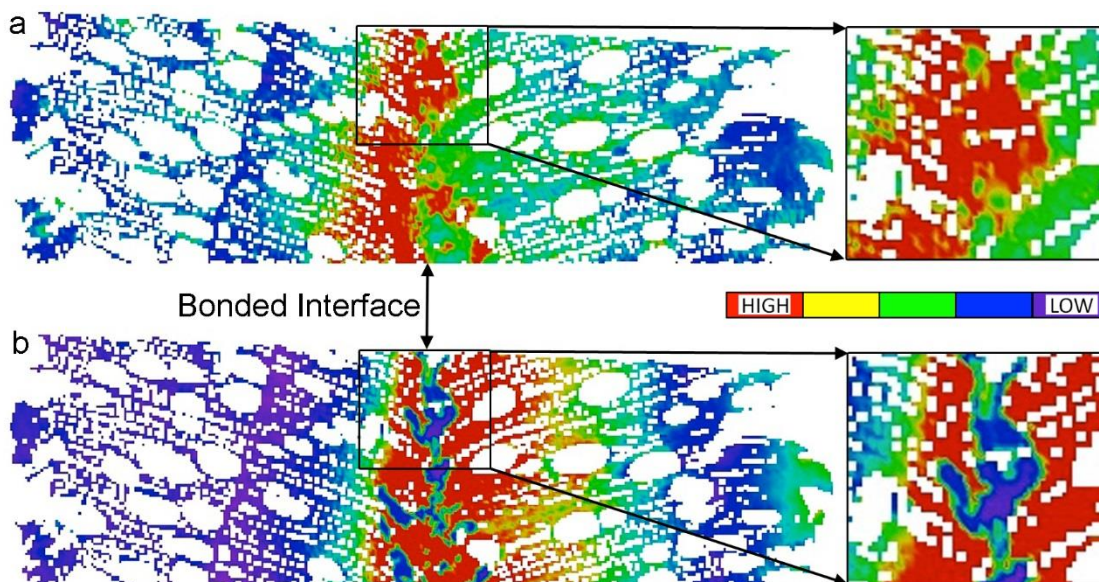


Figure A-11 MPM simulation results for lap-shear specimen loaded in z-direction as viewed in x-y plane; a) equivalent strain, b) equivalent stress

While the potential for this 3D modeling to become a powerful tool for assessing bond performance is clear, the challenge now is to properly interpret the results. All 3D plots of modeling results were done by ParaView (Kitware Inc., Carrboro, North Carolina USA). The plots in Figures A-9 to A-11 were done by thresholding results to mass and projecting a color-coded displacement, strains and stress value maps on the surface. The reason the transverse structure in Figure A-11 looks to be lower resolution than in the MPM model in Figure A-4b is a consequence of 3D visualization methods, which smooth results to a grid prior to plotting. The thresholding step can be done by other scalar results as well. Interesting aspects of the results may be revealed by visualization of the equivalent strain or stress above certain levels with simultaneous color-coded segmentation of cell wall material and adhesive phases. The results are demonstrated in

Figure A-12, where thresholding was used to highlight only regions of highest strain or highest stress, and color-coded blue for adhesive and yellow for cell wall material. Figure A-12a shows the strain result. As in Figure A-11, the strain is high in the adhesive (blue) and localized along the bondline. The 3D plot shows the full extent of the strain concentration. In contrast, the stress concentration in Figure A-12b shows almost no adhesive. All the high stresses are in the wood (yellow), which identifies the likely locations for bond failure. As shown in Table A-1, the modulus of the adhesive is a factor of 30 less than the modulus of the cell wall in the longitudinal direction. Therefore, greater stress, and less strain, is expected in the cell wall.

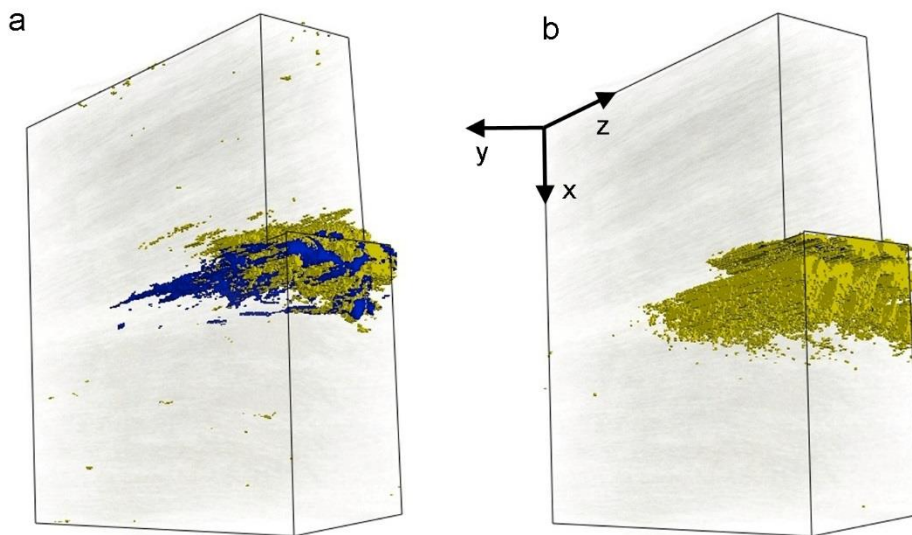


Figure A-12 MPM simulation results showing notched end of lap-shear specimen; (a) Regions of high equivalent strain; (b) Regions of high equivalent stress. Both plots are colored by material, where dark blue is adhesive and yellow is cell wall substance

A.5 Limitations

One limitation of the procedure described here is the inability to represent the effect of adhesive penetration into the cell wall. Evidence from energy dispersive spectroscopy clearly revealed the presence of iodine in the cell wall. Since the iodine did not disassociate from the PF, there must have been some cell wall penetration. The resolution of the XCT scans was too coarse to quantitatively separate PF in the cell wall from bulk PF in the cell lumens. The concentration of iodine in the cell wall was less than the concentration of iodine in the bulk PF. Therefore, less x-ray attenuation occurred in the cell wall regions where penetration occurred than in the bulk PF. Unfortunately, there was not a distinct demarcation, but rather a gradient in gray-scale in the tomograms.

XCT creates artifacts in the reconstructed tomogram as a result of x-ray interference. Interference occurs when a sample is illuminated by coherent x-ray. After free-space propagation behind the sample, x-rays constructively or destructively interfere around features in the sample, which in turn creates bright-dark gray value jumps across feature boundaries in tomograms. In the current study, this phenomenon was observed as light (cell wall side) and dark (lumen side) shadows in the region of the interface of air and cell wall substance. The light shadow cast on the cell wall can have a gray-scale value similar to the adhesive phase. Although the distance between the specimen and scintillator screen was optimized in this experiment to minimize x-ray interference, the artifact persisted. These limitations contributed to the uncertainty of segmenting adhesive from cell wall substance. Quantitative phase contrast XCT is potentially a better approach to not only reduce the artifacts, but also improve the contrast amongst the three principle

material phases (Burvall et al. 2011; Chapman et al. 1997; Momose 2003; Pfeiffer et al. 2006). This is a future direction for this work.

Spatial scale is critical to interrogate the influence of adhesive penetration on bond performance. The XCT apparatus at beamline 2-BM-B at the APS was limited to 1.45 μm per voxel resolution and a field of view of approximately 3 mm. Limitation on spatial resolution also influences the separation of the cell wall from adhesive if the cell wall is smaller than one pixel, or the interface between cell wall and air space falls within one pixel. The result is assignment of an average gray-scale value that is midway between air space (or adhesive) and cell wall substance. This artifact is clearly illustrated in Figure A-5. Finer spatial resolution for XCT below 50 nm is possible at other XCT facilities, but the field of view is correspondingly reduced. Furthermore, finer spatial resolution requires an XCT system, and specimen, that can be accurately indexed, or does not change dimension during the scan. With moisture sensitive materials such as wood, a change of moisture content during a scan will cause indexing errors that become incorporated into the reconstructed tomogram. The true spatial resolution is defined by the ability to separate distinct objects or features. To separate features requires a minimum of two voxels, and consequently, the spatial resolution of the method presented here is 2.9 μm .

A further limitation of the method is the assumption of mechanical properties used for the numerical simulation. Mechanical properties were not measured for the materials used in this study. Property values were obtained from the literature, and perfect adhesion was assumed between the adhesive and the cell wall. No change in cell wall properties was

assumed for the interphase region, even though evidence suggested that the pre-polymer penetrated the cell wall.

A.6 Summary

An integrated method was presented for analyzing the micro-mechanical performance of adhesive bonds in wood. The analysis was performed at a spatial scale approaching 1 μm and true spatial resolution less than 3 μm . A numerical simulation model was created to predict stress transfer as a function of the mechanical properties of cured adhesive and cell wall substance. The physical system used in the simulation accurately represented the 3D anatomical structure of the wood, as well as the 3D pattern of penetration of adhesive in the wood substrate. Micro-XCT created the data that was necessary to define the physical system. Direct measurement of strain development validated that the model was capable of representing the effects of cellular structure and adhesive penetration. The model may be used to analyze stress and strain patterns inside the bond interphase and to perform virtual investigations of the influence of adhesive penetration and polymer properties on the performance of adhesive bonds. Limitations of the method were discussed. Future research is aimed at refining the method, collecting more realistic definition of component material properties, and improving the accuracy of the model.

A.7 Acknowledgements

Use of the Advanced Photon Source, an Office of Science User Facility operated for the U.S. Department of Energy (DOE) Office of Science by Argonne National Laboratory, was supported by the U.S. DOE under Contract No. DE-AC02-06CH11357. Financial support was provided by National Science Foundation Industry/University Cooperative Research Center for Wood-Based Composites, Award No. IIP-1034975.

A.8 References

Burvall, A., Lundström, U., Takman, P. A., Larsson, D. H. and Hertz, H. M. (2011) Phase retrieval in X-ray phase-contrast imaging suitable for tomography. *Opt. Express* 19, 11, 10359-10376.

Chapman, D., Thomlinson, W., Johnston, R., Washburn, D., Pisano, E., Gmür, N., Zhong, Z., Menk, R., Arfelli, F. and Sayers, D. (1997) Diffraction enhanced x-ray imaging. *Phys. Med. Biol.* 42, 11, 2015.

Frihart, C. R. (2009) Adhesive groups and how they relate to the durability of bonded wood. *Journal of Adhesion Science and Technology* 23, 4, 601-617.

Furuno, T., Imamura, Y. and Kajita, H. (2004) The modification of wood by treatment with low molecular weight phenol-formaldehyde resin: a properties enhancement with neutralized phenolic-resin and resin penetration into wood cell walls. *Wood Science and Technology* 37, 5, 349-361.

Gibson, L. J. and Ashby, M. F. *Cellular solids : structure and properties*. Cambridge University Press, Cambridge ; New York, 1997

Gindl, W., Gupta, H., Schöberl, T., Lichtenegger, H. C. and Fratzl, P. (2004) Mechanical properties of spruce wood cell walls by nanoindentation. *Applied Physics A* 79, 8, 2069-2073.

Gindl, W. and Gupta, H. S. (2002) Cell-wall hardness and Young's modulus of melamine-modified spruce wood by nano-indentation. *Composites Part A: Applied Science and Manufacturing* 33, 8, 1141-1145.

Hass, P., Wittel, F., Mendoza, M., Herrmann, H. and Niemz, P. (2012) Adhesive penetration in beech wood: experiments. *Wood Science and Technology* 46, 1-3, 243 - 256.

Jakes, J. E., Yelle, D. J., Beecher, J. F., Frihart, C. R. and Stone, D. S. 2009: Characterizing polymeric methylene diphenyl diisocyanate reactions with wood: 2. Nano-indentation. In: Frihart, C. R., Hunt, C. G. and Moon, R. J., editors, *Proceedings of the International Conference on Wood Adhesives 2009*, Lake Tahoe, NV, USA: Forest Products Society, 11 p.

Kamke, F., Modzel, G. and De Carlo, F. 2010: Investigation of PF adhesive penetration in wood by micro x-ray tomography. In: Frihart, C. R., Hunt, C. G. and Moon, R. J., editors, *Proceedings of the International Conference on Wood Adhesives 2009*, South Tahoe, NV, USA: Forest Products Society, 343 - 347.

Kamke, F. A. and Lee, J. N. (2007) Adhesive penetration in wood - a review. *Wood and Fiber Science* 39, 2, 205-220.

Miroy, F., Eymard, P. and Pizzi, A. (1995) Wood hardening by methoxymethyl melamine. *European Journal of Wood and Wood Products* 53, 4, 276-276.

Modzel, G. 2009: Computed X-ray analysis of wood-adhesive bonds. *Wood Science and Engineering*, Oregon State University, Corvallis, OR: 240.

Modzel, G., Kamke, F. A. and De Carlo, F. (2011) Comparative analysis of a wood-adhesive bondline. *Wood Science and Technology* 45, 1, 147-158.

Momose, A. (2003) Phase-sensitive imaging and phase tomography using X-ray interferometers. *Optics Express* 11, 19, 2303-2314.

Muller, U., Sretenovic, A., Vincenti, A. and Gindl, W. (2005) Direct measurement of strain distribution along a wood bond line. Part 1: Shear strain concentration in a lap joint specimen by means of electronic speckle pattern interferometry. *Holzforschung* 59, 3, 300-306.

Muszyński, L. and Launey, M. 2010: Advanced imaging techniques in wood-based panels research. In: Thoemen, H., Irle, M. and Sernek, M., editors, *Wood-Based Panels - An Introduction for Specialists*, COST Action E49: Brunel University Press, 177 - 201.

Nairn, J. A. (2006) Numerical simulations of transverse compression and densification in wood. *Wood and Fiber Science* 38, 4, 576-591.

Nairn, J. A. 2011: Material point method (NairnMPM) and finite element analysis (Nairn FEA) open-source software In.

NIH. 2013: ImageJ 1.47i. In, National Institute of Health.

Pfeiffer, F., Weitkamp, T., Bunk, O. and David, C. (2006) Phase retrieval and differential phase-contrast imaging with low-brilliance X-ray sources. *Nat. Phys.* 2, 4, 258-261.

Serrano, E. and Enquist, B. (2005) Contact-free measurement and non-linear finite element analyses of strain distribution along wood adhesive bonds. *Holzforschung* 59, 6, 641-646.

Tieman, B. C. 2007: HDF Reader plug-in 3.0. In: ImageJ, Advanced Photon Source, Argonne National Laboratory. Argonne, IL.

Umemura, K., Takahashi, A. and Kawai, S. (1998) Durability of isocyanate resin adhesives for wood I: Thermal properties of isocyanate resin cured with water. *Journal of Wood Science* 44, 3, 204-210.

Wilkins, S., Gureyev, T., Gao, D., Pogany, A. and Stevenson, A. (1996) Phase-contrast imaging using polychromatic hard X-rays. *Nature* 384, 6607, 335-338.

APPENDIX B. REPLICATE WEIGHTED PENETRATION RESULTS

Figures B-1 to B-3 show the individual replicate weighted penetration (WP) results for each adhesive/species treatment combination. These replicates were averaged to provide the treatment means shown in Table 6-1 and Figure 6-4. The data in Figure 6-6a, b and c, is again shown here in Figures B-1c, B-2a, and B-3c, respectively. WP results were averaged for both sides of the bondline for each slice, and each replicate contained approximately 1500 slices. Replicates 1 – 3 and 4 – 6 were excised from two separate, original laminates. Note, the y-axis for the IpMDI replicate graphs (Figure B-3) spans over a broader range than the IPF and hybrid PVAc data, as it had significantly greater penetration.

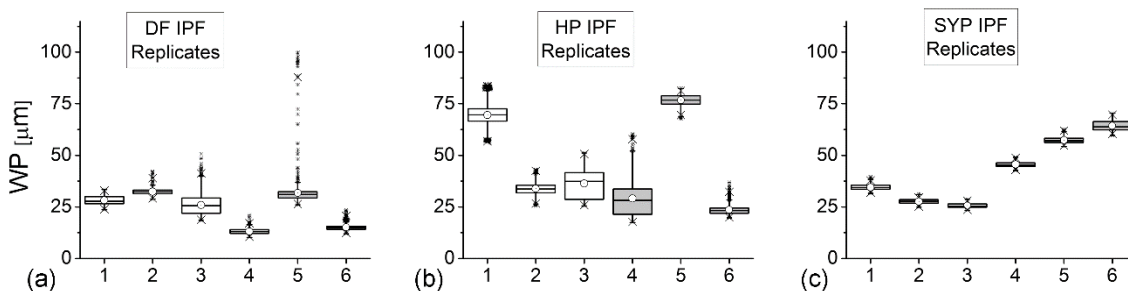


Figure B-1 IPF WP results by replicate for (a) DF, (b) HP, and (c) SYP; center circles = specimen means

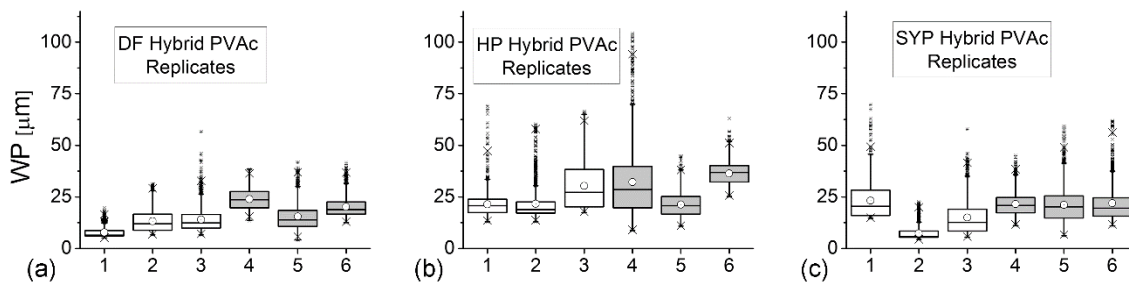


Figure B-2 Hybrid PVAc WP results by replicate for (a) DF, (b) HP, and (c) SYP; center circles = specimen means

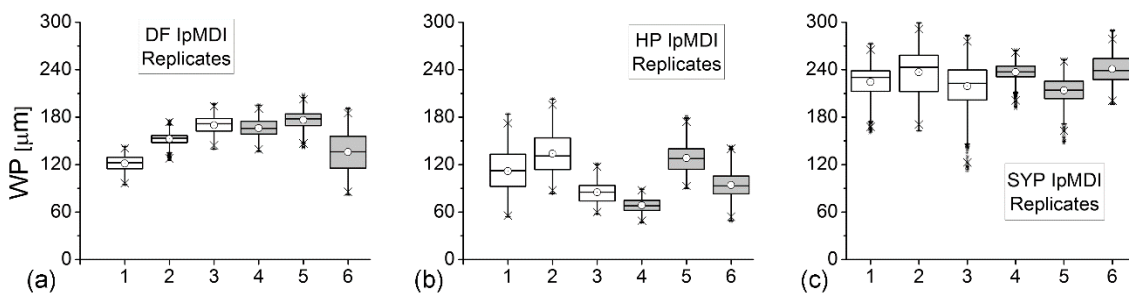


Figure B-3 IpMDI WP results by replicate for (a) DF, (b) HP, and (c) SYP; center circles = specimen means